DEVELOPMENT AND APPLICATION OF SEMI-ANALYTICAL METHOD FOR THERMAL SIMULATION OF LASER POWDER BED FUSION PROCESS

YANG Yang

Development and Application of Semi-Analytical Method for Thermal Simulation of Laser Powder Bed Fusion Process

Development and Application of Semi-Analytical Method for Thermal Simulation of Laser Powder Bed Fusion Process

Dissertation

for the purpose of obtaining the degree of doctor
at Delft University of Technology
by the authority of the Rector Magnificus,
Prof. dr. ir. H. Bijl,
chair of the Board for Doctorates
to be defended publicly on
on Friday 01 May 2026 at 10:00 o'clock

by

Yang Yang

This dissertation has been approved by the promotors

Composition of the doctoral committee:

Rector Magnificus,	chairperson
Prof. dr. ir. A. van Keulen,	Delft University of Technology, promotor
Dr. C. Ayas,	Delft University of Technology, promotor
Independent members:	
Prof. dr. ir. M. Langelaar,	Delft University of Technology
Prof. dr. I. Gibson,	University of Twente
Prof. Dr.-Ing. habil. S. Kollmannsberger,	University of Wuppertal, Germany
Dr. ir. M. J. M. Hermans,	Delft University of Technology
Dr. ir. J. J. C. Remmers,	Eindhoven University of Technology
Prof. dr. P. G. Steeneken,	Delft University of Technology, reserve member

Keywords: Metal additive manufacturing, laser powder bed fusion, thermal simulation, process optimization, phase transformation

Printed by: Proefschriftmaken

Cover art: Laser irradiation on print part. Generated with ChatGPT by Y. Yang.

ISBN 978-94-6518-313-8

An electronic version of this dissertation is available at
http://repository.tudelft.nl/.

Where there is light, there is shadow.

Contents

Summary ix

Samenvatting xi

1 Introduction 3
- 1.1 Additive manufacturing . . . 4
- 1.2 Laser powder bed fusion process . . . 5
- 1.3 Thermal simulation of the LPBF process . . . 7
- 1.4 Motivation of this thesis . . . 8
- 1.5 Outline of this thesis . . . 9
- Bibliography . . . 10

2 Image sources in semi-analytical method 15
- 2.1 Introduction . . . 16
- 2.2 Methodology . . . 19
- 2.3 Numerical examples and comparison of results . . . 30
- 2.4 Discussion . . . 45
- 2.5 Conclusions . . . 45
- Bibliography . . . 46

3 Semi-analytical isogeometric analysis for the LPBF process 53
- 3.1 Introduction . . . 54
- 3.2 IGA-based formulation of the semi-analytical method . . . 57
- 3.3 Numerical examples . . . 61
- 3.4 Conclusions and outlook . . . 75
- Bibliography . . . 76

4 Prevention of local overheating in the LPBF of Magnesium 83
- 4.1 Introduction . . . 84
- 4.2 Experimental method . . . 87
- 4.3 Simulation of the LPBF process . . . 90
- 4.4 Results and discussion . . . 95
- 4.5 Conclusions . . . 104

Bibliography . . . 104

5 Simulation of phase transformations during the LPBF Process 111
5.1 Introduction . . . 112
5.2 Model description . . . 115
5.3 Verification of phase transformation framework . . . 121
5.4 Numerical examples and results . . . 122
5.5 Conclusions . . . 135
Bibliography . . . 136

6 Conclusions and Recommendations 143
6.1 Conclusions . . . 144
6.2 Recommendations . . . 145

APPENDIX 147
APPENDIX A . . . 148
APPENDIX B . . . 148
APPENDIX C . . . 152

Curriculum Vitæ 161

List of Publications 163

SUMMARY

Laser Powder Bed Fusion (LPBF) has emerged as an influential metal additive manufacturing technology capable of producing geometrically complex, high-performance components. However, the process is governed by extremely high thermal gradients, rapid solidification, and repeated thermal cycles, all of which strongly influence microstructure formation, defect generation, and final part quality. Accurate part-scale thermal simulation is therefore essential for predicting process outcomes and guiding process-parameter optimization. This thesis advances the semi-analytical thermal modeling framework for LPBF, addressing limitations in existing semi-analytical methods and demonstrating its applicability to melt-pool prediction, overheating mitigation, and microstructural evolution analysis.

Conventional Finite Element Method (FEM)–based part-scale models face a fundamental challenge due to the multiscale nature of LPBF. The small laser spot size and associated steep temperature gradients require a fine Finite Element (FE) mesh near the heat source, while the large build volume demands computationally efficient discretization. Adaptive remeshing strategies alleviate part of this difficulty but incur high computational cost because the mesh must be updated frequently as the laser traverses the geometry. Semi-analytical methods provide an alternative by employing closed-form thermal solutions for moving point or line heat sources in a semi-infinite medium, thereby capturing the steep temperature gradients analytically without requiring local mesh refinement. However, the state-of-the-art semi-analytical formulations were limited to simple geometries with straight boundaries.

This thesis first extends the semi-analytical method by introducing a generalized image-source formulation capable of handling curved boundaries. Image sources offset the boundary heat flux induced by the regular heat sources, thereby enforcing appropriate boundary conditions, while decoupling the mesh size from the characteristic length scale dictated by laser spot size. Image source positions and power modulation factors are derived using local boundary curvature, supported by NURBS representations of arbitrary geometries, enabling the use of image sources for complex shapes. Numerical examples confirm that the modulated image-source approach dramatically reduces boundary heat-flux error and enables accurate temperature prediction with significantly coarser meshes. This advancement marks an important step in extending semi-analytical approaches to realistic part geometries.

The second methodological development replaces the FEM-based complementary-field computation with isogeometric analysis (IGA) in a semi-analytical thermal modeling framework. IGA employs NURBS basis functions that exactly represent geometry, allowing the simulation of realistic parts with complex geometries. In addition, with the exact geometric representation and higher-order continuity of NURBS basis functions, the numerical complementary field can be resolved with significantly fewer degrees of

freedom. Comparative studies show that the IGA-based formulation reduces computational cost by an order of magnitude while maintaining accuracy, making it highly attractive for large-scale LPBF simulations.

The semi-analytical thermal modeling framework is then applied to study overheating phenomena in LPBF of magnesium alloy. Using a triangular prism part geometry, the study reveals how geometric constraints—particularly decreasing scan vector length toward the tip of a triangular layer—lead to reduced cooling time, rapid heat accumulation, and significant increases in melt-pool depth. However, extremely short vectors experience insufficient heating duration, causing a sudden drop in melt-pool depth. Two mitigation strategies are proposed: extending zero-power ghost vectors and adjusting laser power based on vector length. Both numerical predictions and experimental results validate their effectiveness in homogenizing melt-pool depth and reducing porosity.

Finally, the semi-analytical thermal model is employed to investigate phase transformations in Ti-6Al-4V during LPBF under varying volumetric energy densities. Higher energy densities promote greater decomposition of martensite due to reheating from subsequent layers, whereas layers built at the end of the process contain a higher percentage of martensite phase because rapid cooling favors martensite formation. The semi-analytical model successfully captures the thermal transients required to drive these phase-transformation predictions. Besides, the effects of laser scanning strategies and the number of scanning lasers are also investigated, showing little influence on the overall phase fractions.

In summary, this thesis advances the semi-analytical modeling framework for LPBF and demonstrates its strong potential for predicting melt-pool behavior, mitigating defects, and understanding microstructural evolution.

SAMENVATTING

Laser Powder Bed Fusion (LPBF) is uitgegroeid tot een toonaangevende additieve productietechnologie voor metaal waarmee geometrisch complexe componenten met hoge prestaties vervaardigd kunnen worden. Het proces wordt echter gekenmerkt door extreem hoge thermische gradiënten, snelle stolling en herhaalde thermische cycli, die allemaal een sterke invloed hebben op microstructuurvorming, defectgeneratie en de uiteindelijke kwaliteit van een onderdeel. Nauwkeurige thermische simulatie op onderdeelschaal is daarom essentieel om procesuitkomsten te voorspellen en de optimalisatie van procesparameters te sturen. Dit proefschrift breidt het kader voor semi-analytische thermische modellering voor LPBF uit, pakt beperkingen in bestaande semi-analytische methoden aan en toont de toepasbaarheid ervan aan voor smeltbadvoorspelling, het beperken van oververhitting en de analyse van microstructurele evolutie.

Conventionele Eindige-Elementenmethode (FEM) simulaties op onderdeelschaal hebben een fundamentele uitdaging vanwege het LPBF proces dat op meerdere schalen plaatsvindt. De kleine laserspotgrootte en de bijbehorende steile temperatuurgradiënten vereisen een fijne eindig-elementen (FE) mesh nabij de warmtebron, terwijl het grote onderdeelvolume vraagt om een computationeel efficiënte discretisatie. Strategieën die de mesh adaptief aanpassen verlichten dit probleem gedeeltelijk, maar brengen hoge rekenkosten met zich mee doordat de mesh frequent moet worden bijgewerkt terwijl de laser zich langs de geometrie verplaatst. Semi-analytische methodes bieden een alternatief door gebruik te maken van analytische thermische oplossingen voor bewegende punt- of lijnwarmtebronnen in een semi-oneindig medium, waardoor steile temperatuurgradiënten analytisch worden vastgelegd zonder lokale verfijning van de mesh. De state-of-the-art semi-analytische methodes zijn echter beperkt tot eenvoudige geometrieën met rechte randen.

In dit proefschrift wordt eerst de semi-analytische methode uitgebreid door de introductie van een gegeneraliseerde beeldbronnenformulering die gebogen grenzen kan behandelen. Beeldbronnen compenseren de warmtestroom aan de rand die wordt geïnduceerd door de reguliere warmtebronnen en dwingen zo de juiste randvoorwaarden af, terwijl de meshgrootte wordt ontkoppeld van de karakteristieke lengteschaal die door de laserspotgrootte wordt bepaald. De posities van de beeldbronnen en de vermogensmodulatiefactoren worden afgeleid op basis van de lokale randkromming, ondersteund door NURBS-representaties van willekeurige geometrieën, waardoor het gebruik van beeldbronnen voor complexe vormen mogelijk wordt. Numerieke voorbeelden bevestigen dat de gemoduleerde beeldbronnenformulering de fout in de warmtestroom aan de rand drastisch vermindert en een nauwkeurige temperatuurvoorspelling mogelijk maakt met aanzienlijk grovere meshes. Deze stap vormt een belangrijke stap bij het uitbreiden van semi-analytische benaderingen naar realistische onderdeelgeometrieën.

De tweede methodologische ontwikkeling vervangt de FEM-gebaseerde berekening

van het complementaire veld door isogeometrische analyse (IGA) in een semi-analytisch thermisch modelleringskader. IGA maakt gebruik van NURBS-basisfuncties die de geometrie exact representeren, waardoor de simulatie van realistische onderdelen met complexe geometrieën mogelijk wordt. Bovendien kan dankzij de exacte geometrische representatie en de hogere-orde continuïteit van NURBS-basisfuncties het numerieke complementaire veld worden opgelost met aanzienlijk minder vrijheidsgraden. Vergelijkende studies tonen aan dat de op IGA gebaseerde formulering de rekenkosten met een orde van grootte verlaagt, terwijl de nauwkeurigheid behouden blijft, wat de methode bijzonder aantrekkelijk maakt voor grootschalige LPBF-simulaties.

Vervolgens wordt het semi-analytische thermische modelleringskader toegepast om oververhittingsverschijnselen in LPBF van magnesiumlegeringen te bestuderen. In een geometrie van een driehoekige prisma laat de studie zien hoe geometrische beperkingen, met name de afnemende lengte van de scanvector richting de punt van de driehoekige laag, leiden tot een verkorte afkoeltijd, snelle warmteaccumulatie en een aanzienlijke toename van de smeltbaddiepte. Zeer korte scanvectoren worden echter onvoldoende verwarmd, wat leidt tot een plotselinge afname van de smeltbaddiepte. Twee mitigatiestrategieën worden voorgesteld: het verlengen van nul vermogen ghostvectoren en het aanpassen van het laservermogen op basis van de vectorlengte. Zowel numerieke voorspellingen als experimentele resultaten bevestigen de effectiviteit van deze strategieën om smeltbaddiepte te homogeniseren en porositeit te verminderen.

Ten slotte wordt het semi-analytische thermische model gebruikt om faseovergangen in Ti-6Al-4V tijdens LPBF te onderzoeken onder verschillende volumetrische energiedichtheden. Hogere energiedichtheden zorgen voor een sterk verval van martensiet als gevolg van herverhitting door opeenvolgende lagen, terwijl lagen die aan het einde van het proces worden gevormd een hoger percentage martensiet bevatten, doordat snelle afkoeling de vorming van martensiet bevordert. Het semi-analytische model legt de thermische transiënten die nodig zijn voor deze faseovergangsvoorspellingen succesvol vast. Daarnaast worden ook de effecten van laserscanstrategieën en het aantal scanlasers onderzocht, waarbij slechts een geringe invloed op de totale fasefracties wordt waargenomen.

Samenvattend breidt dit proefschrift het semi-analytische modelleringskader voor LPBF uit en toont het het grote potentieel ervan aan voor het voorspellen van smeltbadgedrag, het beperken van defecten en het begrijpen van microstructurele veranderingen.

1

1

Introduction

In this chapter, we present an overview of the current status of metal Additive Manufacturing (AM), specifically the Laser Powder Bed Fusion (LPBF) process. Then, we provide a state-of-the-art review to motivate the investigation of part-scale thermal and microstructural simulations.

1

Chimpanzees display rudimentary tool-use behaviors—for example, breaking off branches and performing simple modifications, such as stripping leaves from a branch, to obtain food, explore their surroundings, or accomplish specific tasks. Although these behaviors represent a primitive form of tool use among primates, they do not possess systematic manufacturing techniques. Manufacturing and processing reflect humanity's ability to transform raw materials from nature into functional tools. Within the broader context of manufacturing technologies, Additive Manufacturing (AM) provides a fundamentally distinct approach that enables significantly greater design freedom than conventional methods such as subtractive machining, casting, forging, injection molding, and so on. This attribute originates from the distinctive part-fabrication way inherent to AM, commonly known as three-dimensional (3D) printing.

1.1. ADDITIVE MANUFACTURING

Additive manufacturing is widely regarded as a pivotal enabling technology of the fourth industrial revolution, owing to its exceptional capacity to realize complex geometries with virtually unrestricted design freedom [1, 2]. In the AM process, the part is manufactured layer-by-layer on a build platform, shown in Fig. 1.1. The material is added on top of the previously deposited material, finally forming the three-dimensional cylinder. Based on the types of materials employed, additive manufacturing can be categorized into metal, polymer, ceramic, and biological (bioprinting) additive manufacturing. This thesis focuses on metal additive manufacturing, which addresses the growing demand for high-performance, geometrically complex, and highly integrated metal components for structural applications. A representative industrial example is the additively manufactured fuel nozzle developed by GE Aviation, which has been deployed at scale in aircraft engines [3]. The engines equipped with those fuel nozzles can achieve fuel efficiency improvements of up to 15%.

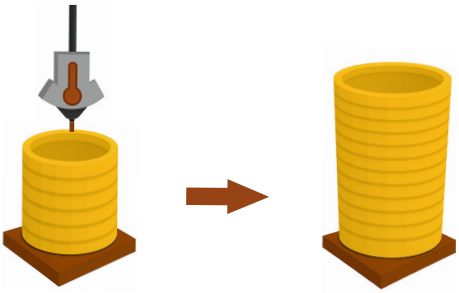

Figure 1.1: Illustration of the additive manufacturing (3D printing) process of a cylinder printed on top of a build platform.

Metal additive manufacturing can be mainly divided into Directed Energy Deposition (DED) and Powder Bed Fusion (PBF). In DED, a guiding energy, such as a laser or electric arc, and coaxial material feed facilitate the deposition of metal layers, and the molten material is deposited onto previously deposited layers or the underlying substrate. For example, Wire Arc Additive Manufacturing (WAAM) employs an electric arc

as the heat source and a metal wire as the feedstock. It is primarily employed for the fabrication of large metal components thanks to its high material deposition rate, but with low dimensional resolution and surface quality. In contrast, Powder Bed Fusion (PBF) utilizes one or multiple high-energy beams to selectively heat and melt predefined regions within a metal powder bed. Depending on the energy source employed, PBF is further classified into Laser Powder Bed Fusion (LPBF) and Electron Beam Powder Bed Fusion (EB-PBF). Owing to its superior dimensional accuracy relative to directed energy deposition (DED), powder bed fusion (PBF) is widely employed in the fabrication of high-precision structures, such as lithography equipment (e.g., conditioning rings), aerospace applications (e.g., engine brackets), and medical implants (e.g., bone substitutes). This thesis focuses on the laser powder bed fusion (LPBF) process, which is described in detail in Section 1.2.

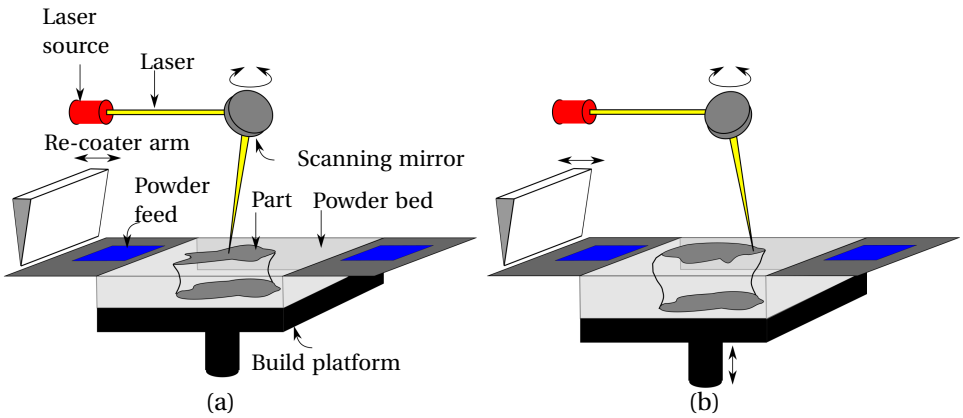

Figure 1.2: Schematic illustration of the laser powder bed fusion process, reproduced from R. Ranjan, PhD thesis, 2023 [4], with permission of the author. (a) A laser beam reflected by the mirror is focused on to heat and melt selected locations on the metal powder bed. The newly deposited material is fused to the previously printed parts below. (b) As the printing process of a layer is finished, the build platform goes down, and a new layer of metal powder is recoated. Then, the laser begins to print a subsequent layer.

1.2. LASER POWDER BED FUSION PROCESS

In the LPBF process, one or multiple lasers are used to heat and melt metal powder to manufacture the designed part layer-by-layer, as shown in Fig. 1.2. The printed part is enclosed in an inert atmosphere. The thickness of the powder layer is usually around 20-100 μm. The laser(s) selectively scan the powder bed and fully melt designated regions in accordance with the predefined geometry of this layer. Once the heat source moves away, the molten pool undergoes rapid cooling, leading to solidification and the formation of localized microstructural features. Moreover, during the process, the microstructure of the previously deposited layers is influenced and modified extensively. As the printing process of the current layer finishes, the build platform goes down, and a new layer of powder is recoated on the top of the printed part, then the laser(s) start to scan the subsequent layer. This repeated sequence of melting, solidification, and layer-

wise bonding ultimately yields a fully consolidated three-dimensional component.

However, parts built by the LPBF process suffer from several defects [5], including lack of fusion pores [6], over-heating pores [6], cracks [7], thermal distortion [8], presence of brittle martensite phase [9], and so on. Illustrations of different defects are given in Fig. 1.3.

Lack-of-fusion pores, shown in Fig. 1.3a, arise from insufficient laser energy input, which prevents full melting and consolidation of neighboring powder particles or melt tracks. Because unmelted material becomes trapped during solidification, these pores typically exhibit irregular or angular shapes. Such defects are commonly associated with low laser power, high scan speeds, or large hatch spacing, and usually lead to reduced tensile properties, poor surface finish, fatigue failure, and lower corrosion resistance.

In contrast, as shown in Fig. 1.3b, overheating-associated keyhole pores form when excessive laser energy creates deep, unstable vapor cavities within the melt pool. Collapse or oscillation of these keyhole traps gas, producing pores that are generally round. High power, slow scan speeds, or repeated laser exposure often promote their formation. Similar to lack-of-fusion pores, this kind of pore will reduce part density, work as a crack initiation [10], and lead to stress concentration.

Cracks, shown in Fig. 1.3c, may develop during both the powder-liquid-solid state changes and the subsequent solid phase cooling process. Rapidly changing steep thermal gradients and local compositional variations can lead to solidification cracking, while residual stresses generated during cooling can cause additional cracking in the solid phase. Thermal distortion results from nonuniform temperature distributions induced by localized laser heating. These steep thermal gradients cause differential expansion and contraction, generating internal stresses that may warp the part or lead to dimensional inaccuracies, as shown in Fig. 1.3d.

The brittle martensitic phase shown in Fig. 1.3e originates from the extremely high cooling rates inherent to the LPBF process, which promote diffusionless phase transformation. In additively manufactured Ti-6Al-4V alloys, the martensitic phase typically exhibits acicular morphology and is a common microstructural feature, particularly in as-built conditions. The presence of this phase reduces ductility, thereby often contributing to the overall brittle mechanical failure of the fabricated components.

All of the aforementioned defects are closely linked to the thermal history experienced during the LPBF process. Reliance on experimental approaches alone is often insufficient for optimizing process parameters and eliminating these defects. Consequently, thermal simulations of the LPBF process provide a powerful and efficient tool for process optimization, enabling the prediction and mitigation of defect formation.

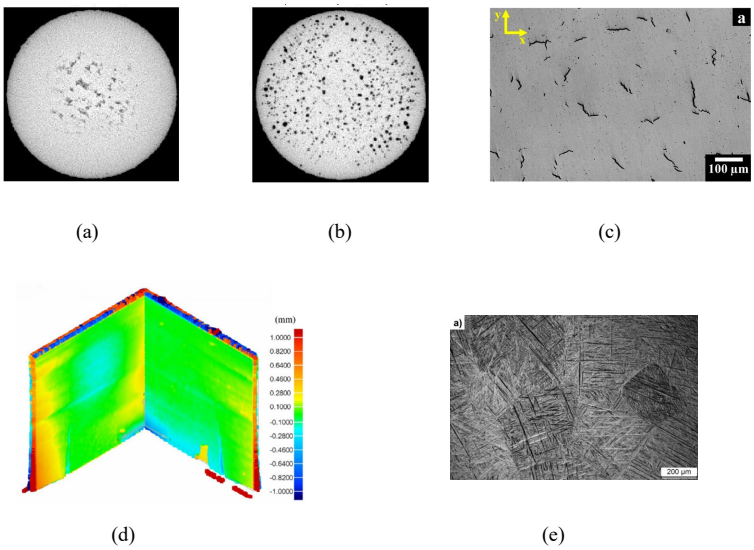

Figure 1.3: Defects commonly observed in the laser powder bed fusion process. (a) Lack-of-fusion pores, adapted from Booth et al. [6], licensed under CC BY 4.0 (https://creativecommons.org/licenses/by/4.0/), (b) over-heating pores, adapted from Booth et al. [6], licensed under CC BY 4.0, (c) cracks, adapted from Marchese et al. [7], licensed under CC BY 4.0, (d) thermal distortion of a thin walled structure, adapted from Lu et al. [8], licensed under CC BY 4.0, (e) brittle martensite phase, adapted from Motyka [9], licensed under CC BY 4.0.

1.3. THERMAL SIMULATION OF THE LPBF PROCESS

The thermal simulation of the LPBF process plays a crucial role in predicting the thermal history of the process, thereby enabling the mitigation or avoidance of process-induced defects. However, the LPBF process is a complex multi-physics process involving numerous physical phenomena, such as laser energy absorption, phase changes between solid, liquid, and even gas states, heat conduction, radiation, convection heat transfer, fluid dynamics, phase transformations, and solid mechanics, which occur in different temperature ranges and together influence the final properties of additive-manufactured parts. Solving this multi-physics problem in a computationally tractable way is almost an impossible task.

Moreover, the LPBF process is inherently multiscale in nature. The melting and solidification phenomena occur on millisecond timescales [11], in contrast to the overall build duration, which may span several hours or even multiple days. In addition, the laser spot typically possesses a radius on the order of 20–100 μm, whereas the characteristic dimensions of manufactured components can reach approximately 20 cm. A significant challenge in thermal analysis of the LPBF process arises from the pronounced mismatch in time scales between the solid–liquid phase transformation and the overall printing duration. Employing time steps sufficiently small to resolve these rapid phase-change events throughout the entire build would result in an impractically large number of time increments. In addition to the temporal disparity, a substantial mismatch in length scales also complicates the analysis. Resolving both scales simultaneously in a

single simulation greatly increases computational cost and complexity.

Besides, in the LPBF process, the part geometry evolves as material is continuously deposited layer by layer, resulting in a time-dependent and expanding computational domain. Efficiently handling this growing domain is also a challenge for numerical simulation frameworks.

Given the inherent complexity of the LPBF process, the challenges outlined above cannot be resolved in a single simulation model. As a result, different LPBF simulation approaches are proposed and generally divided into micro-, meso-, and macro-scale models. For models of different scales, the targets are different. Micro-scale models aim to capture the interactions between the powder and the laser spot, focusing on melt-pool dynamics, powder-scale melting and solidification, and the mechanisms leading to defect formation. As the molten metal forms the melt pool, meso-scale continuum models are used to describe heat transfer and to predict melt-pool morphology and temperature fields by accounting for fluid flow, Marangoni convection, and capillary forces [12, 13]. The macro-scale models, also commonly known as part-scale models, are mainly used for the calculation of part-scale temperature history and thermal stress, and phase distribution [14–17] in a computationally inexpensive way. The details of metal powder melting behavior, melt-pool dynamics, fluid flow, Marangoni convection, and capillary forces in micro and meso-scale models are no longer explicitly considered. For the most simplified part-scale models, even the laser scanning tracks and motion during layer-wise deposition are not modeled [18, 19]. Explicit resolution of laser motion at the part scale is generally computationally expensive and challenging, as demonstrated in, for example, e.g. [20, 21] and detailed in Sections 2.1 and 3.1.

1.4. MOTIVATION OF THIS THESIS

Efficient part-scale modeling is essential for identifying suitable process-parameter windows that mitigate defect formation in the LPBF process. During the entire LPBF process, laser scanning tracks and motion play a critical role in influencing defect evolution. However, existing FEM–based part-scale models that incorporate laser motion exhibit several inherent limitations. The biggest challenge is that, in conventional FEM frameworks, accurately capturing the steep temperature gradients generated by the moving laser source requires continuous adaptive mesh refinement in response to the rapidly changing laser position. This frequent remeshing significantly reduces computational efficiency. The constraints associated with such adaptive mesh refinement are discussed in detail in Section 2.1. To address these challenges, a semi-analytical modeling approach has been introduced that removes the need for adaptive meshing [22, 23]. Nevertheless, the current semi-analytical formulations also present notable limitations. The boundary condition enforcement implemented with FEM exhibits limited computational efficiency, while the boundary condition correction approach based on image sources is applicable only to straight boundaries and extruded part shapes. Details are provided in Sections 2.1 and 3.1. As a result, the current semi-analytical method has yet to be extended to the thermal simulation of LPBF processes involving complex geometries. Therefore, this thesis aims to advance the existing semi-analytical thermal modeling framework and to demonstrate its applicability to predicting melt-pool geometry and phase transformations and distributions in the LPBF process.

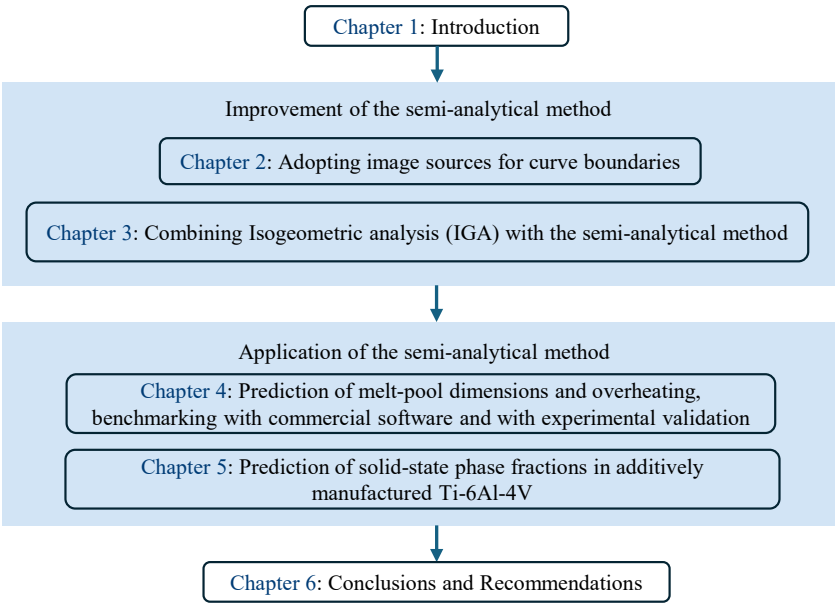

Figure 1.4: A visual overview of the thesis outline. This thesis consists of two core sections: improvement of the state-of-the-art semi-analytical method for part-scale LPBF thermal modeling, and subsequent applications of the models for predicting melt-pool dimensions and volume fractions of solid-state phases.

1.5. OUTLINE OF THIS THESIS

Fig. 1.4 illustrates the overall structure of this thesis, which is organized into two major parts. The first part concerns the methodological development and improvement of the state-of-the-art semi-analytical modeling framework. In its current form, the semi-analytical method cannot account for geometrically complex parts. In this thesis, we extend and generalize the concept of image sources so that they can be effectively applied to curved boundaries. This extension enables the semi-analytical method to accommodate more complex geometric configurations, as detailed in Chapter 2. Additionally, we replace the Finite Element Method (FEM) component of the current semi-analytical methodology with isogeometric analysis (IGA), which provides a more unified geometric representation and leads to notable computational advantages, and unlocks the capability of simulating realistic parts with complex geometry. The incorporation of IGA is presented and analyzed in Chapter 3.

The second part of the thesis focuses on the application of the current semi-analytical methodology to problems in the LPBF process. First, we employ the method to predict melt-pool geometry during the LPBF process, compare the results with those obtained from commercial software and experiments. Then, based on the study of melt-pool geometry, several scanning strategies are proposed and investigated to avoid overheating phenomena, thereby contributing to improved part quality, as discussed in Chapter 4.

Furthermore, the semi-analytical framework that accounts for multiple lasers is used to predict phase transformations and spatial volume fractions of solid-state phases dur-

ing LPBF of Ti-6Al-4V alloy, as elaborated in Chapter 5. Through this study, we identify the key transformation mechanisms that govern the attainment of the desired phase distributions and how process parameters, such as laser power and scanning velocity, influence the phase transformations and distributions.

BIBLIOGRAPHY

[1] I. Gibson, D. Rosen, B. Stucker, and M. Khorasani, *Additive manufacturing technologies*, 3rd (Springer, 2021).

[2] M. Bayat, O. Zinovieva, F. Ferrari, C. Ayas, M. Langelaar, J. Spangenberg, R. Salajeghe, K. Poulios, S. Mohanty, O. Sigmund, and J. Hattel, "Holistic computational design within additive manufacturing through topology optimization combined with multi-physics multi-scale materials and process modelling", Progress in Materials Science **138**, 101129 (2023).

[3] GE Aerospace, *Manufacturing milestone: 30,000 additive fuel nozzles*, (2023) https://www.geaerospace.com/news/articles/manufacturing/manufacturing-milestone-30000-additive-fuel-nozzles (visited on 12/14/2025).

[4] R. Ranjan, "Efficient thermal modelling and topology optimization for additive manufacturing", English, Dissertation (TU Delft) (Delft University of Technology, 2023).

[5] R. Villa, Y. Liu, and Z. Siddique, "Review of defects and their sources in as-built ti6al4v manufactured via powder bed fusion", The International Journal of Advanced Manufacturing Technology **132**, 4105–4134 (2024).

[6] B. G. Booth, R. Heylen, M. Nourazar, D. Verhees, W. Philips, and A. Bey-Temsamani, "Encoding stability into laser powder bed fusion monitoring using temporal features and pore density modelling", Sensors **22**, 10.3390/s22103740 (2022).

[7] G. Marchese, G. Basile, E. Bassini, A. Aversa, M. Lombardi, D. Ugues, P. Fino, and S. Biamino, "Study of the microstructure and cracking mechanisms of hastelloy x produced by laser powder bed fusion", Materials **11**, 10.3390/ma11010106 (2018).

[8] X. Lu, M. Chiumenti, M. Cervera, H. Tan, X. Lin, and S. Wang, "Warpage analysis and control of thin-walled structures manufactured by laser powder bed fusion", Metals **11**, 10.3390/met11050686 (2021).

[9] M. Motyka, "Martensite formation and decomposition during traditional and am processing of two-phase titanium alloys—an overview", Metals **11**, 10.3390/met11030481 (2021).

[10] S. Kramer, H. Wexel, A. Purwitasari, M. Jarwitz, V. Schulze, and F. Zanger, "Impact of different pore types on the tensile and fatigue properties of alsi10mg parts produced by laser powder bed fusion", Progress in Additive Manufacturing **10**, 11305–11317 (2025).

[11] R. Cunningham, C. Zhao, N. Parab, C. Kantzos, J. Pauza, K. Fezzaa, T. Sun, and A. D. Rollett, "Keyhole threshold and morphology in laser melting revealed by ultrahigh-speed x-ray imaging", Science **363**, 849–852 (2019).

[12] M. Bayat, W. Dong, J. Thorborg, A. C. To, and J. H. Hattel, "A review of multi-scale and multi-physics simulations of metal additive manufacturing processes with focus on modeling strategies", Additive Manufacturing **47**, 102278 (2021).

[13]H. Chen, Y. Sun, W. Yuan, S. Pang, W. Yan, and Y. Shi, "A review on discrete element method simulation in laser powder bed fusion additive manufacturing", Chinese Journal of Mechanical Engineering: Additive Manufacturing Frontiers **1**, 100017 (2022).

[14]C. C. Murgau, R. Pederson, and L.-E. Lindgren, "A model for ti–6al–4v microstructure evolution for arbitrary temperature changes", Modelling and Simulation in Materials Science and Engineering **20**, 055006 (2012).

[15]C. Baykasoglu, O. Akyildiz, D. Candemir, Q. Yang, and A. C. To, "Predicting microstructure evolution during directed energy deposition additive manufacturing of ti-6al-4v", Journal of Manufacturing Science and Engineering **140**, 10.1115/1.4038894 (2018).

[16]C. Baykasoğlu, O. Akyildiz, M. Tunay, and A. C. To, "A process-microstructure finite element simulation framework for predicting phase transformations and microhardness for directed energy deposition of ti6al4v", Additive Manufacturing **35**, 101252 (2020).

[17]W. Sun, F. Shan, N. Zong, H. Dong, and T. Jing, "A simulation and experiment study on phase transformations of ti-6al-4v in wire laser additive manufacturing", Materials & Design **207**, 109843 (2021).

[18]R. Ranjan, C. Ayas, M. Langelaar, and F. van Keulen, "Fast detection of heat accumulation in powder bed fusion using computationally efficient thermal models", Materials **13**, 10.3390/ma13204576 (2020).

[19]M. Chiumenti, E. Neiva, E. Salsi, M. Cervera, S. Badia, J. Moya, Z. Chen, C. Lee, and C. Davies, "Numerical modelling and experimental validation in selective laser melting", Additive Manufacturing **18**, 171–185 (2017).

[20]A. Olleak and Z. Xi, "Scan-wise adaptive remeshing for efficient lpbf process simulation: the thermal problem", Manufacturing Letters **23**, 75–78 (2020).

[21]E. R. Denlinger, M. Gouge, J. Irwin, and P. Michaleris, "Thermomechanical model development and in situ experimental validation of the laser powder-bed fusion process", Additive Manufacturing **16**, 73–80 (2017).

[22]Y. Yang, M. Knol, F. van Keulen, and C. Ayas, "A semi-analytical thermal modelling approach for selective laser melting", Additive Manufacturing **21**, 284–297 (2018).

[23]Y. Yang, F. van Keulen, and C. Ayas, "A computationally efficient thermal model for selective laser melting", Additive Manufacturing **31**, 100955 (2020).

2

2

IMAGE SOURCES IN SEMI-ANALYTICAL METHOD

Part-scale thermal process simulations play an important role in improving the part quality of the Laser Powder Bed Fusion (LPBF) process. The semi-analytical simulation method relies on the superposition of analytical fields to represent laser-induced heat sources in a semi-infinite space and a complementary temperature field to enforce boundary conditions. So far, boundary conditions have been imposed by analytical image fields for straight boundaries and numerically for non-straight boundaries. The latter requires considerable refinement on the spatial discretization, at least near the boundaries, and compromises the computational efficiency of the simulations. In this chapter, we derive a closed-form solution for the image fields that can accurately enforce the boundary conditions for non-straight boundaries. A geometrically complex part boundary is represented by B-splines, and with the aid of an offset method and reparameterization, the positions of the image sources are determined. The image field's closed-form expression is then found using the boundary's local curvature calculated from the local tangent lines. Numerical examples on different levels of complexity revealed that the net heat lost along an adiabatic boundary vanishes when the novel image source solutions are used, and the thermal evolution of complex parts can be accurately predicted with high computational efficiency. Simulations involving multiple lasers can also be performed with no extra computational cost.

Parts of this chapter have been published in *International Journal of Heat and Mass Transfer*, **248**, 127059 (2025) by Yang Yang, Ye Ji, Matthias Möller and Can Ayas.

2.1. INTRODUCTION

Laser Powder Bed Fusion (LPBF) is a metal additive manufacturing process that builds parts ranging from a few millimeters to centimeters. In the LPBF, one or multiple lasers serve as localized and instantaneous heat sources, melting and fusing the powder to construct 3D parts layer by layer. Several thermal processes occur during this process, including heat absorption by the metal powder from the laser(s), phase changes between solid, liquid, and even gas states, heat conduction, radiation, and convection. To begin with, the metal powder partially absorbs the laser energy, triggering a phase change from solid to liquid as the temperature reaches the melting point. Subsequently, when the lasers move away, rapid solidification occurs as the molten metal cools. Heat conduction is critical throughout this process in conveying heat to the build platform, which serves as a heat sink. Moreover, the heat transfer between the already solidified part and the surrounding metal powder is insignificant, as the thermal conductivity of the metal powder is approximately 1% of the solid part [1]. Additionally, radiation transfers part of the energy to the surrounding environment, especially in the high-temperature melt pool zone. Convection also occurs between the part and the inert gas in the chamber. These thermal processes collectively influence the microstructural evolution, residual stress, and distortion, thereby, the part quality and mechanical properties [2].

Optimal process parameters (e.g., laser power and scanning velocity) are essential to avoid defects, warping, residual stress, and poor surface finish while ensuring dimensional accuracy and mechanical performance. However, determining the optimal process parameters through experiments alone is challenging and costly. In addition to laser power and scanning velocity, the laser scanning strategy (or path) plays a crucial role in thermal evolution. Currently, advanced 3D metal printers are equipped with multiple lasers, operating simultaneously to enhance the speed of the printing process. Consequently, the complexity of laser scanning further increases since more freedom is allowed in scanning with multiple lasers involved. Therefore, optimizing the laser scan vectors along with laser power and velocity becomes even more burdensome. Thermal simulations of the LPBF process serve as an invaluable tool, providing insights for optimizing process parameters and scanning strategies. Such models help predict thermal behavior, allowing for better control over the process to achieve desired part quality and mechanical properties.

Various numerical methods have been employed to compute the part-scale thermal history of the printing process. Finite Element Method (FEM) is widely adopted for solving the heat conduction process during metal additive manufacturing [3–6]. Sarkar [7] presented a comprehensive review of the state-of-the-art FEM applications in the LPBF process. The use of FEM in this context dates back to welding simulations, as LPBF and welding share many common features [8]. Lindgren [9–11] gave an overview of FEM applications in modeling and simulating welding processes, in which the elements representing filler material addition are activated during simulation, named as element birth and death method. Similarly, the element birth and death method simulates the growing domain nature of the LPBF process. This method can be further categorized into two types: the quiet element method and the inactive element method. In the quiet element method, elements corresponding to layers that are not yet realized are disabled by scaling down their thermal conductivity in the global conductivity matrix [12]. In contrast,

in the inactive element method, these elements are not assembled into the global conductivity matrix [13]. Lu et al. [14] adopted the inactive element method to predict the residual stress and distortion of Ti-6Al-4V thin wall structures. Chiumenti et al. [15, 16] improved this method by adding a new kind of activated elements that correspond to the new activated domain in the current moment. As a result, there are two different types of elements in the computational domain, one corresponding to the previously activated elements and one corresponding to the newly activated elements. The newly activated elements are activated at the material's melting temperature to avoid spurious thermal stresses from interacting with active elements. However, a finite element (FE) mesh must capture steep temperature gradients around the laser. Since lasers scan the entire part and thus interact with the whole simulation domain, albeit in different instances, spatial discretization is bound by the characteristic length scale, i.e. the laser size spot radius [13, 17]. For instance, Roberts et al. [13] adopted an element length of half of the laser source radius. Thus, these approaches can lead to an excessive number of elements in FEM and result in compromised computational efficiency.

Adaptive mesh refinement has been proposed to refine the mesh within laser interaction areas and dynamically coarsen it in regions far from the current laser spot positions. This method attracted significant attention due to its ability to reduce computational costs by reducing the number of degrees of freedom. Both h-refinement (refining the mesh size h) and hp-refinement (refining the mesh size and increasing the polynomial degrees of the trial/test space p) have been utilized [18–22]. Most simulations utilize a layer-wise (static) remeshing scheme, where the mesh is progressively refined after each layer deposition or after the deposition of several layers. Consequently, the mesh remains uniformly fine along the entire scanning path within the uppermost layers [18]. Li et al. [23] proposed an Octree mesh coarsening strategy for 3D printing thin wall structures. In this strategy, the mesh is dynamically coarsened towards the bottom layers, and the length of the finite elements doubles for each coarsening.

In contrast, the scan-wise (dynamic) remeshing scheme refines the mesh in the vicinity of the laser spot to capture steep temperature gradients following the laser motion. A relatively coarse mesh is used in regions away from the laser spot where the local temperature is more uniform [24, 25]. Compared to the layer-wise remeshing scheme, the scan-wise remeshing further decreases the number of degrees of freedom but requires the mesh to be frequently updated according to the laser positions during single-layer scanning. However, a computationally efficient way of adopting an analytical temperature field is proposed to remedy the need for the local mesh refinement [26].

These approaches rely on analytical solutions of heat equation in a semi-infinite space to represent the instantaneous laser exposure [26–30], either in the form of a Riemann sum of individual closed-form expressions of point heat sources generated incrementally [26, 31], or as a line source field through integrating the temperature contribution of infinitesimal point sources along a line [28–30]. Since the analytical field effectively captures the steep temperature gradients near the laser spot, there is no need for a moving fine mesh to capture these gradients numerically, significantly reducing computational complexity. Extensive research has been conducted using the analytical approach, exploring various aspects such as temperature history under different scan-

ning strategies [32, 33], melt pool geometry [31, 34, 35], and temperature-dependent thermal conductivity [29, 36]. Nevertheless, there is not always a closed-form temperature expression for arbitrary shapes of laser sources and complex laser scanning paths. Thus, Forslund et al. [37] introduced a method to integrate each segment of a laser scan path under a moving Gaussian heat source. Depending on the parameters of the heat source, the required quadrature orders are different to achieve the desired level of accuracy. Stump et al. [38] also conducted a study to improve the numerical integration of the point-source temperature field using Gaussian quadrature. This scheme discretizes a continuous line scan into a series of segments with adaptive time integration length. It demonstrates higher computational efficiency and more accurate temperature predictions than just using a simple Riemann sum of closed-form temperature fields from individual point sources [38]. The limited accuracy of the analytical temperature field arises from the assumption of a semi-infinite space, while the additive manufactured parts are finite. Therefore, boundary conditions of the finite part are not satisfied.

In the semi-analytical method, the temperature field is described by the superposition of the above-described analytical temperature field and a complementary numerical field to enforce the boundary conditions [26]. Within this method, adiabatic boundary conditions are usually assumed since the thermal conductivity of the metal powder is approximately 1% of the solid part [1, 28, 39], and the heat loss through convection and radiation on the boundary surface is relatively small compared to heat conduction within the solid part [13, 26, 40]. However, Ning et al. [27] applied the semi-analytical method using negative static point heat sources on boundary surfaces and an equivalent power method to account for heat loss due to convection and radiation. In this chapter, we assume the boundary conditions to be adiabatic and use FEM as the numerical method of choice to calculate the complementary numerical field in the semi-analytical method [28, 39]. Since the closed-form temperature field of the point sources captures steep temperature gradients around the laser spot, FE mesh is decoupled from the characteristic length scale of temperature gradients and hence can be much coarser. However, the FE mesh in the vicinity of the boundary must be sufficiently fine to resolve and correct for the outgoing heat flux due to the laser scanning near the boundary. Therefore, using FEM to apply the boundary conditions will still lead to excessive computational cost.

In our previous work, we incorporated analytical image sources to alleviate this computational burden to enforce the adiabatic boundary conditions by reflecting the point heat sources across the part boundaries [26]. This method allows a significantly coarser mesh for the entire domain and immensely reduces the computational cost. However, only straight boundaries can be considered with this method [26]. This is because only along straight boundaries, heat flux contributions from image and regular sources entirely cancel each other. For complex boundaries, the distances between image sources and boundary points differ from those of regular sources at most locations along the boundaries. Consequently, the adiabatic boundary conditions cannot be satisfied solely through image sources. Steuben et al. [29] proposed a method to achieve zero-flux boundary conditions using an image line source across part curve boundaries. This method provides an analytical description of the temperature field by combining a line source and its corresponding image with no numerical correction field. The intensity of

the image line source is adjusted by a modulation factor that accounts for the relative speed of the regular (i.e., the scanning velocity) and image sources. However, whether the modulated image source can achieve adiabatic boundary conditions everywhere on the local boundary is still unknown. Veldman et al. [41] proposed an imaging method to achieve zero-flux boundary conditions analytically. Nevertheless, the image part is not a solution to the homogeneous heat equation and is thus not related to any physical heat source term.

This chapter aims to fill this knowledge gap by focusing on image sources for geometrically complex parts with curved boundaries to enforce adiabatic boundary conditions. The main contributions in this chapter are as follows:

- A method of modulating the power of image sources is proposed to realize the approximate adiabatic boundary conditions, particularly for complex boundaries represented by B-splines. By offsetting B-spline curves, we can easily generate the regular point source positions in the domain and corresponding image source positions out of the domain. The modulation factor is derived and approximated to a simple closed form based on local curvatures from the B-spline parameter space.

- By employing the analytical temperature fields of regular sources and modulated image sources, the requirement for a fine mesh along part boundaries to impose adiabatic boundary conditions becomes unnecessary. The modulated image sources lead to a much smoother correction field, which requires fewer degrees of freedom to capture numerically. In this way, we achieve higher computational efficiency while ensuring accurate temperature predictions and accounting for the laser scan vectors for parts with complex geometries.

The remainder of the chapter is organized as follows: in Section 2.2, we introduce the semi-analytical method based on the discrete point sources. The position and power modulation of image sources for curved boundaries are described to achieve the desired adiabatic boundary conditions. The closed-form expression for the modulation factor is derived by balancing the flux through the curved boundaries due to regular and image sources. In Section 2.3, we first compare the heat loss rate on part boundaries in a single-source scenario. Next, we examine a case where a laser scans next to an arc boundary. Temperature histories and computational efficiencies are evaluated and compared using only regular sources, regular and non-modulated image sources, and regular and modulated image sources. Finally, the proposed method is extended to dual laser scanning and demonstrated in geometrically complex cases, and the key contributions of the study are reiterated.

2.2. METHODOLOGY

Consider the LPBF process of a 3D part with an arbitrary shape. Printing a new layer starts with recoating a layer of metal powder on the already printed body V. Therefore, the body V is submerged in the powder bed as shown in Fig. 2.1a. The surface ∂V of the body V comprises: the top surface ∂V_{top}, the lateral surface ∂V_{lat}, and the bottom surface ∂V_{bot}, such that $\partial V = \partial V_{\text{top}} \cup \partial V_{\text{lat}} \cup \partial V_{\text{bot}}$, as shown in Fig. 2.1b. The top surface ∂V_{top} and the lateral surface ∂V_{lat} are covered with powder, while the bottom surface ∂V_{bot} is

fused to the build platform. The origin of the coordinate system is shown in Fig. 2.1a, and the build orientation is along the positive x_3-axis. When the metal powder partially absorbs the emitted laser beam, the temperature field of the body evolves, governed by the heat equation

$$\rho c_p \frac{\partial T}{\partial t} = \nabla \cdot (k \nabla T) + Q \quad \text{in } V, \tag{2.1}$$

where T is the temperature field, ρ the mass density, c_p the heat capacity, k the thermal conductivity and Q the applied thermal load due to the laser. When we neglect the temperature dependence of ρ, c_p and k, Eq. (2.1) simplifies to its linear form

$$\frac{\partial T}{\partial t} = \alpha \nabla^2 T + \frac{Q}{\rho c_p} \quad \text{in } V, \tag{2.2}$$

where $\alpha = k/\rho c_p$ is the thermal diffusivity.

To quantify Q, the continuous laser scan is discretized into N regular point sources shown in Fig. 2.1a. The point source I is activated at time $\tilde{t}^{(I)}$ and the subsequent point source $I+1$ is activated at time $\tilde{t}^{(I+1)} = \tilde{t}^{(I)} + \Delta t$, where $I = 1, \ldots N-1$, and Δt is the temporal step size for time integration. Consequently, the distance between source I and $I+1$ is $v\Delta t$, where v is the laser scanning velocity. Since a series of consecutively activated sources represent the continuous laser scan, the accuracy of this representation depends on the number of point sources dictated by the temporal step size Δt. The convergence study in our previous paper shows that the temporal step size is related to the thermal conductivity and should be smaller than 5×10^{-5} s [26]. In all numerical examples that include a line scanning in Section 2.3, we use a relatively conservative $\Delta t = 1 \times 10^{-5}$ s to discretize continuous laser scans. When all laser scanning vectors of the current layer are completed, a new layer of metal powder is recoated.

To obtain the temperature distribution inside the domain V, we solve a boundary value problem (BVP) governed by Eq. (2.2) with boundary conditions on ∂V and the initial condition $T(x_i, 0) = T_c$ at $t = 0$, where T_c is the build platform temperature assumed to be constant. As explained above, the thermal conductivity of the metal powder is approximately 1% of the solid part [1]. Thus, the heat transfer between the solid part and the metal powder is neglected. Moreover, we disregard the heat loss through convection and radiation because their effect is relatively small compared to heat conduction within the solid part [13, 26, 40]. Consequently, adiabatic boundary conditions are applied on ∂V_{lat} and ∂V_{top} as

$$\frac{\partial T}{\partial x_i} n_i = 0 \quad \text{on} \partial V_{\text{lat}} \cup \partial V_{\text{top}}, \tag{2.3}$$

where n_i denotes the components of the surface unit outward normal vector, and the boundary condition for the bottom surface ∂V_{bot} is

$$T = T_c \quad \text{on} \partial V_{\text{bot}}. \tag{2.4}$$

Eqs. (2.2–2.4) do not explicitly consider the powder-liquid-solid state changes. The effects of heat absorption and release during state changes are neglected since the amount of heat absorbed during melting is subsequently released during solidification within short time intervals [26].

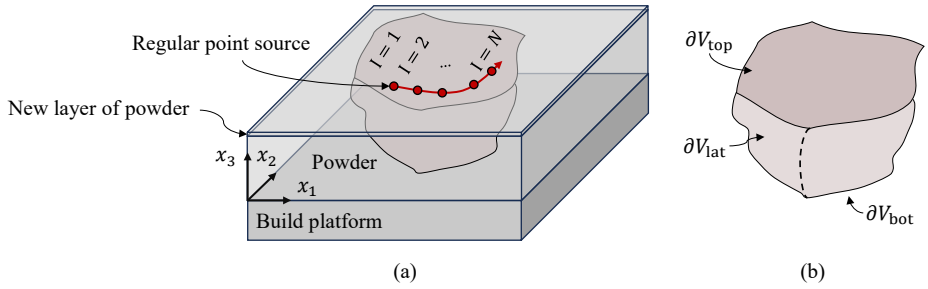

Figure 2.1: Schematic illustration of (a) the body V submerged into the powder bed, ∂V_{bot} fused to the build platform. The laser is emitted on the top layer, scanning along an arbitrary trajectory shown with the red curve. (b) the body V with its surface ∂V consisting of ∂V_{top}, ∂V_{lat} and ∂V_{bot}.

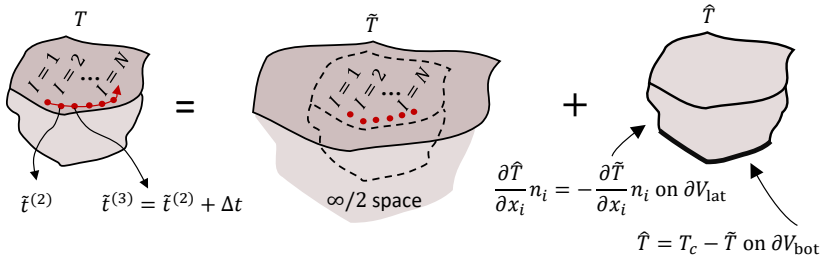

Figure 2.2: A continuous line scan is discretized into a series of point sources. The total temperature field is obtained by the superposition of the temperature field due to point sources in semi-infinite space and the complementary temperature field to enforce boundary conditions.

2.2.1. SEMI-ANALYTICAL METHOD FOR PART-SCALE THERMAL SIMULATION

Consider a laser scanning line as shown in Fig. 2.2. The continuous laser scan is discretized into N point sources on ∂V_{top}. The point sources are activated sequentially in accordance with their respective activation times. For this process, to solve the boundary value problem (BVP) outlined in Eqs. (2.2–2.4), the total temperature field T is expressed as the superposition of two terms [26] shown in Fig. 2.2 as

$$T = \tilde{T} + \hat{T}, \tag{2.5}$$

where $\tilde{T}$ is the analytical temperature field due to currently activated K out of total N sources. The temperature field $\tilde{T}$ is then given as

$$\tilde{T}(x_i, t) = \sum_{I=1}^{K} \tilde{T}^{(I)}(x_i, t), \quad \tilde{t}^{(K)} \leq t \text{ and } K \leq N, \tag{2.6}$$

where

$$\tilde{T}^{(I)}(x_i, t) = \frac{QA}{4\rho c_p (\pi\alpha(t - \tilde{\tau}^{(I)}))^{3/2}} \exp\left(\frac{-(R^{(I)})^2}{4\alpha(t - \tilde{\tau}^{(I)})}\right) \tag{2.7}$$

is the analytical solution of a point source in a half-infinite space, with the origin plane coinciding with ∂V_{top}. The distance between the point source location $\tilde{x}_i^{(I)}$ and the point of interest x_i is $R^{(I)}$. The input energy associated with each point source is $Q = P\Delta t$, where P is the laser power. A is the laser absorptivity fraction of metal powder. To account for the finite radius of the laser source and to avoid singularities at $t = \tilde{t}^{(I)}$, a time shift $\tilde{\tau}^{(I)} = \tilde{t}^{(I)} - r^2/8\alpha$ is applied in Eq. (2.7), where r denotes the laser spot radius. The time shift corresponds to diffusion distance in the material [26]. We note in passing, the temperature field of a point source with the time shift becomes the temperature field of a 3D Gaussian source with the laser spot radius r and a shape factor 2. This is demonstrated in APPENDIX A.

To impose the desired boundary conditions on ∂V, an additional field $\hat{T}$ is introduced to correct the analytically obtained field $\tilde{T}$ such that $\tilde{T} + \hat{T}$ meets the desired boundary conditions. The $\hat{T}$ field is governed by

$$\frac{\partial \hat{T}}{\partial t} = \alpha \nabla^2 \hat{T} \quad \text{in } V, \tag{2.8}$$

with boundary conditions derived from Eqs. (2.3) and (2.4) as

$$\frac{\partial \hat{T}}{\partial x_i} n_i = -\frac{\partial \tilde{T}}{\partial x_i} n_i \quad \text{on} \partial V_{\text{lat}}, \tag{2.9}$$

$$\hat{T} = T_c - \tilde{T} \quad \text{on} \partial V_{\text{bot}}, \tag{2.10}$$

and the initial condition at $t = 0$ is $\hat{T}(x_i, 0) = T(x_i, 0) - \tilde{T}(x_i, 0)$, and $T(x_i, 0) = T_c$. In fact, since $\tilde{T}(x_i, 0) = 0$, the initial condition at $t = 0$ becomes $\hat{T}(x_i, 0) = T_c$. It should be noted that no numerical correction is required on ∂V_{top} since the adiabatic top surface coincides with the origin of semi-infinite space. The adiabatic boundary conditions on the top surface of the part are automatically satisfied and built-in Eq. (2.7). In principle, the $\hat{T}$ is a smooth field since it contains no point sources. Consequently, the temperature field $\hat{T}$ can be solved with a standard numerical method FEM with a mesh size no longer dictated by the laser spot radius.

Nevertheless, when the point source I is located in the vicinity of ∂V_{lat}, the temperature gradients associated with $\tilde{T}^{(I)}$ at the part boundary ∂V_{lat} notably impairs the smoothness of $\hat{T}$, necessitating fine spatial discretization for accurate numerical solutions. Therefore, the FE mesh close to the lateral boundaries ∂V_{lat} needs to be refined in the order of laser spot radius r to resolve the temperature field associated with the laser beam [28]. To maintain computational efficiency without requiring such mesh refinement, we introduce image sources to assist in enforcing the boundary conditions.

Consider the temperature field in response to a laser scan vector, as illustrated in Fig. 2.2. The field is now represented as the superposition of three distinct temperature components, as shown in Fig. 2.3. The analytical field $\tilde{T}$ in Eq. (2.6) is due to regular point sources activated sequentially at each time step, marked by red dots. The corresponding image sources outside the body V are activated simultaneously to offset the high heat flux at the lateral boundary ∂V_{lat} due to nearby regular sources. The temperature decomposition in Eq. (2.5) is thus extended to include three components associated with the activated regular sources, rewritten as the superposition of three terms,

$$T = \tilde{T} + {}^{\epsilon}\check{T} + \hat{T}, \tag{2.11}$$

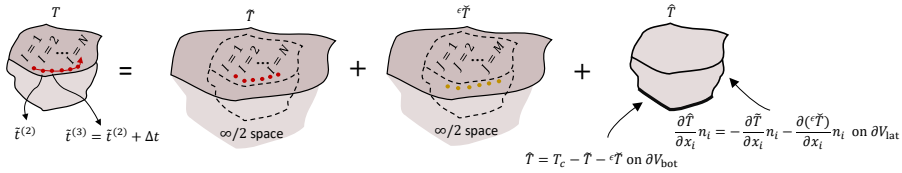

Figure 2.3: The total temperature field represented as the superposition of the temperature field of regular sources in semi-infinite space, the temperature field of image sources in semi-infinite space, and the complementary temperature field to apply boundary conditions.

where

$$ {}^{\epsilon}\breve{T}(x_i,t) = \sum_{J=1}^{K} \epsilon^{(J)} \breve{T}^{(J)}(x_i,t), \quad \breve{t}^{(K)} < t \text{ and } K \le M, \tag{2.12} $$

and

$$ \breve{T}^{(J)}(x_i,t) = \frac{QA}{4\rho c_p(\pi\alpha(t-\breve{\tau}^{(J)}))^{3/2}} \exp\left(\frac{(-R^{(J)})^2}{4\alpha(t-\breve{\tau}^{(J)})}\right). \tag{2.13} $$

Note that, $\breve{T}^{(J)}$ in Eq. (2.13) is similar to $\tilde{T}^{(I)}$ in Eq. (2.7), and also a closed-form solution in a semi-infinite space bounded by the top surface ∂V_{top}. Here, $R^{(J)}$ is the distance between the point of interest x_i and the image source location $\breve{x}_i^{(J)}$ [1]. The activation time of each image source J is $\breve{\tau}^{(J)}$, and at time t, K out of M image sources are activated. Note that the total number of image sources is much less than regular sources, as an image source is only created for a regular source sufficiently close to the lateral boundary. The critical distance d_c of a regular source to ∂V_{lat} is proposed to be less than or equal to $15r$ to induce an image source. Recall that when a regular source is away from a boundary, the temperature field due to the regular source is smooth on the boundary. The complementary field $\hat{T}$ described on a coarse FE mesh is thus sufficient to enforce the boundary condition at a desired level of accuracy. Therefore, there is no need to incorporate an image source when a regular source is away from a boundary. The proposed modulation factor $\epsilon^{(J)}$ scales the power of image source J. This modulation factor approximates the net heat flux from a pair of regular and image sources across the associated complex boundary to zero.

Similarly, for the decomposition in Eq. (2.11) and the BVP given in Eqs. (2.2–2.5), the $\hat{T}$ field remains governed by Eq. (2.2) but with boundary conditions

$$ \frac{\partial \hat{T}}{\partial x_i} n_i = -\frac{\partial \tilde{T}}{\partial x_i} n_i - \frac{\partial({}^{\epsilon}\breve{T})}{\partial x_i} n_i \quad \text{on} \partial V_{\text{lat}}, \tag{2.14} $$

$$ \hat{T} = T_c - \tilde{T} - {}^{\epsilon}\breve{T} \quad \text{on} \partial V_{\text{bot}}, \tag{2.15} $$

and the initial condition at $t = 0$ is $\hat{T}(x_i,0) = T(x_i,0) - \tilde{T}(x_i,0) - {}^{\epsilon}\breve{T}(x_i,0)$. Since $T(x_i,0) = T_c$ and $\tilde{T}(x_i,0) = \breve{T}(x_i,0) = 0$, the initial condition at $t = 0$ becomes $\hat{T}(x_i,0) = T_c$. By and large, the image sources neutralize the heat flux emanating from regular sources

[1] The details of identifying the positions of image sources across a complex boundary are discussed in Section 2.2.3.

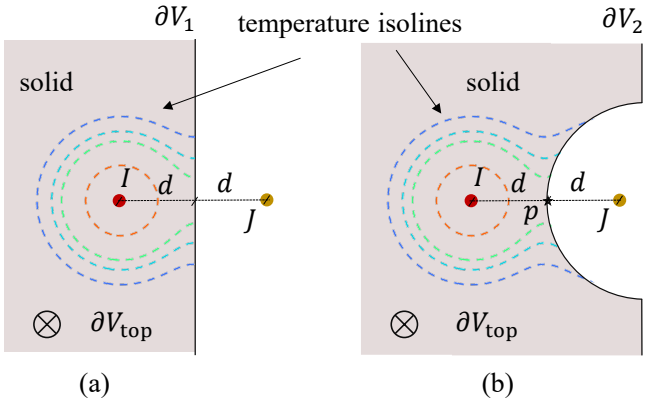

Figure 2.4: Schematic illustration temperature isolines of field of $\tilde{T}^{(I)} + \epsilon^{(J)}\check{T}^{(J)}$. The regular source I and J are on the top surface of the semi-infinite space. (a) The adiabatic boundary ∂V_1 divides the semi-infinite space into two parts, and the part to the left of the adiabatic boundary ∂V_1 is solid. The distances between the boundary and both regular source I and image source J are d, and the adiabatic boundary conditions on ∂V_1 are satisfied. The modulation factor is $\epsilon^{(J)} = 1$. (b) The adiabatic boundary ∂V_2 divides the semi-infinite space into two parts, and the part to the left of the adiabatic boundary ∂V_2 is solid. The adiabatic boundary conditions are not enforced with the regular source I and image source J with the modulation factor $\epsilon^{(J)} = 1$.

close to the lateral boundaries. Consequently, the $\hat{T}$ field remains smooth and can be resolved with a coarse FE mesh. However, image source compensations for straight and curved boundaries are different. In Fig. 2.4a, the exact adiabatic boundary conditions are achieved for the straight boundary ∂V_1 when the image source J and the regular source I are symmetrically located on opposite sides of ∂V_1, and the image source is outside the solid domain, with a modulation factor $\epsilon^{(J)} = 1$. Thus, the power of the regular source I is equal to that of the image source J. It can be easily observed that the heat flux components along the surface normal direction generated by the regular and image sources are equal in magnitude and opposite in sign everywhere along the straight boundary ∂V_1. In Fig. 2.4b, the regular source I is positioned at a distance d from the semicircular boundary. Its corresponding image source J is placed symmetrically across the boundary at the same distance d. At point p, where the semicircular boundary intersects the line connecting the regular and image sources, the distances from p to both sources are equal, and the net heat flux along the surface normal vanishes. However, this is not the case for any other point on the semicircular boundary. As a result, zero heat flux condition is not enforced for the vast majority of points on the part boundary ∂V_2. Nevertheless, approximate adiabatic boundary conditions can be achieved on average along boundary segments by introducing a modulation factor $\epsilon^{(J)}$. The value of $\epsilon^{(J)}$ for each image source J is determined by its distance from the boundary and the local curvature of the boundary.

2.2.2. MODULATION FACTOR DERIVATION ON AN INFINITELY LONG CYLINDER

It remains to derive a general expression for the modulation factor. Consider an infinitely long solid cylinder with the radius R_c shown in Fig. 2.5 where the top surface of the cylinder is at the origin of the semi-infinite space. A regular point source I is located on the top surface of the cylinder at $\tilde{x}_i^{(I)}$, and the distance between the regular source I and the adiabatic boundary is d. The corresponding image source J is placed out of the solid cylinder domain to neutralize the heat flux on the adiabatic boundary due to the point source I. Using Eq. (2.7) and direct differentiation, the component of temperature gradient of the regular point source I is

$$\frac{\partial \tilde{T}^{(I)}(x_i,t)}{\partial x_i} = \frac{QA}{4\rho C_p(\pi\alpha(t-\tilde{\tau}^{(I)}))^{3/2}} \exp\left(\frac{-(R^{(I)})^2}{4\alpha(t-\tilde{\tau}^{(I)})}\right)\frac{2\tilde{x}_i^{(I)}-2x_i}{4\alpha(t-\tilde{\tau}^{(I)})}. \tag{2.16}$$

For a point with coordinates x_i on the lateral surface of the cylinder, the outward normal is

$$[n_1,n_2,n_3]^\top = [\frac{x_1}{R_c},\frac{x_2}{R_c},0]^\top. \tag{2.17}$$

Now, consider the plane $x_3 = \tilde{x}_3^{(I)}$ illustrated on Fig. 2.5b. The heat flux across the surface in the outward direction at a point on the circular boundary due to the regular point source I is

$$\begin{aligned}\tilde{q}^{(I)}(x_i,t) &= -k\frac{\partial \tilde{T}^{(I)}(x_i,t)}{\partial x_i}n_i \\ &= \frac{\nu}{(t-\tilde{\tau}^{(I)})^{3/2}}\exp\left(\frac{-(x_1-\tilde{x}_1^{(I)})^2-(x_2-\tilde{x}_2^{(I)})^2}{4\alpha(t-\tilde{\tau}^{(I)})}\right)\left(\frac{-\tilde{x}_1^{(I)}x_1+(x_1)^2-\tilde{x}_2^{(I)}x_2+(x_2)^2}{2\alpha(t-\tilde{\tau}^{(I)})}\right)\frac{1}{R_c},\end{aligned} \tag{2.18}$$

where ν is

$$\nu = \frac{kQA}{4\rho c_p(\pi\alpha)^{3/2}}. \tag{2.19}$$

It can be observed that ν depends on the laser power and thermal material properties, which are constant in this chapter. The dot product performed in Eq. (2.18) projects the heat flux vector along the outward normal direction. In fact, Eq. (2.18) can be interpreted as the heat loss rate at the point x_i on the boundary. The heat flux along the surface normal direction increases as the point source location gets closer to the cylindrical boundary (i.e. decreasing d shown in Fig. 2.5b). Due to the symmetry of the solid cylinder along the x_1-axis and the regular source also being positioned on the x_1-axis, we investigate the red arc boundary segment above the x_1-axis in Fig. 2.5. An image source J, as shown with a yellow circle in Fig. 2.5b, is placed outside the solid domain to neutralize the heat flux on the red arc emitted from the regular point source, and the image source J is also on the plane $x_3 = \tilde{x}_3^{(I)}$. Similarly, the heat loss rate due to the image source J on the circular boundary is

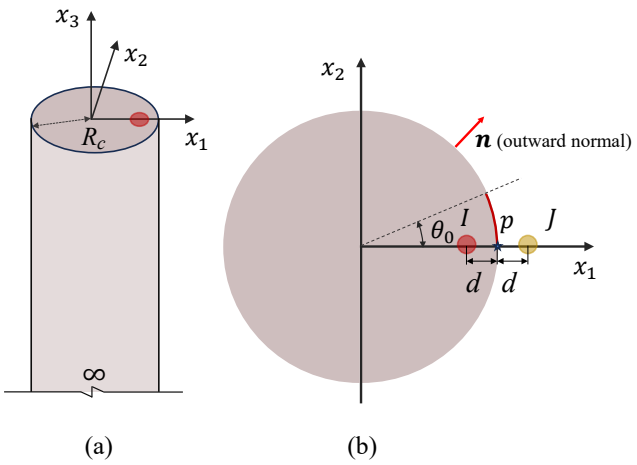

(a) (b)

Figure 2.5: Single source model for modulation factor calculation. (a) A point heat source on the top surface of an infinitely long cylinder with radius R_c. (b) Plane $x_3 = x_3^{(I)}$ contains the image source for the point heat source and line integration arc (red solid line) for calculating local energy conservation. θ_0 is the corresponding central angle of the arc. The distance of the regular source and image source to the boundary is d.

$$\begin{aligned}\breve{q}^{(J)}(x_i,t) &= -\epsilon^{(J)} k \frac{\partial \breve{T}^{(J)}(x_i,t)}{\partial x_i} n_i \\ &= \frac{\epsilon^{(J)} \nu}{(t-\breve{\tau}^{(J)})^{3/2}} \exp\left(\frac{-(x_1-\breve{x}_1^{(J)})^2-(x_2-\breve{x}_2^{(J)})^2}{4\alpha(t-\breve{\tau}^{(J)})}\right)\left(\frac{-x_1^{(J)}x_1+(x_1)^2-x_2^{(J)}x_2+(x_2)^2}{2\alpha(t-\breve{\tau}^{(J)})}\right)\frac{1}{R_c},\end{aligned} \tag{2.20}$$

where the power of the image source is modulated by $\epsilon^{(J)}$. In the simplest case of image sources for straight adiabatic boundaries [42], $\epsilon^{(J)} = 1$, where the power of regular and image sources are equal for an infinitely large radius of curvature R_c. When the radius of curvature R_c is finite, the distance between the image source and point p in Fig. 2.5 is equal to the distance between the regular source and point p. However, for any other point on the boundary segment, these distances differ—the distance from the image source to the point is different from the regular source to the point. As a result, adiabatic boundary conditions on the boundary segment cannot be exactly achieved using an image source. However, the regular source I only heats a limited area around the source, and most of the heat loss due to source I happens from the boundary segments near the source location. Assuming that the heat loss due to the source I during a given time interval along the red arc surface in Fig. 2.5 is $\tilde{\Phi}^{(I)}$, and the corresponding heat loss due to the source J is $\breve{\Phi}^{(J)}$. The average adiabatic boundary condition on the red arc is acquired through

$$\tilde{\Phi}^{(I)} = \breve{\Phi}^{(J)}. \tag{2.21}$$

By solving Eq. (2.21), with simplifications and an approximation given in APPENDIX B, the $\epsilon^{(J)}$ becomes

$$\epsilon^{(J)} = \frac{4R_c + d}{4R_c - d}\sqrt{\frac{R_c + d}{R_c - d}}. \tag{2.22}$$

Through the modulation factor $\epsilon^{(J)}$, the net heat loss is negligible on the boundary segment close to the sources I and J. It should be noted that Eq. (2.22) is based on a convex solid part surface shown in Fig. 2.5. For a concave solid part surface, $\epsilon^{(J)}$ becomes

$$\epsilon^{(J)} = \frac{4R_c - d}{4R_c + d}\sqrt{\frac{R_c - d}{R_c + d}}. \tag{2.23}$$

Moreover, it can be verified that, when $R_c \to \infty$, both Eqs. (2.22) and (2.23) yield $\epsilon^{(J)} = 1$. That corresponds to no modulation needed for image sources on straight boundaries. It remains to find the image source locations and compute the modulation factor for the more general case with complex boundaries.

2.2.3. IMAGE SOURCE GENERATION FOR COMPLEX PART GEOMETRY CONSTRUCTED BY B-SPLINES

An inherent advantage of the LPBF process is its remarkable capacity to manufacture geometrically intricate structures with high precision. This section introduces the B-spline curve generation method for representing the geometrically complex part boundaries. Then, we derive an offset method to express the contour line scan path along part boundaries parametrically. Next, a reparameterization method is introduced to discretize the continuous contour line scan path into uniformly spaced point sources. After the discretization, as shown in Fig. 2.6, the corresponding image source positions for each regular point source are determined based on the local tangent line of the curve. The separation distances between the regular and image point source to the curve tangent line are d, shown in Fig. 2.6. Modulation factors are then computed using Eqs. (2.22) and (2.23), taking into account the local curve curvature.

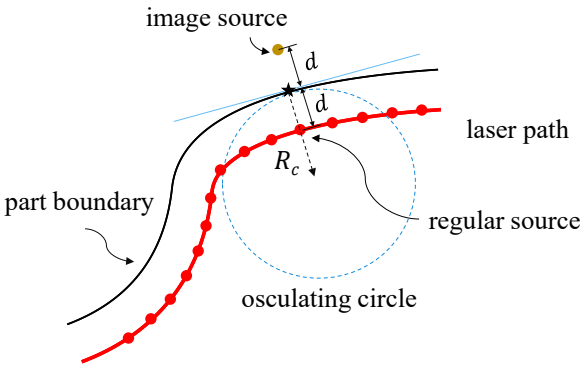

Figure 2.6: Laser scan path generation by offsetting part geometry boundaries and corresponding image source position.

B-SPLINE CURVES

Consider a knot vector, which is a non-decreasing sequence of real numbers, denoted as

$$\Xi = \left[\underbrace{0,0,\ldots,0}_{p+1}, \xi_{p+1}, \xi_{p+2}, \ldots, \xi_n, \underbrace{1,1,\ldots,1}_{p+1} \right].$$

Given this knot vector Ξ, the i-th B-spline basis function of degree p can be generated utilizing the Cox-de Boor recursion formula [43]

$$N_{i,p}(\xi) = \frac{\xi - \xi_i}{\xi_{i+p} - \xi_i} N_{i,p-1}(\xi) + \frac{\xi_{i+p+1} - \xi}{\xi_{i+p+1} - \xi_{i+1}} N_{i+1,p-1}(\xi), \tag{2.24}$$

starting from

$$N_{i,0}(\xi) = \begin{cases} 1, & \text{if } \xi \in [\xi_i, \xi_{i+1}), \\ 0, & \text{otherwise,} \end{cases}$$

where any ratios of the form $0/0$ are conventionally defined as zero.

A Non-Uniform Rational B-Splines (NURBS) curve of degree p can be then characterized as a vector-valued function

$$\mathscr{C}(\xi) = \sum_{i=0}^{n} \mathbf{P}_i R_{i,p}(\xi), \ \xi \in \hat{\Omega} = [0,1], \tag{2.25}$$

where $\mathbf{P}_i \in \mathbb{R}^3$ are the control point coordinates that govern the shape and position of the curve, $\hat{\Omega}$ is referred to as the parametric domain, and $R_{i,p}(\xi)$ are the rational B-spline basis functions defined by

$$R_{i,p}(\xi) = \frac{N_{i,p}(\xi)\omega_i}{\sum_{i=0}^{n} N_{i,p}(\xi)\omega_i}, \ i = 0,1,\ldots,n, \tag{2.26}$$

where ω_i denotes the weight associated with the control point $\mathbf{P}_i$. Fig. 2.7 presents quadratic B-spline basis functions constructed over the knot vector $\Xi = [0,0,0,0.2,0.4,0.6,0.8,0.8,1,1,1]$ along with a B-spline curve defined over these basis functions.

OFFSET CURVE

As laser scans along the part boundary, the laser beam is usually kept at a constant distance from the part boundaries. A straightforward approach to parametrically generate the contour laser scan path is offsetting the boundary curves with a constant distance d. However, directly computing offsets for B-spline curves is complicated. To this end, we introduce an alternative method that transforms the initial curve to create an offset counterpart uniformly distanced from the part geometry by a specified distance. Firstly, we compute the offset of a series of discretized point sources on the part geometry.

After discretizing the part geometry into a series of points $(x_1^{(I)}, x_2^{(I)})$, $I = 1,2,\ldots,N$, we subsequently offset these points by a specified distance d to define the laser path,

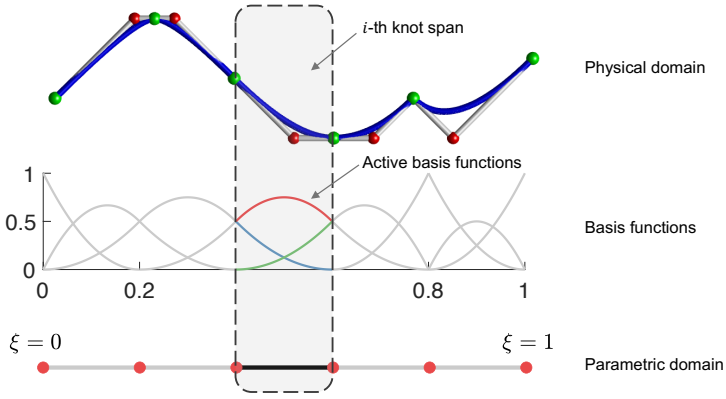

Figure 2.7: A quadratic ($p = 2$) B-spline curve constructed using B-spline basis functions defined over an open knot vector $\Xi = [0,0,0,0.2,0.4,0.6,0.8,0.8,1,1,1]$.

as shown in Fig. 2.6. For each point $(x_1^{(I)}, x_2^{(I)})$, we compute the corresponding tangent vector $\boldsymbol{v}^{(I)}$ by taking the derivative of the B-spline curve, formally expressed as

$$\boldsymbol{v}^{(I)} = \mathscr{C}(\xi^{(I)}) = \sum_{i=0}^{n} \mathbf{P}_i \frac{\partial R_{i,p}(\xi^{(I)})}{\partial \xi_i}, \quad I = 1,2,\ldots,N, \tag{2.27}$$

where $\xi^{(I)}$ denotes the parameter associated with the point $(x_1^{(I)}, x_2^{(I)})$. We then determine the normal vector $[n_1^{(I)}, n_2^{(I)}]^\top$ by rotating $\boldsymbol{v}^{(I)}$ by 90 degrees. The offset vector is computed by scaling the normal vector with the desired offset distance d, expressed as $[dn_1^{(I)}, dn_2^{(I)}]^\top$. This calculation forms the basis for determining the position of the laser path, given by

$$\begin{aligned} \bar{x}_1^{(I)} &= x_1^{(I)} + dn_1^{(I)}, \\ \bar{x}_2^{(I)} &= x_2^{(I)} + dn_2^{(I)}. \end{aligned} \tag{2.28}$$

These coordinates $(\bar{x}_1^{(I)}, \bar{x}_2^{(I)})$ represent the points along the laser path, effectively creating the desired offset from the original curve. However, it should be noted that the distance is not constant for adjacent points $(\bar{x}_1^{(I)}, \bar{x}_2^{(I)})$ along the laser path. With the laser path coordinates now determined, we revert these points to a B-spline curve configuration $\mathscr{C}$ by applying a least-squares fitting with chord-length parameterization, as described in Section 9.4.1 of [43].

ARC-LENGTH REPARAMETRIZATION

After getting the laser scan path by offsetting and fitting a series of points on the geometry boundaries, we need to discretize the continuous laser scan path into evenly distributed discrete point sources as shown in Figs. 2.3 and 2.6, which means the distance between two successive point sources to be constant. A common approach is arc-length parameterization, characterized by the equitable distribution of arc lengths over corresponding curve segments. The formulation process is detailed in APPENDIX C. Fig. 2.8 showcases the input curves alongside their respective reparameterized versions,

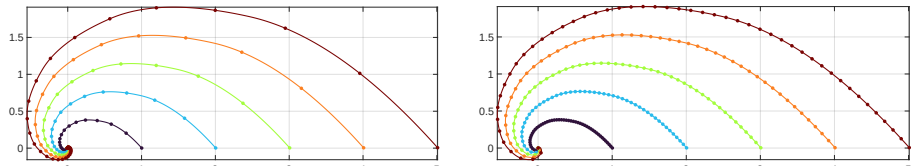

(a) (b)

Figure 2.8: Logarithmic spiral curve before (a) and after (b) arc-length reparameterization, with $m = 50$ control coefficients and polynomial degree $p = 2$.

derived using the proposed approximate arc-length approach. This transformation significantly improves the uniformity of the resulting curves compared to the original. With a reparameterized curve $\mathscr{C}(\xi(\hat{\xi}))$, equidistant points can be easily obtained through uniform sampling. To be more specific, to achieve a sampling with a constant distance d_s between successive points, one would uniformly sample $\lfloor L/d_s \rfloor$ points along the reparameterized curve, where $\lfloor\ \rfloor$ denotes the floor function, rounding down to the nearest integer, L the total length of the curve.

2.3. NUMERICAL EXAMPLES AND COMPARISON OF RESULTS

This section will investigate several part geometries, from simple to more complex ones. Initially, we examine the heat loss rate distribution, i.e., heat flux in the surface outward direction, along a curved boundary, in the presence of a regular point heat source and its image counterpart. Then, we consider a contour laser scan and compare temperature histories and heat loss rate distributions under three temperature decomposition methods. The first approach is decomposing the total temperature field using Eq. (2.5), where the analytical temperature field consists of contributions due to regular sources only. In the second and third methods, the total temperature field is decomposed using Eq. (2.11), where the analytical temperature fields image sources $\breve{T}$ are accounted for without and with modulating the image source power, respectively. Subsequently, we extend our proposed method of using modulated image sources to a dual laser scanning scenario. Lastly, we demonstrate our method in simulating more intricate parts enclosed by boundaries of varying curvatures.

2.3.1. A SINGLE POINT SOURCE ON A CURVED BOUNDARY

In this section, we compare heat loss rate distribution q, of a regular source Eq. (2.18) and its image part Eq. (2.20), on the simple part shown in Fig. 2.9. The part features a curved boundary with a fixed radius of curvature $R_c = 2\,\text{mm}$. A laser exposure time $1 \times 10^{-5}\,\text{s}$, a laser power $P = 82.5\,\text{W}$, a spot radius $r = 20\,\mu\text{m}$ and an energy absorptivity fraction 0.77 are assumed. The non-modulated image source J has the same power and spot radius. The regular point source is located on the top surface of the part as shown in Fig. 2.9. Since the image source is reflected symmetrically in the radial direction of the arc boundary, the arc center, regular source, and image source are on a line. The shortest distance between the image source and the arc boundary is $100\,\mu\text{m}$, the same as that

Table 2.1: Ti-6Al-4V thermal properties:

Conductivity	Heat capacity	Density
42 (W/mK)	990 (J/kgK)	4420 (kg/m^3)

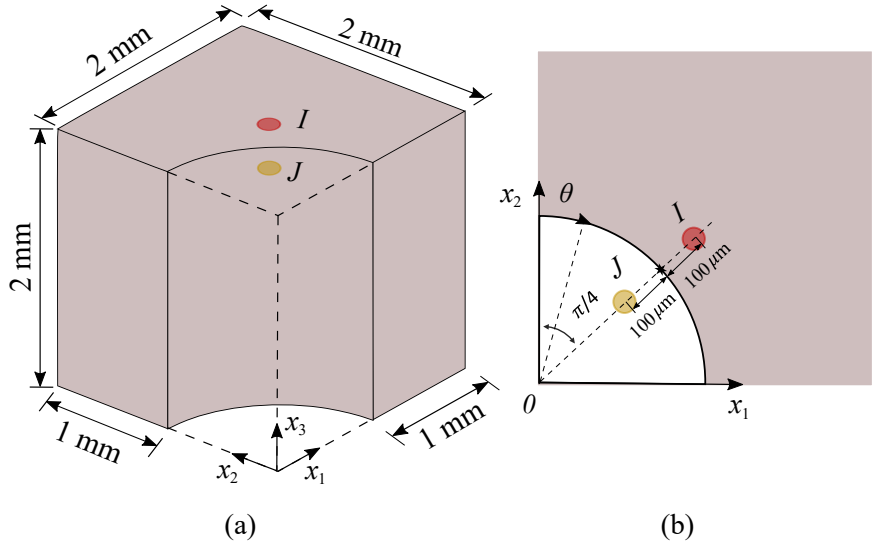

Figure 2.9: (a) A regular point source (red) is located near the curved surface on a 2 mm × 2 mm × 2 mm cube where a cylinder with a radius R_c = 1 mm is carved out from its corner, and the corresponding image source (yellow). (b) Top view of the part. The regular source, the image source, and the arc center are on a line. The shortest distances from the image and the regular source to the arc are 100 μm. The image and regular sources are located at $\theta = \pi/4$ with respect to the x_2 axis.

of the regular source. The angular coordinate θ is defined with respect to the x_2-axis. The lateral surfaces of the part are considered to be adiabatic, and the bottom surface is assumed to be kept at a constant temperature. We consider the thermal properties representative of Ti-6Al-4V throughout the chapter given in Table 2.1.

The numerical complementary field $\hat{T}$ is omitted in this section only to study the heat loss rate distribution of the regular and image sources. Therefore, we calculate the heat loss rate q distribution along the arc boundary on the top surface for the regular source ($\tilde{q}$), the non-modulated image source ($\breve{q}$), the modulated image source ($^{\epsilon}\breve{q}$), and pairs of the regular and the non-modulated image ($\tilde{q}+\breve{q}$) and the regular and the modulated image sources ($\tilde{q}+{}^{\epsilon}\breve{q}$). From Eq. (2.23), the modulation factor is calculated as $\epsilon^{(J)} = 0.86$, which scales down the heat loss rate distribution of the image source. The heat loss rate distribution at the boundary is plotted as a function of θ in Fig. 2.10. The two sources are generated at $t = 0$, and the activation time of the sources is calculated with a time shift $\tau = 0 - r^2/8\alpha$, as discussed in Section 2.2.1. The heat loss rate distribution is plotted at two different time instances. In Fig. 2.10a at $t = 1 \times 10^{-4}$ s, the heat loss rate approximately reaches its maximum, then rapidly decreases with time shown

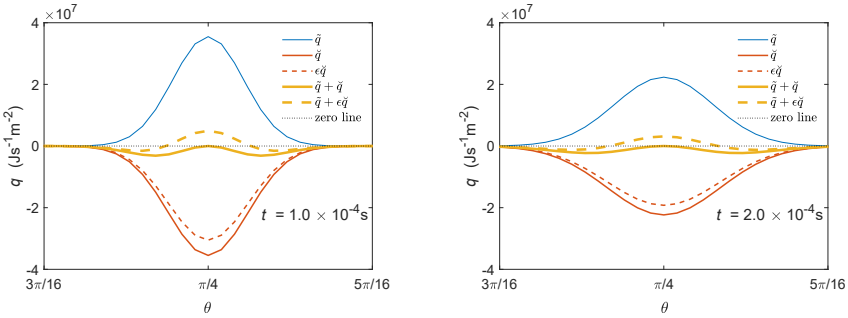

(a) (b)

Figure 2.10: Heat loss rate q distribution along the arc boundary of five cases at (a) $t = 1.0 \times 10^{-4}$ s and (b) $t = 2.0 \times 10^{-4}$ s. Heat loss rate distribution of the regular source $\tilde{q}$, heat loss rate distribution of the non-modulated image source $\breve{q}$, heat loss rate distribution of the modulated image source ${}^{\epsilon}\breve{q}$, heat loss rate distribution of the regular and non-modulated image sources $\tilde{q} + \breve{q}$, and heat loss rate distribution of the regular and modulated image sources $\tilde{q} + {}^{\epsilon}\breve{q}$. Both the image and regular sources are located at $\theta = \pi/4$ with respect to the x_2 axis.

in Fig. 2.10b at $t = 2 \times 10^{-4}$ s. For the regular source, the heat loss rate $\tilde{q}$ is positive, which means the heat is evacuated. In contrast, the heat loss rate $\tilde{q}$ is negative for the image source, signifying a heat gain for the part. When only the regular source I is considered, the total heat loss rate across the curve boundary at $t = 1 \times 10^{-4}$ s is

$$\int_0^{\pi/2} \tilde{q}(x_i) R_c \mathrm{d}\theta = 3.8 \times 10^3 \,\mathrm{J s^{-1} m^{-1}}.$$

When the regular and non-modulated image sources are considered, the heat loss rate distribution is less than zero for all values of θ, which means the flux due to the regular source is overcompensated by the non-modulated image source. The total heat loss rate across the curve boundary at $t = 1 \times 10^{-4}$ s is

$$\int_0^{\pi/2} (\tilde{q}(x_i) + \breve{q}(x_i)) R_c \mathrm{d}\theta = -4.8 \times 10^2 \,\mathrm{J s^{-1} m^{-1}}.$$

When the regular and modulated image sources are considered, the heat loss rate fluctuates with θ along the boundary. The net heat loss rate along the boundary at $t = 1 \times 10^{-4}$ s becomes

$$\int_0^{\pi/2} (\tilde{q}(x_i) + {}^{\epsilon}\breve{q}(x_i)) R_c \mathrm{d}\theta = 1.1 \times 10^2 \,\mathrm{J s^{-1} m^{-1}},$$

which is around 3% of that of only adopting the regular source. When using the regular and non-modulated image sources, the total heat loss rate across the curved boundary is around 13% of that of only adopting the regular source. Therefore, the adiabatic boundary conditions are better enforced on average using the modulated image source than the non-modulated image source.

It remains to simulate a contour line scanning (discretized into multiple point sources) close to the curved boundary and study the effect of the modulation factor of image sources.

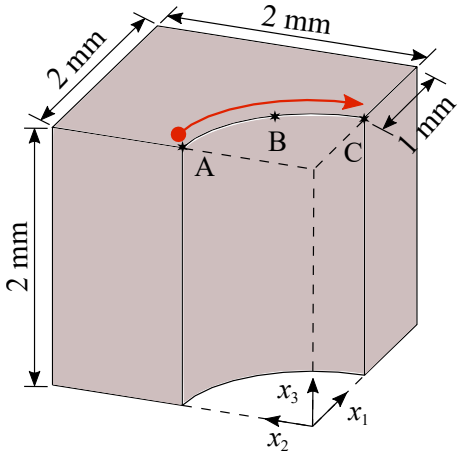

Figure 2.11: Single contour line scan along the curved boundary. Temperature histories of points A, B, and C are compared with different temperature decomposition methods.

2.3.2. SINGLE LASER SCAN ALONG A CURVED BOUNDARY

This section aims to compare the effect of multiple image sources with and without modulation in a contour line scan case and study the heat loss rate distribution on the curved boundary. As discussed in Section 2.2.2, the heat flux component in the outward normal direction given in Eq. (2.18) is the heat loss rate at a boundary point. The part geometry remains the same, and the laser scan path is shown in Fig. 2.11. The laser power is taken as 82.5 W, scanning velocity 0.5 m/s, absorptivity fraction 0.77 and laser spot radius 20 μm. The continuous laser scan is discretized into a series of point sources with time intervals of $\Delta t = 1 \times 10^{-5}$ s [2]. The distance between the point sources and the curved boundary is 100 μm. Therefore, the modulation factor remains $\epsilon = 0.86$ for all the modulated image sources.

We compare temperature history and heat loss rate distribution among three distinct temperature decomposition methods. The three points A, B, and C along the boundary depicted in Fig. 2.11 are used to compare the temperature histories. The first is a reference case using the temperature decomposition method in Eq. (2.5). The total temperature field is the superposition of the analytical temperature field of regular sources $\tilde{T}$ and the complementary temperature field $\hat{T}$ computed with FEM to impose adiabatic boundary conditions along the curved surface. It should be noted that the $\hat{T}$ field is solved with a time step 1×10^{-4} s larger than the time step to discretize the continuous laser scan. There is no image source in this reference case. Therefore, to achieve adiabatic boundary conditions, the FE mesh should be sufficiently fine, shown in Fig. 2.12a, to capture the steep temperature gradients and the resulting heat flux due to the regular heat sources. For the reference case, the average element size in the proximity of the boundary is around 20 μm that is equal to the laser spot radius and 10 times smaller than the FE mesh depicted in Fig. 2.12b utilized for the other two cases with non-modulated and modulated image sources, respectively. In the second and third cases, image sources

[2] Previous research has proposed that $\Delta t \leq 5 \times 10^{-5}$ s, and we choose a conservative value here.

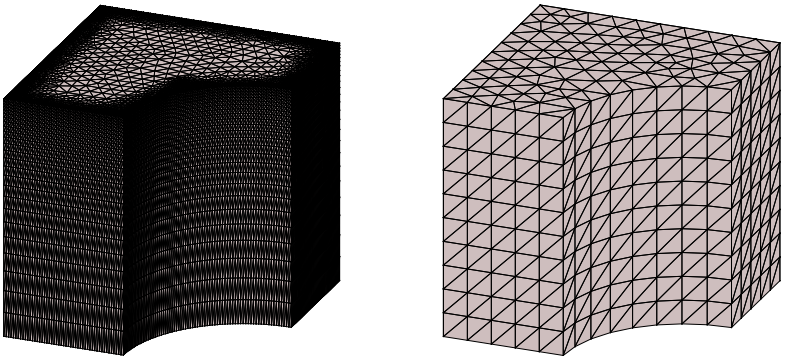

(a) fine mesh (24385 nodes, 102488 elements, average boundary element size 20 μm)

(b) coarse mesh (1264 nodes, 5775 elements, average boundary element size 200 μm).

Figure 2.12: Finite element mesh for the contour scan simulation (a) with no image sources where the BCs are enforced numerically through $\hat{T}$, (b) using non-modulated image sources and modulated image sources .

are introduced to counterbalance the heat flux arising from regular sources. Thus, the resulting temperature gradients due to the regular and image sources are gradual on the part boundary. Both the temperature field $\tilde{T} + \check{T}$ (using image sources without modulation) in the second case, and the temperature field $\tilde{T} + ^{\epsilon}\check{T}$ (using modulated image sources) in the third case exhibit a smoother profile. As a result, when the boundary condition is enforced with Eq. (2.14), a much coarser mesh shown in Fig. 2.12b can be employed, containing around only 5% of the total nodes in the reference case mesh. The total CPU time for the three simulations is given in Table 2.2. The computational time when adopting image sources is around 5% of the reference case, and there is almost no difference in CPU times between using the modulated and non-modulated image sources.

Usually, the finite element size should be in the same order as the laser spot radius to capture the steep-temperature gradient from the laser spot. Cao et al. [44] adopted a fine element size of 50 μm for the laser spot radius of 70 μm. Roberts et al. [13] adopted the element size as 25 μm when the laser spot radius is 50 μm. Vanini et al. [45] adopted fine element size as 20 μm for laser spot radii of 45 μm and 25 μm. Zhang et al. [46] proposed using fine element size of 5 μm to solve the temperature distribution of laser spot with radius with 50 μm. Consequently, the minimum element size 20 μm used in the reference case (only along the boundaries) is in line with the literature. While using image sources, the element size can be coarsen to 200 μm. As a result, numerical calculations speed up significantly.

The temperature histories of points A, B, and C given in Fig. 2.11 during the contour laser scanning along the curved surface are shown in Fig. 2.13 for the three cases. Overall, the temperature histories with modulated image sources (red lines) better approximate the reference temperature history (blue lines). Table 2.3 gives three measures to evaluate the error between using non-modulated and modulated image sources compared to the reference case. The three measures reported are the absolute difference of peak temper-

Table 2.2: Computation time of the single laser scan along a curved boundary. The calculations are performed on an Intel i7-11850H processor with a clock speed of 2.50 GHz, using a single core, and 16 GB of RAM.

Simulation method	CPU time (s)
Reference	11450.0
Using non-modulated image sources and linear elements	658.3
Using modulated image sources and linear elements	614.3
Using non-modulated image sources and quadratic elements	1683.6
Using modulated image sources and quadratic elements	1715.7

Table 2.3: Metrics computed for thermal history differences at Points A, B, and C. The absolute difference of maximum temperatures between the using image sources and reference case is defined as $\Delta T_{\max}$ (°C). The integral of the absolute temperature differences over the full history are defined as $\int |\Delta T| \mathrm{d}t$ (°C·s). The Symmetric Mean Absolute Percentage Error (SMAPE) of temperature histories compared to the reference case. Since the temperature of the build platform is 200 °C, only the data points with temperature higher than 400 °C are used to calculate SMAPE.

Points	using non-modulated image sources			using modulated image sources		
	$\Delta T_{\max}$	$\int \lvert\Delta T\rvert \mathrm{d}t$	SMAPE	$\Delta T_{\max}$	$\int \lvert\Delta T\rvert \mathrm{d}t$	SMAPE
A	31.2	4.5×10^{-2}	3.6	16.4	4.1×10^{-2}	2.6
B	43.0	5.9×10^{-2}	1.8	2.7	2.8×10^{-2}	1.4
C	14.6	6.7×10^{-2}	7.8	3.9	4.6×10^{-2}	5.1

atures with respect to the reference case $\Delta T_{\max}$, the Symmetric Mean Absolute Percentage Error (SMAPE)[3] of temperature histories, and the absolute temperature differences over the full history, i.e. $\int |\Delta T| \mathrm{d}t$. All three measures indicate that modulated image sources lead to a better approximation of the reference case. Moreover, the temperature histories with non-modulated image sources (yellow lines) are consistently overestimated at the three sampling points. Fig. 2.14 gives snapshots of the temperature field contours of the three temperature decomposition methods at $t = 2 \times 10^{-3}$ s. The temperature isolines are perpendicular to the curved boundary, indicating adiabatic boundary conditions are achieved. Moreover, we compare the area of the layer where the temperature exceeds $T = 1400$ °C. This area is 2.24×10^{-8} m^2, 2.77×10^{-8} m^2 and 2.52×10^{-8} m^2 respectively in the reference, using non-modulated image sources and using modulated image sources cases. The area in the case of adopting non-modulated image sources is 24% larger than that of the reference case, which indicates that non-modulated image sources lead to an overestimation temperature. While in the reference case and adopting non-modulated image sources, the difference is decreased to 13%. So, we conclude that the modulated image sources can better approximate the temperature history compared to the non-modulated image sources.

Next, we check again the heat loss rate distribution along the curved boundary at $t = 2 \times 10^{-3}$ s in Fig. 2.15. This is when the temperature at Point B peaks in Fig. 2.13. Fig. 2.15a gives the heat loss rate distribution of the reference case, where there is no

[3] SMAPE is a metric that measures the error between two curves or two sets of data points.

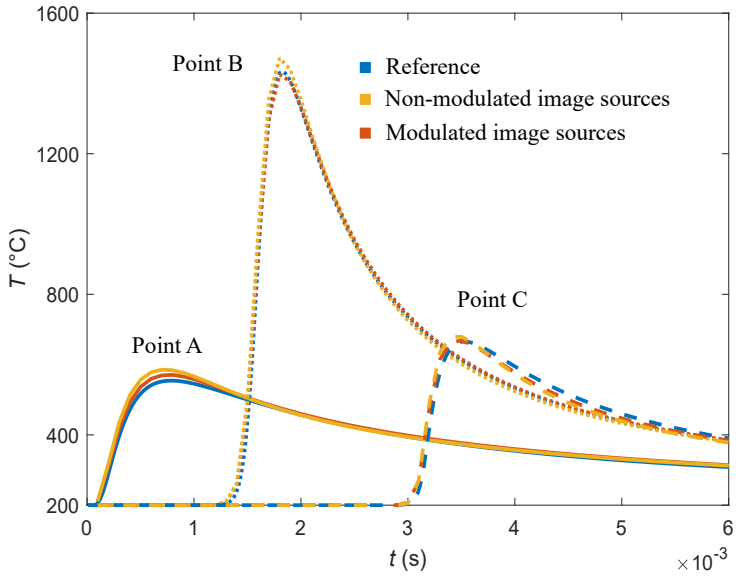

Figure 2.13: Comparison of temperature histories by using three temperature decomposition methods. The reference case with no image sources, temperature decomposition $T = \bar{T} + \hat{T}$; using the non-modulated image source case, temperature decomposition $T = \bar{T} + \breve{T} + \hat{T}$; using the modulated image source case, temperature decomposition $T = \bar{T} +^{e} \breve{T} + \hat{T}$. $\hat{T}$ is solved using linear tetrahedron elements (C3D4 element in ABAQUS).

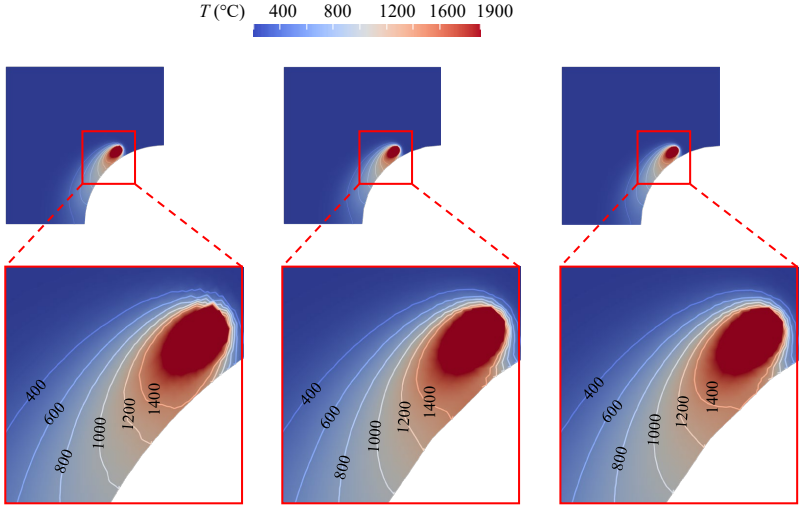

Figure 2.14: Temperature distribution at $t = 2 \times 10^{-3}$ s. Three temperature decomposition methods are adopted. Temperature decomposition is $T = \bar{T} + \hat{T}$ in the reference case. When using non-modulated image sources, temperature decomposition is $T = \bar{T} + \breve{T} + \hat{T}$. When using modulated image sources, temperature decomposition is $T = \bar{T} +^{e} \breve{T} + \hat{T}$. The area with $T > 1400\,^{\circ}\mathrm{C}$ is $2.24 \times 10^{-8}\,\mathrm{m}^2$, $2.77 \times 10^{-8}\,\mathrm{m}^2$ and $2.52 \times 10^{-8}\,\mathrm{m}^2$ respectively in the reference, using non-modulated image sources and using modulated image sources cases.

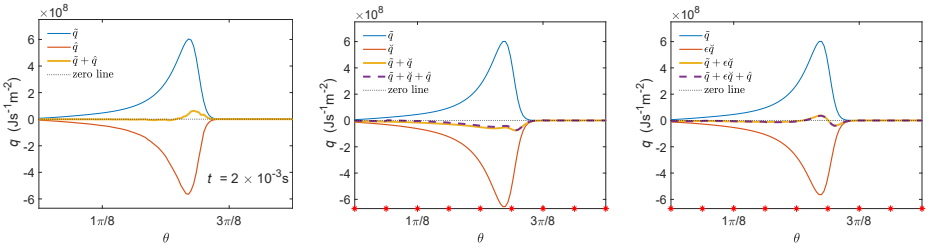

Figure 2.15: Heat loss rate distribution q, (a) reference case, the average boundary element size is 5 μm, temperature decomposition $T = \tilde{T} + \hat{T}$, (b) using non-modulated image sources with temperature decomposition $T = \tilde{T} + \breve{T} + \hat{T}$, (c) using modulated image sources with temperature decomposition $T = \tilde{T} + {}^{\epsilon}\breve{T} + \hat{T}$. Heat loss rate distribution due to regular sources $\tilde{q}$, non-modulated image sources $\breve{q}$, modulated image sources ${}^{\epsilon}\breve{q}$, complementary field $\hat{q}$. $\hat{T}$ is solved using linear tetrahedron elements (C3D4 element in ABAQUS).

image source and the finite element size is further decreased to 5 μm near the boundary. The heat loss rate on the curved boundary is

$$\int_0^{\pi/2} (\tilde{q}(x_i) + \hat{q}(x_i)) R_c \mathrm{d}\theta = 4.7 \times 10^3 \,\mathrm{Js^{-1}m^{-1}}.$$

Note that the element size around the boundary to acquire accurate q distribution is 5 μm much finer than that of Fig. 2.12a (20 μm) used for the reference temperature calculation in Fig. 2.13 and Fig. 2.14a. Further refinement of elements around the boundary from approximately 20 μm to approximately 5 μm makes only 2.6 °C difference for the peak temperature of point B, i.e. convergence of temperature has more lenient spatial discretization requirement than the heat flux. This is reasonable because q represents the heat flux at a specific time step, capturing how much heat is lost at that moment. In contrast, temperature histories show the total change in the system's internal energy, reflecting the cumulative heat losses over time, correlating with the time integration of q. Therefore, a finer mesh must be used to ensure the convergence of the heat loss rate distribution at a specific time step. Fig. 2.15c illustrates the q distribution when employing the regular sources, modulated image sources, and complementary field ($\tilde{T} + {}^{\epsilon}\breve{T} + \hat{T}$). At the same time, Fig. 2.15b presents the results obtained with regular sources, image sources, and complementary field ($\tilde{T} + \breve{T} + \hat{T}$). The nine red asterisks represent the angular coordinates of the nine finite element nodes on the curve boundary shown in Fig. 2.12b. The abrupt change in the heat loss rate at the nodes in Fig. 2.15b and c is caused by the discontinuity of temperature gradients in the two adjacent linear elements.

Upon using regular and modulated image sources, the modulation factor $\epsilon = 0.86$ scales down the heat loss rate distribution of image sources. The total heat loss rate distribution (purple solid line in Fig. 2.15c) fluctuates around zero, and the adiabatic boundary conditions are achieved on average. The total heat loss rate across the curve

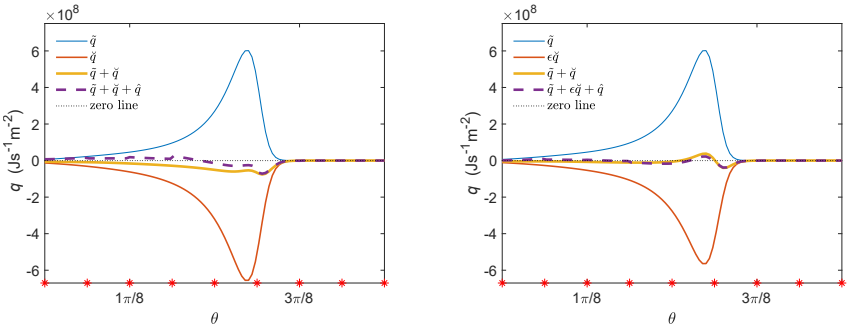

Figure 2.16: Heat loss distribution q, (a) using non-modulated image sources with temperature decomposition $T = \tilde{T} + \breve{T} + \hat{T}$ and (b) using modulated image sources with temperature decomposition $T = \tilde{T} + {}^{\epsilon}\breve{T} + \hat{T}$. Heat loss rate distribution due to regular sources $\tilde{q}$, non-modulated image sources $\breve{q}$, and numerical correction ${}^{\epsilon}\breve{q}$; complementary field $\hat{q}$. $\hat{T}$ is solved by using quadratic tetrahedron elements (C3D10 element in ABAQUS).

boundary at $t = 2 \times 10^{-3}$ s is

$$\int_0^{\pi/2} (\tilde{q}(x_i) + {}^{\epsilon}\breve{q}(x_i) + \hat{q}(x_i)) R_c \mathrm{d}\theta = -5.7 \times 10^3 \,\mathrm{Js}^{-1}\mathrm{m}^{-1},$$

where the magnitude is almost the same as the total heat loss rate in the reference case. In contrast, the total heat loss rate distribution (purple solid line in Fig. 2.15b) is negative for all angular coordinates in the case of having the image sources without modulation since the amount of heat flux across the boundary into the domain is an overestimation, leading to over-heating near the part's boundary. The total heat loss rate across the curve boundary at this time step is

$$\int_0^{\pi/2} (\tilde{q}(x_i) + \breve{q}(x_i) + \hat{q}(x_i)) R_c \mathrm{d}\theta = -2.3 \times 10^4 \,\mathrm{Js}^{-1}\mathrm{m}^{-1}.$$

The sign of the heat loss rate indicates a heat gain and the magnitude of the heat gain is one order of magnitude larger than that in the reference case and modulated image source case, which rationalizes higher temperature values in the non-modulated image source case as shown in Fig. 2.13 and larger high-temperature zones in the non-modulated image source case as shown in Fig. 2.14. Moreover, we observe that with the given coarse mesh size, the $\hat{q}$ has almost no contribution to the heat loss rate distribution shown in Fig. 2.15c compared to the effect of $\hat{q}$ in Figs 15a and b. This also implies that the outgoing heat flux is almost perfectly counter-balanced, and $\hat{q}$ is unnecessary if modulated image sources are used. However, when we adopt p refinement, the same mesh with quadratic shape functions for the tetrahedron elements (C3D10 element in ABAQUS) for computing $\hat{q}$, a more pronounced effect of $\hat{q}$ can be especially seen in Fig. 2.16a since the non-modulated image sources are inadequate in enforcing the adiabatic boundary condition. The total heat loss rate across the curve boundary at

this time step in Fig. 2.16a is

$$\int_0^{\pi/2} (\tilde{q}(x_i) + \check{q}(x_i) + \hat{q}(x_i)) R_c \mathrm{d}\theta = -2.2 \times 10^3 \,\mathrm{Js}^{-1}\mathrm{m}^{-1},$$

which is one order of magnitude smaller than the total heat flux rate in Fig. 2.15b, which utilizes linear elements. Thus, now the heat loss rate field $\hat{q}$ more accurately enforces adiabatic conditions in Fig. 2.16a than Fig. 2.15b with higher order shape functions. For the Fig. 2.16b, the heat loss rate field $\hat{q}$ still does not make a significant contribution, which further indicates that the modulated image sources more accurately enforce the adiabatic boundary conditions better than non-modulated image sources in Fig. 2.16a. However, it should be noted that the p refinement increases computational time three times as shown in Table 2.2.

In general, unlike for straight boundaries [42], when we place image sources next to a curved boundary, the adiabatic boundary conditions can only be approximately achieved by modulating the power of image sources in case of a coarse mesh preferred for computational efficiency. The temperature history shows little difference between the modulated image source and reference cases. Therefore, the adiabatic boundary conditions are easily achieved with a coarse FE mesh comprising linear elements and the modulated image sources. However, when using the image sources without modulation, the image sources overcompensate the heat loss rate from regular sources and lead to an artificial heat gain, thus resulting in larger high-temperature zones. As a result, the modulated image sources more effectively counteract the heat loss, reducing the need for $\hat{q}$ field correction.

2.3.3. DUAL LASERS SCAN ALONG PART BOUNDARY

In the previous section, we investigated the simulation of a single laser contour scan with the proposed semi-analytical method using modulated image sources that well represent the adiabatic boundary conditions. One key advantage of the semi-analytical method is that no local mesh refinement is needed to follow the laser motion since the steep temperature gradients in the vicinity of the laser beams are captured by analytical fields. Therefore, the semi-analytical method can be readily applied to the simulation of the LPBF process with multiple laser scanning simultaneously with no extra computational cost. In this section, we simulate the contour scanning with two laser beams using the proposed temperature decomposition method $T = \tilde{T} +^{\epsilon} \check{T} + \hat{T}$. The laser scanning strategy is shown in Fig. 2.17. The two lasers start scanning next to each other, scan along the part boundary, and finally meet when the contour scan is complete. The part geometry, laser velocity, laser power, and material thermal properties are the same as those in the previous section. The mesh density is the same as Fig. 2.12b. For the straight boundaries, we use the image sources without modulation. For the curved boundary, we modulate the image source power according to the radius of curvature. The snapshots of temperature fields at two instances are shown in Fig. 2.18. It can be observed that the temperature isolines remain perpendicular to straight and curved boundaries, which indicates adiabatic boundary conditions are enforced. Moreover, the number of simultaneously acting lasers can be increased with no additional computational cost.

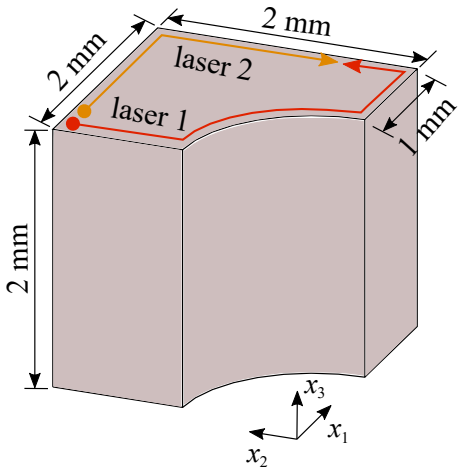

Figure 2.17: Schematic illustration of contour scan by two lasers. Scanning of two lasers starts and ends simultaneously, with identical scanning speeds. The two lasers are positioned next to each other at the beginning and end of the scanning process.

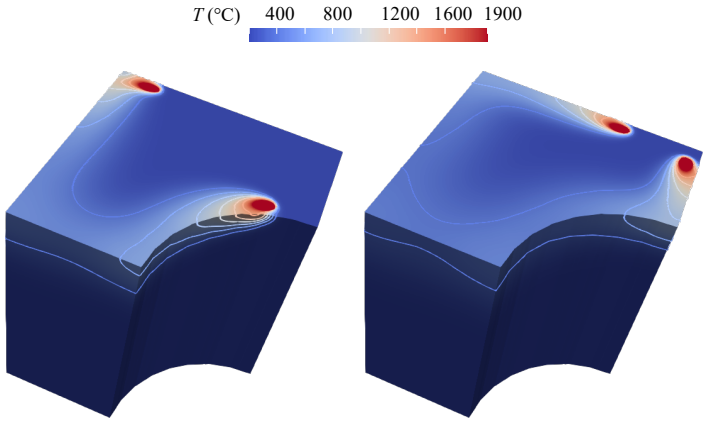

(a) $t = 4.0 \times 10^{-3}$ s (b) $t = 6.0 \times 10^{-3}$ s

Figure 2.18: Snapshots of temperature distribution at (a) $t = 4.0 \times 10^{-3}$ s and (b) $t = 6.0 \times 10^{-3}$ s. Two lasers are scanning simultaneously along the part boundary.

2.3.4. SCANNING ALONG AN ELLIPTIC BOUNDARY

In the preceding sections, we discussed using image sources along an arc boundary with a constant radius of curvature, and a constant power modulation factor can be calculated from Eq. (2.23) for all image sources. In this section, we consider applying the proposed method to elliptic boundaries with gradually varying radius of curvature, shown in Fig. 2.19a. The laser parameters and material properties are the same as above. A laser scanning along the edge of the part is also depicted in Fig. 2.19a. The part is meshed with linear tetrahedral elements with an average size 0.2 mm, which is ten times larger than

the laser spot radius, as shown in Fig. 2.19b. We use osculating circles shown in Fig. 2.6 to approximate the local curvature of the ecliptic boundaries and calculate the image source modulation factors based on the relative position of the regular source, osculating circles and image source positions as discussed in Section 2.2.3. The temperature fields at $t = 5.3 \times 10^{-3}$ s and $t = 1.2 \times 10^{-2}$ s are shown in Fig. 2.20. At $t = 5.3 \times 10^{-3}$ s, the laser is scanning along the elliptic boundary, while at $t = 1.2 \times 10^{-2}$ s, the laser transitions between the arc boundary and elliptic boundary. Observe that the isolines of the temperature field are perpendicular to the part edge, which indicates that the adiabatic boundary conditions are satisfied for both time instances. Through the numerical example in the section, it can be demonstrated that our method can applied to non-constant curvature boundaries.

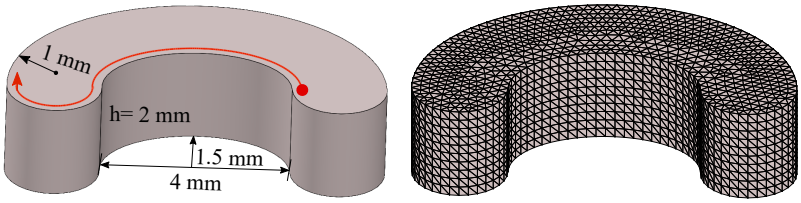

Figure 2.19: (a) elliptic part geometry with changing local radii of curvature. The model plane boundary is constructed by two elliptical and circular arcs. (b) discretization of the part with finite elements with an average element size 200 μm.

2.3.5. SCANNING ALONG A GEOMETRICALLY COMPLEX PART CONSTRUCTED BY B-SPLINES

In this section, we simulate a scanning process on a more complicated butterfly geometry shown in Fig. 2.21, constructed by cubic B-splines and control points. The laser scans along the part boundary consisting of concave and convex boundary segments. First, we offset the points on the B-spline boundary using Eq. (2.28). Through parameterization, we get a continuous laser scan path. Then, the continuous laser line scan is discretized into a series of equidistant point heat sources by using arc-length parameterization and solving the constrained optimization problem given in Eq. (C.11). Following the procedure shown in Fig. 2.6, the image source positions are determined by osculating circles and corresponding regular source positions, with the modulation factors calculated according to local radii of curvatures with Eqs. (2.22) and (2.23).

Similarly, two temperature decomposition methods are adopted in this section. The first serves as a case where the temperature decomposition $T = \tilde{T} + \hat{T}$ is used with the element size of approximately 20 μm near the boundary as shown in Fig. 2.21. The second method is the proposed method in this chapter, i.e., $T = \tilde{T} + {}^{\epsilon}\breve{T} + \hat{T}$ where modulated image sources are incorporated. A non-zero value for the complementary field $\hat{T}$ compensates for the heat loss rate from the regular sources in the reference case (without image sources). To examine the extent to which the modulated image source can make $\hat{T}$ field redundant, the same fine mesh is also utilized with the proposed method

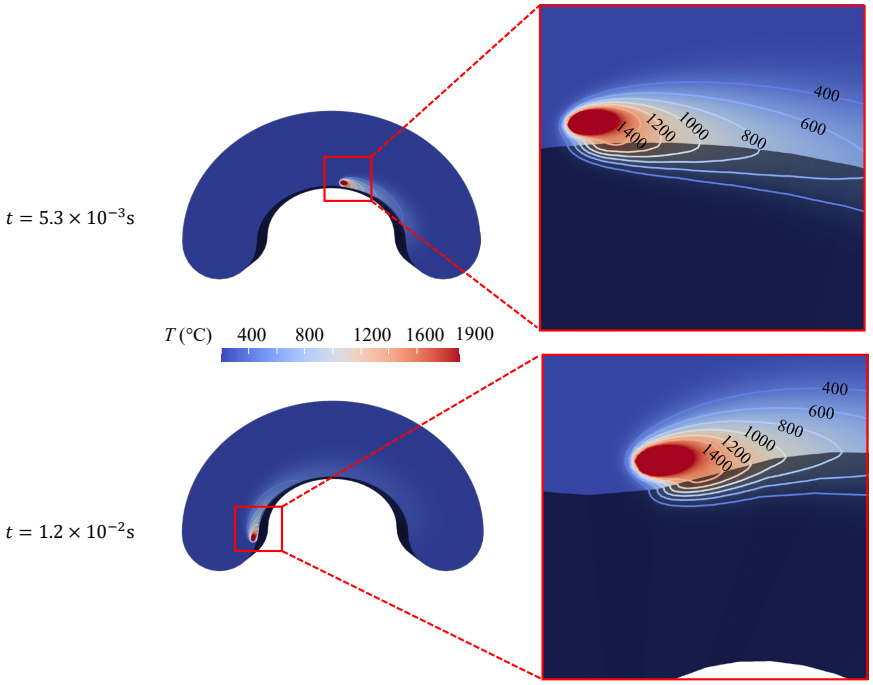

Figure 2.20: Snapshots of temperature distribution at $t = 5.3 \times 10^{-3}$ s and $t = 1.2 \times 10^{-2}$ s during a single laser scanning along the edge of an elliptic part.

in this chapter. Fig. 2.22 gives the temperature distribution at $t = 0.020$ s in the case of using the modulated image sources, where the temperature isolines are perpendicular to the boundaries and hence adiabatic boundary conditions are satisfied. Fig. 2.23 provides the FEM solutions of complementary field $\hat{T}$ for the two cases. In the reference case, Fig. 2.23a, since no image sources are adopted, $\hat{T}$ field needs to correct for the heat loss rate (or heat flux in the surface outward normal direction) due to regular sources to achieve adiabatic boundary conditions. As a result, the contribution of $\hat{T}$ to the overall temperature prediction is necessary. Fig. 2.23b shows the $\hat{T}$ temperature distribution where the total temperature field is decomposed using $T = \tilde{T} +^{\epsilon} \check{T} + \hat{T}$. The modulated image sources compensate for the heat loss rate across the boundary due to regular sources to enforce adiabatic boundary conditions. Then, the contribution of $\hat{T}$ to the overall temperature prediction is almost negligible. This implies the utilization of modulated image sources can almost perfectly approximate adiabatic boundary conditions for a geometrically complex boundary, thereby allowing for the use of a coarser mesh in FEM to solve the $\hat{T}$ field for higher computational efficiency.

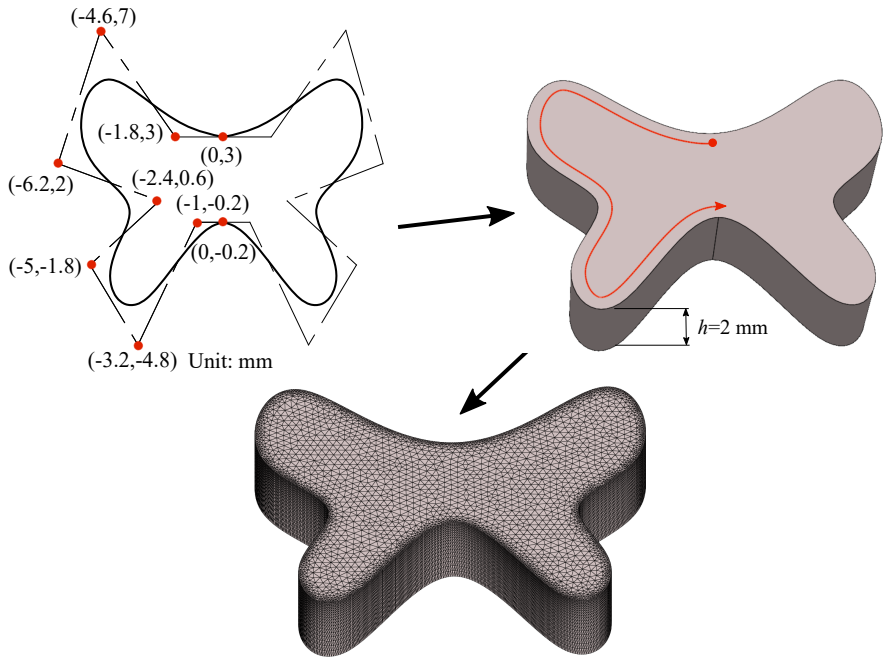

Figure 2.21: A butterfly-shaped boundary constructed by B-spline curves and control points. The 3D STL file for the butterfly-shaped part is created through the extrusion of the boundary. The laser scan path is on top of the 3D part. To simulate the temperature history, the 3D part is discretized using linear tetrahedron elements (C3D4 element in ABAQUS), and the boundary element size is approximately 20 μm.

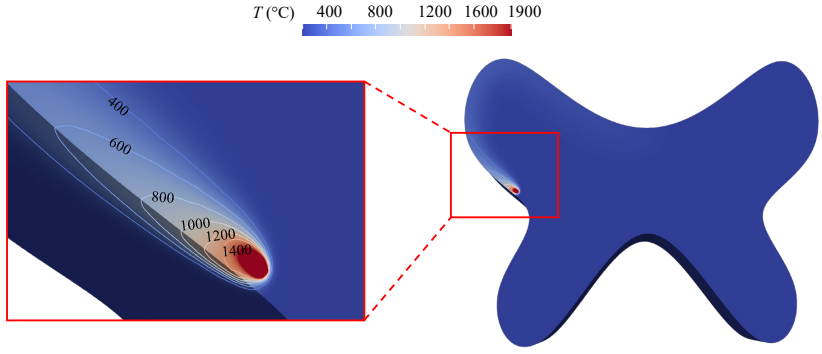

Figure 2.22: Temperature distribution at $t = 0.020$ s. The temperature decomposition $T = \tilde{T} +^{\epsilon} \check{T} + \hat{T}$ is adopted with modulated image sources.

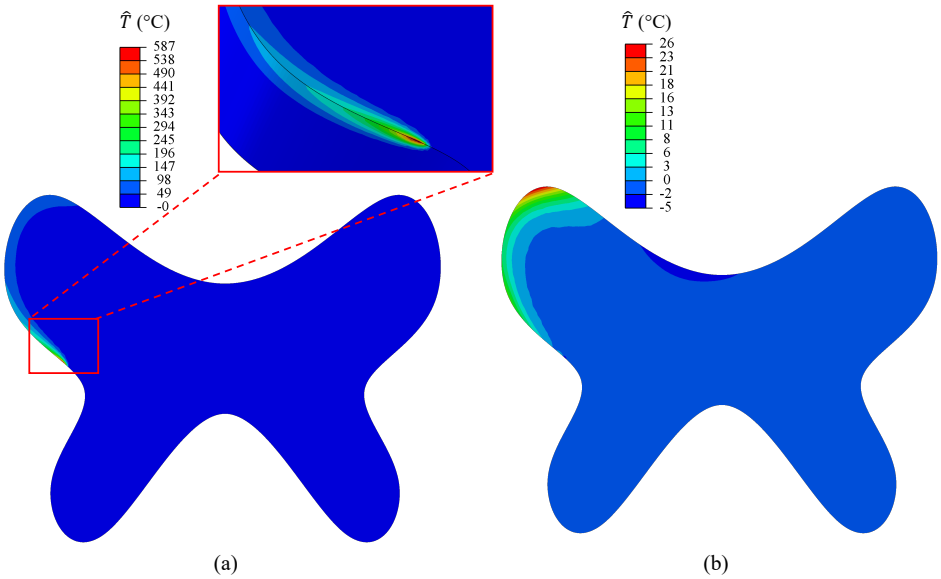

Figure 2.23: $\hat{T}$ complementary field at $t = 0.020\,\mathrm{s}$. (a) without image sources and the temperature field is decomposed using $T = \tilde{T} + \hat{T}$. (b) using the modulated image sources, and the temperature field is decomposed using $T = \tilde{T} + {}^{\epsilon}\breve{T} + \hat{T}$.

2.4. DISCUSSION

We have proposed a method to modulate the power of image sources to enforce the adiabatic boundary conditions. This modulation factor accounts for the radii of curvature along the boundary curves, enabling the modulated image sources to effectively offset the heat loss rate due to regular sources near the local boundary. This approach reduces the integrated heat loss across the local boundary to zero. However, the resulting net heat loss rate distribution from the regular and modulated image sources still fluctuates along the part boundary.

According to Saint-Venant's Principle, this redistribution of heat loss rate around the boundary will influence the temperature field less when sampling points are away from the current laser scanning area [47, 48]. Furthermore, the amount of redistributed heat loss rate accounts for a small proportion of the heat loss rate from regular sources, meaning that the modulated image sources effectively compensate the heat loss rate from regular sources. As a result, even when sampling points are close to the laser scan path, the temperature history will have negligible differences compared with the reference case. The difference of maximum temperature is as small as 2.7 °C. Besides, the maximum SMAPE is within 5.1%, indicating a good agreement with the reference temperature histories. In contrast, when non-modulated image sources are used, the peak temperature deviates by 43.0 °C from the reference case. This suggests that the non-modulated image sources may also be an alternative option to coarsen the mesh and alleviate computational costs while maintaining certain acceptable accuracy.

Adiabatic boundary conditions are assumed on the powder-part boundary in this chapter. However, in the LPBF process, a small amount of heat is conducted to the surrounding powder. The proposed method can also be applied under the low boundary conductivity consideration. In this case, the modulated image sources should partly compensate for the regular source's heat loss rate to approximate the powder-part boundary's real heat loss rate. Besides, this chapter proposes that an image source should be induced when the distance of a regular source to the boundary is proposed to be less than $15r$. This method, in principle, can be applied in the thermal simulation of 3D print structures with small cross sections, such as thin walls or lattice structures (one dimension less than $30r$). However, boundaries on the opposite side of a structure can be close to each other. As discussed in [26], more image sources corresponding to the same regular source through multi-reflection along the boundaries should be included.

2.5. CONCLUSIONS

The semi-analytical method is a fast part-scale thermal simulation approach for the LPBF process. This method requires a complementary field to enforce the boundary conditions. To solve the complementary field numerically, the traditional semi-analytical method requires spatial discretization on part boundaries to be as fine as the laser spot radius. Consequently, the computational efficiency of the method is limited due to the excessive degrees of freedom.

In this chapter, we propose incorporating image sources to compensate for the heat loss from regular heat sources representing laser scanning at the powder-part boundary. The powder-part boundary is assumed to be adiabatic. The positions and intensity

of image sources can be easily determined for straight boundaries. However, utilizing image sources for curved boundaries, commonly the case for intricate parts additively manufactured, was an open question.

In our novel method, image source power is modulated according to image position and local radius of curvature near a curved boundary to almost perfectly compensate for the heat flux emanating from laser-associated point heat sources. In this way, the numerical temperature field to be solved becomes smoother, and hence, we can coarsen the mesh for the numerical correction field around 10 times on the part boundary. Therefore, the computational efficiency can be increased by 20 times.

The peak temperature difference between the reference case and the simulation with modulated image sources is as small as several degrees. In contrast, the difference with the non-modulated case becomes 43.0 °C. Furthermore, the semi-analytical method employed in this chapter is suitable for multiple laser scans acting simultaneously, obviating the need for local mesh refinement based on the laser scanning path. This capability further contributes to the computational efficiency of the proposed method with no additional cost.

Despite the promising results, this study has limitations. The temperature-independent thermal properties of Ti6Al4V are assumed to make use of the superposition principle, which may introduce certain deviations depending on the temperature dependence of the material used.

BIBLIOGRAPHY

[1] A. V. Gusarov, I. Yadroitsev, P. Bertrand, and I. Smurov, "Model of radiation and heat transfer in laser-powder interaction zone at selective laser melting", Journal of Heat Transfer **131**, 072101 (2009).

[2] M. Bayat, O. Zinovieva, F. Ferrari, C. Ayas, M. Langelaar, J. Spangenberg, R. Salajeghe, K. Poulios, S. Mohanty, O. Sigmund, and J. Hattel, "Holistic computational design within additive manufacturing through topology optimization combined with multi-physics multi-scale materials and process modelling", Progress in Materials Science **138**, 101129 (2023).

[3] B. Schoinochoritis, D. Chantzis, and K. Salonitis, "Simulation of metallic powder bed additive manufacturing processes with the finite element method: a critical review", Proceedings of the Institution of Mechanical Engineers, Part B: Journal of Engineering Manufacture **231**, 96–117 (2017).

[4] Z. Luo and Y. Zhao, "A survey of finite element analysis of temperature and thermal stress fields in powder bed fusion additive manufacturing", Additive Manufacturing **21**, 318–332 (2018).

[5] M. Francois, A. Sun, W. King, N. Henson, D. Tourret, C. Bronkhorst, N. Carlson, C. Newman, T. Haut, J. Bakosi, J. Gibbs, V. Livescu, S. Vander Wiel, A. Clarke, M. Schraad, T. Blacker, H. Lim, T. Rodgers, S. Owen, F. Abdeljawad, J. Madison, A. Anderson, J.-L. Fattebert, R. Ferencz, N. Hodge, S. Khairallah, and O. Walton, "Modeling of additive manufacturing processes for metals: challenges and opportunities", Current Opinion in Solid State and Materials Science **21**, 198–206 (2017).

[6] G. Vastola, G. Zhang, Q. Pei, and Y.-W. Zhang, "Controlling of residual stress in additive manufacturing of ti6al4v by finite element modeling", Additive Manufacturing **12**, Special Issue on Modeling & Simulation for Additive Manufacturing, 231–239 (2016).

[7] D. Sarkar, A. Kapil, and A. Sharma, "Advances in computational modeling for laser powder bed fusion additive manufacturing: a comprehensive review of finite element techniques and strategies", Additive Manufacturing **85**, 104157 (2024).

[8] E. R. Denlinger, M. Gouge, J. Irwin, and P. Michaleris, "Thermomechanical model development and in situ experimental validation of the laser powder-bed fusion process", Additive Manufacturing **16**, 73–80 (2017).

[9] L.-E. Lindgren, "Finite element modeling and simulation of welding part 1: increased complexity", Journal of Thermal Stresses **24**, 141–192 (2001).

[10] L.-E. Lindgren, "Finite element modeling and simulation of welding. part 2: improved material modeling", Journal of Thermal Stresses **24**, 195–231 (2001).

[11] L.-E. Lindgren, "Finite element modeling and simulation of welding. part 3: efficiency and integration", Journal of Thermal Stresses **24**, 305–334 (2001).

[12] A. Olleak and Z. Xi, "Part-scale finite element modeling of the selective laser melting process with layer-wise adaptive remeshing for thermal history and porosity prediction", Journal of Manufacturing Science and Engineering **142**, 121006 (2020).

[13] I. Roberts, C. Wang, R. Esterlein, M. Stanford, and D. Mynors, "A three-dimensional finite element analysis of the temperature field during laser melting of metal powders in additive layer manufacturing", International Journal of Machine Tools and Manufacture **49**, 916–923 (2009).

[14] X. Lu, X. Lin, M. Chiumenti, M. Cervera, Y. Hu, X. Ji, L. Ma, H. Yang, and W. Huang, "Residual stress and distortion of rectangular and s-shaped ti-6al-4v parts by directed energy deposition: modelling and experimental calibration", Additive Manufacturing **26**, 166–179 (2019).

[15] M. Chiumenti, E. Neiva, E. Salsi, M. Cervera, S. Badia, J. Moya, Z. Chen, C. Lee, and C. Davies, "Numerical modelling and experimental validation in selective laser melting", Additive Manufacturing **18**, 171–185 (2017).

[16] M. Chiumenti, M. Cervera, A. Salmi, C. Agelet de Saracibar, N. Dialami, and K. Matsui, "Finite element modeling of multi-pass welding and shaped metal deposition processes", Computer Methods in Applied Mechanics and Engineering **199**, 2343–2359 (2010).

[17] A. Foroozmehr, M. Badrossamay, E. Foroozmehr, and S. Golabi, "Finite element simulation of selective laser melting process considering optical penetration depth of laser in powder bed", Materials & Design **89**, 255–263 (2016).

[18] M. Gouge, E. Denlinger, J. Irwin, C. Li, and P. Michaleris, "Experimental validation of thermo-mechanical part-scale modeling for laser powder bed fusion processes", Additive Manufacturing **29**, 100771 (2019).

[19]S. Kollmannsberger, A. Özcan, M. Carraturo, N. Zander, and E. Rank, "A hierarchical computational model for moving thermal loads and phase changes with applications to selective laser melting", Computers & Mathematics with Applications **75**, 1483–1497 (2018).

[20]J. P. Leonor and G. J. Wagner, "Go-melt: gpu-optimized multilevel execution of lpbf thermal simulations", Computer Methods in Applied Mechanics and Engineering **426**, 116977 (2024).

[21]P. Kopp, E. Rank, V. M. Calo, and S. Kollmannsberger, "Efficient multi-level hp-finite elements in arbitrary dimensions", Computer Methods in Applied Mechanics and Engineering **401**, 115575 (2022).

[22]C. A. Moreira, M. A. Caicedo, M. Cervera, M. Chiumenti, and J. Baiges, "A multi-criteria h-adaptive finite-element framework for industrial part-scale thermal analysis in additive manufacturing processes", Engineering with Computers **38**, 4791–4813 (2022).

[23]C. Li, E. R. Denlinger, M. F. Gouge, J. E. Irwin, and P. Michaleris, "Numerical verification of an octree mesh coarsening strategy for simulating additive manufacturing processes", Additive Manufacturing **30**, 100903 (2019).

[24]A. Olleak and Z. Xi, "Scan-wise adaptive remeshing for efficient lpbf process simulation: the thermal problem", Manufacturing Letters **23**, 75–78 (2020).

[25]A. Olleak, F. Dugast, P. Bharadwaj, S. Strayer, S. Hinnebusch, S. Narra, and A. C. To, "Enabling part-scale scanwise process simulation for predicting melt pool variation in lpbf by combining gpu-based matrix-free fem and adaptive remeshing", Additive Manufacturing Letters **3**, 100051 (2022).

[26]Y. Yang, M. Knol, F. van Keulen, and C. Ayas, "A semi-analytical thermal modelling approach for selective laser melting", Additive Manufacturing **21**, 284–297 (2018).

[27]J. Ning, E. Mirkoohi, Y. Dong, D. E. Sievers, H. Garmestani, and S. Y. Liang, "Analytical modeling of 3d temperature distribution in selective laser melting of ti-6al-4v considering part boundary conditions", Journal of Manufacturing Processes **44**, 319–326 (2019).

[28]Y. Yang, F. van Keulen, and C. Ayas, "A computationally efficient thermal model for selective laser melting", Additive Manufacturing **31**, 100955 (2020).

[29]J. C. Steuben, A. J. Birnbaum, J. G. Michopoulos, and A. P. Iliopoulos, "Enriched analytical solutions for additive manufacturing modeling and simulation", Additive Manufacturing **25**, 437–447 (2019).

[30]A. J. Wolfer, J. Aires, K. Wheeler, J.-P. Delplanque, A. Rubenchik, A. Anderson, and S. Khairallah, "Fast solution strategy for transient heat conduction for arbitrary scan paths in additive manufacturing", Additive Manufacturing **30**, 100898 (2019).

[31]E. J. Schwalbach, S. P. Donegan, M. G. Chapman, K. J. Chaput, and M. A. Groeber, "A discrete source model of powder bed fusion additive manufacturing thermal history", Additive Manufacturing **25**, 485–498 (2019).

[32]Y. Wang, X. Ji, and S. Y. Liang, "Analytical modeling of temperature distribution in laser powder bed fusion with different scan strategies", Optics & Laser Technology **157**, 108708 (2023).

[33] P. R. Zagade, B. Gautham, A. De, and T. DebRoy, "Analytical modelling of scanning strategy effect on temperature field and melt track dimensions in laser powder bed fusion", Additive Manufacturing **82**, 104046 (2024).

[34] A. Plotkowski, M. M. Kirka, and S. Babu, "Verification and validation of a rapid heat transfer calculation methodology for transient melt pool solidification conditions in powder bed metal additive manufacturing", Additive Manufacturing **18**, 256–268 (2017).

[35] A. Ross, I. Bitharas, K. Perkins, and A. Moore, "Volumetric heat source calibration for laser powder bed fusion", Additive Manufacturing **60**, 103267 (2022).

[36] Y. Jia, Y. Saadlaoui, J.-C. Roux, and J.-M. Bergheau, "Steady-state thermal model based on new dedicated boundary conditions–application in the simulation of laser powder bed fusion process", Applied Mathematical Modelling **112**, 749–766 (2022).

[37] R. Forslund, A. Snis, and S. Larsson, "Analytical solution for heat conduction due to a moving gaussian heat flux with piecewise constant parameters", Applied Mathematical Modelling **66**, 227–240 (2019).

[38] B. Stump and A. Plotkowski, "An adaptive integration scheme for heat conduction in additive manufacturing", Applied Mathematical Modelling **75**, 787–805 (2019).

[39] T. Moran, D. Warner, and N. Phan, "Scan-by-scan part-scale thermal modelling for defect prediction in metal additive manufacturing", Additive Manufacturing **37**, 101667 (2021).

[40] A. Robert and T. Debroy, "Geometry of laser spot welds from dimensionless numbers", Metallurgical and Materials Transactions B **32**, 941–947 (2001).

[41] D. Veldman, R. Fey, H. Zwart, M. van de Wal, J. van den Boom, and H. Nijmeijer, "Semi-analytic approximation of the temperature field resulting from moving heat loads", International Journal of Heat and Mass Transfer **122**, 128–137 (2018).

[42] H. S. Carslaw and J. C. Jaeger, *Conduction of heat in solids* (Oxford Science Publications, Clarendon Press, 1986).

[43] L. Piegl and W. Tiller, *The nurbs book* (Springer Science & Business Media, 2012).

[44] Y. Cao, X. Lin, N. Kang, L. Ma, L. Wei, M. Zheng, J. Yu, D. Peng, and W. Huang, "A novel high-efficient finite element analysis method of powder bed fusion additive manufacturing", Additive Manufacturing **46**, 102187 (2021).

[45] M. Vanini, S. Searle, K. Vanmeensel, and B. Vrancken, "Avoiding heat source calibration for finite element modeling of the laser powder bed fusion process", Additive Manufacturing **92**, 104369 (2024).

[46] Z.-D. Zhang, S. Imani Shahabad, O. Ibhadode, C. F. Dibia, A. Bonakdar, and E. Toyserkani, "3-dimensional heat transfer modeling for laser powder bed fusion additive manufacturing using parallel computing and adaptive mesh", Optics & Laser Technology **158**, 108839 (2023).

[47] B. A. Boley and J. H. Weiner, *Theory of thermal stresses* (John Wiley & Sons, 1960).

[48] T. Bar-Kohany and A. Jain, "Dissipation of boundary effects in multilayer heat conduction problems", International Journal of Heat and Mass Transfer **223**, 125207 (2024).

3

3

SEMI-ANALYTICAL ISOGEOMETRIC ANALYSIS FOR THE LPBF PROCESS

Thermal modeling of Laser Powder Bed Fusion (LPBF) is challenging because of the steep, rapidly moving thermal gradients difficult to capture with conventional Finite Element Method (FEM). Accurately resolving these gradients typically requires highly refined, dynamically updated spatial discretization, resulting in substantial computational cost. Semi-analytical modeling approaches partially address this challenge by superimposing an analytical point-source solution in an infinite or semi-infinite medium with a complementary smoother numerical field that enforces boundary conditions. However, state-of-the-art semi-analytical simulations still demand mesh refinement near part boundaries or rely on restrictive image-source techniques. In this study, we reformulate the semi-analytical framework using isogeometric analysis (IGA). While the analytical temperature solution of point heat sources is used to mimic the laser-induced heat input, the complementary numerical correction temperature field for imposing the boundary conditions is solved via spline-based IGA discretization. IGA provides an exact geometric representation and enhanced continuity with fewer degrees of freedom, unlocking the thermal modeling of realistic parts with complex geometry. The governing heat equation with Neumann and Dirichlet boundaries is cast into a weak form, discretized with NURBS basis functions, and advanced in time using an implicit θ-scheme. This strategy removes the need for scan-wise remeshing and is robust against intricate geometric features such as sharp corners and varying cross-sections. Numerical examples confirm that the proposed semi-analytical IGA method delivers accurate temperature predictions and substantial computational efficiency gains over FEM, offering a novel, powerful tool for thermal simulation of realistic parts with LPBF.

Parts of this chapter have been accepted in *Computer Methods in Applied Mechanics and Engineering* by Yang Yang, Ye Ji, Matthias Möller and Can Ayas.

3.1. INTRODUCTION

Laser Powder Bed Fusion (LPBF) is a metal additive manufacturing (AM) technology that offers exceptional form freedom to fabricate geometrically complex parts. It has been widely adopted for manufacturing topology-optimized structures and meta-materials [1–3]. In LPBF, one or multiple laser beams are guided by mirrors and focused onto the metal powder bed. The absorbed laser energy locally melts the powder to form small melt pool(s). As the laser continuously moves, the melt pool(s) rapidly cool and solidify, realizing the layer-by-layer growth. During this, powder–liquid–solid phase changes, and several thermal phenomena arise. Heat conduction within the solid, from the localized melt pool toward the build platform acting as a heat sink, accounts for conveying most of the heat input through laser(s). In contrast, heat transfer to the surrounding loose powder dissipates only about 1% of the heat conducted [4], while radiation and convection to the surroundings result in only minor heat losses.

Accurate thermal simulations play an important role in predicting the temperature histories of additively manufactured parts. Manufacturing parameters such as laser power, scanning speed, and layer thickness can be optimized based on the temperature histories. Moreover, reliable temperature fields inform models of phase transformations, microstructure evolution, residual stress, and distortion, and ultimately improve part quality.

The Finite Element Method (FEM) remains the most widely used approach for part-scale temperature simulations in LPBF. The temperature fields obtained from these simulations have been used for predicting thermal stress [5, 6], porosity formation mechanisms [7] and melt-pool shape [8]. Comprehensive review of state-of-the-art FEM applications can be found in [9]. To represent the layer-by-layer growth of a part during the AM process, FEM typically employs element birth–death techniques. Two common variants are the quiet element method, where undeveloped layers remain in the global conductivity matrix but are rendered thermally inactive by drastically reducing their conductivity [10], and the inactive element method, where the elements associated with these layers are excluded entirely until activated during deposition [11].

Accurate resolution of steep temperature gradients near the moving laser spot demands extremely fine meshes on the order of the laser spot radius [11, 12]. For example, Roberts et al. [11] used 25 μm elements for a 50 μm spot radius, Vanini et al. [13] refined further to 20 μm, and Zhang et al. [14] proposed 5 μm elements for similar conditions. While such fine discretization is required for accuracy, it dramatically increases the total number of elements and thus the computational cost, limiting the practicality of FEM for part-scale LPBF simulations.

Rather than utilizing a uniformly fine mesh across the entire computational domain, adaptive mesh refinement improves computational efficiency while retaining the accuracy of numerical simulations by dynamically adjusting the spatial resolution in response to the changing position of the laser spot. In this approach, high-resolution meshes are employed in the laser–material interaction region, while the mesh is progressively coarsened in areas distant from the heat source. This strategy enables the efficient resolution of steep, localized temperature gradients induced by the moving heat source, which would otherwise necessitate a globally fine mesh and incur substantial computational cost. Within adaptive mesh refinement, two principal refinement strategies are

commonly employed: h-refinement (reducing the mesh size h) and hp-refinement (refining h while simultaneously increasing the polynomial order p of the approximation space) [15–18]. Moreover, generally, there are two types of h refinement applied. The more prevalent is the layer-wise (static) remeshing scheme, in which the refinement focuses on the active layer while keeping the underlying previously solidified layers coarser [15, 19, 20]. The other is the scan-wise (dynamic) remeshing, which refines the mesh locally around the moving laser spot while maintaining a coarser discretization in regions of nearly uniform temperature [21, 22]. The layer-wise remeshing strategy primarily focuses on mesh adaptation along the build direction (orthogonal to the layer), ensuring adequate resolution across the successively deposited layers. In contrast, the scan-wise remeshing strategy refines the mesh within the current printing plane, allowing for a more detailed physical representation of the thermal process in the plane. Besides, the scan-wise remeshing strategy can employ finer local meshes, thereby enhancing the accuracy of melt pool size, shape, and cooling rate predictions. However, the scan-wise strategy also introduces greater computational complexity, as it requires much more frequent updates of the mesh and the corresponding thermal conductivity matrix and thermal load vector. Olleak and Xi [21] optimized the remeshing region length and corresponding remeshing frequency in the scan-wise adaptive remeshing strategy; however, even the most effective configuration achieves only about a 60% reduction in total computational time relative to the layer-wise remeshing approach. Thus, in general, most of the simulation research is based on the layer-wise remeshing strategy.

In addition to FEM, isogeometric analysis (IGA) [23] has emerged as a powerful alternative for thermal simulation in a geometrically complex domain [24–26] and moving heat source during the LPBF [27]. By employing spline-based basis functions such as NURBS [28] or T-splines [29–32], IGA preserves the exact CAD geometry, whereas FEM often degrades geometric fidelity during mesh generation. Given the geometric complexity of typically LPBF-fabricated components, this exact representation makes IGA particularly well suited for capturing intricate geometric features accurately [33]. Furthermore, the higher-order basis functions used in IGA provide increased continuity across elements, enabling more accurate temperature predictions with significantly fewer degrees of freedom than conventional FEM [34]. Such characteristics are especially valuable in LPBF simulations, where steep thermal gradients and rapidly moving heat sources impose demanding requirements on both spatial accuracy and computational efficiency. Carraturo et al. [35, 36] demonstrated that THB-spline refinement and coarsening can be used to dynamically remesh and track the moving laser spot within an IGA framework—similar in concept to scan-wise remeshing in FEM. In this study, the ratio between the largest and smallest element lengths typically ranges from 20 to 100. However, despite the use of adaptive remeshing strategies, both FEM and IGA typically require highly refined meshes and frequent mesh updates to accurately capture the steep laser-induced thermal gradients and the movement of the laser source.

Another class of thermal modeling for LPBF employs analytical solutions of the heat equation in infinite or semi-infinite domains to model the laser scanning process [37–42]. The movement of the laser spot is captured by sequentially activating discrete point heat sources, thereby representing the continuous motion of the laser as a series of temporally and spatially evolving heat inputs. These closed-form fields of discrete point

sources capture the steep temperature gradients near the laser spot analytically, eliminating the need for an adaptive mesh refinement to resolve temperature gradients numerically and thereby reducing computational complexity. However, since the analytical solution assumes a semi-infinite medium, its accuracy becomes limited when applied to finite additively manufactured parts, as the thermal boundary conditions of the part are not satisfied [42].

To enforce the correct boundary conditions, semi-analytical methods augment the analytical field with a complementary numerical field so that the total temperature is represented as their superposition [37]. The point-source solution effectively resolves the local thermal gradients, rendering the complementary numerical field smooth. As a result, the numerical mesh can be decoupled from the characteristic length scale of the problem, i.e., laser-spot radius, allowing for a significantly coarser discretization without loss of accuracy. Nevertheless, near the part boundaries, the mesh must still be locally refined as dictated by the length scale of the laser spot to accurately capture and counteract the outgoing heat flux of heat sources at close proximity to a boundary. This translates into additional computational cost.

In our previous work, analytical image sources were applied across adiabatic boundaries to eliminate the need for mesh refinement near part edges [37, 42]. For straight boundaries, the application of this method is straightforward [37], as illustrated in Fig. 3.1a. The image source J is positioned equidistant from the actual source I across the boundary ∂V_1, thereby readily satisfying the adiabatic (no flux) boundary conditions. For curved boundaries, its implementation is more involved [42]. However, the image source method exhibits inherent limitations when applied to part geometries with multiple connected boundaries, multi-disconnected cross-sections, and cross-sectional variation along the building direction. In the presence of sharp corners where multiple boundaries meet, the reflection behavior of the image source becomes considerably more intricate, as illustrated in Fig. 3.1b. The reflection of the primary source I across the boundary ∂V_1 requires an image source J_1, which simultaneously exerts an influence on the adjacent boundary ∂V_2. Conversely, the reflection of the source I across the boundary ∂V_2 requires an additional image source J_2, which, in turn, affects the boundary ∂V_1. To balance the heat flux from the image sources J_1 on ∂V_2 and J_2 on ∂V_1, more image sources should be introduced. As a result, multiple reflections should be considered until the newly generated image sources are sufficiently far from all the boundaries. In Fig. 3.1c, the image source J is generated in another neighboring solid domain, which artificially heats it. In Fig. 3.1d, the image source J and the actual source I satisfy the adiabatic boundary condition solely on the top plane, where they are positioned at equal distances from the boundary. However, for planes at previously deposited layers, this condition is no longer maintained. Thus, while image sources can reduce mesh density and computational burden for relatively simple part geometries, they are not universally applicable to all geometries.

This chapter reformulates the semi-analytical thermal simulation framework by replacing image sources and or FEM with IGA for computing the complementary boundary correction field. The proposed formulation provides two key benefits. First, it leverages the analytical temperature solution capable of resolving the steep, localized gradients induced by the moving laser, eliminating the need for an extremely fine mesh that

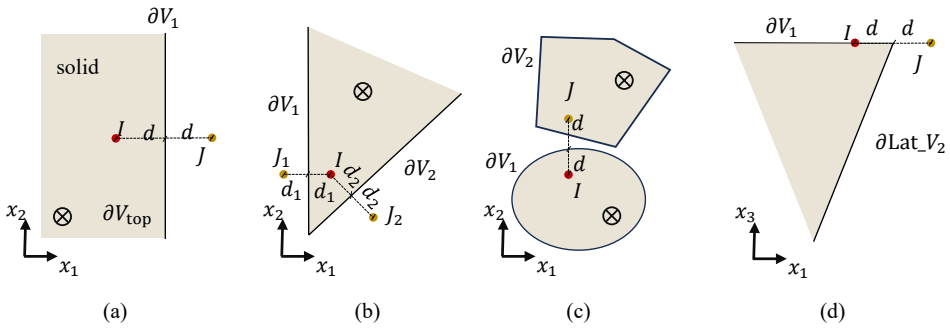

Figure 3.1: Schematic of the image source problems: (a) Single straight boundary, for imaging through a simple straight boundary ∂V_1, the adiabatic boundary conditions can be easily satisfied by introducing a single image source J. (b) Multiple connected boundaries, in cases involving multiple connected boundaries, the image source J_1 reflected from one boundary ∂V_1 may also influence another boundary ∂V_2, and similarly, the image source J_2 reflected from ∂V_2 may affect ∂V_1. (c) Two adjacent solid boundaries, when imaging between two neighboring solid boundaries, the image source J reflected by one boundary ∂V_1 may be located within the solid domain associated with the other boundary. (d) Cross-sectional variation along the building direction (x_3), when the cross section varies along the x_3 direction, the image source J can only satisfy the adiabatic boundary conditions on the top plane. In this case, the physical source I and its image J are separated by an equal distance d to the boundary only on the top plane.

follows the laser trajectory through frequent remeshing. This leads to a smooth field of the complementary field at least away from the boundaries. Second, IGA offers an exact geometric representation and higher-order continuity through spline-based basis functions, making it particularly effective for addressing boundary conditions for complex parts even when the laser is in close proximity. These properties enable accurate temperature predictions for realistic parts with complex geometries, while requiring substantially fewer degrees of freedom than conventional FEM. The improvements in accuracy (in terms of relative errors) and in computational efficiency (in terms of degrees of freedom and minimum element size) are demonstrated with numerical examples comparing the proposed method with FEM based semi-analytical approaches from the literature.

The remainder of this chapter is organized as follows. Section 3.2 presents the reformulation of the semi-analytical method based on discrete point sources, incorporating an IGA-enabled boundary-correction strategy through the complementary field, and further details the IGA discretization and the time-integration procedure employed to compute the numerical field. Section 3.3 evaluates the efficiency and accuracy of FEM and IGA under varying mesh densities for a point-source, and further demonstrates the robustness of the proposed method for continuous laser scanning and geometrically complex parts. Finally, conclusions are provided in Section 3.4.

3.2. IGA-BASED FORMULATION OF THE SEMI-ANALYTICAL METHOD

We consider the LPBF process of a freeform three-dimensional part. To print a new layer, a thin layer of metal powder is recoated over the previously built body V (see Fig. 3.2)

with the coordinate origin defined in Fig. 3.2a. The boundary ∂V of V consists of three surfaces: the bottom surface ∂V_{bot} fused to the build platform, the lateral surface ∂V_{lat} surrounded by loose powder, and the top surface ∂V_{top} covered by the newly recoated layer (Fig. 3.2b). When laser scans ∂V_{top} to fuse the powder, partial absorption of laser energy by the powder drives transient heat conduction within the solid part, governed by

$$\rho c_p \frac{\partial T}{\partial t} = \nabla \cdot (k \nabla T) + Q, \quad \text{in } V, \tag{3.1}$$

where $T(\mathbf{x}, t)$ is temperature, ρ is mass density, c_p is specific heat capacity, k is thermal conductivity, and Q is the volumetric heat source. Neglecting the temperature dependence of ρ, c_p, and k, the equation becomes

$$\frac{\partial T}{\partial t} = \alpha \nabla^2 T + \frac{Q}{\rho c_p}, \tag{3.2}$$

where $\alpha = \frac{k}{\rho c_p}$ is the linear form with thermal diffusivity.

The thermal load Q is represented as a superposition of N instantaneous point sources obtained by discretizing the continuous laser scan (see Fig. 3.2a). The I-th source is activated at time $t^{(I)}$ and the next at $t^{(I+1)} = t^{(I)} + \Delta t$; thus the arc-length spacing between successive sources along the scan path is $v \Delta t$, where v denotes the laser scanning speed. Guided by our previous convergence study [37, 42], we set $\Delta t = 1 \times 10^{-5}$ s for all simulations. After completing the scan of the current layer, a fresh powder layer is recoated.

The temperature field $T(\mathbf{x}, t)$ within the domain V under the thermal load Q in Eq. (3.2) is obtained by solving a boundary value problem with prescribed conditions on ∂V. The initial condition $t = 0$ is

$$T(\mathbf{x}, 0) = T_c, \tag{3.3}$$

where T_c is the constant temperature of the build platform.

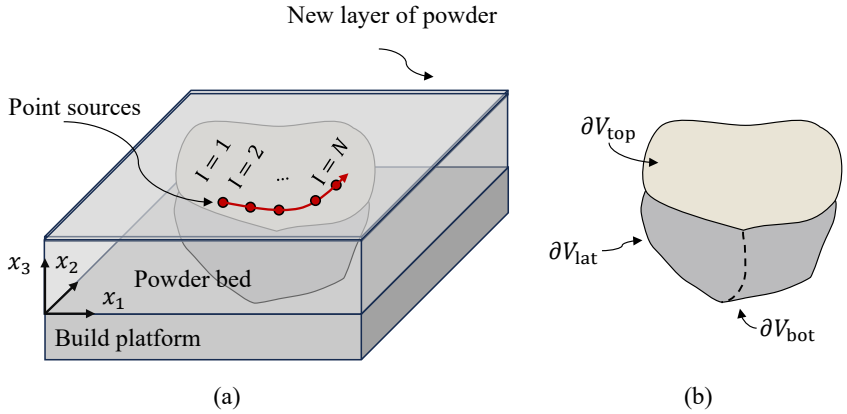

Figure 3.2: Schematic of the LPBF process: (a) Body V submerged in the powder bed, with bottom ∂V_{bot} fused to the build platform and a thin powder layer on ∂V_{top}; (b) Boundary decomposition of V, showing ∂V_{bot}, ∂V_{lat}, and ∂V_{top}.

Because the thermal conductivity of the surrounding powder is only about 1% of that of the solid material [4], the lateral surface ∂V_{lat} (see Fig. 3.2) is treated as adiabatic [39, 40]. Heat loss by convection and radiation on the top surface ∂V_{top} is negligible compared with conduction inside the solid, hence ∂V_{top} is also assumed adiabatic. Thus, homogeneous Neumann conditions on the lateral and top boundaries are

$$\frac{\partial T}{\partial \mathbf{n}} = 0, \qquad \text{on } \partial V_{\text{lat}} \cup \partial V_{\text{top}}, \tag{3.4}$$

where $\mathbf{n}$ is the outward unit normal. At the bottom surface, which is in contact with the build platform, a Dirichlet boundary condition is applied to prescribe the temperature:

$$T = T_c, \qquad \text{on } \partial V_{\text{bot}}. \tag{3.5}$$

3.2.1. TEMPERATURE DECOMPOSITION

To facilitate numerical treatment, the temperature field $T(\mathbf{x}, t)$ is decomposed into an analytical component and a numerical correction:

$$T(\mathbf{x}, t) = \tilde{T}(\mathbf{x}, t) + \hat{T}(\mathbf{x}, t), \tag{3.6}$$

where $\tilde{T}$ is a known analytical solution of the temperature evolution due to discretized point sources, and $\hat{T}$ is the complementary field to be solved numerically. The analytical component is expressed as a sum of K point-source solutions:

$$\tilde{T}(\mathbf{x}, t) = \sum_{I=1}^{K} \tilde{T}^{(I)}(\mathbf{x}, t), \qquad \tau^{(K)} \le t, \quad K \le N, \tag{3.7}$$

with each contribution given by

$$\tilde{T}^{(I)}(\mathbf{x}, t) = \frac{E^{(I)}}{\rho c_p \left[4\pi\alpha(t-\tau^{(I)})\right]^{3/2}} \exp\left(-\frac{\|\mathbf{x}-\mathbf{x}^{(I)}\|^2}{4\alpha\left(t-\tau^{(I)}\right)}\right) H\left(t-\tau^{(I)}\right), \tag{3.8}$$

where $\mathbf{x}^{(I)}$ is the location of the I-th heat source, $R^{(I)} = \|\mathbf{x}-\mathbf{x}^{(I)}\|$ is the Euclidean distance to the source, $E^{(I)} = AP\Delta t$ is the deposited energy, and H is the Heaviside step function ensuring causality, the factor A accounts for the laser absorptivity of metal powder. The modified time $\tau^{(I)} = t^{(I)} - r^2/8\alpha$ is introduced to avoid singularity at the point-source activation time $t^{(I)}$, and accounts for the finite radius of the laser source.

Substituting Eq. (3.6) into Eq. (3.2) and isolating $\hat{T}$:

$$\rho c_p \frac{\partial \hat{T}}{\partial t} = k\nabla^2 \hat{T}, \qquad \mathbf{x} \in V. \tag{3.9}$$

The boundary conditions for $\hat{T}$ become

$$q_N := -k\frac{\partial \hat{T}}{\partial \mathbf{n}} = k\frac{\partial \tilde{T}}{\partial \mathbf{n}}, \quad \text{on } \partial V_{\text{lat}}, \tag{3.10}$$

$$\hat{T} = T_c - \tilde{T}, \quad \text{on } \partial V_{\text{bot}}, \tag{3.11}$$

with the initial condition $\hat{T}(\mathbf{x},0) = T_c$ due to $\tilde{T}(\mathbf{x},0) = 0$. Neumann conditions are not explicitly imposed on ∂V_{top} in Eq. (3.10), as the specified Neumann condition, i.e., the adiabatic boundary condition on the top surface, is inherently satisfied and embedded in Eq. (3.8), owing to the coincidence of the top surface of the build part with the origin of the semi-infinite domain.

The temperature field is decomposed as $T = \tilde{T} + \hat{T}$ according to (3.6). The analytical component $\tilde{T}$ represents the superposition of point-source contributions of the discretized laser scan (Fig. 3.3), while the correction field $\hat{T}$ enforces the adiabatic and Dirichlet boundary conditions of the solid domain. We solve numerically for $\hat{T}$ using an isogeometric Galerkin method combined with an implicit time-integration scheme.

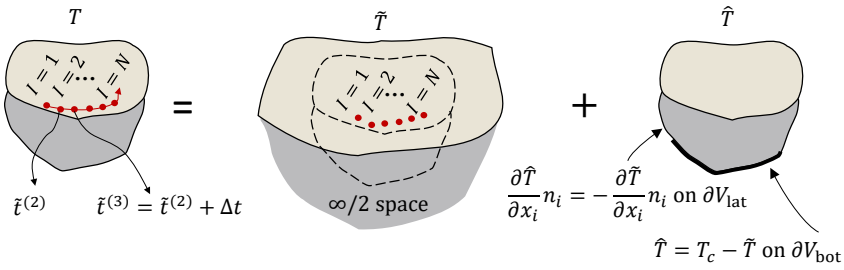

Figure 3.3: A curvilinear (contour) laser scan discretized into a sequence of point sources. The total temperature field is obtained by superimposing the semi-infinite point-source solutions with the complementary field that enforces the finite-part boundary conditions.

3.2.2. WEAK FORM

The strong form of the governing equation for the $\hat{T}$ field is expressed in Eq. (3.9), with the modified Neumann and Dirichlet boundary conditions specified in Eqs. (3.10) and (3.11). Let $w \in H^1(V)$ be a test function vanishing on ∂V_{bot} after Dirichlet enforcement. Multiplying the governing equation by w and integrating over V, and applying the divergence theorem, we obtain

$$\int_V \rho c_p \frac{\partial \hat{T}}{\partial t} w \, dV + \int_V k \nabla \hat{T} \cdot \nabla w \, dV = \int_{\partial V_{\text{lat}}} (-q_N) w \, dS, \tag{3.12}$$

with q_N defined in (3.10). This weak form incorporates the laser-induced heat flux implicitly through q_N and preserves the adiabatic boundaries on ∂V_{lat}.

3.2.3. ISOGEOMETRIC DISCRETIZATION

The geometry of the printed part is exactly represented by a NURBS mapping $\mathbf{\Phi} : \hat{V} \to V$ from the parametric domain $\hat{V}$. Let $\{N_i(\boldsymbol{\xi})\}_{i=1}^n$ be the B-spline or NURBS basis functions of order p defined on the knot vectors of $\hat{V}$. The unknown field $\hat{T}$ and the test function w are approximated as

$$\hat{T}_h(\boldsymbol{\xi}, t) = \sum_{i=1}^{n} N_i(\boldsymbol{\xi}) \hat{T}_i(t), \qquad w_h(\boldsymbol{\xi}) = N_j(\boldsymbol{\xi}). \tag{3.13}$$

Using the standard isoparametric concept,

$$\nabla_{\mathbf{x}} N_i = \mathbf{J}^{-\top} \nabla_{\boldsymbol{\xi}} N_i, \qquad dV = J\, d\boldsymbol{\xi}, \tag{3.14}$$

with $\mathbf{J} = \partial \mathbf{x}/\partial \boldsymbol{\xi}$ and $J = \det(\mathbf{J})$. Substituting into (3.12) and assembling element contributions lead to the semi-discrete matrix system

$$\mathbf{M}\,\dot{\hat{T}}(t) + \mathbf{K}\hat{\mathbf{T}}(t) = \mathbf{F}(t), \tag{3.15}$$

where

$$M_{ij} = \int_{\widehat{V}} \rho c_p N_i N_j J\, d\boldsymbol{\xi}, \tag{3.16}$$

$$K_{ij} = \int_{\widehat{V}} k(\nabla_{\mathbf{x}} N_i) \cdot (\nabla_{\mathbf{x}} N_j) J\, d\boldsymbol{\xi}, \tag{3.17}$$

$$F_i(t) = \int_{\partial V_{\text{lat}}} (-q_N) N_i\, dS. \tag{3.18}$$

Dirichlet conditions (3.11) are enforced on control variables whose basis functions have support on ∂V_{bot}. The analytical component $\tilde{T}$ is updated explicitly at each laser position and contributes only to the boundary terms via q_N.

3.2.4. TIME INTEGRATION

The semi-discrete system is integrated using an implicit θ-method:

$$\mathbf{M}\frac{\hat{\mathbf{T}}^{n+1} - \hat{\mathbf{T}}^{n}}{\Delta t} + \theta \mathbf{K}\hat{\mathbf{T}}^{n+1} + (1-\theta)\mathbf{K}\hat{\mathbf{T}}^{n} = \theta \mathbf{F}^{n+1} + (1-\theta)\mathbf{F}^{n}, \tag{3.19}$$

where $0 \le \theta \le 1$, and the superscripts n and $n+1$ refer to the current and next time steps, respectively. We adopt $\theta = 0.5$ (Crank–Nicolson) for second-order accuracy and unconditional stability, consistent with the temporal resolution $\Delta t = 1 \times 10^{-5}$ s used in the laser discretization (Section 3.2). At each time step, the linear system

$$\left(\frac{\mathbf{M}}{\Delta t} + \theta \mathbf{K}\right)\hat{\mathbf{T}}^{n+1} = \left(\frac{\mathbf{M}}{\Delta t} - (1-\theta)\mathbf{K}\right)\hat{\mathbf{T}}^{n} + \theta \mathbf{F}^{n+1} + (1-\theta)\mathbf{F}^{n} \tag{3.20}$$

is solved for $\hat{\mathbf{T}}^{n+1}$. The reconstructed temperature field is then obtained as

$$T^{n+1} = \tilde{T}^{n+1} + \hat{T}^{n+1}, \tag{3.21}$$

which satisfies both the transient laser heating and the boundary conditions of the printed part.

3.3. NUMERICAL EXAMPLES

To evaluate the accuracy and computational efficiency of the proposed semi-analytical IGA method, we present a sequence of numerical experiments. The cases progress from a single point heat source (Section 3.3.1), to continuous laser scanning along a simple boundary (Section 3.3.2), and finally culminate in a complex freeform geometry (Section 3.3.3).

3.3.1. SINGLE HEAT SOURCE COMPARISON

In this section, we compare the simulation efficiency and predictive accuracy of FEM and IGA using a single point heat source. The test geometry is an extruded part obtained by removing a quarter-cylinder from a cube (Fig. 3.4); the cube measures 2 mm × 2 mm × 2 mm and the cylindrical radius is $R_c = 1$ mm. The control points of the part used for the NURBS representation are given in Table 3.1, and knot vectors in three directions are shown as $\Xi = \{0,0,0,0.5,0.5,1,1,1\}$, $H = \{0,0,1,1\}$, $Z = \{0,0,1,1\}$.

Table 3.1: Control net for the top surface of the part (unit: mm).

i	$B_{i,1}$	$B_{i,2}$
1	$(1,0,2)$	$(0,0,2)$
2	$(1,\sqrt{2}-1,2)$	$(0,1,2)$
3	$(2-\sqrt{2}/2,\sqrt{2}/2,2)$	$(0,2,2)$
4	$(3-\sqrt{2},1,2)$	$(1,2,2)$
5	$(2,1,2)$	$(2,2,2)$

A laser pulse of duration $\Delta t = 1.0 \times 10^{-5}$ s and power $P = 82.5$ W is applied to the top surface. Because the laser spot radius is only $r_{\text{laser}} = 20\,\mu$m and the exposure time is extremely short, the heat input is approximated as a point source I (red circle in Fig. 3.4). The point source is positioned 100 μm from the curved boundary, with the line connecting it to the coordinate origin forming a $\pi/4$ angle with the x_2-axis (Fig. 3.4b). The metal powder absorptivity is $A = 0.77$, giving an applied thermal load of each point source $E_p = AP\Delta t = 6.35 \times 10^{-4}$ J. The thermal properties of Ti–6Al–4V used in all simulations are listed in Table 3.2.

Both FEM and IGA are employed to compute the complementary temperature field $\hat{T}$ defined in Eqs. (3.9–3.11), induced by the point source I shown in Fig. 3.4.

For the Finite Element (FE) simulations, a series of meshes with varying mesh densities, from coarse to highly refined, is generated and analyzed using ABAQUS. An example of a FE mesh is provided in Fig. 3.5a. In this mesh, elements near the point source are refined to approximately 50 μm to resolve steep temperature gradients accurately, while coarser elements of about 200 μm are used farther apart from the source position to reduce computational cost. Additionally, a highly refined mesh with a minimum element size of 5 μm near the source is adopted and designated as the reference solution for accuracy assessment.

Table 3.2: Thermal properties of Ti–6Al–4V.

Conductivity	Heat capacity	Density
42 W/(m K)	990 J/(kg K)	4420 kg/m^3

Similarly, for IGA, meshes of varying mesh density are employed to calculate the $\hat{T}$ field. One representative IGA mesh is shown in Fig. 3.5b, where the minimum element size is approximately 50 μm.

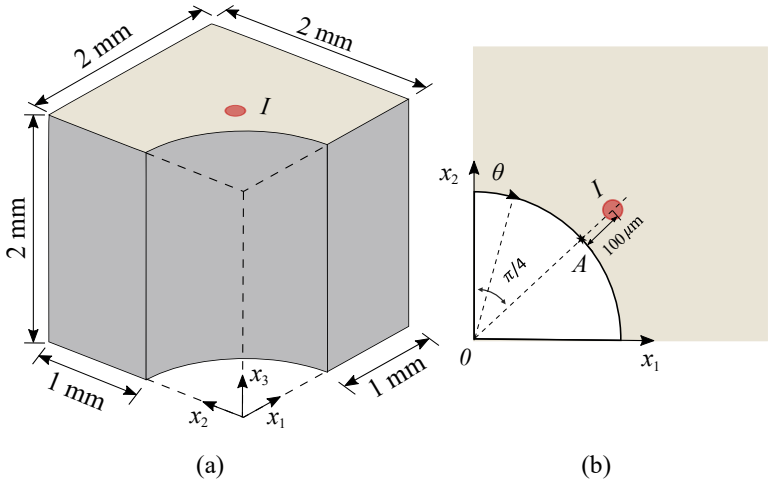

Figure 3.4: (a) A point source (red) positioned near the curved boundary of a 2 mm×2 mm×2 mm cubic domain, where a quarter-cylinder of radius $R_c = 1$ mm has been removed. (b) Top view of the part. The shortest distance from the point source to the arc is 100 μm, located at $\theta = \pi/4$ relative to the x_2-axis.

To evaluate and compare the simulation efficiency and predictive accuracy of FEM and IGA, we examine the temperature at point A (marked in Fig. 3.4b). The source is activated at $t = 0$, and the comparison is performed at $t = 1.9 \times 10^{-4}$ s, which corresponds to the time instance when the complementary temperature $\hat{T}$ at A reaches its peak value. The reference FE simulation with a minimum element size of 5 μm yields $\hat{T}_{\text{ref}} = 20.79\,^{\circ}$C, which is adopted as the benchmark solution.

As the mesh is coarsened, the number of degrees of freedom (DOFs) decreases, and the computed temperatures gradually deviate from the reference, introducing a relative error, calculated as

$$e_r = \frac{|\hat{T} - \hat{T}_{\text{ref}}|}{\hat{T}_{\text{ref}}}$$

Fig. 3.6a reports the relative error (e_r) as a function of the ratio l_e between the minimum element size (l_{min} in μm) and the laser spot radius (r_{laser} in μm)

$$l_e = \frac{l_{\text{min}}}{r_{\text{laser}}}.$$

Fig. 3.6b illustrates the variation of e_r with respect to DOFs.

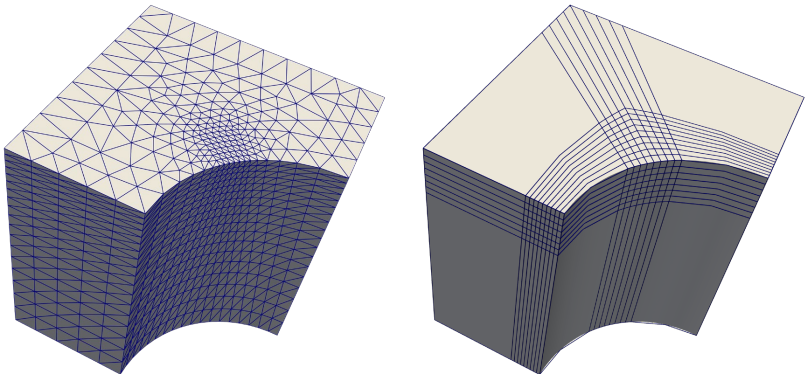

(a) FE mesh (minimum element size 50 µm, DOFs 3302)

(b) IGA mesh, minimum element size around 50 µm, DOFs 4845)

Figure 3.5: Finite Element (FE) and IGA mesh for computing $\hat{T}$. Small elements of approximately 50 μm are used to refine the boundary near the point source.

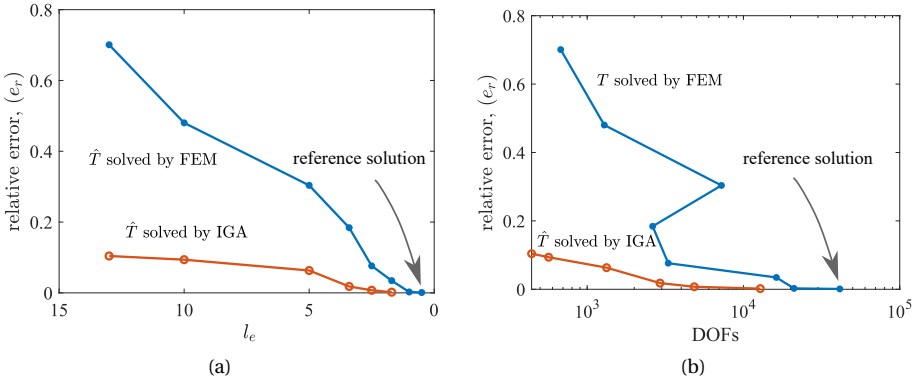

Figure 3.6: Relative error (e_r) of $\hat{T}$ solved by FEM and IGA with respect to (a) the ratio l_e between minimum element size (l_{min} in μm) and the laser spot radius (r_{laser} in μm), and (b) system degrees of freedom. The reference result is calculated using FEM with linear tetrahedron elements of minimum element size around 5 μm (C3D4 element in ABAQUS).

In this study, the minimum element size is normalized by the laser spot radius. The laser spot radius serves as a key parameter that characterizes the spatial intensity of the energy distribution. Since accurately capturing the steep temperature gradients induced by the laser requires the mesh resolution to be on the order of the laser spot radius [11–14], this normalization provides a consistent measure of discretization quality, as discussed in Section 3.1. Although the heat flux intensity decreases as energy dissipates toward the boundaries, leading to smaller thermal gradients because of the increased source-to-boundary distance, the minimum element size could, in principle, also be normalized by this distance. However, for the boundary value problem to solve the complementary field $\hat{T}$, the nearest distance from the heat source to the boundary is influ-

enced by both the laser spot radius and the input laser energy. To maintain a consistent and general formulation, the minimum element size is therefore normalized by the laser spot radius.

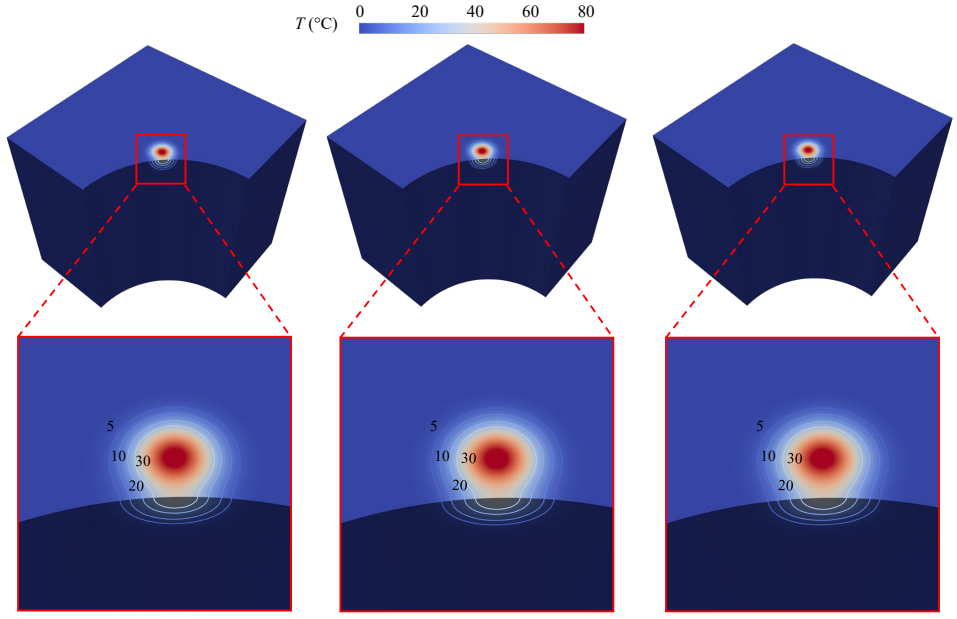

(a) FEM solution, $l_e = 0.5$ element size 10 µm (b) IGA solution, $l_e = 2.5$ element size 50 µm (c) IGA solution, $l_e = 3.4$ element size 68 µm

Figure 3.7: Temperature distribution at $t = 1.9 \times 10^{-4}$ s. Three simulations with different numerical methods and minimum element sizes are adopted.

For FEM, in Fig. 3.6, the relative error e_r increases drastically when $l_e = 2.5$, meaning that the minimum element size is 50 μm, 2.5 times the laser spot radius (20 μm), and corresponding to 3302 DOFs. Interestingly, when l_e increases from 3.4 to 5, the DOF count unexpectedly rises from 2624 to 7231. This counterintuitive behavior results from the meshing strategy: for $l_e = 3.4$, i.e., the minimum element size 68 μm, local refinement is applied near the laser spot while coarser elements are used elsewhere, producing a relatively low DOF count. In contrast, with $l_e = 5$ (the minimum element size 100 μm), the small overall dimensions (2 mm cube) remove the need for local refinement, so a uniform mesh is adopted, substantially increasing the total DOFs despite the larger element size.

For the IGA simulations, the relative error e_r is evaluated against the FEM reference solution with a minimum element size of 5 μm. As shown in Fig. 3.6a, e_r remains around 0.1 (10%) even when the IGA element size is as large as $l_e = 13$. This comparison indicates that, for a given error tolerance, IGA requires fewer degrees of freedom and permits substantially larger element sizes than FEM.

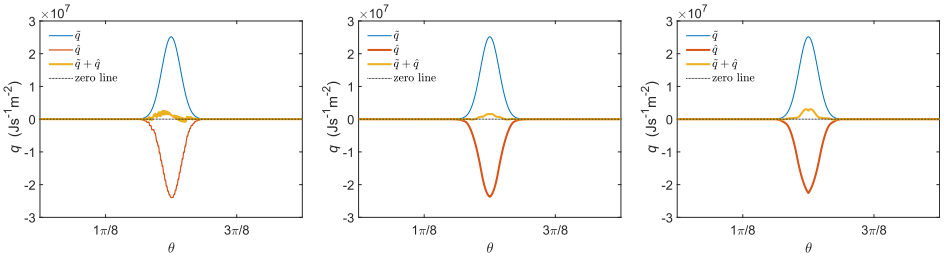

(a) (b) (c)

Figure 3.8: Heat loss rate distribution q along the curve boundary on the top surface for the three simulations with different methods and minimum element sizes at $t = 1.9 \times 10^{-4}$ s. (a) $\hat{q}$ solved by FEM, $l_e = 0.50$ the minimum element size on the boundary is around 10 μm, and $\hat{T}$ is solved using linear tetrahedron elements (C3D4 element in ABAQUS). (b) $\hat{q}$ solved by IGA, $l_e = 2.5$ the minimum element size on the boundary is around 50 μm. (c) $\hat{q}$ solved by IGA, $l_e = 3.4$ the minimum element size on the boundary is around 68 μm.

The total temperature ($\tilde{T} + \hat{T}$) distribution produced by the point source at $t = 1.9 \times 10^{-4}$ s is presented in Fig. 3.7. Figs. 3.7b and c display temperature contours obtained with the IGA method with $l_e = 2.5$ and 3.4, respectively, while Fig. 3.7a shows the corresponding FEM result with $l_e = 0.50$. In all cases, the temperature isolines are orthogonal to the part boundary surfaces, confirming that the adiabatic boundary conditions are satisfied. Besides, we also calculate the net heat loss rate q,

$$q := -k \frac{\partial T}{\partial \mathbf{n}} = -k \left(\frac{\partial \tilde{T}}{\partial \mathbf{n}} + \frac{\partial \hat{T}}{\partial \mathbf{n}} \right),$$

along the curve boundary of the part to compare the differences between IGA and FEM. For the exact adiabatic boundary condition, the net heat loss rate q should be everywhere zero along the boundary, as illustrated in Eq. (3.4). As shown in Fig. 3.8, the blue line in the three subfigures represents the heat loss rate ($\tilde{q}$) due to the point source analytical solution ($\tilde{T}$) and is identical across the three subfigures, while the orange line represents the heat loss rate ($\hat{q}$) due to the complementary field ($\hat{T}$). The yellow line is the net heat loss distribution due to the superposition of two fields ($q = \tilde{q} + \hat{q}$). It can be observed that the $\hat{q}$ field compensates the $\tilde{q}$ to achieve adiabatic boundary conditions, while there is still some residual heat loss through the boundary. The heat loss rate distribution obtained using IGA with a mesh size of $l_e = 2.5$ is lower than that of by using FEM with a mesh size of $l_e = 0.50$. Furthermore, the IGA results with a mesh size of $l_e = 3.4$ demonstrate a performance comparable to that of FEM with a mesh size of $l_e = 0.5$.

The net heat loss rates obtained from the IGA and FE simulations with various mesh sizes are presented in Fig. 3.9. Besides, the corresponding performance metrics derived from the temperature histories are summarized in Table 3.3, where the integration path l is the arc boundary on the top surface in Fig. 3.4. The results indicate that the IGA simulations with minimum element sizes of $l_e = 2.5$ and $l_e = 3.4$ achieve high numerical accuracy, with deviations within 10% relative to the reference case. In terms of heat loss rate, the IGA simulations with these two mesh sizes yield results comparable to those of the FE simulation $l_e = 2.5$ (minimum element size 10 μm).

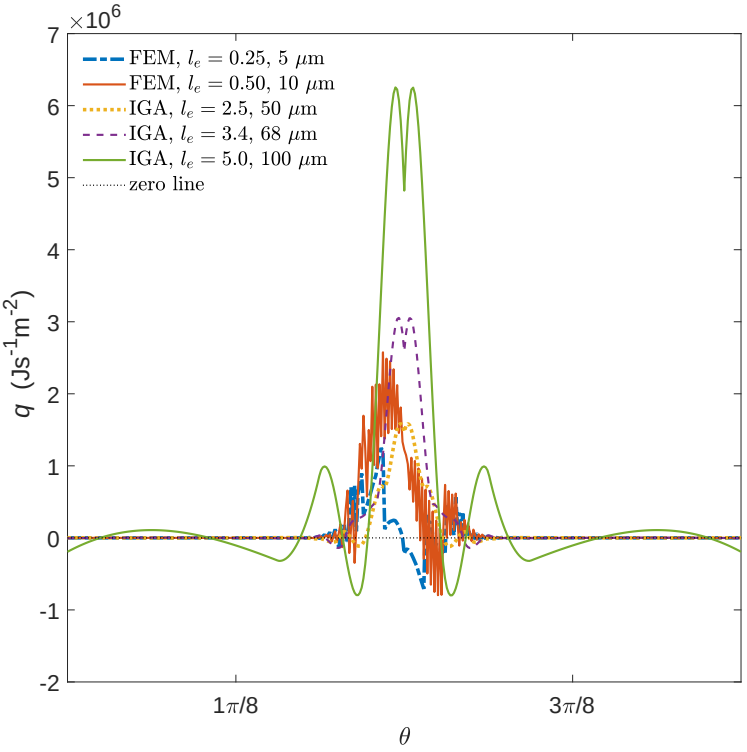

Figure 3.9: Heat loss rate distribution along the curve boundary on the top surface at $t = 1.9 \times 10^{-4}$ s from simulations with different minimum element lengths in FEM and IGA.

However, the IGA results with a mesh size of $l_e = 5.0$ exhibit a higher heat loss rate distribution along the boundary in Fig. 3.9 and Table 3.3. It should be noted that the single point heat source is located along the line that bisects the part into two equal halves, as illustrated in Fig. 3.4. Along this line, according to the knot multiplicity, the solution field exhibits the lowest level of continuity, namely (C^0) continuity. In the subsequent example involving continuous laser scanning, the results demonstrate that the simulation using an IGA element size of $l_e = 5.0$ (minimum element size 100 μm) achieves accuracy comparable to that obtained with an element size of $l_e = 0.5$ (minimum element size 10 μm) in FEM.

3.3.2. CONTINUOUS LASER SCANNING ALONG PART BOUNDARY

Building on the single point-source analysis from the previous section, we next examine a continuous laser scanning case using the same part geometry (Section 3.3.1, Fig. 3.10), extruded without cross-section variation along the build (x_3) direction, as shown in Fig. 3.10.

The laser operates at a power of $P = 82.5$ W, scanning speed of 0.5 m s^{-1}, and spot radius of $r_{\text{laser}} = 20\,\mu$m, with the scan path offset by 100 μm from the part boundary. As

Table 3.3: Metrics computed for thermal history differences at $t = 1.9 \times 10^{-4}$ s, the line integral path l is the arc boundary on the top surface of the part in Fig. 3.4.

	FEM 5 μm	FEM 10 μm	IGA 50 μm	IGA 68 μm	IGA 100 μm
l_e	0.25	0.50	2.5	3.4	5.0
$\lvert\Delta T_{\max}\rvert$	/	0.021	0.15	0.38	1.3
e_r	/	0.10%	0.73%	1.8%	6.3%
$\int_l \lvert q\rvert \mathrm{d}s$	6.13×10^1	2.62×10^2	1.67×10^2	3.23×10^2	9.74×10^2
$\int_l \lvert q\rvert \mathrm{d}s \Big/ \int_l \lvert \tilde{q}\rvert \mathrm{d}s$	1.74%	7.44%	4.75%	9.17%	27.64%

discussed earlier, the continuous scan is discretized into a sequence of point sources using a temporal step size of $\Delta t = 1 \times 10^{-5}$ s. The same material properties representative of Ti-6Al-4V listed in Table 3.2 are used, with a metal powder absorptivity of $A = 0.77$. For FEM, a minimum element size of 10 μm ($l_e = 0.5$ finest test mesh for FEM) is adopted, resulting in 45,773 DOFs (Fig. 3.11a), whereas for IGA, a minimum element size of 100 μm ($l_e = 5.0$) with 6,137 DOFs is used (Fig. 3.11b).

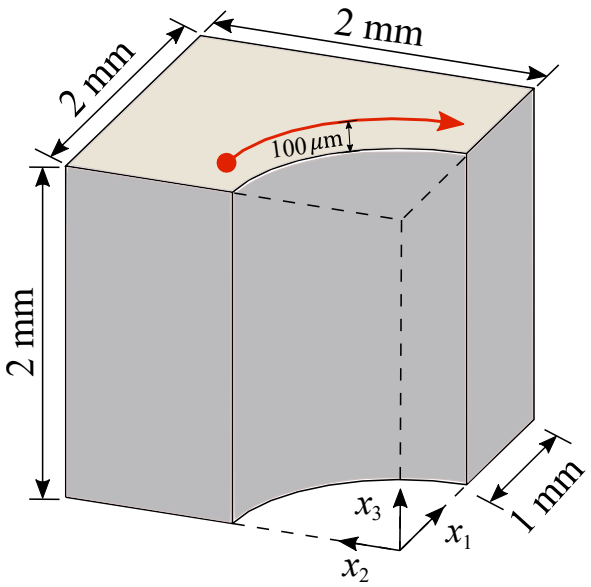

Figure 3.10: Geometry for the continuous contour laser scan along the part boundary. The scan path is offset by 100 μm from the boundary.

The laser starts scanning at $t = 0$, and the temperature fields at $t = 2.0 \times 10^{-3}$ s and $t = 3.0 \times 10^{-3}$ s obtained from FEM and IGA are shown in Fig. 3.12. The temperature contour lines remain orthogonal to the part boundaries, confirming that the adiabatic boundary conditions are satisfied. In addition, the heat loss rates along the curve boundary on the top surface obtained from the two simulation methods are compared in Fig. 3.13 for the time step $t = 2.0 \times 10^{-3}$ s and Fig. 3.14 for the time step $t = 3.0 \times 10^{-3}$ s. It can be observed

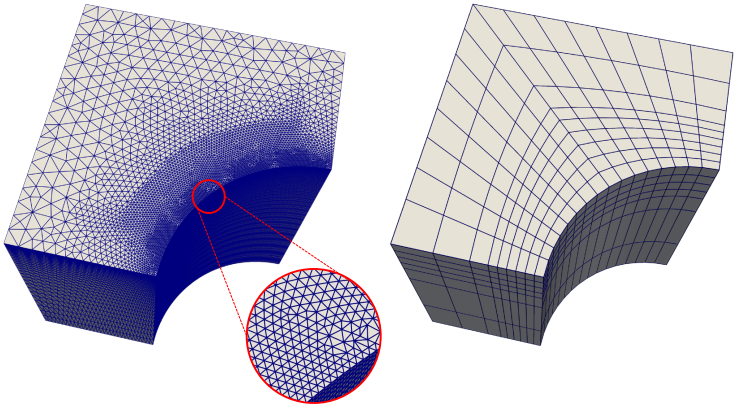

(a) FE mesh ($l_e = 0.5$, minimum element size 10 µm, DOFs 45773) (b) IGA mesh ($l_e = 5.0$, minimum element size 100 µm, DOFs 5415)

Figure 3.11: Finite Element (FE) and isogeometric analysis (IGA) meshes for the continuous laser scan simulation. The left panel shows the FE mesh, and the right panel shows the IGA mesh.

that at both time steps, the peak net heat loss rate on the boundary predicted by IGA with a minimum element size of $l_e = 5.0$ is lower than that obtained with the FE simulation with $l_e = 0.5$. The corresponding integrated net heat loss rates along the curve boundary are summarized in Table 3.4, where the line integral path l is the arc boundary on the top surface of the part in Fig. 3.10.

For the IGA simulations, the integrated net heat loss rates correspond to 14.94% and 8.03% of the total outgoing heat loss predicted by the analytical solutions at the two respective time instances, while the corresponding values for the FE simulations are 17.76% and 17.30%. At $t = 2.0 \times 10^{-3}$ s, the numerical accuracy of IGA is slightly higher than that of FEM. In contrast, at $t = 3.0 \times 10^{-3}$ s, the IGA results exhibit significantly greater accuracy, as the integrated net heat loss rate is nearly half of that obtained from FEM. This improvement occurs because, at $t = 2.0 \times 10^{-3}$ s, the laser source is positioned closer to the C^0 continuity line, whereas at $t = 3.0 \times 10^{-3}$ s, it is located farther away, thereby reducing the effect of the lower level of continuity and enhancing the solution accuracy.

Table 3.4: Metrics computed for thermal history differences at $t = 2.0 \times 10^{-3}$ s and $t = 3.0 \times 10^{-3}$ s, the line integral path l is the arc boundary on the top surface of the part in Fig. 3.10.

	$t = 2.0 \times 10^{-3}$ s		$t = 3.0 \times 10^{-3}$ s	
	FEM 10 μm	IGA 100 μm	FEM 10 μm	IGA 100 μm
l_e	0.50	5.0	0.50	5.0
$\int_l \lvert q \rvert \mathrm{d}s$	2.86×10^4	2.41×10^4	2.89×10^4	1.34×10^4
$\int_l \lvert q \rvert \mathrm{d}s \Big/ \int_l \lvert \tilde{q} \rvert \mathrm{d}s$	17.76%	14.94%	17.30%	8.03%

These results indicate that the overall numerical accuracy of IGA with a minimum el-

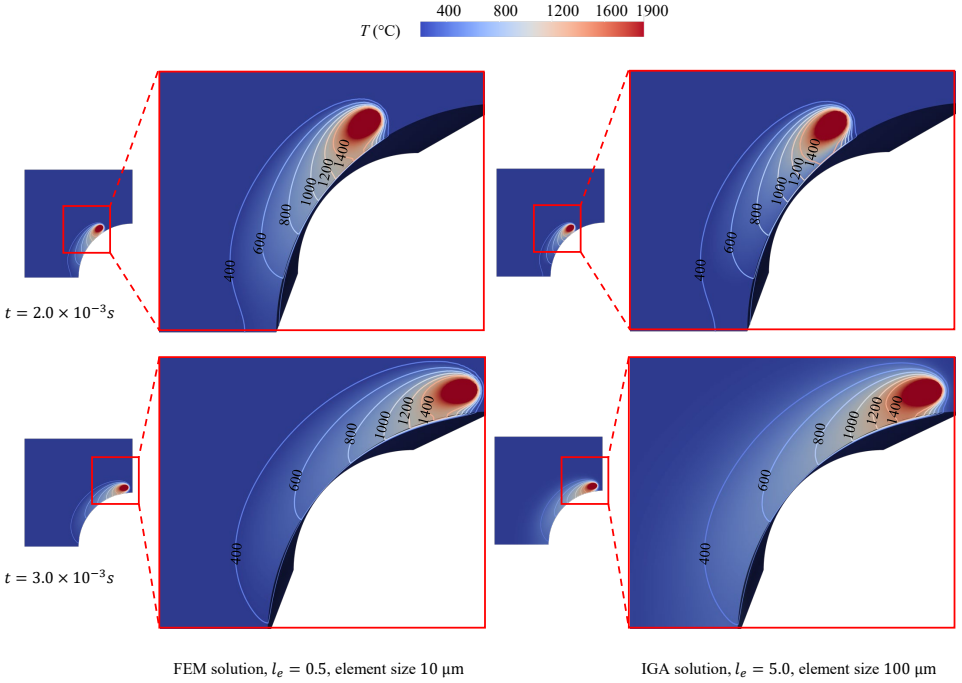

Figure 3.12: Temperature distributions at $t = 2.0 \times 10^{-3}$ s and $t = 3.0 \times 10^{-3}$ s during the laser scan along the part boundary. FEM uses a minimum element size of 10 μm ($l_e = 0.5$), while IGA uses 100 μm ($l_e = 5.0$). Despite the coarser mesh, the IGA contours closely match the FEM results, demonstrating comparable accuracy with significantly fewer DOFs.

ement size of 100 μm and FEM with a minimum element size of 10 μm methods is comparable. Furthermore, the close agreement observed between the FEM and IGA temperature contour patterns demonstrates that the IGA approach, even when using a 10 times coarser mesh, can accurately reproduce the FEM results. Therefore, in the subsequent section, the same minimum element size is adopted for the IGA simulation of a more complex geometry to further evaluate its performance and computational efficiency.

3.3.3. CONTINUOUS LASER SCANNING ALONG A COMPLEX PART BOUNDARY

This section extends the simulation to a more complex geometry—a butterfly-shaped part illustrated in Fig. 3.15a. The geometry mapping is generated using the parameterization method of [43]. Unlike the butterfly part in our previous work [42], which maintained identical cross-sections along the build (x_3) direction, the present geometry features cross-sections that vary nonlinearly along the height direction. The full geometric model is provided as supplementary material. A laser scan is performed with a 100 μm offset from the boundary. The corresponding IGA geometry mesh is used along the scanning path shown in Fig. 3.15b. A minimum element size of approximately 100 μm along the scanning path is adopted for the IGA discretization. All process parameters—including laser power, scanning speed, spot radius, Ti–6Al–4V thermal properties,

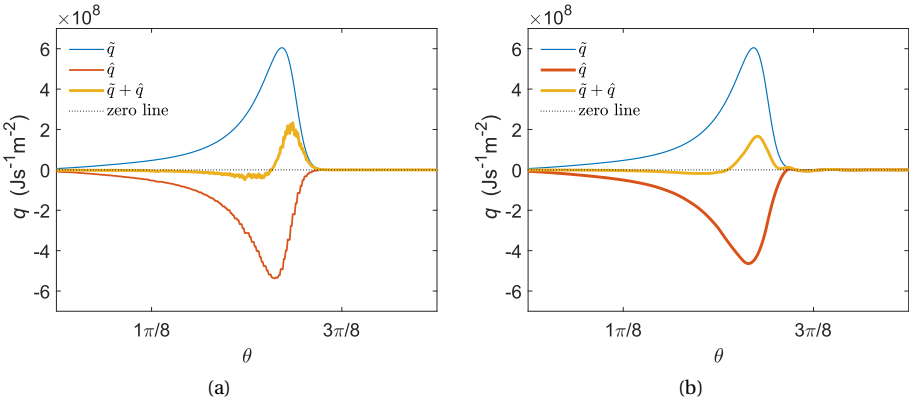

Figure 3.13: Heat loss rate distribution q along the curve boundary on the top surface for the two simulations with different methods and minimum element sizes at $t = 2.0 \times 10^{-3}$ s. (a) $\hat{q}$ solved by FEM with $l_e = 0.5$, the minimum element size on boundary is around 10 μm, and $\hat{T}$ is solved using linear tetrahedron elements (C3D4 element in ABAQUS). (b) $\hat{q}$ solved by IGA with $l_e = 5.0$, the minimum element size on boundary is around 100 μm.

and metal powder absorptivity—are identical to those used in the previous section. This part has a length and width of approximately 10 mm and a height of 2 mm. The IGA simulation is conducted using the mesh with a minimum element size of 100 μm ($l_e = 5.0$), resulting in a total of 27 456 degrees of freedom. However, to simulate the same scanning process using FEM, it leads to excessive DOFs, which is far more computationally prohibitive.

Temperature distributions at $t = 5.0 \times 10^{-3}$ s and $t = 1.2 \times 10^{-2}$ s are presented in Fig. 3.16. At both time steps, the temperature iso-surface remain orthogonal to the part boundary surface, confirming that the adiabatic boundary conditions are properly enforced. The corresponding temperature contours of the top surface and of a cross section located 50 μm below the top surface are shown in Fig. 3.17. On both surfaces, the temperature contour lines exhibit an orientation approximately orthogonal to the part boundaries. It is also evident that the cross-section located 50 μm below the top surface contains a smaller region of high temperature.

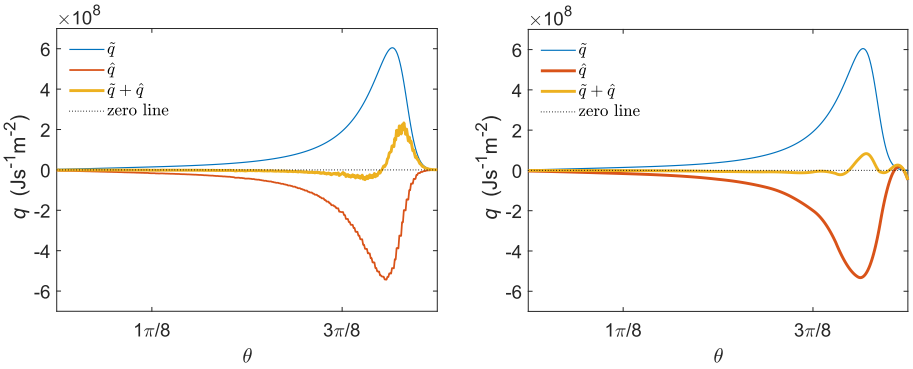

Figure 3.14: Heat loss rate distribution q along the curve boundary on the top surface for the two simulations with different methods and minimum element sizes at $t = 3.0 \times 10^{-3}$ s. (a) $\hat{q}$ solved by FEM $l_e = 0.5$, the minimum element size on the boundary is around 10 μm, and $\hat{T}$ is solved using linear tetrahedron elements (C3D4 element in ABAQUS). (b) $\hat{q}$ solved by IGA with $l_e = 5.0$, the minimum element size on the boundary is around 100 μm.

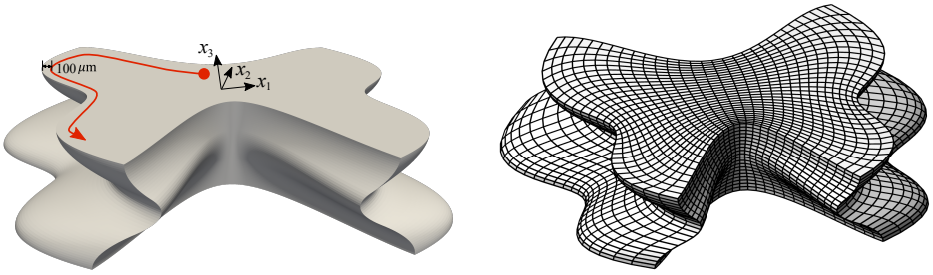

Figure 3.15: Butterfly-shaped part constructed using NURBS and control points. The cross-sections vary nonlinearly along the build (x_3) direction. The complete geometric model is provided in the supplementary material. The laser contour scan is offset by 100 μm from the boundary, and an IGA minimum element size of 100 μm is used for the simulation.

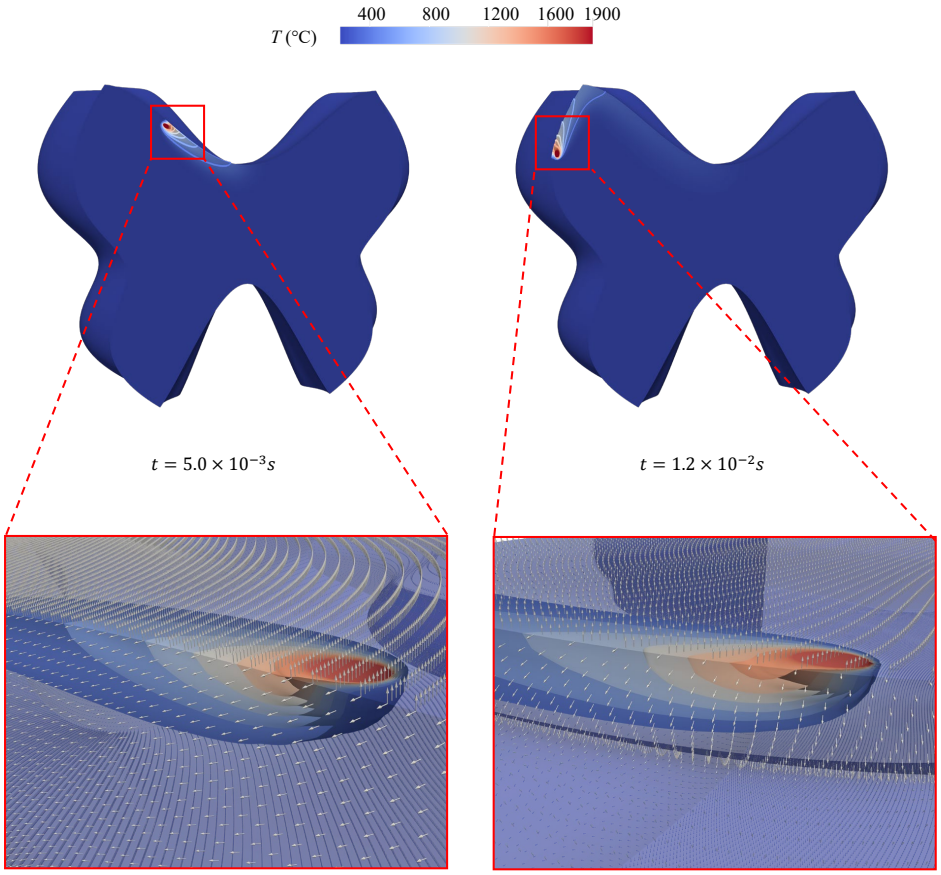

Figure 3.16: IGA temperature field snapshots for the butterfly-shaped part at $t = 5.0 \times 10^{-3}$ s and $t = 1.2 \times 10^{-2}$ s during the laser contour scan. The temperature contour surfaces remain orthogonal to the boundary surfaces, confirming proper enforcement of adiabatic boundary conditions.

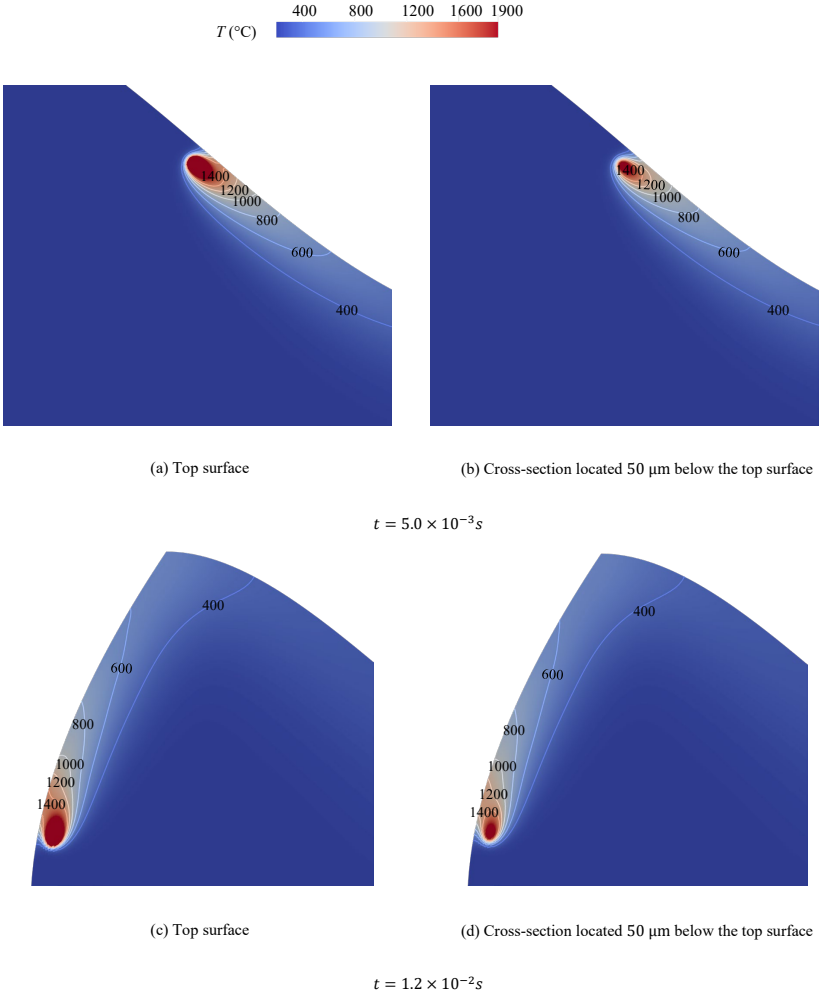

Figure 3.17: IGA temperature field snapshots of the top surface and a cross-section located 50 μm below the top surface for the butterfly-shaped part at $t = 5.0 \times 10^{-3}$ s and $t = 1.2 \times 10^{-2}$ s during the laser contour scan.

3.4. CONCLUSIONS AND OUTLOOK

In this work, we have proposed and validated a semi-analytical thermal simulation framework for Laser Powder Bed Fusion that combines an analytical point-source solution with a complementary numerical field solved using isogeometric analysis. By superposing the closed-form temperature contributions of discrete laser exposures with an IGA-computed boundary correction field, the method enforces adiabatic and Dirichlet boundary conditions without requiring locally refined or scan-wise remeshed finite element meshes.

The numerical examples confirm three main findings:

- **Accuracy and efficiency:** For a single point source near a curved boundary, IGA achieved comparable accuracy to a highly refined FEM reference while using orders of magnitude fewer degrees of freedom. Even with element sizes of 5 times of laser spot radius, the IGA error remained well below typical engineering tolerances, whereas FEM required element sizes of half of laser spot radius or smaller to achieve similar accuracy.

- **Robustness for continuous scanning:** In simulations of contour laser scans along both simple and butterfly-shaped boundaries, IGA reproduced FEM temperature distributions with far coarser meshes. Temperature iso-lines remained orthogonal to the part boundaries throughout the scan, demonstrating that the complementary field enforces adiabatic boundary conditions reliably—even for non-extruded geometries with nonlinear cross-sectional variation.

- **Geometric flexibility:** The spline-based representation allowed the complementary field to conform exactly to complex boundaries without resorting to image-source reflections or boundary-fitted remeshing strategies that become impractical for sharp corners and disconnected cross-sections.

These results indicate that combining semi-analytical source superposition with IGA provides a robust and computationally efficient alternative that can be applied to any realistic geometry for the first time. The proposed approach eliminates the need for dynamic mesh refinement following the moving heat source and drastically reduces sensitivity to geometric complexity, offering a scalable framework for part-scale thermal modeling.

Future work will extend the method in several directions. First, coupling the thermal field with phase change and fluid flow models could provide a more complete description of melt-pool dynamics. Second, adaptive local refinement of the IGA basis or hierarchical spline techniques could further reduce computational cost for extremely large parts or multi-laser systems. Third, integration with process parameter optimization and feedback control would enable real-time thermal management in industrial LPBF machines. Finally, experimental validation against in-situ temperature measurements will further establish the predictive capability of the proposed framework for a wide range of materials and geometries.

BIBLIOGRAPHY

[1] M. Bayat, O. Zinovieva, F. Ferrari, C. Ayas, M. Langelaar, J. Spangenberg, R. Salajeghe, K. Poulios, S. Mohanty, O. Sigmund, and J. Hattel, "Holistic computational design within additive manufacturing through topology optimization combined with multi-physics multi-scale materials and process modelling", Progress in Materials Science **138**, 101129 (2023).

[2] C. Liu, M. Zhang, G. Bi, J. Chen, Y. Bai, D. Wang, and M. Deng, "Research on comprehensive heat dissipation characteristics of alsi7mg tpms heat sinks manufactured by laser powder bed fusion", Applied Thermal Engineering **261**, 124941 (2025).

[3] C. Biffi, C. Soyarslan, J. Fiocchi, C. Bregoli, A. du Plessis, A. Tuissi, and M. Mehrpouya, "Additive manufacturing of niti architected metamaterials", Additive Manufacturing Letters **10**, 100216 (2024).

[4] A. V. Gusarov, I. Yadroitsev, P. Bertrand, and I. Smurov, "Model of radiation and heat transfer in laser-powder interaction zone at selective laser melting", Journal of Heat Transfer **131**, 072101 (2009).

[5] M. Jimenez Abarca, R. Darabi, J. C. de Sa, M. Parente, and A. Reis, "Multi-scale modeling for prediction of residual stress and distortion in ti–6al–4v semi-circular thin-walled parts additively manufactured by laser powder bed fusion (lpbf)", Thin-Walled Structures **182**, 110151 (2023).

[6] Y. Yang, X. Zhou, Q. Li, and C. Ayas, "A computationally efficient thermo-mechanical model for wire arc additive manufacturing", Additive Manufacturing **46**, 102090 (2021).

[7] G. Vastola, Q. Pei, and Y.-W. Zhang, "Predictive model for porosity in powder-bed fusion additive manufacturing at high beam energy regime", Additive Manufacturing **22**, 817–822 (2018).

[8] J. Trejos-Taborda, L. Reyes-Osorio, C. Garza, P. del Carmen Zambrano-Robledo, and O. Lopez-Botello, "Finite element modeling of melt pool dynamics in laser powder bed fusion of 316l stainless steel", The International Journal of Advanced Manufacturing Technology **120**, 3947–3961 (2022).

[9] D. Sarkar, A. Kapil, and A. Sharma, "Advances in computational modeling for laser powder bed fusion additive manufacturing: a comprehensive review of finite element techniques and strategies", Additive Manufacturing **85**, 104157 (2024).

[10] A. Olleak and Z. Xi, "Part-scale finite element modeling of the selective laser melting process with layer-wise adaptive remeshing for thermal history and porosity prediction", Journal of Manufacturing Science and Engineering **142**, 121006 (2020).

[11] I. Roberts, C. Wang, R. Esterlein, M. Stanford, and D. Mynors, "A three-dimensional finite element analysis of the temperature field during laser melting of metal powders in additive layer manufacturing", International Journal of Machine Tools and Manufacture **49**, 916–923 (2009).

[12] A. Foroozmehr, M. Badrossamay, E. Foroozmehr, and S. Golabi, "Finite element simulation of selective laser melting process considering optical penetration depth of laser in powder bed", Materials & Design **89**, 255–263 (2016).

[13]M. Vanini, S. Searle, K. Vanmeensel, and B. Vrancken, "Avoiding heat source calibration for finite element modeling of the laser powder bed fusion process", Additive Manufacturing **92**, 104369 (2024).

[14]Z.-D. Zhang, S. Imani Shahabad, O. Ibhadode, C. F. Dibia, A. Bonakdar, and E. Toyserkani, "3-dimensional heat transfer modeling for laser powder bed fusion additive manufacturing using parallel computing and adaptive mesh", Optics & Laser Technology **158**, 108839 (2023).

[15]M. Gouge, E. Denlinger, J. Irwin, C. Li, and P. Michaleris, "Experimental validation of thermo-mechanical part-scale modeling for laser powder bed fusion processes", Additive Manufacturing **29**, 100771 (2019).

[16]S. Kollmannsberger, A. Özcan, M. Carraturo, N. Zander, and E. Rank, "A hierarchical computational model for moving thermal loads and phase changes with applications to selective laser melting", Computers & Mathematics with Applications **75**, 1483–1497 (2018).

[17]J. P. Leonor and G. J. Wagner, "Go-melt: gpu-optimized multilevel execution of lpbf thermal simulations", Computer Methods in Applied Mechanics and Engineering **426**, 116977 (2024).

[18]C. A. Moreira, M. A. Caicedo, M. Cervera, M. Chiumenti, and J. Baiges, "A multi-criteria h-adaptive finite-element framework for industrial part-scale thermal analysis in additive manufacturing processes", Engineering with Computers **38**, 4791–4813 (2022).

[19]C. Li, E. R. Denlinger, M. F. Gouge, J. E. Irwin, and P. Michaleris, "Numerical verification of an octree mesh coarsening strategy for simulating additive manufacturing processes", Additive Manufacturing **30**, 100903 (2019).

[20]D. Rauner, K.-U. Beuerlein, R. Zhang, and M. F. Zaeh, "Multi-scale simulation approach for the prediction of overheating under consideration of process parameters in powder bed fusion of metals using a laser beam", Journal of Materials Processing Technology **338**, 118769 (2025).

[21]A. Olleak and Z. Xi, "Scan-wise adaptive remeshing for efficient lpbf process simulation: the thermal problem", Manufacturing Letters **23**, 75–78 (2020).

[22]A. Olleak, F. Dugast, P. Bharadwaj, S. Strayer, S. Hinnebusch, S. Narra, and A. C. To, "Enabling part-scale scanwise process simulation for predicting melt pool variation in lpbf by combining gpu-based matrix-free fem and adaptive remeshing", Additive Manufacturing Letters **3**, 100051 (2022).

[23]J. A. Cottrell, T. J. Hughes, and Y. Bazilevs, *Isogeometric analysis: toward integration of cad and fea* (John Wiley & Sons, 2009).

[24]R. Duvigneau, "An introduction to isogeometric analysis with application to thermal conduction", PhD thesis (INRIA, 2009).

[25]Q. Zang, J. Liu, W. Ye, and G. Lin, "Isogeometric boundary element method for steady-state heat transfer with concentrated/surface heat sources", Engineering Analysis with Boundary Elements **122**, 202–213 (2021).

[26]V. Gupta, S. K. Verma, S. Anand, A. Jameel, and Y. Anand, "Transient isogeometric heat conduction analysis of stationary fluid in a container", Proceedings of the Institution of Mechanical Engineers, Part E: Journal of Process Mechanical Engineering **239**, 531–541 (2025).

[27]Y. Ji, M.-Y. Wang, Y. Wang, and C.-G. Zhu, "Curvature-based r-adaptive planar nurbs parameterization method for isogeometric analysis using bi-level approach", Computer-Aided Design **150**, 103305 (2022).

[28]M. J. Borden, M. A. Scott, J. A. Evans, and T. J. Hughes, "Isogeometric finite element data structures based on bézier extraction of nurbs", International Journal for Numerical Methods in Engineering **87**, 15–47 (2011).

[29]Y. Bazilevs, V. M. Calo, J. A. Cottrell, J. A. Evans, T. J. R. Hughes, S. Lipton, M. A. Scott, and T. W. Sederberg, "Isogeometric analysis using t-splines", Computer methods in applied mechanics and engineering **199**, 229–263 (2010).

[30]M. R. Dörfel, B. Jüttler, and B. Simeon, "Adaptive isogeometric analysis by local h-refinement with t-splines", Computer methods in applied mechanics and engineering **199**, 264–275 (2010).

[31]M. A. Scott, M. J. Borden, C. V. Verhoosel, T. W. Sederberg, and T. J. Hughes, "Isogeometric finite element data structures based on bézier extraction of t-splines", International Journal for Numerical Methods in Engineering **88**, 126–156 (2011).

[32]E. Evans, M. Scott, X. Li, and D. Thomas, "Hierarchical t-splines: analysis-suitability, bézier extraction, and application as an adaptive basis for isogeometric analysis", Computer Methods in Applied Mechanics and Engineering **284**, 1–20 (2015).

[33]T. J. Hughes, J. A. Cottrell, and Y. Bazilevs, "Isogeometric analysis: cad, finite elements, nurbs, exact geometry and mesh refinement", Computer methods in applied mechanics and engineering **194**, 4135–4195 (2005).

[34]T. Yu, B. Chen, S. Natarajan, and T. Q. Bui, "A locally refined adaptive isogeometric analysis for steady-state heat conduction problems", Engineering Analysis with Boundary Elements **117**, 119–131 (2020).

[35]M. Carraturo, C. Giannelli, A. Reali, and R. Vázquez, "Suitably graded thb-spline refinement and coarsening: towards an adaptive isogeometric analysis of additive manufacturing processes", Computer Methods in Applied Mechanics and Engineering **348**, 660–679 (2019).

[36]M. Carraturo, M. Torre, C. Giannelli, and A. Reali, "An isogeometric approach to coupled thermomechanics in 3d via hierarchical adaptivity", Computers & Mathematics with Applications **162**, 133–144 (2024).

[37]Y. Yang, M. Knol, F. van Keulen, and C. Ayas, "A semi-analytical thermal modelling approach for selective laser melting", Additive Manufacturing **21**, 284–297 (2018).

[38]J. Ning, E. Mirkoohi, Y. Dong, D. E. Sievers, H. Garmestani, and S. Y. Liang, "Analytical modeling of 3d temperature distribution in selective laser melting of ti-6al-4v considering part boundary conditions", Journal of Manufacturing Processes **44**, 319–326 (2019).

[39]Y. Yang, F. van Keulen, and C. Ayas, "A computationally efficient thermal model for selective laser melting", Additive Manufacturing **31**, 100955 (2020).

[40]J. C. Steuben, A. J. Birnbaum, J. G. Michopoulos, and A. P. Iliopoulos, "Enriched analytical solutions for additive manufacturing modeling and simulation", Additive Manufacturing **25**, 437–447 (2019).

[41]A. J. Wolfer, J. Aires, K. Wheeler, J.-P. Delplanque, A. Rubenchik, A. Anderson, and S. Khairallah, "Fast solution strategy for transient heat conduction for arbitrary scan paths in additive manufacturing", Additive Manufacturing **30**, 100898 (2019).

[42]Y. Yang, Y. Ji, M. Möller, and C. Ayas, "Computational efficient process simulation of geometrically complex parts in metal additive manufacturing", International Journal of Heat and Mass Transfer **248**, 127059 (2025).

[43]Y. Ji, Y.-Y. Yu, M.-Y. Wang, and C.-G. Zhu, "Constructing high-quality planar nurbs parameterization for isogeometric analysis by adjustment control points and weights", Journal of Computational and Applied Mathematics **396**, 113615 (2021).

4

4

Prevention of local overheating in the LPBF of Magnesium

Additive manufacturing is gaining traction in the aerospace industry thanks to the possibility of manufacturing highly optimized, complex, and lightweight structures. Laser Powder Bed Fusion (LPBF) of Magnesium offers additional benefits due to the combination of a very low density and high specific strength. However, magnesium alloys are highly susceptible to overheating during LPBF, causing process instabilities, defects, and inhomogeneous and unpredictable material behavior. We investigate LPBF of regular triangular prism Magnesium parts and identify overheating through variations of the melt pool dimensions. Overheating is reduced by delaying the consecutive scan vectors and scaling the power, evidenced by the homogenization of melt pools. We also investigate the underlying mechanisms leading to overheating through part-scale simulations that are purely analytical, semi-analytical, and numerical commercial finite element analysis as direct numerical simulation. Model predictions capture the overheating trends and their prevention by favorable process conditions, while semi-analytical simulations prove their predictive capability with remarkable computational efficiency. Simulations revealed that towards the tip of a triangular layer, poor conductivity across part powder boundaries and short scanning vectors with short cycle times predispose to overheating. However, below a threshold scan vector length, peak temperatures decrease abruptly, which should be accounted for in preventive process conditions to achieve a stable LPBF process and higher-quality components for use in aerospace.

Parts of this chapter have been done as a manuscript and will be submitted to an academic journal.

4.1. INTRODUCTION

The Laser Powder Bed Fusion (LPBF) process is a metal additive manufacturing (AM) method that can realize highly detailed complex parts with excellent mechanical properties. LPBF involves spreading a thin layer of powder, which is then selectively melted and fused using a high-power laser beam to create a solid object layer by layer. Due to layer-wise manufacturing, geometrically complex, optimal, lightweight, and multi-functional parts can be built, reducing the need for assembly. These aspects drive the broader application of metal AM in the aerospace industry, for example, for high-temperature applications with Nickel super alloys, optimized lightweight structural applications with titanium alloys, and thermal management systems with aluminum alloys. Magnesium alloys are also used in the aerospace industry due to Magnesium's low density combined with high specific strength. This combination makes it a good material to be applied in aerospace components such as helicopter transmission castings and satellite components [1]. However, the production of Magnesium parts by LPBF is still in the early stages of research, especially for aerospace applications. Research on magnesium Laser Powder Bed Fusion (LPBF) began with Ng et al.'s study in 2009, which explored the production of single tracks with varying process parameters [2]. Subsequent studies include the production of structures with a relative density of 82% using a Mg-9%Al powder mixture by Zhang et al. in 2011 [3], and Jauer et al.'s investigation of LPBF of magnesium for medical applications using the AZ91 alloy in 2012 [4]. Furthermore, Gieseke et al. developed a customized LPBF system for processing at elevated pressures to increase the boiling temperature, although this approach did not yield improved material quality [5]. Due to the low boiling point and high reactivity with oxygen and water vapor, the production of high quality LPBF magnesium components remains an open point for research.

It is well known that the part's geometry can significantly influence the local microstructure and defect prevalence in LPBF. Complex thermal histories inherent to the LPBF process can result in significant variations in porosity levels, microstructure, and crack formation, and ultimately the local mechanical properties [6–8]. Consequently, the effect of geometric features on thermal history can lead to print failures or part rejections, resulting in excessive and expensive manufacturing trials. Magnesium alloys are especially susceptible to overheating due to their low boiling point. In the LPBF processing of Magnesium alloys, the local heat accumulation results in significant porosity formation due to evaporation [9], detrimental to the part's quality. Therefore, for the production of components with homogeneous and predictable material properties, it is crucial to understand, predict, and prevent these effects associated with overheating. Depending on the part geometry, heat accumulation can occur over multiple layers or locally due to notable reheating of previous or subsequent scan vectors.

There are multiple approaches to mitigate heat accumulation in the LPBF process. Laser power scaling was employed in numerous studies to reduce overheating and improve process stability. Yeung et al. [10, 11] have developed methods to scale the laser power based on a geometric conductance factor and a residual heat factor to obtain a thermally more stable process. Druzgalski et al. [12] employed feature extraction to identify local regions where scan parameter adjustments are required and optimized the laser power in these regions with feed-forward control. Liu et al. [13] observed a significant increase in peak temperature and melt pool size when the laser track length was smaller

than 1 mm. This results from the limited time available for the heat generated by the previous laser track to dissipate before the subsequent short laser track is deposited. Thus, for short tracks, they proposed a method to utilize virtual scanning—namely, scanning with zero laser power—as an interval to facilitate cooling. After optimization of the scanning strategy, simulations reveal uniform peak temperatures and melt pool sizes, while experimental results demonstrate reduced distortion, improved surface quality, and decreased porosity in the fabricated parts. Shahabad et al. [14] studied the melt-pool width and depth at the center and end of scanning tracks with different lengths of tracks. Results show that melt-pool width increases more due to heat accumulation from previous laser tracks when the track length is shorter than 0.5 mm. Furthermore, the melt pool geometries at the track end exhibit larger dimensions than those at the track center. In addition to power scaling and extending the cooling time between adjacent tracks, increasing the inter-layer time is also commonly employed at the part scale to mitigate heat accumulation across multiple layers [6].

Heat accumulation over multiple layers is well understood and thus can be predicted and prevented using simplified numerical simulations, e.g. [6, 7, 15]. Usually, these simulations are based on the assumption of the whole layer being simultaneously exposed to a heat source [16, 17], and focus on heat accumulation from the inter-layer deposition process. However, local heat accumulation also happens within a single-layer deposition due to subsequent scan vectors, and a model resolution of individual scan vectors is required. Thus, it is much more difficult to predict the heat accumulation effect considering intra-layer effects. In this chapter, we employ analytical and semi-analytical methods that can capture both heat accumulation effects for the entire additive manufacturing process. However, we limit the scope of our study to the intra-layer overheating to better understand the mechanisms of heat accumulation. Hence, optimal LPBF process parameters for Mg alloys, e.g., laser scanning velocity and power, depending on local layer geometry and scan vector orientation, are still determined through trial and error.

Computationally tractable modeling of the LPBF process that accounts for individual scan vectors can be a valuable tool to reduce the burden of time-consuming and expensive experiments. In general, the simulation of the LPBF process can be classified into three groups based on the characteristic time and length scales. Micro-scale models resolve individual metal powder particles, powder melting behavior, and fluid flow under the interaction with the laser beam in a small simulation domain [18, 19]. Computationally tractable modeling of the LPBF process that accounts for individual scan vectors can be a valuable tool to reduce the burden of time-consuming and expensive experiments. In general, the simulation of the LPBF process can be classified into three groups based on the characteristic time and length scales. Micro-scale models resolve individual metal powder particles, powder melting behavior, and fluid flow under the interaction with the laser beam in a small simulation domain [18, 19]. Meso-scale models are mainly used to simulate the melt pool shape and dynamics based on computational fluid dynamics [20, 21], where finite volume methods are usually adopted. Moreover, phase Field, cellular automaton, and Kinetic Monte Carlo models are common methods used to simulate the microstructure evolution during the LPBF process [22–24]. In macro-scale models, also called part-scale, the Finite Elements method (FEM) is widely applied to predict the part-

scale thermal history, distortion, and residual stresses, usually simulating simultaneous deposition of an entire layer [25–27].

Chia et al. [28] employed a mesoscale model to simulate the melt pool shape, requiring approximately 12 hours for single-track cases and 32 hours for double-track cases. Therefore, part-scale thermal analysis is imperative to predict the melt pool shape in a computationally tractable manner for realistic metal parts. Extensive research shows that part-scale thermal simulations can achieve the desired level of accuracy despite neglecting several physical phenomena like fluid flow [29–32]. Roberts et al. [30] adopted a FEM-based part-scale model to predict the temperature field for the LPBF process and reported strong similarities with experimental measurements. Olleak et al. [31] predicted melt pool geometry based on FEM simulations. Their work mainly focuses on the model development for part-scale LPBF simulations. However, the predicted melt pool width is overestimated, and the melt pool depth is underestimated in contrast to the experimental findings. They conclude that the deviations can be because the simulated melt pool is from multiple-track scanning cases, while the experimental melt pool geometry is from one-track experiments. Moreover, even though the proposed remeshing technique is proven to be computationally more efficient than the existing element death and birth approaches, it still takes more than 10 hours to scan a 5 mm^2 area with four processor cores in parallel computing. Zhang et al. [32] also compared the melt pool depth from FEM and experiments, and varied anisotropically thermal conductivity, the thermal conductivity of metal powder, and varied absorptivity are considered in their simulation. The simulation results show only a maximum 10% discrepancy with the experimental results. However, they only simulated a single track scanning process; their method is difficult to apply to predict the temperature history for the entire LPBF process.

The multi-scale nature of the LPBF process is an essential aspect in part-scale thermal simulations and is responsible for the trade-off between computational burden and accuracy. The laser spot radius is typically around 50 μm, while print parts have a size of several centimeters. To capture the resulting steep temperature gradients numerically, parts must be discretized with an element size scaling with the laser spot radius [30]. Thus, there will be an excessive number of elements in a typical FEM discretization. Besides, to capture the transient temperature behavior for a typical laser scanning speed, the time step should be around 5×10^{-5} s [29], while the total print time can last for several hours or even days, leading to excessive time steps. ABAQUS is a commercially available software highly optimized for FEM-based simulations at part-scale. In contrast to most commercially available part-scale simulation software, the ABAQUS AM suite is still able to resolve the individual scan vectors in the LPBF process. Built-in AM subroutines can be used to define a moving heat source as well as element creation when depositing a new LPBF layer. Adaptive mesh refinement is proposed to reduce the number of elements. A fine mesh following high-temperature zones tracing the laser beam, and a coarser mesh away from the high-temperature zones [33–35]. In this way, the number of degrees of freedom in FEM is reduced. However, the mesh must be continuously adapted according to the laser positions.

Methods based on the analytical solution of the heat equation are proposed to remedy computationally costly FE calculations and adaptive mesh refinement [29, 36, 37].

The analytical solutions of the heat equation in a semi-infinite space are used to represent the instantaneous laser exposure, either in the form of a Riemann sum of individual closed-form expressions of point heat sources generated incrementally [29, 38] or as a line source through integrating the temperature contribution of infinitesimal point sources along a line [36, 37]. These closed-form solutions effectively capture the steep temperature gradients analytically near the laser spot, eliminating the need for a refined mesh to resolve these gradients numerically. Therefore, the computational gains are remarkable. However, the analytical solutions constructed for (semi)-infinite domains do not meet the boundary conditions of finite parts. Consequently, the accuracy of the analytical temperature fields is severely limited near part boundaries.

The semi-analytical method was proposed to resolve this issue. The semi-analytical method decomposes the temperature field into the analytical field to capture the laser motion and associated heat sources and a complementary numerical field to enforce the boundary conditions [36]. Since the temperature gradients due to the laser source are analytically accounted for, the numerical discretization for the complementary field is decoupled from the characteristic length scale of the problem. It can thus be solved with a coarse FE mesh in a computationally efficient manner. This method was applied in temperature history prediction [36, 39, 40], melt pool geometry prediction [29], and thermal stress and strain calculation [41].

This study focuses on part-scale thermal modeling to better understand the local heat accumulation mechanisms in LPBF and support the development of preventive measures. Various simulation approaches that can resolve individual laser tracks, namely, analytical methods, semi-analytical methods, and the commercial ABAQUS FEM software with built-in AM subroutines are compared in terms of computational cost and predictive power. Model predictions are validated through experiments using a Magnesium alloy. Moreover, two preventive measures to avoid local heat accumulation are employed experimentally. Furthermore, the analytical method isolates four key mechanisms contributing to local overheating observed during the LPBF process, which is instrumental in improving overheating prevention.

The remainder of this chapter is organized as follows. Section 4.2 describes the experimental setup for the LPBF process. Section 4.3 introduces the analytical and semi-analytical methods used for computationally efficient prediction of temperatures, as well as the ABAQUS AM modeling subroutines for direct numerical simulation. Section 4.4 compares the simulation and experimental results to validate the three modeling methods and to highlight the differences. In Section 4.4.2, the different phenomena playing a role in local heat accumulation are discussed. Subsequently, Section 4.4.3 describes the measures employed to prevent local heat accumulation and demonstrates the effectiveness and shortcomings of these measures. Finally, the most salient points of the study are reiterated in Section 4.5.

4.2. EXPERIMENTAL METHOD

In this study, triangular prism specimens prone to local overheating were manufactured with the magnesium alloy WE43. First, a reference specimen with fixed scanning parameters was built to investigate overheating. Subsequently, two more triangular prism specimens were built with overheating prevention methods.

4.2.1. REFERENCE SPECIMEN

The geometry of interest in this study is a regular triangular prism with an equilateral triangle side length of 10 mm with a height of 5 mm as shown in Fig. 4.1a. The specimen comprises 100 layers with a layer thickness of 50 μm. To promote heat accumulation, in the final layer, the scan pattern was oriented parallel to the base of the triangle as shown in Fig. 4.1b. Scanning orientation was rotated by 67°every layer, representative of the regular LPBF process. Only one contour scan was performed to allow for accurate measurements in the tip of the triangle, as shown in red in Fig. 4.1b. This contour was printed first, followed by the hatch vectors. For the hatch vectors, a laser power of 154 W, hatch distance of 0.12 mm, and a scan velocity of 775 mm/s were used as illustrated in Fig. 4.3a. These process parameters are based on a preliminary parameter optimization study for minimum porosity in cubic specimens. A SLM 280HL and a WE43 Mg alloy powder with a particle size of 20–63 μm supplied by SFM SA (Switzerland) were used. The part was printed on 4 mm thick sacrificial support as shown in Fig. 4.2.

After manufacturing, a cross-section was made through the triangle's center perpendicular to the top layer's scanning direction. Image analysis was performed with ImageJ software using optical microscopy images of the polished cross-section to measure the degree of porosity. Thereafter, the cross-section was etched with 75% diluted Keller's etchant to visualize the melt pools for further analysis and to compare with numerical results.

4.2.2. OVERHEATING PREVENTION EXPERIMENTS

It was observed that the melt pool depth starts to increase significantly, indicating overheating, when the scan vector length drops below 5 mm for the triangular layer. Due to the shorter scan vectors towards the tip of the triangle, the time between two subsequent passes of the laser intersecting a line orthogonal to the base of the triangle decreases. This time between two consecutive laser passes is defined as the cycle time t_{cycle}. In the tip area with a shorter cycle time, the material has less time to cool down, causing overheating. The cycle time in the process is determined as $t_{\text{cycle}} = t_{\text{scan}} + t_{\text{jump}}$, comprising the time required to scan the vector, t_{scan}, as well as the jump (waiting) time between two subsequent scan vectors, t_{jump}.

Two methods were investigated to prevent overheating. The first overheating prevention method increases the cycle time of each scan vector shorter than 5 mm with an additional cycle time to match the t_{cycle} of a scan vector of 5 mm. In the SLM 280HL used in this study, the jump time t_{jump} between hatch vectors is a fixed machine setting, hence cannot be varied for different scanning vectors. Therefore, to obtain a constant cycle time for all scan vectors, vectors shorter than 5 mm are extended to 5 mm, where the extension is scanned with turning off laser as illustrated with blue lines in Fig. 4.3b. An in-house script adjusts and writes the LPBF machine input to implement the above-described so-called ghost vectors. Fig. 4.3a displays the scan vector pattern in the final layer for the reference specimen, whereas a specimen with additional ghost vectors (blue) is depicted in Fig. 4.3b.

The second overheating prevention method is the linear laser power scaling applied to shorter vectors. This reduces heat input in low-cycle time regions, mitigating heat accumulation. Within this prevention strategy, the laser power scales linearly from 154

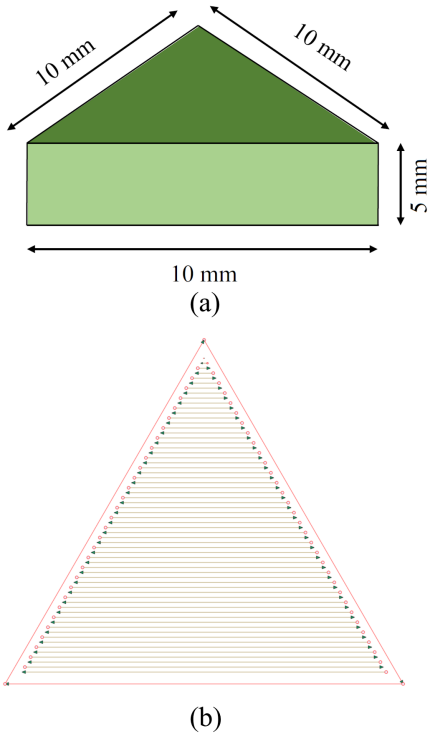

Figure 4.1: (a) The regular triangular prism geometry and (b) the scanning pattern applied in the top layer of the specimen. A single contour scan, shown in red, is performed first. Subsequently, hatch vectors that are parallel to the base of the triangle are scanned starting from the base to promote heat accumulation in the tip region.

Figure 4.2: WE43 magnesium alloy specimen manufactured by LPBF.

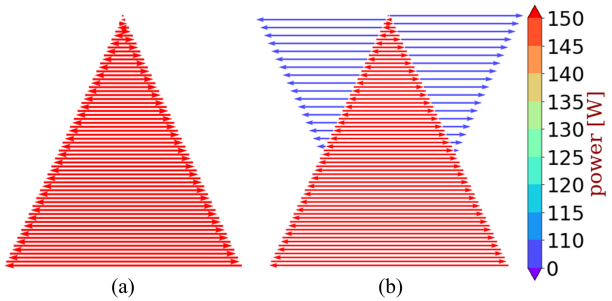

Figure 4.3: Laser scan power for (a) reference specimen and (b) the specimen with melt pool homogenization using extended scanning vectors with zero power to keep the cycle time t_{cycle} constant throughout the layer.

to 104 W for vectors shorter than 5 mm. Scaling in laser power was performed in steps of 5 W, resulting in 10 different laser power values that can be used depending on the scan vector length. For all scan vector lengths above 5 mm, the nominal laser power of 154 W was employed. The in-house variable scan parameter script was used to scale the laser power based on scan vector length for all layers in a triangular specimen. Fig. 4.4 displays the contour levels of the scan vectors' power in two different layers of the regular triangular prism specimen with laser power scaling.

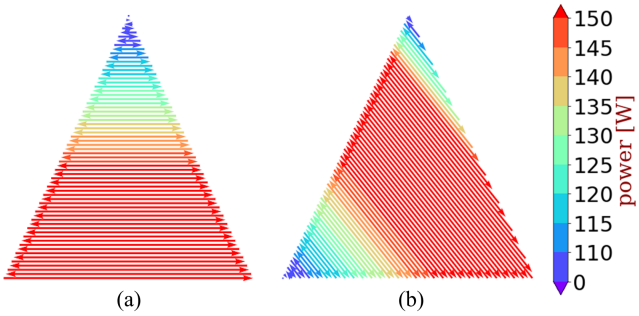

Figure 4.4: Contour levels of scan vector power of (a) in final layer (b) second to last layer for the specimen with melt pool homogenization using power scaling. Scan vector powers in the triangle are linearly scaled from 154 W to 104 W for scan vectors with a length between 5 mm and 0.

Similar to the reference specimen, etched cross-sections of the specimens with variable process conditions were observed to measure the effect of process parameters on the melt pool dimensions. The specimens' densities were measured using light microscopy images of the polished cross-sections.

4.3. SIMULATION OF THE LPBF PROCESS

Three different thermal simulation methods are described in this section after formulating the thermal boundary value problem. Firstly, an analytical model based on the analytical solution of a line source in the semi-infinite space is described. Subsequently,

a semi-analytical method will be given. This method decomposes the total temperature field into two parts: the analytical field representing the laser scanning and the numerical complementary field to enforce boundary conditions. Finally, the commercial software ABAQUS FEM with built-in AM subroutines is described. Based on the temperature transients obtained with each method, the melt pool depth in the top layer of the regular triangular prism is predicted.

4.3.1. THERMAL BOUNDARY VALUE PROBLEM

Consider the LPBF process as shown in Fig. 4.5a. After a new layer of powder is laid on the top surface of the already printed triangular prism V, the prism is submerged in the powder bed. In Fig. 4.5b, the triangular prism V and its the boundary surfaces ∂V, consisting of the top surface ∂V_{top}, the lateral surface ∂V_{lat}, and the bottom surface ∂V_{bot}, such that $\partial V = \partial V_{\text{top}} \cup \partial V_{\text{lat}} \cup \partial V_{\text{bot}}$ is illustrated.

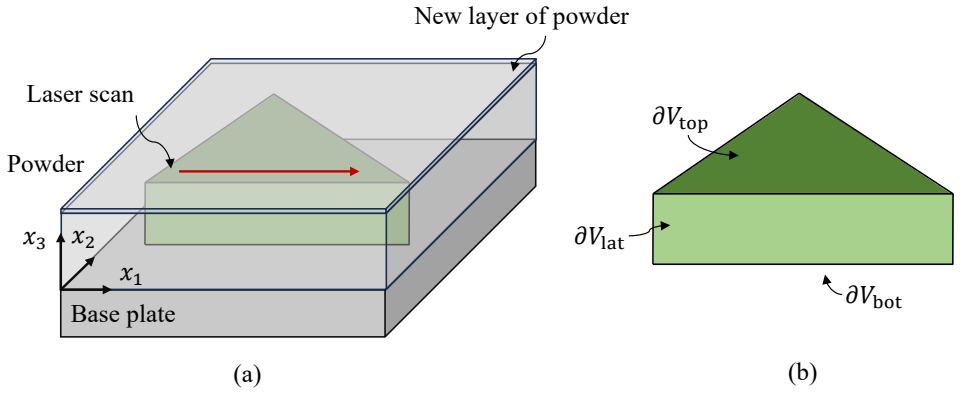

Figure 4.5: Schematic illustration of the regular triangular prism body (a) during the LPBF and (b) its boundary surfaces.

When the laser begins to scan in the current layer, the governing equation for the heat conduction is

$$\rho c_p \frac{\partial T}{\partial t} = \nabla \cdot (k \nabla T) + q \quad \text{in } V, \tag{4.1}$$

where ρ is density, c_p is specific heat and k is thermal conductivity, which are all temperature-dependent. T and q are temperature and volumetric heat generation rates, respectively. V is the simulation domain. It has been shown that the linear heat equation

$$\frac{\partial T}{\partial t} = \alpha \nabla^2 T + \frac{q}{\rho c_p} \quad \text{in } V, \tag{4.2}$$

where $\alpha = k/\rho c_p$ is thermal diffusivity, can well approximate Eq. (4.1) when adopting suitable temperature-independent thermal diffusivity [38, 42–44].

A boundary value problem (BVP) governed by Eq. (4.2) needs to be solved with boundary conditions on ∂V to obtain the temperature distribution as a function of time in the solid domain. Besides, for any material point x_i within the body V, the

initial condition $T(x_i, 0) = T_c$ is applied at $t = 0$, where T_c is the constant temperature maintained in the base plate. Since the thermal conductivity of the metal powder is approximately 1% of the solid part [45], the heat transfer between the solid material and the metal powder is considered negligible. Moreover, we neglect heat loss through surfaces by convection and radiation as they are secondary in contrast to the heat conduction within the solid part [30]. Consequently, adiabatic boundary conditions are assumed on ∂V_{lat} and ∂V_{top} as

$$\frac{\partial T}{\partial x_i} n_i = 0, \quad \text{on} \partial V_{\text{lat}} \cup \partial V_{\text{top}}, \tag{4.3}$$

where n_i denotes the surface unit outward normal vector components. The constant temperature boundary condition on the bottom surface ∂V_{bot} is

$$T = T_c \quad \text{on} \partial V_{\text{bot}}. \tag{4.4}$$

4.3.2. ANALYTICAL METHOD

The analytical method is based on the solution of Eq. (4.2) in a semi-infinite space. Consider a single point heat source with energy Q on the top surface (∂V_{top}) in a semi-infinite space bounded by ∂V_{top}. The analytical solution of Eq. (4.2) at time t reads

$$\tilde{T}^{(I)}(x_i, t) = \frac{QA}{4\pi\rho C_p (\pi\alpha\tau^{(I)})^{3/2}} \exp\left(\frac{-R^2}{4\alpha\tau^{(I)}}\right), \tag{4.5}$$

where $\tau^{(I)} = t - t_0^{(I)} + t_r$ is the time elapsed after the source I is activated at $t_0^{(I)}$. The parameter $t_r = r^2/8\alpha$ is the time shift introduced for the point source to account for the finite laser spot radius r while avoiding a singularity. The distance between the point of interest x_i and the point source position $\tilde{x}_i^{(I)}$ is R. The laser absorptivity fraction of metal powder is A.

The temperature solution for a line source representing a scanning vector can be constructed in the semi-infinite space by integrating the point source solution over time t_0

$$\tilde{T}(x_i, t) = \frac{PA}{4\rho C_p (\pi\alpha)^{(3/2)}} \int_{t_0'}^{t_e} \frac{\exp\left(-\frac{R^2}{4\alpha(t - t_0 + t_r)}\right)}{(t - t_0 + t_r)^{3/2}} \mathrm{d}t_0, \tag{4.6}$$

where P is the laser power, t_0' and t_e mark the initiation and termination of the scanning vector. Eq. (4.6) cannot always be simplified into a closed form. However, the closed form for a straight line source can be acquired. For the sake of brevity, we refer to Eq. (7) in [36].

4.3.3. THE SEMI-ANALYTICAL METHOD

When adopting the analytical solutions for the laser scanning on a finite part shown in Fig. 4.5, the boundary conditions on the ∂V_{lat} and ∂V_{bot} in Eqs. (4.3) and (4.4) are not satisfied. However, to solve the boundary value problems (BVPs) described by Eqs. (4.2–4.4), the total temperature field can be decomposed into two parts as

$$T = \tilde{T} + \hat{T}, \tag{4.8}$$

where $\tilde{T}$ is the sum of the analytical solution of all heat sources in the semi-infinite space, and $\hat{T}$ is the complementary field to impose boundary conditions given in Eqs. (4.3) and (4.4). Then, the complementary temperature field $\hat{T}$ is computed using FEM discretization of the governing equation

$$\frac{\partial \hat{T}}{\partial t} = \alpha \nabla^2 \hat{T} \quad \text{in } V, \tag{4.9}$$

and boundary conditions obtained by substituting Eq. (4.8) into Eqs. (4.3) and (4.4), which becomes

$$\frac{\partial \hat{T}}{\partial x_i} n_i = -\frac{\partial \tilde{T}}{\partial x_i} n_i \quad \text{on} \partial V_{\text{lat}}, \tag{4.10}$$

$$\hat{T} = T_c - \tilde{T} \quad \text{on} \partial V_{\text{bot}}. \tag{4.11}$$

and the initial condition at $t = 0$ is

$$\hat{T}(x_i, 0) = T_c - \tilde{T}(x_i, 0). \tag{4.12}$$

Note that a boundary condition for numerical correction on ∂V_{top} is omitted since the adiabatic boundary conditions are built into Eq. (7). Since the $\hat{T}$ field does not contain any heat source due to scanning, apart from the close vicinity of the boundaries where the steep temperature gradients arise due to Eq. (4.10), $\hat{T}$ is a smooth field that can be resolved with a coarse mesh.

4.3.4. ABAQUS AM SUBROUTINES

Besides the analytical and semi-analytical methods, a thermal FE simulation is performed using commercial software ABAQUS. The built-in additive manufacturing subroutines [46] were employed to simulate the scanning of the final layer of the triangular specimen. The Toolpath-Mesh intersection module is used to implement a moving heat source and a transient thermal analysis following the final layer's prescribed toolpath. This direct numerical simulation (DNS) will serve as a reference to verify the accuracy of the above described analytical and semi-analytical models. The ABAQUS AM subroutines employ a Goldak heat source with a radius and depth equal to the radius of the laser spot to obtain the same semi-spherical volumetric heat source as the (semi-)analytical model considers. To allow for a fair comparison between the semi-analytical model and the ABAQUS AM subroutines, convection and radiation losses were switched off. Fig. 4.6a displays the FE mesh required in ABAQUS, and Fig. 4.6b shows the FE mesh required for the semi-analytical method. For the ABAQUS AM subroutine, the FE model employs 281,926 hexahedral linear elements to realistically capture the melt pool evolution while scanning the final layer. In contrast, the semi-analytical model only requires fine elements along the boundary, resulting in a total of 11,047 tetrahedral elements. Table 4.1 gives the material and process parameters used in modeling the LPBF process for the WE43 magnesium alloy [47].

Table 4.1: Material and process parameters used in the analytical, semi-analytical, and ABAQUS to simulate the LPBF process with the Magnesium alloy WE43.

Simulation parameter [unit]	Value
Absorbtivity (A) [-]	0.55
Spot radius (r) [mm]	0.04
Initial temperature (T_c) [° C]	107
Thermal conductivity (k) [W·m^{-1}·°C]	51.3
Specific heat (c_p) [W·kg^{-1}·°C^{-1}]	1,000
Density (ρ) [kg·m^3]	1,840

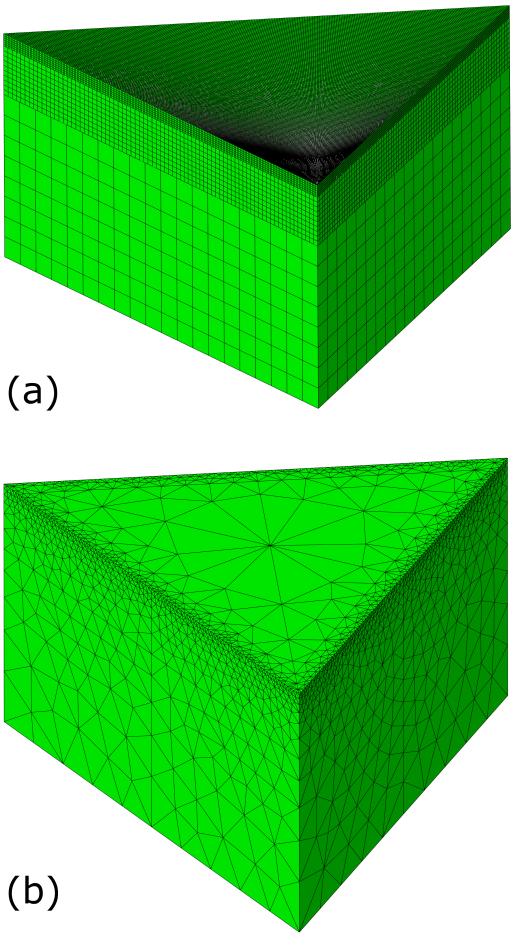

Figure 4.6: The finite element meshes required for (a) a high fidelity LPBF simulation with ABAQUS AM subroutines of a single layer and (b) the coarser mesh used for determining the correction field $\hat{T}$ in the semi-analytical method, showing a fine region along the lateral boundary.

4.4. RESULTS AND DISCUSSION

This section discusses the reference specimen's experimental findings, simulation predictions, and the two specimens realized with overheating prevention approaches.

4.4.1. REFERENCE SPECIMEN RESULTS

Fig. 4.7 displays the cross-section of the triangular reference specimen manufactured with fixed scan parameters. The etching procedure has exposed the melt pools. Overheating near the tip of the triangle affected the appearance significantly. Due to local heat accumulation, the local temperatures are elevated, resulting in higher temperatures in and around the melt pool once the material is scanned by the passing laser. This elevation in temperatures results in a steady increase in melt pool size as well as more evaporation of material in the melt pool, resulting in more and larger spherical pores. The melt pool depths near the tip of the triangle steadily increase and become darker in color, see Fig. 4.7b. The darker color, i.e., a different response to the etchant, indicates an alteration in the microstructure. Furthermore, significant porosity formation can be observed in the tip region of the triangle. Fig. 4.7c displays the entire polished cross-section with an increasing pore population towards the tip. Analysis of the optical microscopy images with ImageJ has shown that outside the tip region (red box in Fig. 4.7c), the relative density of the material is 99.84%, whereas in the tip region (orange box in Fig. 4.7c), the relative density is reduced to 98.79%. The increase in melt pool depth and porosity appears not only in the final layer but throughout the specimen in layers where the scan orientation is favorable for overheating. Furthermore, the spherical shape of the pores is associated with key-holing, which is indicative of too high energy input. This implies that overheating is primarily caused by local heat accumulation instead of heat accumulation over multiple layers.

Fig. 4.8 displays temperature fields predicted by the three different modeling methods at three different instances during the scanning of the final layer of the triangular prism. It is observed that during the scanning of the first vector, the melt pool dimensions are in perfect agreement with each other. This agreement between semi-analytical and analytical predictions is as expected, as the influence of boundary conditions is insignificant, while the agreement between the semi-analytical and ABAQUS DNS manifests the accuracy of the semi-analytical method despite the coarser mesh it relies on. The minor effect of the boundaries near the triangle's base is more apparent in the temperature history depicted in Fig. 4.9a. At point A (labeled in Fig. 4.8), which is close to the base of the triangle, the analytical and semi-analytical predictions are initially almost on top of each other. With the initial pass of the scan vector, the temperature increases far above the melting point of 650 °C. Upon cooling after the initial pass of the laser and subsequent heating cooling cycles, there is only a small discrepancy between the analytical method and the two other methods, ABAQUS DNS and semi-analytical. This is because the analytical model allows heat to conduct through the part boundaries, while the FEM and semi-analytical methods impose adiabatic boundary conditions over the part boundary. The boundary conditions' effect is more evident towards the tip of the triangle. Here, the semi-analytical and ABAQUS DNS method predictions are very similar in terms of temperature and melt pool size. However, the analytical model underestimates the temperature values and melt pool dimensions (Fig. 4.8). Similarly, temper-

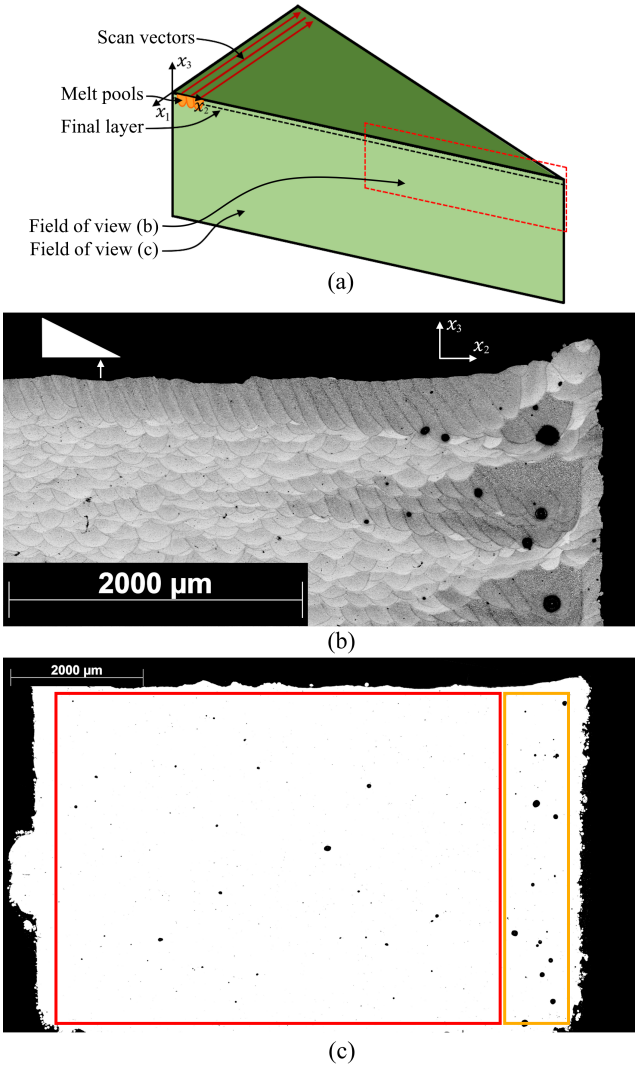

Figure 4.7: (a) Schematic illustration of the cross-section on the half of the regular triangular prism specimen, (b) optical micrograph of the etched cross-section displaying the evolution of the melt pools and increase in porosity caused by local overheating near the tip of the triangle and (c) the optical microscopy image of the polished cross-section showing in red the region representative of the whole specimen and orange the region near the tip of the triangle.

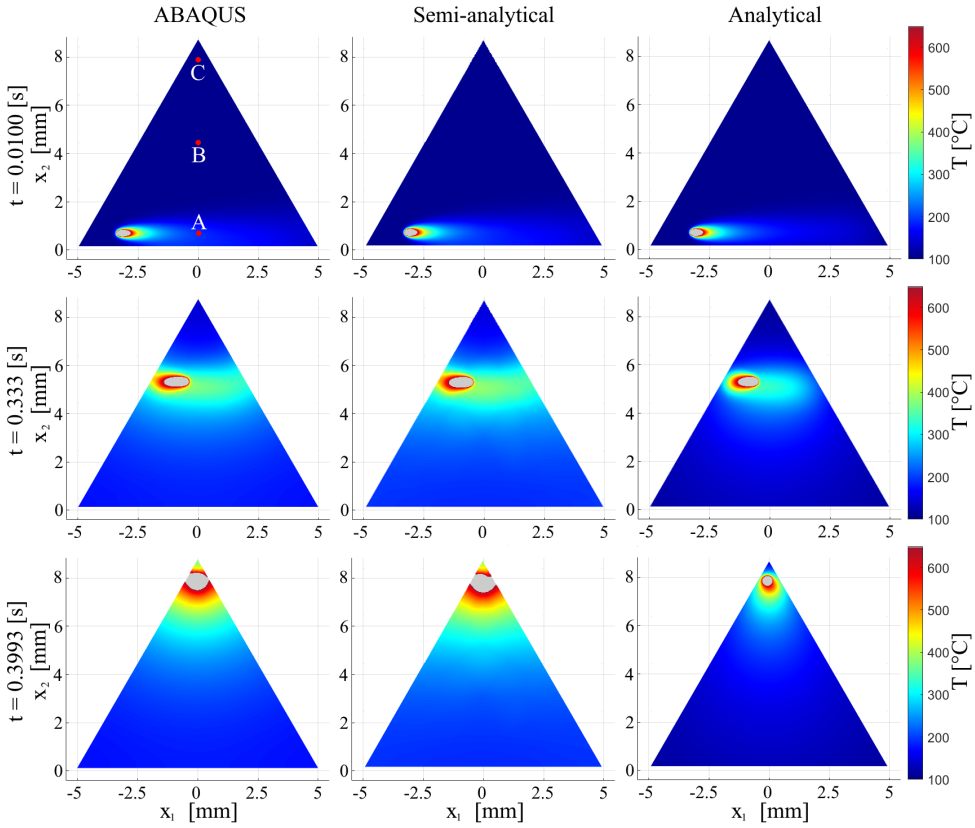

Figure 4.8: Snapshots of temperature contour level predictions for the final layer according to ABAQUS DNS, semi-analytical, and purely analytical models. The top row during the scanning of the first vector, the middle row at the start of scan vector 40, and the bottom row while scanning the second to last vector at the tip of the triangle.

ature peaks observed at points B and C (Fig. 4.9b and Fig. 4.9c of the analytical method are smaller, which leads to remarkably smaller melt pool predictions in the tip region compared to other methods. The main reason behind this discrepancy is the prominent impact of the boundary conditions near the tip region from both sides of the triangle on the temperature field, which is not accounted for in the analytical model. We refer to this phenomenon as boundary confinement at the tip in the remainder.

To validate the numerical results, melt pool depths were measured at each scan vector location. This is performed according to the standard developed by NASA [48] for the cross-section displayed in Fig. 4.7b. Both the numerical and experimental melt pool depths as a function of distance from the base of the triangle are displayed in Fig. 4.10. The experimental results show a clear trend with a significant increase in melt pool depth starting from 4 mm from the tip. The peak in melt pool depth occurs at 0.5 mm from the tip of the triangle. The melt pool depth suddenly decreases significantly for scan vectors closer than 0.5 mm to the tip of the triangle. The same trend is observed in the numeri-

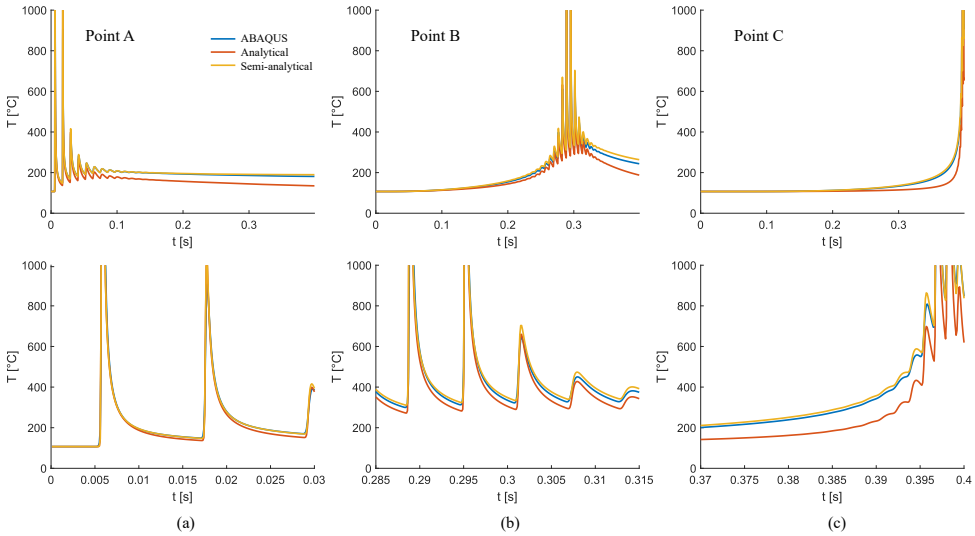

Figure 4.9: Temperature history according to the analytical, semi-analytical, and ABAQUS DNS simulations (a) at point A, (b) at point B, and (c) at point C as indicated in Fig. 4.8.

cal results. The semi-analytical and ABAQUS DNS methods give very similar qualitative behavior for the melt pool depth but slightly underestimate the experimental findings. Far away from the tip of the triangle, the analytical model predicts the same melt pool depth as the two more sophisticated numerical models. However, near the tip of the triangle, the effect of the boundary conditions significantly impacts analytical predictions, resulting in the analytical model's prominent underestimation of melt pool depth. We note in passing that adiabatic boundary conditions imposed for the ABAQUS DNS and semi-analytical simulations do not fully mimic reality. Even though the surrounding powder bed is a good thermal insulator, some heat is inevitably lost to the surrounding powder [49]. Additionally, heat is lost at the top surface through convection, and radiation is not accounted for in the current semi-analytical and ABAQUS DNS simulations. However, we conjecture that discrepancies between the numerical and experimental results concern the unknown temperature dependency of the material properties and laser absorptivity. For example, thermal conductivity has a strong temperature dependence depending on the chemical composition of the Magnesium alloy [47].

Table 4.2 provides the computation times for the different modeling methods. Even though the semi-analytical model's predictions perfectly agree with ABAQUS DNS, its computational efficiency significantly outperforms that of ABAQUS DNS. The ABAQUS DNS requires 4 hours and 22 minutes to simulate the triangular surface on 8 CPUs. The analytical model requires 5 minutes to compute the analytical temperature field, with an additional 10 minutes for the semi-analytical model to compute the boundary correction numerically on 8 CPUs. The semi-analytical method is thus 17.5 times faster compared to the FEM without compromising on the accuracy.

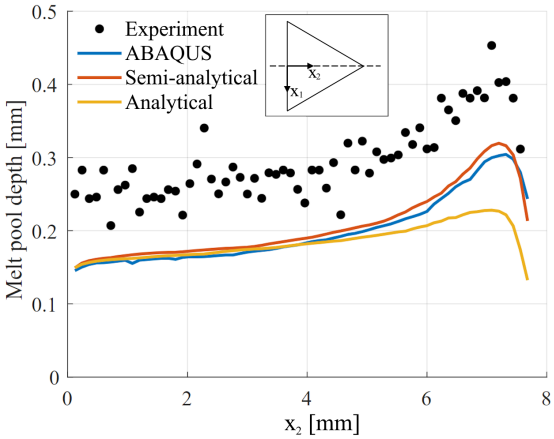

Figure 4.10: Melt pool depths extracted at scan vector locations from the base of the triangle to the tip along the dashed line illustrated in the inset. The three different model predictions are superimposed onto the experimental results obtained from the etched cross-sections.

Table 4.2: Computation times to complete the thermal analysis of one LPBF layer.

Analysis type	Computation time [hr:min]
FEM	4:22
Semi-analytical	0:15
analytical	0:05

4.4.2. OVERHEATING MECHANISMS

Even though the analytical model underestimates the melt pool depth and heat accumulation near the tip of the triangle due to the absence of boundary effects, it still captures an overheating phenomenon in the triangular prism specimen, which apparently cannot only be explained due to the boundary confinement. It remains to rationalize the origins of this to gain insight into the mechanisms leading to overheating phenomena and improve overheating prevention measures.

The melt pool depth evolution from the base to the tip of the triangle, shown in Fig. 4.11a using the analytical method along the center line is again demonstrated in Fig. 4.11b. For comparison, melt pool depths of square and rectangular final layers of a cube and a rectangular prism (see Fig. 4.11a) are also depicted in Fig. 4.11b. When scanning a square or a rectangular layer, the scanning vector length and hence the cycle time t_{cycle} remains fixed throughout the layer. When the scanning commences, the melt pool depth increases along the x_2 for all layer geometries as the initial scan vectors heat the specimen. Still, the melt pool depth reaches a steady state for the square and rectangular layers. The melt pool depth observed in this steady state correlates with the length of the scan vectors. When scanning a square layer with 8.8 mm long scan vectors, similar to the length of the base of the triangular layer, the steady state melt pool depth is 0.165 mm. A rectangular area of width 4.4 mm results in a significantly larger steady-state melt pool depth of just over 0.18 mm. This is mainly due to the reduction in cycle time. Cycle time

$t_{cycle} = t_{scan} + t_{jump}$ decreases as t_{scan} decreases to half but t_{jump} remains constant. In contrast, during the scanning of the triangular layer from the base to the tip, melt pool depth monotonically increases until the 59th scanning vector. This is because the cycle time keeps decreasing with decreasing vector length, allowing for a further increase in the temperature. The intersection between the melt pool depths in the triangle and the 4.4 mm rectangle in Fig. 4.11a indicates where the scan vector length is 4.4 mm, equal to that of the rectangular layer. Consequently, with the analytical model in the absence of boundary effects, the cycle time is the main mechanism behind the increase in melt pool depth in the triangular layer.

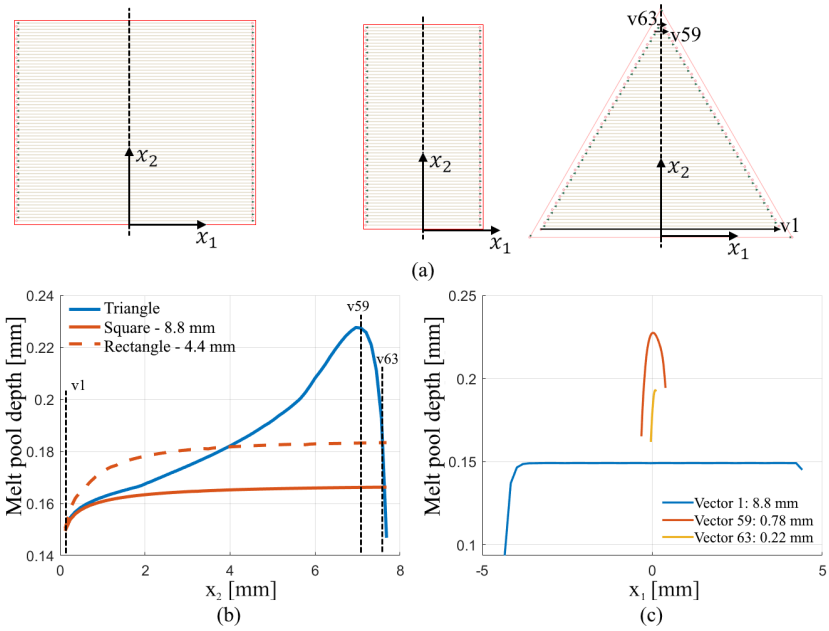

Figure 4.11: (a) Schematic illustration of square and rectangular layers with scan vector lengths of 8.8 mm and 4.4 mm as well as the triangular layer with the 1st vector (v1), 59th (v59) and 63rd (v63) vectors highlighted. The dashed lines indicate the location along which the melt pool depth is determined using the analytical model, as shown in (b). In (c), the melt pool depth along the length of three vectors, v1, v59, and v63, are plotted for the triangular layer.

Next, the sharp decrease in the melt pool depth in the triangular layer starting at approximately 1 mm away from the triangle tip is explained (see Fig. 4.11b). From this point onward, even though the cycle time keeps reducing towards the tip, the melt pool depth sharply decreases in the triangular layer. The main reason behind this melt pool depth reduction is the insufficient length and hence heating time of an individual scan vector. Fig. 4.11b displays the evolution of melt pool depth along the length of three distinct scan vectors v1, v59, and v63 indicated in Fig. 4.11a. From the melt pool evolution of the v1 scan vector, it is evident that a certain scan vector length is required to develop fully and reach a steady melt pool depth. With a length of 0.78 mm, vector 59 has just

enough length to develop the melt pool, resulting in the deepest melt pool because of a very low cycle time. However, the vector length is too short for the subsequent vectors to have sufficient heating for the melt pool to develop fully, resulting in shallower melt pools.

4.4.3. OVERHEATING PREVENTION RESULTS

This section discusses the results of the two overheating prevention methods. The two magnesium regular triangular prisms were manufactured by extending scanning vectors with ghost vectors and scaling laser power. Fig. 4.12 displays the etched cross-sections of the specimens. In Fig. 4.12a, extended scanning vectors with ghost vectors, and in Fig. 4.12b, scaled laser power micrographs are given. Both specimens show a substantial improvement in melt pool depth homogeneity at the tip of the triangle, whereas the reference specimen in Fig. 4.7, as discussed above, displays a notable variance in melt pool depths along with significant pore formation. The relative densities are measured as 99.81% and 99.78% for the ghost vectors and power scaling, respectively. No major increase in porosity was observed in the tip region for both specimens. This indicates more than 1% improvement in relative density compared with the porosity measurement in the tip of the reference specimen. The melt pool depths in the final layer of

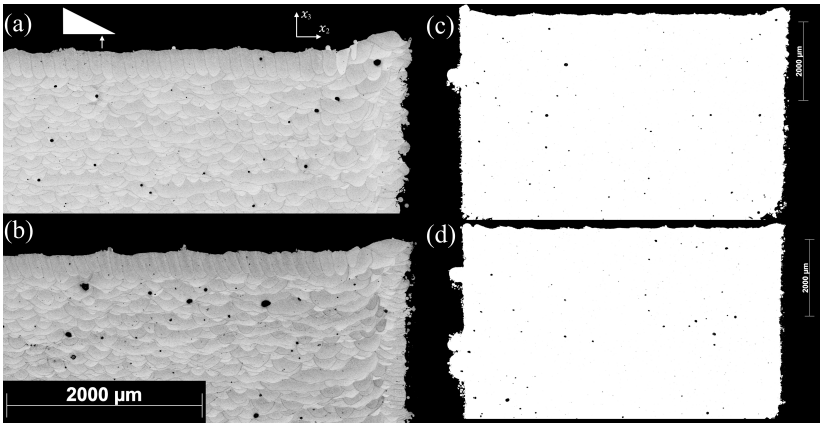

Figure 4.12: Optical micrographs of cross-sections of the two triangular prism specimens using two different methods to homogenize the melt pool depth with (a) and (c) the use of extended zero power vectors, which increases t_{cycle} and (b) and (d) the linear reduction of laser power for short vectors to reduce heat input in scan vectors with short cycle times.

the triangles employing the two overheating prevention strategies were measured and compared with the reference measurement. The results are shown in Fig. 4.13. From the experimental results, it can be seen that the melt pool depth in the region with low cycle time is significantly reduced when using both of the overheating prevention methods. Due to the scatter in the measured data, it is indistinguishable which preventive method is the best for the homogenization of the melt pool depth in the triangular prism specimen. It is important to note that in close proximity to the tip, the melt pool depth still decreases due to the insufficient length of scanning vectors, as explained above. To fur-

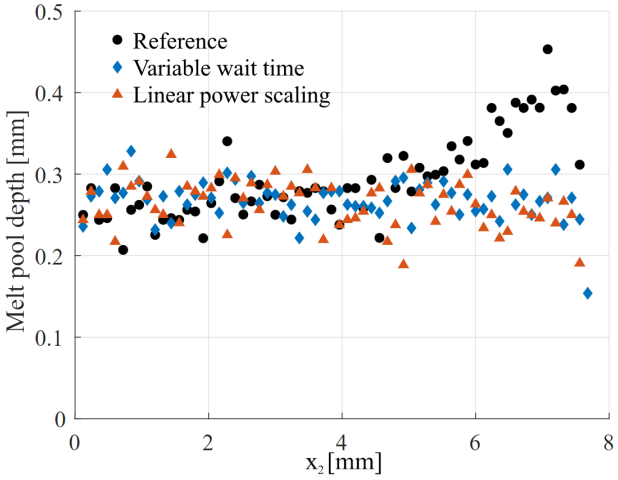

Figure 4.13: Experimentally measured melt pool depth along the x_2 direction showing the effect of the melt pool homogenization methods compared with the reference specimen.

ther homogenize the melt pool depths, this mechanism should be accounted for while designing process parameters to prevent overheating and homogenize melt pool depths. Fig. 4.14 displays the analytical and semi-analytical model predictions for the melt pool depth using ghost vectors and the linear power scaling superimposed onto the experimental measurements. To better compare the trends observed in the three different specimens, the melt pool depths are normalized based on the average melt pool depth of the first 30 scan vectors, which are not prone to overheating. Fig. 4.14a shows that the semi-analytical method captures the trend in melt pool depth. It is observed that the experimental melt pool depth lies between the semi-analytical and the analytical model predictions. This is as expected, as the adiabatic boundary conditions imposed in the semi-analytical model and the absence of boundary conditions in the analytical method represent the two idealized extremes. When overheating prevention methods are employed, the normalized melt pool depth is stable within the scatter observed in non-overheating regions. The semi-analytical and analytical melt pool depth predictions for ghost vectors agree with the experimental results. Like the reference specimen, the experimental melt pool depths are largely between the semi-analytical and the analytical predictions. Especially for the linear power scaling specimen, the semi-analytical model seems to slightly overpredict the melt pool depth with respect to the experimental results.

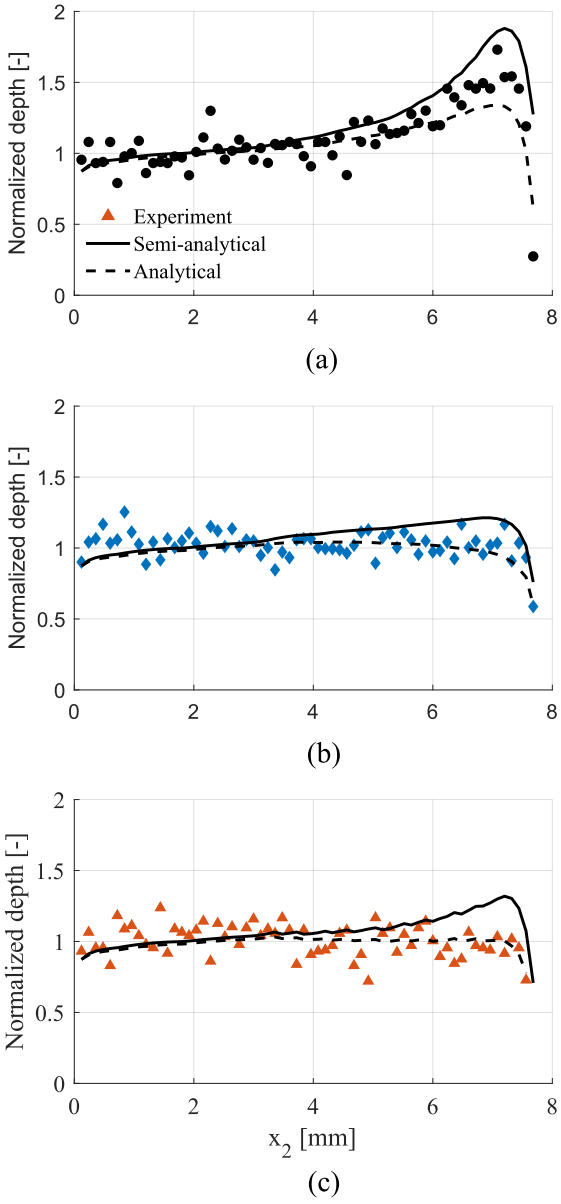

Figure 4.14: Normalized melt pool depths from the base of the triangle to the tip along the center-line depicting experimentally measured melt pool depths along with the analytical and semi-analytical predictions for (a) the reference specimen, (b) variable wait time, and (c) with linear power scaling.

4.5. CONCLUSIONS

This study employs three modeling methods to analyze and predict the local heat accumulation phenomena observed in the LPBF process with WE43 magnesium alloy. Experimental investigation on triangular prism specimens showed a significant increase in melt pool depth and porosity formation in the region with shorter scan vectors and boundary confinement. The semi-analytical method perfectly agreed with DNS performed with commercial ABAQUS software using AM subroutines with a 17.5-fold enhanced computational efficiency. Both methods predict the experimentally observed trends in melt pool depth well. Using the analytical formulation with no due account for the boundary conditions also displays similar trends in melt pool depth in the triangular specimen while being extremely computationally efficient. Therefore, it is ideal for making a quick qualitative, approximate assessment of the overheating of parts, process parameters, and scanning strategy. However, the melt pool depth increase due to heat accumulation is underestimated since the contribution of the boundary confinement is neglected. Further investigation on temperature-dependent material properties and laser absorptivity of the WE43 alloy is required to obtain higher accuracy in the actual melt pool depth predictions.

Two additional mechanisms besides the boundary confinement are isolated using the analytical method, influencing the melt pool depth in the triangular prism specimen. It was observed that diminishing cycle time, i.e. the time required for the scanning of a vector to complete, increases the melt pool depth. The cycle time correlates with the vector length. Therefore, shorter subsequent scan vectors in the triangular layer result in increasing melt pool depth. Finally, if the scan vector length drops below a threshold level of roughly 0.8 mm with the process parameters used in our study, the melt pool depth decreases dramatically. This is due to the underdevelopment of the melt pool, which requires a certain length and time to reach a steady-state depth.

The two overheating prevention techniques developed in a preliminary study were analyzed experimentally and numerically using analytical and semi-analytical simulations. Both the increase in cycle time and the reduction in laser power as a function of the vector length work well in preventing local overheating in the triangular specimens, except very near the tip, since the decrease in the melt pool depth due to very short scan vectors is not accounted for. Even without a thorough characterization of the temperature-dependent material parameters and laser absorptivity, the semi-analytical model captures well the effect of variable wait time and linear power scaling on the melt pool depth in a computationally inexpensive manner. This shows the potential for such a fast analysis method to predict local overheating and optimize local scan parameters in more complex geometries with a very low cost, allowing for feed-forward control of the LPBF process for magnesium alloys.

BIBLIOGRAPHY

[1] J. Bai, Y. Yang, C. Wen, J. Chen, G. Zhou, B. Jiang, X. Peng, and F. Pan, "Applications of magnesium alloys for aerospace: a review", Journal of Magnesium and Alloys **11**, Magnesium and Its Alloys for Better Future - JMA 10th Anniversary, 3609–3619 (2023).

[2]N. Chi Chung, M. Savalani, and H. Man, "Fabrication of magnesium using selective laser melting technique", Rapid Prototyping Journal - RAPID PROTOTYPING J **17**, 479–490 (2011).

[3]B. Zhang, H. Liao, and C. Coddet, "Effects of processing parameters on properties of selective laser melting mg–9%al powder mixture", Materials & Design **34**, 753–758 (2012).

[4]L. Jauer, "Laser Powder Bed Fusion von Magnesiumlegierungen; 1. Auflage", Druckausgabe: 2018. - Auch veröffentlicht auf dem Publikationsserver der RWTH Aachen University 2019; Dissertation, RWTH Aachen University, 2018, Dissertation (RWTH Aachen University, Aachen, 2018), 1 Online–Ressource (II, 165 Seiten) : Illustrationen, Diagramme.

[5]M. Gieseke, C. Noelke, S. Kaierle, V. Wesling, and H. Haferkamp, "Selective laser melting of magnesium and magnesium alloys", in *Magnesium technology 2013*, edited by N. Hort, S. N. Mathaudhu, N. R. Neelameggham, and M. Alderman (Springer International Publishing, Cham, 2016), pp. 65–68.

[6]T. Koenis, M. Montero-Sistiaga, M. de Smit, and E. Amsterdam, "Simulation-based process optimization towards homogeneous ti6al4v l-pbf components", IVth International Conference on Simulation for Additive Manufacturing (2023).

[7]A. Riensche, B. D. Bevans, Z. Smoqi, R. Yavari, A. Krishnan, J. Gilligan, N. Piercy, K. Cole, and P. Rao, "Feedforward control of thermal history in laser powder bed fusion: toward physics-based optimization of processing parameters", Materials & Design **224**, 111351 (2022).

[8]J. Munk, E. Breitbarth, T. Siemer, N. Pirch, and C. Häfner, "Geometry effect on microstructure and mechanical properties in laser powder bed fusion of ti-6al-4v", Metals **12**, 10.3390/met12030482 (2022).

[9]H. Hyer, L. Zhou, G. Benson, B. McWilliams, K. Cho, and Y. Sohn, "Additive manufacturing of dense we43 mg alloy by laser powder bed fusion", Additive Manufacturing **33**, 101123 (2020).

[10]H. Yeung, B. Lane, and J. Fox, "Part geometry and conduction-based laser power control for powder bed fusion additive manufacturing", en, Additive Manufacturing **30**, 100844 (2019).

[11]H. Yeung and B. Lane, "A residual heat compensation based scan strategy for powder bed fusion additive manufacturing", en, Manufacturing Letters **25**, 56–59 (2020).

[12]C. Druzgalski, A. Ashby, G. Guss, W. King, T. Roehling, and M. Matthews, "Process optimization of complex geometries using feed forward control for laser powder bed fusion additive manufacturing", en, Additive Manufacturing **34**, 101169 (2020).

[13]Y. Liu, J. Li, K. Xu, T. Cheng, D. Zhao, W. Li, Q. Teng, and Q. Wei, "An optimized scanning strategy to mitigate excessive heat accumulation caused by short scanning lines in laser powder bed fusion process", Additive Manufacturing **60**, 103256 (2022).

[14]S. I. Shahabad, U. Ali, Z. Zhang, A. Keshavarzkermani, R. Esmaeilizadeh, A. Bonakdar, and E. Toyserkani, "On the effect of thin-wall thickness on melt pool dimensions in laser powder-bed fusion of hastelloy x: numerical modeling and experimental validation", Journal of Manufacturing Processes **75**, 435–449 (2022).

[15]C. Pauzon, K. Dietrich, P. Forêt, E. Hryha, and G. Witt, "Mitigating oxygen pick-up during laser powder bed fusion of Ti-6Al-4V by limiting heat accumulation", en, Materials Letters **288**, 129365 (2021).

[16]M. A. Chaudry, G. Mohr, and K. Hilgenberg, "Experimental and numerical comparison of heat accumulation during laser powder bed fusion of 316l stainless steel", Progress in Additive Manufacturing **7**, 1071–1083 (2022).

[17]R. Ranjan, C. Ayas, M. Langelaar, and F. van Keulen, "Fast detection of heat accumulation in powder bed fusion using computationally efficient thermal models", Materials **13**, 10.3390/ma13204576 (2020).

[18]S. Afazov, A. Roberts, L. Wright, P. Jadhav, A. Holloway, H. Basoalto, K. Milne, and N. Brierley, "Metal powder bed fusion process chains: an overview of modelling techniques", Progress in Additive Manufacturing, 289–314 (2022).

[19]M. Bayat, O. Zinovieva, F. Ferrari, C. Ayas, M. Langelaar, J. Spangenberg, R. Salajeghe, K. Poulios, S. Mohanty, O. Sigmund, and J. Hattel, "Holistic computational design within additive manufacturing through topology optimization combined with multi-physics multi-scale materials and process modelling", Progress in Materials Science **138**, 101129 (2023).

[20]C. Panwisawas, C. Qiu, M. J. Anderson, Y. Sovani, R. P. Turner, M. M. Attallah, J. W. Brooks, and H. C. Basoalto, "Mesoscale modelling of selective laser melting: thermal fluid dynamics and microstructural evolution", Computational Materials Science **126**, 479–490 (2017).

[21]D. Sarkar, A. Kapil, and A. Sharma, "Advances in computational modeling for laser powder bed fusion additive manufacturing: a comprehensive review of finite element techniques and strategies", Additive Manufacturing **85**, 104157 (2024).

[22]J. Y. Choi, T. Xue, S. Liao, and J. Cao, "Accelerating phase-field simulation of three-dimensional microstructure evolution in laser powder bed fusion with composable machine learning predictions", Additive Manufacturing **79**, 103938 (2024).

[23]A. Zinoviev, O. Zinovieva, V. Ploshikhin, V. Romanova, and R. Balokhonov, "Evolution of grain structure during laser additive manufacturing. simulation by a cellular automata method", Materials & Design **106**, 321–329 (2016).

[24]S. Sunny, H. Yu, R. Mathews, A. Malik, and W. Li, "Improved grain structure prediction in metal additive manufacturing using a dynamic kinetic monte carlo framework", Additive Manufacturing **37**, 101649 (2021).

[25]P. Promoppatum and V. Uthaisangsuk, "Part scale estimation of residual stress development in laser powder bed fusion additive manufacturing of inconel 718", Finite Elements in Analysis and Design **189**, 103528 (2021).

[26]L. Isidore Besong and J. Buhl, "A review of constitutive models used in macroscale finite element analysis of additive manufacturing and post-processing of additively manufactured components", Virtual and Physical Prototyping **19**, e2356079 (2024).

[27]M. Carraturo, J. Jomo, S. Kollmannsberger, A. Reali, F. Auricchio, and E. Rank, "Modeling and experimental validation of an immersed thermo-mechanical part-scale analysis for laser powder bed fusion processes", Additive Manufacturing **36**, 101498 (2020).

[28]H. Y. Chia, L. Wang, and W. Yan, "Influence of oxygen content on melt pool dynamics in metal additive manufacturing: high-fidelity modeling with experimental validation", Acta Materialia **249**, 118824 (2023).

[29]Y. Yang, M. Knol, F. van Keulen, and C. Ayas, "A semi-analytical thermal modelling approach for selective laser melting", Additive Manufacturing **21**, 284–297 (2018).

[30]I. Roberts, C. Wang, R. Esterlein, M. Stanford, and D. Mynors, "A three-dimensional finite element analysis of the temperature field during laser melting of metal powders in additive layer manufacturing", International Journal of Machine Tools and Manufacture **49**, 916–923 (2009).

[31]A. Olleak and Z. Xi, "Part-scale finite element modeling of the selective laser melting process with layer-wise adaptive remeshing for thermal history and porosity prediction", Journal of Manufacturing Science and Engineering **142**, 121006 (2020).

[32]Z.-D. Zhang, S. Imani Shahabad, O. Ibhadode, C. F. Dibia, A. Bonakdar, and E. Toyserkani, "3-dimensional heat transfer modeling for laser powder bed fusion additive manufacturing using parallel computing and adaptive mesh", Optics & Laser Technology **158**, 108839 (2023).

[33]A. J. Dunbar, E. R. Denlinger, M. F. Gouge, and P. Michaleris, "Experimental validation of finite element modeling for laser powder bed fusion deformation", Additive Manufacturing **12**, 108–120 (2016).

[34]J. P. Leonor and G. J. Wagner, "Go-melt: gpu-optimized multilevel execution of lpbf thermal simulations", Computer Methods in Applied Mechanics and Engineering **426**, 116977 (2024).

[35]M. Liu, L. N. Chiu, D. Liu, A. Huang, C. Davies, X. Wu, and W. Yan, "A macroscale thermal simulation strategy with track-scale resolution for laser powder bed fusion", Materials & Design **226**, 111622 (2023).

[36]Y. Yang, F. van Keulen, and C. Ayas, "A computationally efficient thermal model for selective laser melting", Additive Manufacturing **31**, 100955 (2020).

[37]A. J. Wolfer, J. Aires, K. Wheeler, J.-P. Delplanque, A. Rubenchik, A. Anderson, and S. Khairallah, "Fast solution strategy for transient heat conduction for arbitrary scan paths in additive manufacturing", Additive Manufacturing **30**, 100898 (2019).

[38]J. Ning, E. Mirkoohi, Y. Dong, D. E. Sievers, H. Garmestani, and S. Y. Liang, "Analytical modeling of 3d temperature distribution in selective laser melting of ti-6al-4v considering part boundary conditions", Journal of Manufacturing Processes **44**, 319–326 (2019).

[39]T. Moran, D. Warner, and N. Phan, "Scan-by-scan part-scale thermal modelling for defect prediction in metal additive manufacturing", Additive Manufacturing **37**, 101667 (2021).

[40]Y. Yang, Y. Ji, M. Möller, and C. Ayas, "Computational efficient process simulation of geometrically complex parts in metal additive manufacturing", International Journal of Heat and Mass Transfer **248**, 127059 (2025).

[41]Y. Yang, X. Zhou, Q. Li, and C. Ayas, "A computationally efficient thermo-mechanical model for wire arc additive manufacturing", Additive Manufacturing **46**, 102090 (2021).

[42] D. Rosenthal, "The theory of moving sources of heat and its application of metal treatments", Transactions of ASME **68**, 849–866 (1946).

[43] M. Tang, P. C. Pistorius, and J. L. Beuth, "Prediction of lack-of-fusion porosity for powder bed fusion", Additive Manufacturing **14**, 39–48 (2017).

[44] P. Promoppatum, S.-C. Yao, P. C. Pistorius, and A. D. Rollett, "A comprehensive comparison of the analytical and numerical prediction of the thermal history and solidification microstructure of inconel 718 products made by laser powder-bed fusion", Engineering **3**, 685–694 (2017).

[45] A. V. Gusarov, I. Yadroitsev, P. Bertrand, and I. Smurov, "Model of radiation and heat transfer in laser-powder interaction zone at selective laser melting", Journal of Heat Transfer **131**, 072101 (2009).

[46] *Additive Manufacturing Process Simulation - SIMULIA User Assistance 2023*, July 2023.

[47] S. Li, X. Yang, J. Hou, and W. Du, "A review on thermal conductivity of magnesium and its alloys", Journal of Magnesium and Alloys **8**, 78–90 (2020).

[48] G. C. M. S. F. Center, *Specification for control and qualification of laser powder bed fusion metallurgical processes*, tech. rep. (National Aeronautics and Space Administration (NASA), 2017).

[49] M. Chiumenti, E. Neiva, E. Salsi, M. Cervera, S. Badia, J. Moya, Z. Chen, C. Lee, and C. Davies, "Numerical modelling and experimental validation in selective laser melting", Additive Manufacturing **18**, 171–185 (2017).

5

5

SIMULATION OF PHASE TRANSFORMATIONS DURING THE LPBF PROCESS

Additively manufactured Ti-6Al-4V parts suffer from brittle martensite phase α' formed within columnar prior-β grains. Recent experimental studies show that increasing the volumetric energy density can promote in-situ α' decomposition into $\alpha + \beta$ phases both in the LPBF and directed energy deposition (DED) processes, thus leading to the increase of ductility in Ti-6Al-4V parts. However, because the thermal history comprises numerous heating and cooling cycles and the associated phase transformation behaviors are complex, identifying the key mechanisms for α' decomposition remains challenging. In addition, simulating these repeated thermal cycles in the LPBF process poses significant computational difficulties. Therefore, in this chapter, a semi-analytical thermal model is employed to enable efficient thermal predictions for the LPBF process. Then, a temperature history to phase transformation (one-way coupled) prediction framework is introduced to simulate the phase evolution in Ti-6Al-4V. Our calculations confirm that increasing energy density decreases the amount of α' phase. When a particular layer is scanned, the α' phase is dominant regardless of the volumetric energy density due to rapid cooling. However, the deposition process of several successive layers triggers α' decomposition into α. Moreover, higher volumetric energy density leads to a higher number of successive layers to promote α' decomposition. In addition, multi-laser scanning is investigated to examine the influence of scanning strategies on phase distribution. The results indicate that different laser scanning strategies have only a limited effect on the average phase volume fraction. Our simulations reveal the α' decomposition mechanism in the LPBF process, and can further help to optimize scanning parameters—such as laser power and scanning velocity—for the microstructure of spatial variation on demand.

Parts of this chapter will be submitted to a journal.

5.1. INTRODUCTION

Laser Powder Bed Fusion (LPBF) is an additive manufacturing (AM) technique in which high-energy laser(s) selectively heat and melt metallic powder to fabricate geometrically complex and customized metal parts. In the process, CAD models of the parts are decomposed into hundreds or thousands of layers with different shapes. Then, the laser beams scan to heat, melt, and fuse metallic powder according to the 2D shape of each layer. The energy from the laser beams heats localized areas instantaneously above the material's melting point and creates melt pools in the powder bed. When the laser beams move away, melt pools rapidly solidify. In fact, the LPBF process is a complex multi-physics process involving a number of physical phenomena, such as heat transfer, fluid dynamics, phase transformations, and solid mechanics [1], which occur in different temperature ranges and together influence the final properties of additive manufactured parts. Simulation of this multi-physics process helps to optimize the process parameters and improve the part quality. In this chapter, we aimed at predicting the phase transformations and distributions in the Ti-6Al-4V LPBF process.

Among titanium alloys, Ti-6Al-4V is the most widely used alloy in metal additive manufacturing. This dominance in AM applications is attributed to its favorable combination of low density, high specific strength, excellent fatigue performance, and superior resistance to aggressive environments, which has led to its widespread adoption in aerospace, biomedical, and marine sectors [2]. Ti-6Al-4V alloy maintains a dual-phase (hexagonal close-packed alpha (α) and body centered-cubic beta (β) phases) at room temperature. The morphologies and phase volume fractions of α and β phases substantially change depending on the thermal cycles during the metal additive manufacturing process [3]. Upon cooling from the melting temperature, the high-temperature–stabilized β phase forms initially. With further decrease in temperature, rapid cooling promotes a diffusionless transformation of the β phase into α' martensite, whereas, with moderate cooling rates, the formation of the equilibrium $\alpha+\beta$ phases proceeds through a diffusion based transformation [4].

Thijs *et al.* [5] studied the effects of single-laser scanning strategies on microstructure and grain orientation. In this research, α' martensite in acicular shape was observed in the final printed parts. Xu *et al.* [6] studied the influence of laser velocity, laser power, and layer thickness on *in situ* α' martensite decomposition. In that study, the powder bed preheating to 200 °C is expected to reduce the cooling rate and increase time intervals at high temperature, which may facilitate the decomposition of α' martensite in the temperature range of 600-850 °C [7]. When adopting higher laser power (increasing the volumetric energy density), the ultrafine lamellar $\alpha+\beta$ structure from the decomposition of α' leads to both high yield strength and ductility, which are comparable with or better than those of the forged Ti-6AL-4V [6, 7]. Zafari *et al.* [8] got the same experimental results that α' decomposition occurred when higher volumetric energy density was adopted. Wei *et al.* [9] systematically investigated the microstructural evolution of Ti-6Al-4V in regions processed by multiple lasers, either scanning simultaneously or scanning in different sequences, and all fabricated samples exhibited a microstructure dominated by acicular α' martensite within the prior-β matrix, regardless of the laser scanning order. Besides, for the DED process, proper scanning strategy and process parameters can lead to in-situ decomposition of α' martensite [10]. The majority of exist-

ing studies rely on experimental investigations, in which the range of process parameter combinations and laser scanning strategies is inherently limited due to high experimental costs. Consequently, numerical simulation of the phase transformation process plays a crucial role, as it enables systematic investigation of a broader parameter space and the evaluation of diverse scanning strategies.

Simulation of Ti-6Al-4V phase transformation in rapid thermal cycles is mainly based on four types of solid phase transformations. During cooling cycles, phase transformations from β to α and from β to α' (martensite phase) occur. In contrast, during heating cycles, the reverse transformations take place, including the decomposition of α' into $\beta + \alpha$ as well as the transformation of α to β.

Upon cooling from the liquid state, β grains firstly nucleate and grow. The β phase is stable at temperatures higher than the β-transus temperature ($T_\beta = 994\,^\circ\mathrm{C}$) [11, 12]. When cooling proceeds with a low rate ($< 20\,^\circ\mathrm{C\,s^{-1}}$) below T_β, diffusion controlled β to α transformation initiates [12]. Two kinds of α phases are generated as grain boundary alpha α_{gb} the plate-like Widmanstatten alpha α_w [11]. The α_{gb} grows first at the β boundaries, and then plate-like α_w grows from the α_{gb} into the rest β phases. Grain boundary α_{gb} has a higher transformation rate at the higher temperature [11] existing around prior β grains. Furthermore, α_w can be classified into colony α_C and basket-weave α_B [13–15]. When the temperature is above the intragranular nucleation temperature $T_{IG} = 827\,^\circ\mathrm{C}$, the newly formed α_w is α_C. Otherwise, it is α_B [13]. It is found that the basket-weave α_B could help to increase the ductility of additive manufactured parts by exhibiting more interfaces between β and α phases [16], while the colony α_C leads to relatively lower ductility [17]. Rapid cooling ($> 410\,^\circ\mathrm{C\,s^{-1}}$) below martensite start temperature (T_{ms}), the β phase is transformed into α' [12]. When the cooling rates are moderate ($> 20\,^\circ\mathrm{C\,s^{-1}}$ and $< 410\,^\circ\mathrm{C\,s^{-1}}$), $\beta \rightarrow \alpha_m$ (massive alpha) transformation occurs. Usually, during the first cooling cycle from T_β in LPBF Ti-6AL-4V, there will be a significant amount of alpha martensite (α') due to the extremely fast cooling process. As the temperature rises again, some portion of the alpha martensite decomposes into $\beta+\alpha$ phases. Only part of alpha martensite could be decomposed at low temperatures, which means there will be retained martensite even when decomposition is complete at low temperature ranges. However, at high temperatures, the martensite can be fully decomposed into $\beta + \alpha$ phases. At the same time, α can also be transformed back into β since the equilibrium volume fraction of β rises at high temperatures. In this chapter, the transformations β to α and α' to $\beta+\alpha$ transformations are described by the discrete Johnson-Mehl-Avrami-Kolmogorov (JMAK) model [11, 18] in diffusion-controlled manner. On the other hand, β to α' transformation is predicted by the discrete Koistinen-Marburger (KM) model in a diffusionless manner [11, 18]. Finally, the α to β phase transformation is described by a simplified one-dimensional parabolic rate law [11, 18]. The details of these transformation models are given in Section 5.2.3. All of the phase transformation process are strongly governed by the thermal history. To simulate the temperature evolution during the LPBF process, computational models with varying levels of physical fidelity have been employed.

The computational thermal models for the LPBF process are classified as micro, meso, and macro-scale. Models at different scales have different aims. Micro- and meso-scale models provide detailed descriptions of the process physics, focusing on

powder–laser interactions, powder melting, molten pool flow, solidification, Marangoni effects, and capillary forces in the LPBF process. However, the micro and meso-scale models can be used only for the simulation of one track or several tracks due to the complexity in explicit resolution of the physics. Macro-scale (part-scale) models are primarily employed to predict the overall thermal history, residual stress, and phase distribution of additively manufactured parts. At this scale, Finite Element Method (FEM) is commonly adopted, while molten pool fluid flow and other detailed physics are neglected to substantially reduce computational costs. Consequently, part-scale models offer the highest computational efficiency at the expense of reduced accuracy in resolving thermal and stress fields.

Nevertheless, even part-scale thermal simulation of the LPBF process is challenging. To simulate the growing volume of the additive manufacturing process, the element birth and death approach [19–22] is adopted. The elements in the finite element (FE) mesh need to be activated during the simulation, thus requiring continuous update of the global thermal stiffness matrix.

Another challenge is the inherent multi-scale nature of the LPBF process. Mismatch of time scales between the solid-liquid state transformation time and total printing time is one challenge for thermal analysis in the LPBF process. The solid-liquid state transformation happens within several milliseconds [23], but the total printing process can continue for several hours. Using a time step that can resolve solid-liquid state transformation for a time integration scheme for the entire process leads to a massive number of time steps, rendering the problem computationally intractable. Besides, a mismatch of length scales between the radius of the laser spot and the part dimensions makes the problem multiscale in the spatial domain. The laser spot radius in the LPBF process ranges between 20-100 μm, while the size of additive-manufactured metal parts ranges between several millimeters to a few centimeters. To capture steep temperature gradients around the laser spot and melt pool, the spatial numerical discretization in FEM should be smaller than the radius of the laser spot. Moreover, since laser travels on the entire domain, the mesh density needs to be high everywhere, leading to an excessive number of degrees of freedom in numerical discretization.

Adaptive mesh refinement [24–28] has been proposed to further increase computational efficiency. In the method, the localised finer mesh is used to simulate the shape of melt pools and heat-affected zones (HAZs), while a coarse mesh is kept in the area away from the laser spot. The basic idea of adaptive mesh refinement is that, since the temperature field is smooth in the areas far away from the heat source, the elements can be coarsened in previously printed layers and at the base plate when the laser spot is away, thus decreasing degrees of freedom and increasing computational efficiency. As a result, accuracy in the steep temperature gradient zone is preserved, and computational efficiency is increased. This method has been widely employed in the simulation of LPBF process and DED process, while the mesh size in the first process should be much smaller and around the laser spot radius to obtain an accurate temperature distribution [24]. Nevertheless, the mesh must be frequently updated according to the laser positions in the adaptive mesh refinement.

A semi-analytical method [29–33] is proposed to alleviate the need for frequent mesh updates. In the semi-analytical method, an analytical solution of a linear heat equation

for a localised heat source in infinite or semi-infinite space is adopted to capture steep temperature gradients in the vicinity of the laser sources [29–33]. Besides, a complementary temperature field is used to impose realistic boundary conditions for a finite-sized part under consideration. So, the total solution of the temperature field is the superposition of the analytical field and the complementary field. Since steep temperature gradients are captured by the analytical solution, a smooth field of complementary solution can be solved using a coarse spatial discretization [29, 30]. Yang *et al.* [29, 30] adopted the analytical solution of point heat source and line heat source, respectively, to perform part-scale simulations. In the presented cases, the finite cell size was 0.5 mm, about 28 times of the laser spot radius. In this chapter, the semi-analytical method is adopted for fast thermal simulation of the LPBF process.

Phase proportions and spatial distributions play a critical role in determining the mechanical performance of additively manufactured Ti-6Al-4V components. The main contribution of this study is that fast thermal simulation during the entire LPBF process is achieved through the semi-analytical method. Then, the phase proportions and distributions during the entire LPBF process are predicted based on the predicted temperature histories. Finally, the key mechanisms governing phase transformations are identified, and the influences of a wide range of process parameters—including laser scanning velocity, laser power, the number of lasers, and laser scanning strategies—are systematically investigated.

The rest of this chapter is organized as follows: Section 5.2 introduces the semi-analytical method for thermal analysis and the framework of four phase transformations in the laser printing process. Section 5.3 verifies the phase transformation framework using temperature histories reproduced from the literature. Section 5.4 investigates the influence of different process parameters, the number of scanning lasers, and laser scanning strategies through numerical examples. The phase evolution during the LPBF process, as well as the resulting phase distributions after fabrication, are systematically analyzed and discussed. Section 5.5 gives the conclusions of how phase distribution is influenced under different scanning parameters and strategies.

5.2. MODEL DESCRIPTION

Consider the LPBF process of printing an arbitrary 3D part. At the start of printing a new layer, a new layer of metal powder is recoated on the already printed body V. The body V is submerged into the powder bed shown in Fig. 5.1a. The surface ∂V of body V consists of the top surface ∂V_{top}, the lateral surface ∂V_{lat}, and the bottom surface ∂V_{bot}, so that $\partial V = \partial V_{\text{top}} \cup \partial V_{\text{lat}} \cup \partial V_{\text{bot}}$, as shown in Fig. 5.1b. The top and lateral surfaces (∂V_{top} and ∂V_{top}) are covered with metal powder. The coordinate system is shown in Fig. 5.1a with part building direction along x_3-axis. As the lasers start to melt the metal powder, the governing equation for the heat conduction process can be simplified as the form

$$\rho c_p \frac{\partial T}{\partial t} = \nabla \cdot (k \nabla T) + q_{\text{v}} \quad \text{in } V, \tag{5.1}$$

where ρ is the density, c_p is the constant-pressure specific heat and k is the thermal conductivity. The three material properties are all temperature-dependent. T and q_{v} are the temperature and the rate of volumetric heat generation, respectively. Earlier studies

[32, 34–37] show the linear heat equation

$$\frac{\partial T}{\partial t} = \alpha \nabla^2 T + \frac{q_v}{\rho c_p} \quad \text{in } V \tag{5.2}$$

can well approximate the Eq. (5.1) when adopting suitable temperature-independent thermal parameters, where $\alpha = k/\rho c_p$ is the thermal diffusivity. To obtain temperature distribution in the solid domain, boundary conditions need to be applied

$$\frac{\partial T}{\partial x_i} n_i = 0 \quad \text{on } \partial V_{\text{lat}} \cup \partial V_{\text{top}}, \tag{5.3}$$

$$T = T_c \quad \text{on } \partial V_{\text{bot}}, \tag{5.4}$$

where Eq. (5.3) is the Neumann boundary condition, Eq. (5.4) is the Dirichlet boundary condition. The unit outward normal is denoted by n_i.

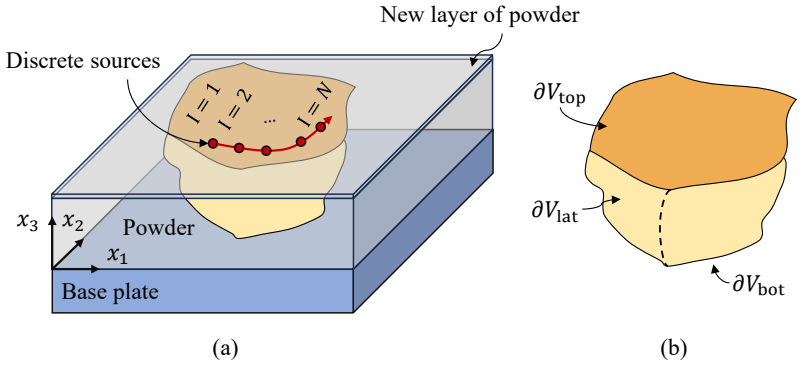

Figure 5.1: Schematic illustration of the LPBF process. (a) The laser is scanning a new layer of metal powder, and the printed body V is fused to the base plate. (b) The printed body V with its surface ∂V consisting of ∂V_{top}, ∂V_{lat} and ∂V_{bot}.

5.2.1. GAUSSIAN HEAT SOURCE MODEL

In the LPBF process, the laser spot has a finite radius and scans with a constant speed. Different heat source models including point, Gaussian, and Goldak's double ellipsoidal sources have been proposed [38–40]. In this chapter, the Gaussian heat source model is adopted with the energy density distribution as Eq. (5.5)

$$q(x_i) = \frac{4\sqrt{2}Q}{\pi\sqrt{\pi}r^3} \exp\left(-\frac{(x_i - x_{i,G}^{(\mathrm{I})})^2}{r^2}\right), \tag{5.5}$$

where q represents for the absorbed energy at the point x_i; Q is the total absorbed energy from the Gaussian source, and $x_{i,G}^{(I)}$ is the Gaussian source center, and r is the laser source radius. In the Gaussian source model, each point in the semi-infinite space absorbs non-zero energy from the laser. But most of the energy absorbed is within the limited area close to the source center.

5.2.2. SEMI-ANALYTICAL METHOD

To solve the boundary value problem (BVP) described by Eqs. (5.2–5.4), the semi-analytical method has been proposed [29, 30, 41]. the total temperature field is decomposed into

$$T = \tilde{T} + \hat{T}, \tag{5.6}$$

where $\tilde{T}$ is the analytical solution of heat sources in a semi-infinite space, and it is mainly used to capture high temperature gradients around the heat sources. Since the print part is not infinite and usually has enclosed surfaces, the $\hat{T}$ is the complementary solution to apply proper boundary conditions. For different kinds of sources, $\tilde{T}$ has different analytical forms. The analytical temperature field due to a point heat source I generated at t_0 in a semi-infinite space is

$$\tilde{T}^{(I)}(x_i, t) = \frac{q}{4\pi\alpha\rho c_p (t-t_0)^{3/2}} \exp\left(-\frac{(R^{(I)})^2}{4\alpha(t-t_0)}\right) \tag{5.7}$$

where $R^{(I)}$ is the distance between point of interest x_i and point source location $x_i^{(I)}$, t the time, q the input energy at the point $x_i^{(I)}$. Thus, the temperature field due to a Gaussian source I is acquired by substituting Eq. (5.5) into Eq. (5.7) and integrating the distributed energy of the Gaussian source as

$$\tilde{T}_G^{(I)}(x_i, t) = \frac{4\sqrt{2}Q}{\rho c_p \pi\sqrt{\pi}(8\alpha(t-t_0)+r^2)^{\frac{3}{2}}} \exp\left(-\frac{2(R_G^{(I)})^2}{8\alpha(t-t_0)+r^2}\right), \tag{5.8}$$

where $R_G^{(I)}$ is the distance between point of interest x_i and Gaussian source center $x_{i,G}^{(I)}$.

We consider a continuously scanned line with a laser source profile characterized by the Gaussian distribution. The continuous line source is first discretized into a series of discrete Gaussian heat sources. Then, the temperature field of the line scan in a semi-infinite space is written as the integration due to currently activated discrete Gaussian heat sources,

$$\tilde{T}(x_i, t) = \frac{PA}{4\rho c_p (\pi\alpha)^{3/2}} \int_{t_0}^{t_e} \frac{\exp\left(-\frac{(R_G)^2}{4\alpha(t-t_0'+t_r)}\right)}{(t-t_0'+t_r)^{3/2}} \mathrm{d}t_0', \tag{5.9}$$

where the temperature is calculated at time t, the line scanning starts at t_0 and ends at t_f. The end time for integrating the temperature fields is t_e. When $t \le t_f$, $t_e = t$. Otherwise, $t_e = t_f$. The distances between point of interest and the currently activated discrete Gaussian source centers are represented by R_G. It should be noted that Eq. (5.9) does not always lead to a closed form. However, in this chapter, we adopt straight line scanning, of which the closed form is illustrated in [30]. Besides, we assume a zero flux condition between parts and powder, and parts and air chamber. As mentioned above, the temperature at the bottom of the base plate is constant. Then, the boundary conditions in Eqs. (5.3) and (5.4) are rewritten as

$$\frac{\partial \hat{T}}{\partial x_i} n_i = -\frac{\partial \tilde{T}}{\partial x_i} n_i \quad \text{on } \partial V_{\text{lat}} \cup \partial V_{\text{top}}, \tag{5.10}$$

$$\hat{T} = T_c - \tilde{T} \quad \text{on } \partial V_{\text{bot}}. \tag{5.11}$$

5.2.3. PHASE TRANSFORMATION

After the thermal history is obtained by using the semi-analytical method, solid-state phase transformations can be evaluated. The temperature history during LPBF is subject to a series of heating and cooling cycles, it can be discretized as a series of isothermal steps. For each isothermal process, phase transformation occurs in different conditions. Besides, it is important to note that a one-way coupling is introduced, i.e., the effect of phase transformations on the temperature is neglected. As mentioned above, the transformation between solid state phases is based on four phase transformations, and the overall flow diagram for the phase transformation is shown in Fig. 5.2. Above the β-transus temperature, the β phase is stable. Therefore, once the temperature is higher than $T_\beta = 1269\,\mathrm{K}$, all other phases will be transformed to β phase. For the phase transformation over a small time interval $\Delta t = t^{(n+1)} - t^{(n)}$, the corresponding phase fractions and the temperature $T^{(n)}$ at time $t^{(n)}$ are assumed to be known. Besides, the temperature $T^{(n+1)}$ at time $t^{(n+1)}$ is known. Thus, the temperature change during the time interveal is $\Delta T = T^{(n+1)} - T^{(n)}$. Based on this information, the phase fractions at time $t^{(n+1)}$ will be calculated.

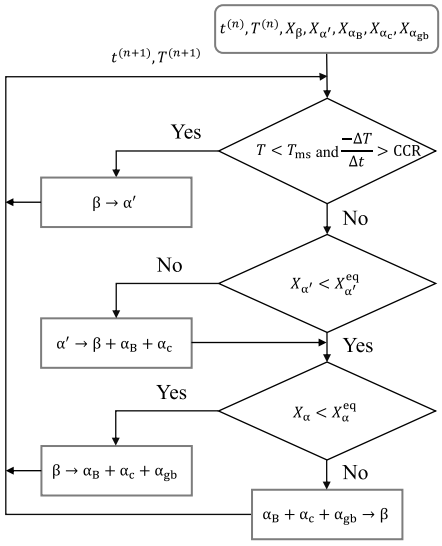

Figure 5.2: Overall phase transformation for Ti-6Al-4V in the LPBF process.

During a cooling cycle that goes below T_β, transformation from β to α_w and α_{gb} happens in a diffusion-controlled manner governed by the discrete JMAK model [11, 18]. When volume fraction of α is less than the equilibrium volume fraction of X_α^{eq}, incomplete transformation of phase α_{gb} with initial concentrations is updated by

$$X_{\alpha_{gb}}^{(n+1)} = (1 - \exp(-k_{gb}(t_c + \Delta t)^{N_{gb}}))(X_\beta^{(n)} + X_\alpha^{(n)})X_\alpha^{eq} - X_{\alpha_w}^{(n)}, \tag{5.12}$$

$$t_c = \left(-\ln\left(1 - \frac{X_\alpha^{(n)}}{X_\alpha^{eq}(X_\alpha^{(n)} + X_\beta^{(n)})}\right)/k_{gb}\right)^{\frac{1}{N_{gb}}} \tag{5.13}$$

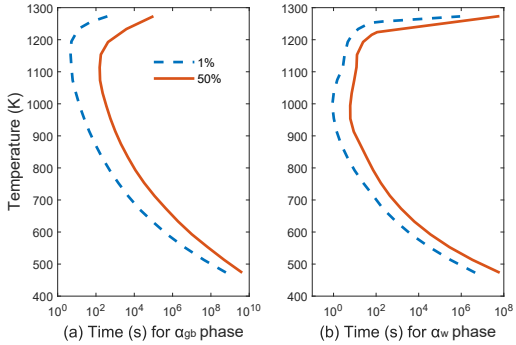

Figure 5.3: Time-temperature-transformation (TTT) diagram of Ti-6Al-4V

where $X_{\beta}^{(n)}$ is the fraction of β phase at time $t^{(n)}$ and $X_{\alpha}^{(n)}$ is the fraction of α phase including all the alpha phase variants at time $t^{(n)}$, i.e., $X_{\alpha}^{(n)} = X_{\alpha_w}^{(n)} + X_{\alpha_{gb}}^{(n)}$. The fictive time t_c represents the transformation time from no α phase to current α phase fraction $X_{\alpha}^{(n)}$ [11, 15, 42]. Besides, the current time interval $\Delta t = t^{(n+1)} - t^{(n)}$ is used for the phase transformation. The parameters k_{gb} and N_{gb} in the JMAK model are dependent on temperatures and materials. The values of the two parameters are calculated using time-temperature-transformation (TTT) diagrams shown in Fig. 5.3. The equilibrium volume fraction X_{α}^{eq} of α phase is given by [11],

$$X_{\alpha}^{eq}(T^{(n+1)}) = \sum_{i=0}^{8} \mathrm{p}(i) \left(\frac{T^{(n+1)} - 273}{1000} \right)^{8-i}. \tag{5.14}$$

The parameter $\mathrm{p} = \{-31188.514, 170526.26, 388991.69, 471927.45, 315178.49, 99079.891, 1667.1991, 9726.8403, 1884.7280\}$. The temperature $T^{(n+1)}$ is in Kelvin. Similarly, the phase α_w is updated by

$$X_{\alpha_w}^{(n+1)} = (1 - \exp(-k_c(t_w + \Delta t)^{N_w}))(X_{\beta}^{(n)} + X_{\alpha}^{(n)}) X_{\alpha}^{eq} - X_{\alpha_{gb}}^{(n)}, \tag{5.15}$$

$$t_c = \left(-\ln \left(1 - \frac{X_{\alpha}^{(n)}}{X_{\alpha}^{eq}(X_{\alpha}^{(n)} + X_{\beta}^{(n)})} \right) / k_w \right)^{\frac{1}{N_w}}. \tag{5.16}$$

When the temperature is above T_{IG}, the new generated α_w is α_C. Otherwise, it is α_B. Similarly, the parameters k_w and N_w are dependent on temperature and material, also calculated using time-temperature-transformation (TTT) diagrams shown in Fig. 5.3. The total volume fraction X_{α_w} has the relation

$$X_{\alpha_w} = X_{\alpha_B} + X_{\alpha_C}. \tag{5.17}$$

α' and α_m have similar microstructures, and the formation processes of both are all diffusionless, so we don't distinguish between α' and α_m. The transformation β to α' happens when cooling rates higher than 20 K/s as the temperatures drop below martensite

start temperature ($T_{ms} = 923\,K$ [12]). When the α martensite formation process happens, we assume that no other phase transformation can occur. The cooling rate is calculated as $CR^{(n)} = |T^{(n)} - T^{(n+1)}|/(t^{(n+1)} - t^{(n)})$ and the discrete Koistinen-Marburger model is used to describe the formation of α' phase [43]

$$X_{\alpha'}^{(n+1)} = \begin{cases} (1-\exp(-b_{KM}(T_{ms} - T^{(n)})))(X_{\beta}^{(n)} + X_{\alpha'}^{(n)}), & CR^{(n)} > 410\,K/s, \\ (1-\exp(-b_{KM}(T_{ms} - T^{(n)})))(X_{\beta}^{(n)} + X_{\alpha'}^{(n)} - X_{\beta}^{eq}), & 410\,K/s > CR^{(n)} > 20\,K/s, \end{cases} \tag{5.18}$$

where $b_{KM} = 0.005$ is dependent on material properties. X_{β}^{eq} is the equilibrium volume fraction of β phase, which satisfies the relation $X_{\beta}^{eq} + X_{\alpha}^{eq} = 1$. If the temperature is increasing or $X_{\alpha'}^{(n)}$ is greater than the equilibrium volume fraction $X_{\alpha'}^{eq}(T^{(n+1)})$, α' will dissolve back to α and β. The process is also governed by the discrete JMAK model [15]

$$X_{\alpha'}^{(n+1)} = X_{\alpha'}^{eq} + (\exp(-k_m(t_c + \Delta t)^{N_m}))(X_{\alpha'}^{(n)} + X_{\beta}^{(n)} - X_{\alpha'}^{eq}(T^{(n+1)})), \tag{5.19}$$

$$X_{\alpha'}^{eq}(T^{(n+1)}) = 0.5(1 + \tanh\frac{T_A - T^{(n+1)}}{80}), \tag{5.20}$$

$$t_c = \left(-\ln\left(\frac{x_{\alpha'}^{(n)} - x_{\alpha'}^{eq}}{x_{\alpha'}^{(n)} + x_{\beta}^{(n)} - x_{\alpha'}^{eq}}\right)/K_m\right)^{\frac{1}{N_m}}, \tag{5.21}$$

$$k_m(T^{(n+1)}) = \begin{cases} C_1 T^{(n+1)} + C_2, & T^{(n+1)} < 500\,°C, \\ C_3 T^{(n+1)} + C_4, & T^{(n+1)} \geq 500\,°C, \end{cases} \tag{5.22}$$
$$C_1 = -4.58 \times 10^{-5}, C_2 = 1.04,$$
$$C_3 = 5.40 \times 10^{-5}, C_4 = 0.99,$$

$$N_m(T^{(n+1)}) = \begin{cases} C_5 T^{(n+1)} + C_6, & T^{(n+1)} < 500\,°C, \\ C_7 T^{(n+1)} + C_8 & T^{(n+1)} \geq 500\,°C, \end{cases} \tag{5.23}$$
$$C_5 = -4.39 \times 10^{-3}, C_6 = -1.09,$$
$$C_7 = 7.33 \times 10^{-4}, C_8 = 0.74,$$

where $T_A = 450\,°C$, k_m and N_m are the parameters for the JMAK model in α' dissolution process. Following the same process in [13], the decreased α' is transformed back into α_w and β described by the equation

$$X_{\alpha_w}^{(n+1)} = X_{\alpha_w}^{(n)} + (X_{\alpha'}^{(n)} - X_{\alpha'}^{(n+1)})X_{\alpha}^{eq}, \tag{5.24}$$
$$X_{\beta}^{(n+1)} = X_{\beta}^{(n)} + (X_{\alpha'}^{(n)} - X_{\alpha'}^{(n+1)})X_{\beta}^{eq}. \tag{5.25}$$

Similarly, when the temperature is above T_{IG}, the newly generated α_w is α_C. Otherwise, it is α_B. If α phase volume fraction is larger than the equilibrium X_{α}^{eq}, α phase is transformed into β phase in a one dimensional parabolic rate way as follows:

$$X_{\alpha}^{(n+1)} = \begin{cases} 1 - X_{\beta}^{eq} f_{diss}(T^{(n)})\sqrt{t^* + \Delta t}, & 0 < t^* + \Delta t < t_{crit}, \\ 1 - X_{\beta}^{eq} & t^* + \Delta t > t_{crit}, \end{cases} \tag{5.26}$$

where

$$t^* = \left(\frac{X_\beta^{(n)}}{X_\beta^{\text{eq}} f_{\text{diss}}(T^{(n)})} \right)^2,$$
$$t_{\text{crit}} = \left(\frac{1}{f_{\text{diss}}(T^{(n)})} \right)^2,$$
$$f_{\text{diss}}(T^{(n)}) = 2.2 \times 10^{-31} (T^{(n)})^{9.89}.$$

Also, if the temperature is below T_{IG}, only α_{B} will be transformed into β. If the temperature is above T_{IG}, α_{B} and α_{C} will be transformed with the proportion of $X_{\alpha_{\text{B}}}^{(n)}/(X_{\alpha_{\text{B}}}^{(n)} + X_{\alpha_{\text{C}}}^{(n)})$ and $X_{\alpha_{\text{C}}}^{(n)}/(X_{\alpha_{\text{B}}}^{(n)} + X_{\alpha_{\text{C}}}^{(n)})$. When there is no α_{B} and α_{C}, phase α_{gb} will be consumed [13].

5.3. VERIFICATION OF PHASE TRANSFORMATION FRAMEWORK

In this section, the proposed phase transformation framework is verified through the comparison of the time evolution of solid-state phases. A cyclic thermal history from Babu *et al.* [44] between 273 K and 1473 K, shown in Fig. 5.4, is widely adopted for verification of phase transformation models [11, 13, 15]. Fig. 5.4 illustrates volume fraction histories of different phases from [13, 15] and the predictions in this chapter, where a good agreement is observed. At the start of the thermal history, the volume fraction of α_{w} phase ($X_{\alpha_{\text{w}}}$) is around 0.9 at room temperature. As temperature increases, $X_{\alpha_{\text{w}}}$ decreases rapidly, and no α_{w} exists when the temperature is above T_β. Consequently, only β phase exists with $X_\beta = 1$. When the temperature begins to decrease in the first cooling cycle, β phase is transformed into α_{w} and α_{gb}. Since α_{w} phase grows faster than α_{gb} phase during cooling stages, the volume fraction of α_{w} phase significantly exceeds that of α_{gb} phase. As the temperature continues to decrease and drops below T_{ms}, since the cooling rate is higher than 20 K/s, α' forms. So, there exists a mixture of multiple phases including $\alpha_{\text{w}}, \alpha_{\text{gb}}, \alpha'$ and β when the temperature finally cools down to 350 K. Next, the temperature increases in the second heating cycle, and α martensite decomposes into α_{w} and β. As a result, there is a slight increase of α_{w} phase when α' phase dissolves completely. Then, with the temperature increasing continuously, all the α_{w} and α_{gb} phases are transformed into the β phase again. For the rest thermal cycles, similar phase transformations occur. However, due to the continuous decrease of cooling rates in the subsequent cycles, there is no α' generated in the rest of cooling process. In all, there are three sets of curves for phase $\alpha_{\text{w}}, \alpha_{\text{gb}}$ and α'. Different models give similar phase change histories with a few small differences. The small differences, for example α_{w} in the second cycle, can come from approximations of phase transformation curves in the different models. In the next section, the phase transformation model is used for volume fraction prediction of solid-state phases during LPBF.

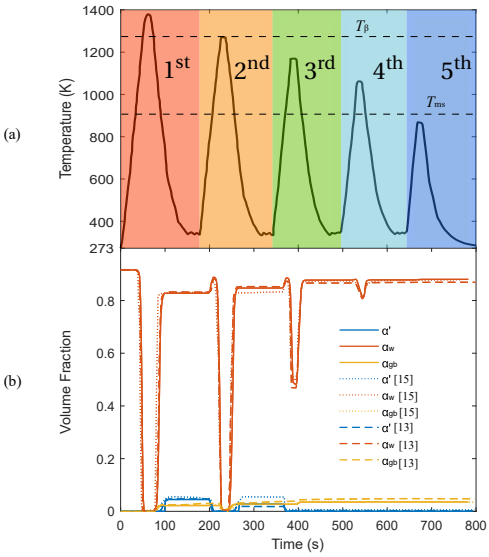

Figure 5.4: (a) Temperature history with five thermal cycles for verification of phase transformation models (extracted from Babu *et al.* [44]). (b) Predicted phase transformation histories and comparison of results with the literature [13, 15].

5.4. NUMERICAL EXAMPLES AND RESULTS

After the verification of the phase transformation framework, we adopt two numerical examples to simulate the phase transformation history and the solid phase's volume fraction distributions during the LPBF process. In the first case, different scanning strategies and process parameters, including laser power and scanning velocity, are studied on a simple cuboid. Different phase distributions are acquired based on different temperature histories. The second case comprises a simulation of a bridge-shaped part to investigate the effect of part geometry on the phase distribution.

Table 5.1: Laser scanning parameters used for the cuboid.

Group	1 [45]	2	3	4	5
Laser power (P, W)	95	186	248	310	496
Scanning velocity (v, m/s)	0.6	1	1	1	2
Absorption rate (A)	0.4	1	1	1	1
Layer thickness (t, μm)	40	60	60	60	60
Hatching space (h, μm)	100	100	100	100	100
Volumetric energy density (E_v, J/mm^3)	15.8	31.0	41.3	51.7	41.3
Interlayer time (s)	10	10	10	10	10

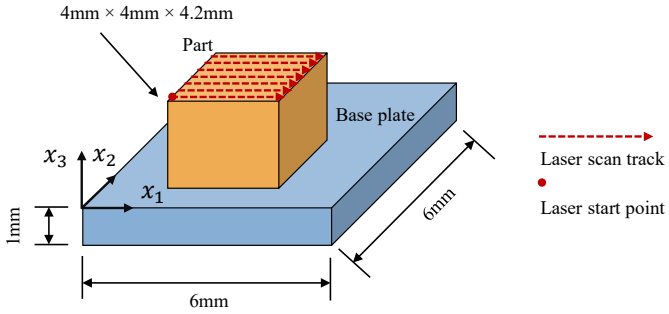

Figure 5.5: Cuboid geometry for the simulation of phase distribution, the part is additively manufactured on top of the base plate.

5.4.1. SCANNING OF A CUBOID CASE

We consider a 4 mm × 4 mm × 4.2 mm cuboid to be additive manufactured on a 6 mm × 6 mm × 1 mm base plate as shown in Fig. 5.5. The temperature at the bottom surface of the base plate is kept constant at $T = 200\,^{\circ}\mathrm{C}$. All other faces of the base plate, i.e, the top surface and the lateral surfaces of the part, are considered as adiabatic. Five sets of process parameters listed in Table 5.1 are studied. Group 1 was fabricated with a layer thickness of 40 μm, resulting in a total of 105 scanned layers for a build height of 4.2 mm. In contrast, Groups 2–5 employed a layer thickness of 60 μm, corresponding to 70 scanned layers. The process parameters in Group 1 are identical to those reported in [45], which correspond to the lowest volumetric energy density. In Groups 2 to 4, the laser power is progressively increased, while all other process parameters are kept the same as those in [6]. Consequently, the volumetric energy density increases from Groups 1 to 4. For Group 5, the laser scanning power and velocity were both doubled compared to those in Group 3, with all other parameters maintained at the same values. Therefore, the energy densities in Groups 3 and 5 are identical.

PHASE DISTRIBUTIONS AT DIFFERENT CROSS SECTIONS

Volume fractions of different phases, at the end of AM process, obtained under various scanning parameters are summarized in Table 5.2 (phase distributions on bottom cross section in $x_1 - x_2$ plane, Layer 1) and Table 5.3 (phase distributions on the cross section at the height of 1.8 mm, Layer 45 for Group 1, Layer 30 for Groups 2 - 5). In Table 5.2, when we employ the scanning parameters in Group 1, the volumetric energy density E_v is the smallest among all the groups. The average α phase fraction has its smallest fraction, $X_\alpha = 0.0065$, while the average α' martensite phase fraction has its largest fraction $X_{\alpha'} = 0.82$. With E_v increasing from Group 1 to Group 4, it can be found that the average α phase fraction (X_α) increases, while the average α martensite phase fraction ($X_{\alpha'}$) decreases with increasing E_v. The model predictions are consistent with the observation that increasing volumetric energy density leads to more α phase in Ti-6Al-4V LPBF experiments [6]. When comparing the average phase fractions of Group 3 and Group 5, it is observed that although Group 5 employs doubled laser power and scanning velocity relative to Group 3, the volumetric energy density remains identical between the two groups. Consequently, the resulting average phase fractions in Group 5 are nearly

Table 5.2: Phase volume fraction at the bottom cross section (Layer 1) for different process parameters using the single laser scanning strategy.

	Group 1 $E_v = 15.8\,J/mm^3$	Group 2 $E_v = 31.0\,J/mm^3$	Group 3 $E_v = 41.3\,J/mm^3$	Group 4 $E_v = 51.7\,J/mm^3$	Group 5 $E_v = 41.3\,J/mm^3$
Phase	Volume fraction: 0.0 0.2 0.4 0.6 0.8 1.0				
α	$X_\alpha = 0.0065$	0.17	0.28	0.40	0.26
α'	$X_{\alpha'} = 0.82$	0.67	0.55	0.43	0.56
β	$X_\beta = 0.17$	0.16	0.16	0.16	0.18

identical to those observed in Group 3. This suggests that, under conditions of constant volumetric energy density, variations in laser power and scanning speed exert minimal influence on the average volume fractions of the α and α' phases. For all groups, the average β phase fraction (X_β) stays almost the same around 0.17, which almost does not change with respect to the volumetric energy density E_v.

The trend of the average volume fraction of different phases at the cross section with the height of 1.8 mm, shown in Table 5.3, is almost the same as that at the bottom cross section in all groups. It should be noted that the cross section with height of 1.8 mm corresponds to Layer 45 in Group 1 and Layer 30 in other groups due to different layer thickness as given in Table 5.1. From Group 1 to Group 4, the average α phase fraction (X_α) increases, while the average α martensite phase fraction ($X_{\alpha'}$) decreases with more input energy E_v. The average phase fractions of α and α' phase (X_α and X'_α) in Groups 3 are the same as those in Group 5. For all groups, the average β phase fraction (X_β) is almost the same.

However, when we compare the average phase fractions between the bottom cross section in $x_1 - x_2$ plane and the cross section at the height of 1.8 mm under the same process parameters, the average α martensite phase fraction ($X_{\alpha'}$) decreases, and the average α phase fraction (X_α) increases. For example, in Group 3 where $E_v = 41.3\,J/mm^3$

Table 5.3: Phase volume fraction in the cross section at the height of 1.8 mm (Layer 45 for Group 1 and Layer 30 for other groups due to different layer thickness shown in Table 5.1) using the single laser scanning strategy.

	Group 1 $E_v = 15.8\text{J/mm}^3$	Group 2 $E_v = 31.0\text{J/mm}^3$	Group 3 $E_v = 41.3\text{J/mm}^3$	Group 4 $E_v = 51.7\text{J/mm}^3$	Group 5 $E_v = 41.3\text{J/mm}^3$
Phase	Volume fraction: 0.0 0.2 0.4 0.6 0.8 1.0				
α	$X_\alpha = 0.0093$	0.21	0.40	0.61	0.37
α'	$X_{\alpha'} = 0.82$	0.58	0.42	0.25	0.45
β	$X_\beta = 0.17$	0.21	0.18	0.14	0.18

as shown in Table 5.1, the average α phase fraction (X_α) is 0.28 and the average volume fraction of the α' phase is 0.55 in the bottom cross section (Layer 1), shown in Table 5.2. Besides, the average α phase fraction (X_α) is 0.40, and the average volume fraction of the α' phase is 0.42 in the cross section at the height of 1.8 mm (Layer 45 in Group 1, and Layer 30 for other groups), shown in Table 5.3. These results indicate that layers at different heights exhibit different phase distributions. This is because the section with the height of 1.8 mm is away from the base plate. So, the cooling rates are smaller, leading higher number of successive layer depositions triggering α martensite decomposition, accounting for more α phases. Details of this process will be explained in Section 5.4.1.

Therefore, in addition to giving phase distributions of cross sections at different heights, we also provide phase distributions for a vertical cross section, as shown in Table 5.4. Here, the phase distributions using process parameters in Group 5 are not given since the average phase fractions are almost the same as those in Group 3. From the phase distributions observed in the vertical cross section, it is evident that the volume fraction of the α phase increases with increasing volumetric energy density, whereas the volume fraction of the α' martensite phase correspondingly decreases as the volumetric energy density increases. Additionally, for the phase distributions in Group 1, there are two distinct lines on either side of the vertical cross-section. At the two lines, the α phase

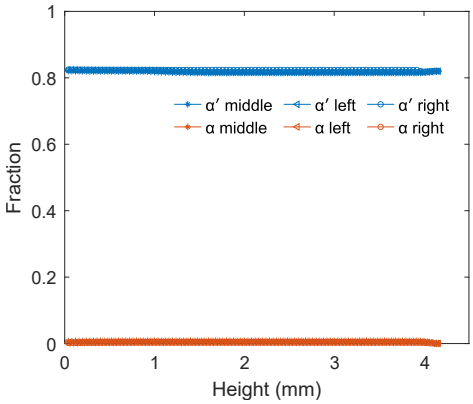

(a) Group 1, $E_v = 15.8 \text{J/mm}^3$.

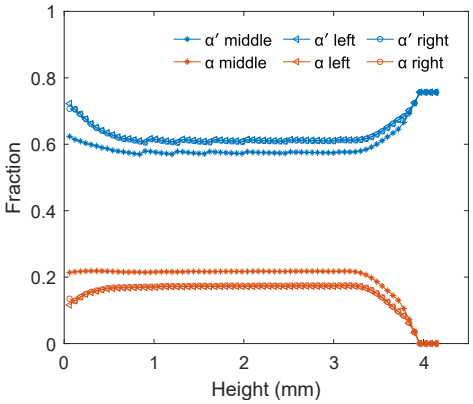

(b) Group 2, $E_v = 31.0 \text{J/mm}^3$.

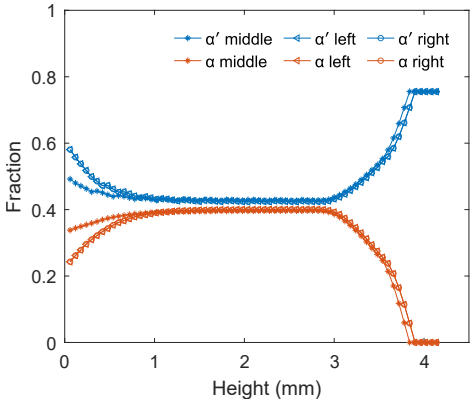

(c) Group 3, $E_v = 41.3 \text{J/mm}^3$.

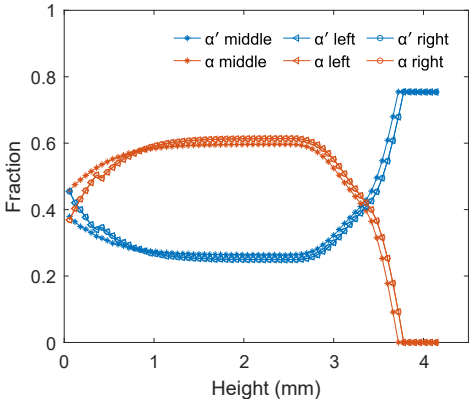

(d) Group 4, $E_v = 51.7 \text{J/mm}^3$.

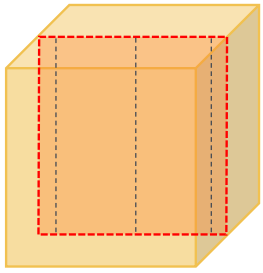

(e) Position of the three lines.

Figure 5.6: α phase distribution in three vertical lines under different volumetric energy densities.

Table 5.4: Vertical α distribution on the middle vertical plane under different scanning parameters.

	Group 1 $E_v = 15.8 J/mm^3$	Group 2 $E_v = 31.0 J/mm^3$	Group 3 $E_v = 41.3 J/mm^3$	Group 4 $E_v = 51.7 J/mm^3$
Phase	Volume fraction: 0.0 0.2 0.4 0.6 0.8 1.0			
α	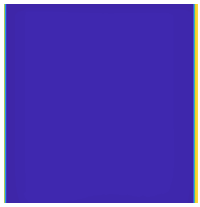			
α'	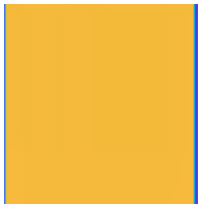			
β	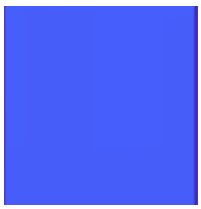			

volume fraction is at maximum around 0.9, where the β phase volume fraction is around 0.1. This occurs because the volumetric energy density in Group 1 is too low for the material at the two edges to melt or even reach T_β. As a result, only two phases are present, which are nearly identical to those in the initial state. To better analyze the phase distributions along the vertical direction, the phase fractions along three representative vertical lines are shown in Fig. 5.6. For Groups 2-4, along the building direction, the α phase volume fraction firstly increases and then decreases for Groups 2 to 4. At the same time, the α' phase volume fraction firstly decreases and then increases. This is because the deposition of the next several layers leads to the decomposition of α martensite into α phases. And, for the last several layers at the top part of the cuboid, there are not enough successive layers to be printed, as a result of which, the α phase volume fraction decreases, and the α' phase volume fraction increases in the last several layers. Details of this process will be given in Section 5.4.1. Moreover, with a higher volumetric energy

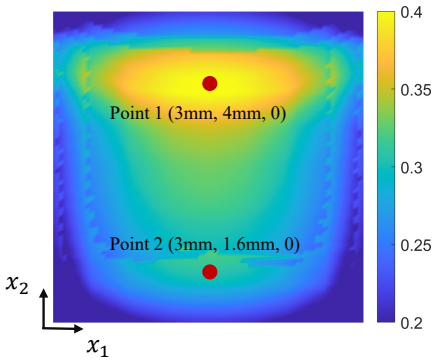

Figure 5.7: Position of point 1 and point 2 at the bottom cross section and α phase distribution with Group 3 scanning parameters $E_v = 41.3\text{J/mm}^3$.

density, the martensite-dominated section is thicker. For Group 1, since the volumetric energy density is too low and the decomposition of the α' phase is negligible henceforth, the α and α' phase volume fractions almost do not change in the building direction.

PHASE TRANSFORMATIONS DURING THE LPBF PROCESS

To gain insight into the evolution of phase transformations during the additive manufacturing process, we examine the phase transformation behavior at two representative locations on the bottom cross section in $x_1 - x_2$ plane (Layer 1), as indicated in Fig. 5.7. After completing the additive manufacturing process of the cuboid using the Group 3 scanning parameters, the α phase in on the bottom cross section (Layer 1) exhibits a non-uniform spatial distribution, with a maximum volume fraction of approximately 0.4. Moreover, the α phase fraction at Point 1 is notably higher than that at Point 2. This behavior arises because the laser scans from the front to the back side of the cuboid, as shown in Fig. 5.5. Heat therefore accumulates at the back side, leading to a relatively larger decomposition of martensite. Subsequently, the evolution of phase fractions, especially the decomposition of martensite, at these two points is tracked after the deposition of each subsequent layer, as shown in Fig. 5.8a. Immediately after the deposition of Layer 1, the martensite phase fraction ($X_{\alpha'}$) reaches a peak value of approximately 0.8, while the α phase fraction (X_α) remains near zero. As additional layers are scanned, X_α gradually increases at the expense of $X_{\alpha'}$, indicating a continuous transformation from the martensite α' phase to the stable α phase. A similar trend is observed for the two points as shown Fig. 5.8b with the Group 4 scanning parameters applied. However, with higher volumetric energy E_v in Group 4, the increase in the α phase fraction is more pronounced, and the corresponding decrease in the martensite phase fraction is greater. This is because, with higher volumetric energy density E_v, more energy from successive deposition processes leads to the decomposition of α' martensite phase in Layer 1. Moreover, due to more heat accumulated at Point 2, there are more critical layers for α' martensite decomposition, e.g., 20 layers in Group 3 and 22 layers in Group 4, as shown in Fig. 5.8. Details of this decomposition process will be discussed.

To analyze the effect of scanning of subsequent layers on the temperature history

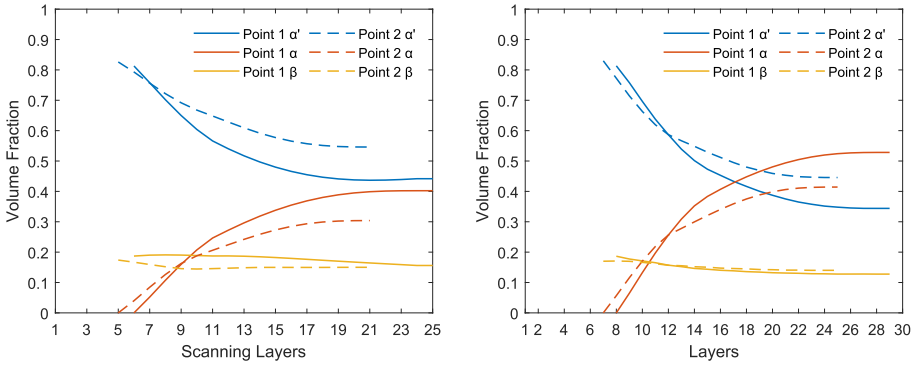

(a) Group 3, $E_v = 41.3\text{J/mm}^3$, for point 1, the layers to determine the microstructure distribution are from 6 to 25, totally 20 layers. For point 2, the layers to determine the microstructure distribution are from 5 to 21, totally 17 layers.

(b) Group 4, $E_v = 51.7\text{J/mm}^3$, for point 1, the layers to determine the microstructure distribution are from 8 to 29, totally 22 layers. For point 2, the layers to determine the microstructure distribution are from 7 to 25, totally 19 layers.

Figure 5.8: Phase volume fraction change for points 1 and 2 at the bottom cross section (a) with Group 3 ($E_v = 41.3\text{J/mm}^3$) and (b) with Group 4 ($E_v = 51.7\text{J/mm}^3$) scanning parameters.

and microstructure, the phase transformations at Point 1 with respect to time are shown in Fig. 5.9 ($E_v = 41.3\text{J/mm}^3$) and Fig. 5.10 ($E_v = 51.7\text{J/mm}^3$). In Fig. 5.9, during the deposition of Layer 6, the temperature at Point 1 rises above the β-transus temperature (T_β) for the final time, where all α phases transform to the β phase when the temperature reaches its peak. With the subsequent rapid cooling process, most of the β are transformed into α' phase with approximately 20% retained β phase. As Layer 7 is being scanned, during the temperature increase cycle, only part of the α' phase is transformed into the high temperature phase, while part of the α' is transformed into the α phase. The subsequent cooling cycle again transforms approximately 80% of the β into α', while the volume fraction of α phase stays intact. Consequently, the amount of α' continuously decreases with every subsequent layer scanning until Layer 21 where the temperature changes are no longer capable of inducing any phase transformations. As a comparison, for the higher $E_v = 51.7\text{J/mm}^3$ case in Fig. 5.10, the layer number for full recovery to β phase and the final layer which increases the volume fraction of α are 8 and 23, respectively. Moreover, due to the higher volumetric energy density, cooling rates diminish, allowing for more α' phase to transform to α phase. In other words, more heat from subsequent layers is available for the α' to α transformation.

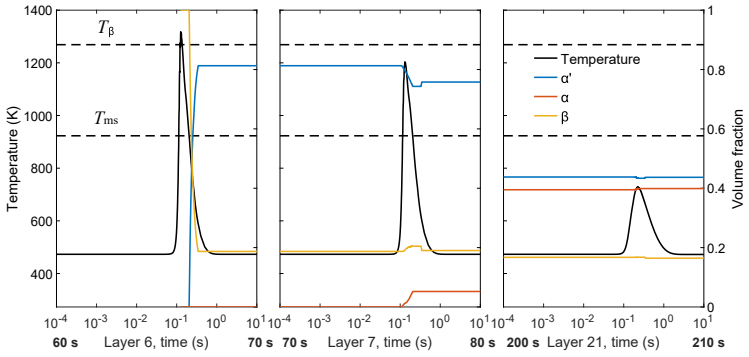

Figure 5.9: Evolution of temperature and volume fraction of phases histories at Point 1 on Layer 1 with E_v = 41.3J/mm^3 process parameters under single laser scanning strategy when Layer 6, Layer 7, and Layer 21 are scanned.

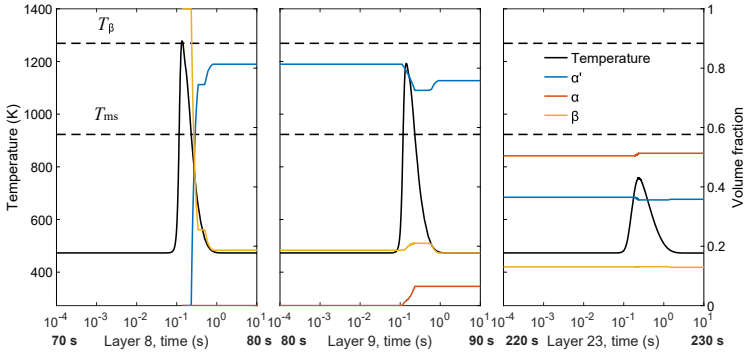

Figure 5.10: Evolution of temperature and volume fraction of phases histories at Point 1 on Layer 1 with E_v = 51.7J/mm^3 process parameters under single laser scanning strategy when Layer 8, Layer 9, and Layer 23 are scanned.

5.4.2. MULTI-LASER SCANNING

In the previous section, the cuboid geometry was built using a single laser, and the corresponding phase distributions were analyzed. This section extends the study to simultaneous scanning with multiple lasers. Different laser scanning strategies are shown in Fig. 5.11. Scanning strategy (a) represents the single laser scanning used in the previous section and is included for comparison. Strategies (b)–(d) involve two lasers, differing in their respective starting points and scanning directions. Strategy (e) considers simultaneous scanning with four lasers. The phase distribution and average phase volume fraction at the bottom cross section under different scanning strategies are shown in Table 5.5. Although different scanning strategies are adopted, it can be found that there is almost no change of average α phase X_α and average α martensite phase $X_{\alpha'}$. This is due to, as heat is conducted to the bottom printed layers, the temperature field within a bottom layer becomes more uniform. The sequence of laser scanning is not important anymore and leads to a similar warming-up effect in the bottom layers.

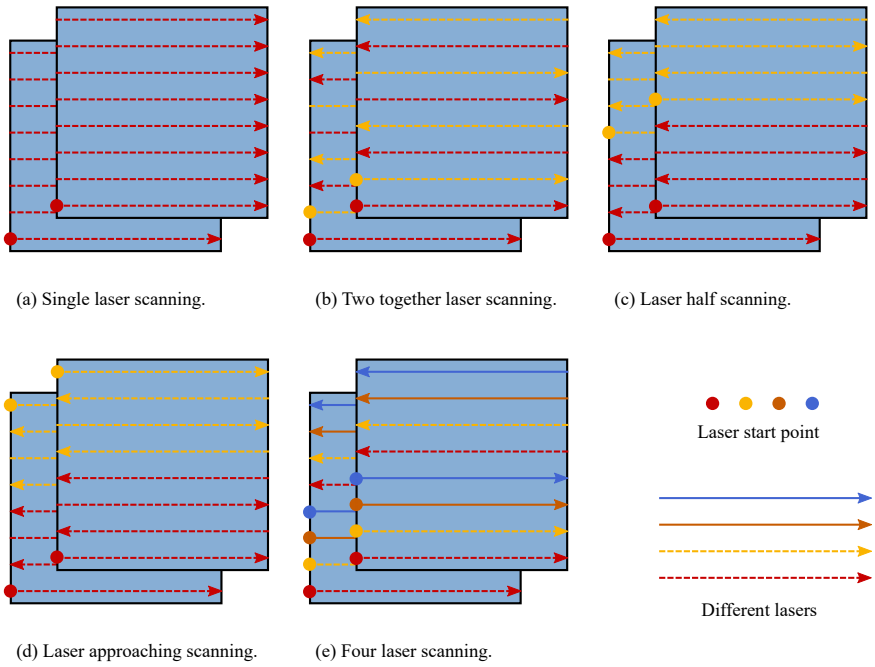

(a) Single laser scanning. (b) Two together laser scanning. (c) Laser half scanning.

(d) Laser approaching scanning. (e) Four laser scanning.

Figure 5.11: Laser scanning strategies involving different numbers of lasers.

Table 5.5: Phase volume fraction at bottom cross section for different scanning strategies (a), (b), (c), (d), (e) and (f) with scanning parameter Group 3 ($E_v = 41.3 J/mm^3$) and Group 4 ($E_v = 51.7 J/mm^3$)

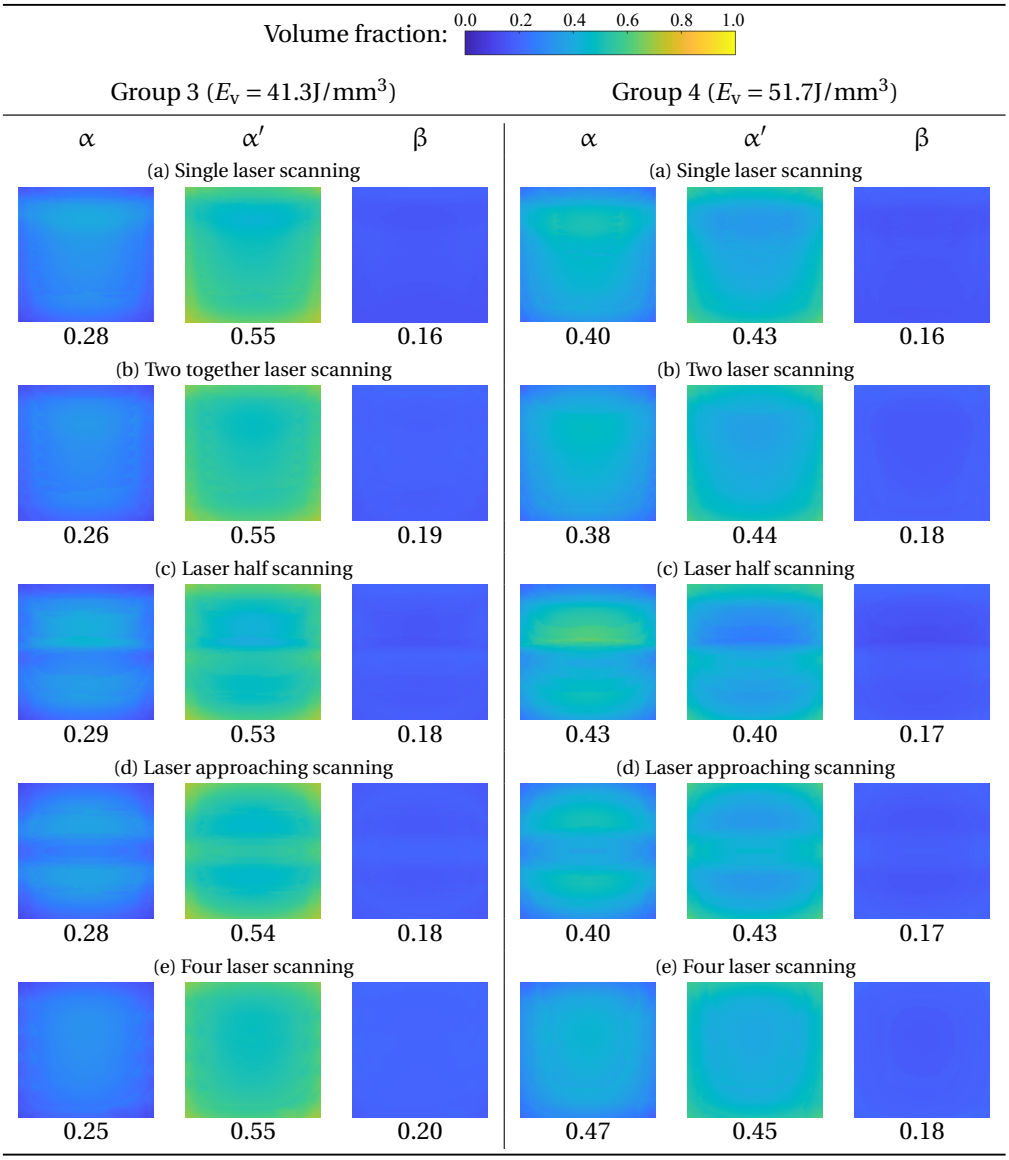

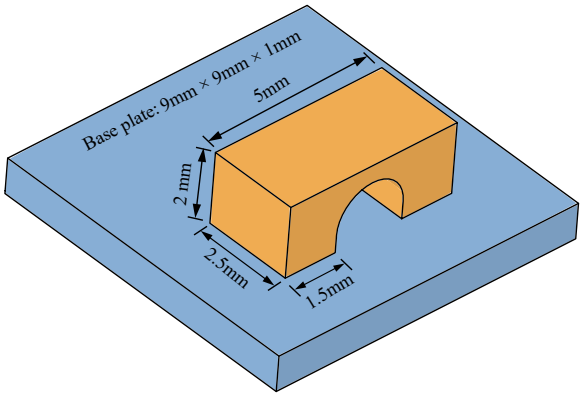

Figure 5.12: Bridge geometry for the simulation of phase transformations and distributions, the bridge is additively manufactured on top of the base plate.

5.4.3. BRIDGE CASE

In the previous section, phase transformations and their spatial distributions were examined in a simple cubic part. In this section, we extend the analysis to the LPBF process for a component with a more complex geometry—a bridge-shaped part—to investigate how geometry influences the resulting phase evolution and distribution. As shown in Fig. 5.12, the bridge is 2 mm high with a semi-circle hole with radius of 1 mm inside. This bridge is also built on a base plate of 9 mm × 9 mm × 1 mm. Because the geometry considered here is irregular, FEM is employed to resolve the complementary field, as indicated in Eqs. (5.6), (5.10) and (5.11). The corresponding FE mesh is shown in Fig. 5.13. As discussed in Section 5.1, the analytical solutions for point and line heat sources adequately capture the steep temperature gradients in the vicinity of the laser spot(s), eliminating the need for dynamically refined meshes that track laser motion. However, within the semi-analytical framework adopted for solving the heat conduction problem, the outgoing heat flux remains finite when the laser spot(s) approach the boundaries of the part. Consequently, mesh refinement is required near the boundaries at a length scale comparable to the laser spot radius. This requirement leads to a mesh that is relatively fine along the part boundaries and comparatively coarse within the interior of the bridge, as illustrated in Fig. 5.13.

The α' martensite phase distribution for the whole bridge after the entire building process is shown Fig. 5.14. Similar to the cubic case, the bridge also exhibits a martensite-dominated region near the top surface, as no subsequent layer deposition occurs to induce the decomposition of the martensite. In the middle layers of the bridge, the α' is comparably lower. Moreover, in the bottom cross sections, the martensite fraction increases again because these layers are closer to the base plate and therefore experience more rapid cooling. These trends are consistent with those observed for the cubic part, as shown in Fig. 5.6. However, it can be observed that martensite accumulates near the top of the semicircular region, where its fraction is noticeably higher. This occurs because, during deposition on top of the semicircle, no underlying solid material

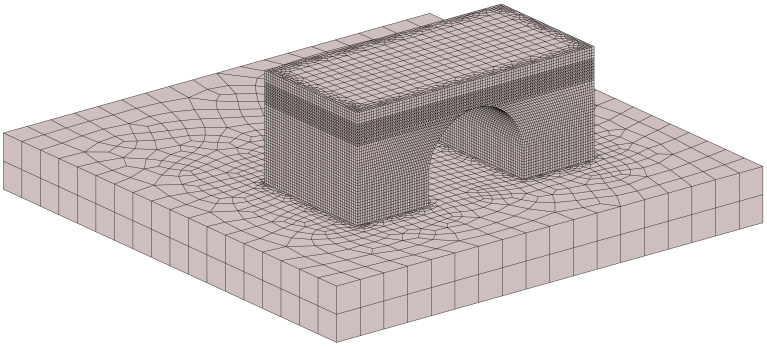

Figure 5.13: Mesh for the thermal simulation of the bridge additive manufacturing process, 64125 nodes with 42468 linear hexahedral elements (C3D8 in ABAQUS) and 57985 linear tetrahedral elements (C3D4 in ABAQUS).

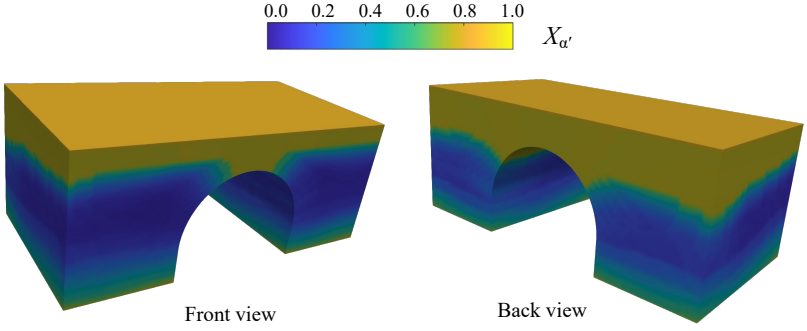

Figure 5.14: α' martensite distribution for the bridge after printing under $E_v = 41.3 \text{J/mm}^3$.

is present to facilitate effective heat dissipation. As a result, heat accumulates, and the local temperature repeatedly exceeds the β transus temperature with the deposition of subsequent layers. Upon cooling, the material in this region consistently transforms into the martensite phase. Moreover, the front side shows less martensite phase accumulation than that at the back side in Fig. 5.14. This phenomenon occurs because, in a single-layer deposition process, the laser scan path progresses from the front side to the back side of the component, leading to greater heat accumulation in the latter. Each preceding scan effectively preheats subsequent scan tracks within the same layer. As a result, a larger portion of the back side of the part reaches the β-transus temperature, and more martensite phase accumulates at the back side.

5.5. CONCLUSIONS

This chapter presents an integrated approach that combines a semi-analytical thermal analysis with a microstructure transformation framework to predict phase evolution and spatial phase distributions during the LPBF process. In the semi-analytical method, the temperature field is described by the superposition of an analytical solution of line sources in semi-infinite space and a complementary solution for realistic boundary conditions. In addition, within the microstructure transformation framework, the solid-state phase transformation process is described by four fundamental transformation processes.

It can be concluded that, with volumetric energy density increasing, average α phase fraction X_α increases and average α' martensite phase fraction $X_{\alpha'}$ decreases in the middle layers of final additively manufactured parts. However, also due to higher volumetric energy density, the thickness of the martensite-dominated top part in the last printed layers increases. The key mechanism for the Ti-6Al-4V phase transformation during the LPBF process is that the α' martensite phase will always form initially due to high cooling rates. As a result, when the scanning process of the current layer is finished, α' martensite phase always accounts for the highest proportions. Then, the heat from the deposition process of the next several layers leads to the decomposition of α martensite phase into the $\alpha+\beta$ phases. Thus, the volume fraction of the α phase increases. The distribution of volume fraction for each phase in one cross section is closely related to the total layers accounted for phase transformations, which indicates that, for different points in the same cross section, more layers for α' martensite decomposition lead to more fraction of α phase. Since the different laser scanning strategies lead to similar warming-up effects and relative uniform temperature increase in bottom layers, for the multi-laser scanning process, there is a minor difference in the average volume fraction of α phase and α' martensite phase among different cases. Moreover, at a constant volumetric energy density, proportional changes in laser power and scanning velocity also result in negligible differences in the average phase fractions. For the bridge part with overhang geometry, martensite phases tend to accumulate in the overhang area as a result of localized heat accumulation that raises the temperature above the β-transus, followed by rapid cooling from the β-transus temperature.

BIBLIOGRAPHY

[1] T. DebRoy, H. Wei, J. Zuback, T. Mukherjee, J. Elmer, J. Milewski, A. M. Beese, A. d. Wilson-Heid, A. De, and W. Zhang, "Additive manufacturing of metallic components–process, structure and properties", Progress in Materials Science **92**, 112–224 (2018).

[2] S. Pradhan, S. Singh, C. Prakash, G. Królczyk, A. Pramanik, and C. I. Pruncu, "Investigation of machining characteristics of hard-to-machine ti-6al-4v-eli alloy for biomedical applications", Journal of Materials Research and Technology **8**, 4849–4862 (2019).

[3] L. Bian, S. M. Thompson, and N. Shamsaei, "Mechanical properties and microstructural features of direct laser-deposited ti-6al-4v", Jom **67**, 629–638 (2015).

[4] S. Liu and Y. C. Shin, "Additive manufacturing of ti6al4v alloy: a review", Materials & Design **164**, 107552 (2019).

[5] L. Thijs, F. Verhaeghe, T. Craeghs, J. Van Humbeeck, and J.-P. Kruth, "A study of the microstructural evolution during selective laser melting of ti–6al–4v", Acta materialia **58**, 3303–3312 (2010).

[6] W. Xu, M. Brandt, S. Sun, J. Elambasseril, Q. Liu, K. Latham, K. Xia, and M. Qian, "Additive manufacturing of strong and ductile ti–6al–4v by selective laser melting via in situ martensite decomposition", Acta Materialia **85**, 74–84 (2015).

[7] W. Xu, E. W. Lui, A. Pateras, M. Qian, and M. Brandt, "In situ tailoring microstructure in additively manufactured ti-6al-4v for superior mechanical performance", Acta Materialia **125**, 390–400 (2017).

[8] A. Zafari, M. Barati, and K. Xia, "Controlling martensitic decomposition during selective laser melting to achieve best ductility in high strength ti-6al-4v", Materials Science and Engineering: A **744**, 445–455 (2019).

[9] K. Wei, F. Li, G. Huang, M. Liu, J. Deng, C. He, and X. Zeng, "Multi-laser powder bed fusion of ti–6al–4v alloy: defect, microstructure, and mechanical property of overlap region", Materials Science and Engineering: A **802**, 140644 (2021).

[10] T. Song, T. Dong, S. Lu, K. Kondoh, R. Das, M. Brandt, and M. Qian, "Simulation-informed laser metal powder deposition of ti-6al-4v with ultrafine α-β lamellar structures for desired tensile properties", Additive Manufacturing **46**, 102139 (2021).

[11] C. C. Murgau, R. Pederson, and L.-E. Lindgren, "A model for ti–6al–4v microstructure evolution for arbitrary temperature changes", Modelling and Simulation in Materials Science and Engineering **20**, 055006 (2012).

[12] T. Ahmed and H. Rack, "Phase transformations during cooling in α+ β titanium alloys", Materials Science and Engineering: A **243**, 206–211 (1998).

[13] W. Sun, F. Shan, N. Zong, H. Dong, and T. Jing, "A simulation and experiment study on phase transformations of ti-6al-4v in wire laser additive manufacturing", Materials & Design **207**, 109843 (2021).

[14] C. Baykasoglu, O. Akyildiz, D. Candemir, Q. Yang, and A. C. To, "Predicting microstructure evolution during directed energy deposition additive manufacturing of ti-6al-4v", Journal of Manufacturing Science and Engineering **140**, 10.1115/1.4038894 (2018).

[15]C. Baykasoğlu, O. Akyildiz, M. Tunay, and A. C. To, "A process-microstructure finite element simulation framework for predicting phase transformations and microhardness for directed energy deposition of ti6al4v", Additive Manufacturing **35**, 101252 (2020).

[16]Y. Ren, X. Lin, X. Fu, H. Tan, J. Chen, and W. Huang, "Microstructure and deformation behavior of ti-6al-4v alloy by high-power laser solid forming", Acta Materialia **132**, 82–95 (2017).

[17]Z. Zhao, J. Chen, X. Lu, H. Tan, X. Lin, and W. Huang, "Formation mechanism of the α variant and its influence on the tensile properties of laser solid formed ti-6al-4v titanium alloy", Materials Science and Engineering: A **691**, 16–24 (2017).

[18]L.-E. Lindgren, A. Lundbäck, M. Fisk, R. Pederson, and J. Andersson, "Simulation of additive manufacturing using coupled constitutive and microstructure models", Additive Manufacturing **12**, 144–158 (2016).

[19]I. Roberts, C. Wang, R. Esterlein, M. Stanford, and D. Mynors, "A three-dimensional finite element analysis of the temperature field during laser melting of metal powders in additive layer manufacturing", International Journal of Machine Tools and Manufacture **49**, 916–923 (2009).

[20]A. Olleak and Z. Xi, "Part-scale finite element modeling of the selective laser melting process with layer-wise adaptive remeshing for thermal history and porosity prediction", Journal of Manufacturing Science and Engineering **142**, 121006 (2020).

[21]P. Michaleris, "Modeling metal deposition in heat transfer analyses of additive manufacturing processes", Finite Elements in Analysis and Design **86**, 51–60 (2014).

[22]A. Mechanical, "R2, advanced analysis guide", ANSYS® Academic Research Mechanical (2019).

[23]R. Cunningham, C. Zhao, N. Parab, C. Kantzos, J. Pauza, K. Fezzaa, T. Sun, and A. D. Rollett, "Keyhole threshold and morphology in laser melting revealed by ultrahigh-speed x-ray imaging", Science **363**, 849–852 (2019).

[24]E. R. Denlinger, J. Irwin, and P. Michaleris, "Thermomechanical modeling of additive manufacturing large parts", Journal of Manufacturing Science and Engineering **136** (2014).

[25]E. R. Denlinger, M. Gouge, J. Irwin, and P. Michaleris, "Thermomechanical model development and in situ experimental validation of the laser powder-bed fusion process", Additive Manufacturing **16**, 73–80 (2017).

[26]Y. Zhang, G. Guillemot, M. Bernacki, and M. Bellet, "Macroscopic thermal finite element modeling of additive metal manufacturing by selective laser melting process", Computer Methods in Applied Mechanics and Engineering **331**, 514–535 (2018).

[27]C. Li, E. R. Denlinger, M. F. Gouge, J. E. Irwin, and P. Michaleris, "Numerical verification of an octree mesh coarsening strategy for simulating additive manufacturing processes", Additive Manufacturing **30**, 100903 (2019).

[28]K. Zeng, D. Pal, H. Gong, N. Patil, and B. Stucker, "Comparison of 3dsim thermal modelling of selective laser melting using new dynamic meshing method to ansys", Materials Science and Technology **31**, 945–956 (2015).

[29]Y. Yang, M. Knol, F. van Keulen, and C. Ayas, "A semi-analytical thermal modelling approach for selective laser melting", Additive Manufacturing **21**, 284–297 (2018).

[30]Y. Yang, F. van Keulen, and C. Ayas, "A computationally efficient thermal model for selective laser melting", Additive Manufacturing **31**, 100955 (2020).

[31]J. C. Steuben, A. J. Birnbaum, J. G. Michopoulos, and A. P. Iliopoulos, "Enriched analytical solutions for additive manufacturing modeling and simulation", Additive Manufacturing **25**, 437–447 (2019).

[32]J. Ning, E. Mirkoohi, Y. Dong, D. E. Sievers, H. Garmestani, and S. Y. Liang, "Analytical modeling of 3d temperature distribution in selective laser melting of ti-6al-4v considering part boundary conditions", Journal of Manufacturing Processes **44**, 319–326 (2019).

[33]T. Moran, D. Warner, and N. Phan, "Scan-by-scan part-scale thermal modelling for defect prediction in metal additive manufacturing", Additive Manufacturing **37**, 101667 (2021).

[34]D. Rosenthal, "The theory of moving sources of heat and its application of metal treatments", Transactions of ASME **68**, 849–866 (1946).

[35]M. Tang, P. C. Pistorius, and J. L. Beuth, "Prediction of lack-of-fusion porosity for powder bed fusion", Additive Manufacturing **14**, 39–48 (2017).

[36]P. Promoppatum, S.-C. Yao, P. C. Pistorius, and A. D. Rollett, "A comprehensive comparison of the analytical and numerical prediction of the thermal history and solidification microstructure of inconel 718 products made by laser powder-bed fusion", Engineering **3**, 685–694 (2017).

[37]T. Childs, M. Berzins, G. Ryder, and A. Tontowi, "Selective laser sintering of an amorphous polymer—simulations and experiments", Proceedings of the Institution of Mechanical Engineers, Part B: Journal of Engineering Manufacture **213**, 333–349 (1999).

[38]N. Nguyen, A. Ohta, K. Matsuoka, N. Suzuki, and Y. Maeda, "Analytical solutions for transient temperature of semi-infinite body subjected to 3-d moving heat sources", WELDING JOURNAL-NEW YORK- **78**, 265–s (1999).

[39]Y. Yang and X. Zhou, "A volumetric heat source model for thermal modeling of additive manufacturing of metals", Metals **10**, 1406 (2020).

[40]Z. Zhang, Y. Huang, A. R. Kasinathan, S. I. Shahabad, U. Ali, Y. Mahmoodkhani, and E. Toyserkani, "3-dimensional heat transfer modeling for laser powder-bed fusion additive manufacturing with volumetric heat sources based on varied thermal conductivity and absorptivity", Optics & Laser Technology **109**, 297–312 (2019).

[41]Y. Yang, X. Zhou, Q. Li, and C. Ayas, "A computationally efficient thermo-mechanical model for wire arc additive manufacturing", Additive Manufacturing **46**, 102090 (2021).

[42]J. W. Christian, *The theory of transformations in metals and alloys* (Newnes, 2002).

[43]D. P. Koistinen, "A general equation prescribing the extent of the austenite-martensite transformation in pure iron-carbon alloys and plain carbon steels", Acta metallurgica **7**, 59–60 (1959).

[44] S. Babu, S. Kelly, E. Specht, T. Palmer, and J. Elmer, "Measurement of phase transformation kinetics during repeated thermal cycling of ti-6al-4v using time-resolved x-ray diffraction", in International conference on solid-solid phase transformations in inorganic materials 2005 (2005).

[45] W. Zhang, M. Tong, and N. M. Harrison, "Scanning strategies effect on temperature, residual stress and deformation by multi-laser beam powder bed fusion manufacturing", Additive Manufacturing **36**, 101507 (2020).

6

6

Conclusions and Recommendations

6.1. CONCLUSIONS

Additive manufacturing exhibits exceptional potential for producing components with highly intricate geometries, including topology-optimized structures and meta-materials. Among metal additive manufacturing technologies, the LPBF offers the highest precision for fabricating fine and complex metallic parts. Nevertheless, defects generated during the LPBF process lead to substantial uncertainties in the resulting material properties and potentially cause failure. Consequently, accurate thermal simulation is essential for predicting temperature evolution, optimizing LPBF process parameters, and mitigating defect formation.

In this thesis, a semi-analytical approach is adopted, which utilizes analytical solutions of heat conduction for point or line heat sources in a semi-infinite domain. This formulation eliminates the need for dynamic mesh motion to follow the laser path and obviates the use of adaptive mesh refinement required in conventional finite element methods. Therefore, the number of degrees of freedom in the thermal simulation is reduced. However, appropriate boundary conditions must still be enforced, as the printed part in the LPBF process has finite dimensions. To this end, a complementary field is introduced to correct the boundary conditions, and this field is typically solved using FEM. Existing studies indicate that resolving the complementary field often requires a highly refined mesh near the part boundaries, owing to the steep temperature gradients that develop as the laser spot approaches these regions.

The semi-analytical method for thermal simulation developed in this work is first enhanced by incorporating image-source techniques for curved boundaries. The use of image sources with analytical closed forms enables coarser spatial discretization near part boundaries, thereby reducing the computational cost associated with numerically resolving steep thermal gradients. However, the applicability of the imaging method is restricted to specific geometrical configurations and cannot be readily extended to arbitrarily complex boundary shapes. To overcome this limitation, a more general formulation is introduced by computing the complementary field with isogeometric analysis (IGA) instead of FEM that has been used so far. Owing to the exact geometric representation and higher-order continuity provided by NURBS basis functions, the number of degrees of freedom required in the complementary-field computation can be reduced by approximately an order of magnitude.

The improved semi-analytical framework is then applied to a triangular-prism part geometry manufactured from a magnesium alloy, demonstrating how geometric constraints substantially intensify localized overheating in LPBF. As the scan-vector length decreases toward the tip of the prism, the shortened cycle time leads to rapid heat accumulation, resulting in a pronounced increase in melt-pool depth. Conversely, extremely short vectors do not provide adequate heating duration, producing an abrupt reduction in melt-pool depth near the tip. Two mitigation strategies—introducing zero-power ghost vectors and implementing a linear reduction of laser power with respect to scan-vector length—are shown to effectively homogenize melt-pool depth and suppress porosity formation except in the close proximity of the tip. Perfect quantitative agreement is observed between the simulations and experiments.

Finally, the influence of volumetric energy density on microstructural evolution in Ti-6Al-4V is examined. Variations in laser power and scanning speed directly affect the

cooling rates and consequently modify the resulting ductile α and brittle α' (martensitic) phase fractions. Under a larger volumetric energy density, a greater proportion of α' formed in prior layers is decomposed into α, owing to the additional heat input from successive layer depositions. In contrast, across the final layers of the part, the martensitic fraction remains relatively high. This is attributed to the absence of successive layer deposition, which leads to a lack of additional annealing that would otherwise promote the decomposition of martensitic phases.

Overall, the proposed semi-analytical framework is computationally efficient and effective in predicting the transient thermal behavior in the LPBF process. The resulting temperature histories enable accurate prediction of melt-pool geometry and facilitate the mitigation of overheating-related phenomena. Furthermore, the temperature fields obtained from the semi-analytical framework can be employed to predict phase transformations and the spatial distributions of solid-state phases, thereby allowing systematic optimization of scanning parameters based on these predictions.

6.2. RECOMMENDATIONS

Several limitations remain in the present work. Within the proposed semi-analytical framework, temperature-independent thermal properties are assumed. This simplification may lead to discrepancies in the predicted temperature histories when compared with models incorporating temperature-dependent material properties. Such differences may be non-negligible for certain physical phenomena, such as thermal stress evolution, while their impact may be less significant for others. Therefore, a systematic sensitivity analysis with respect to the assumption of temperature-independent thermal properties is required, depending on the targeted physical predictions.

Additionally, the boundary between the solid part and the surrounding metal powder is assumed to be adiabatic. However, in practice, thermal conduction across this interface does occur, which may also introduce deviations in the computed temperature histories. Moreover, radiation is not directly considered, and convection is neglected.

Based on the findings of this thesis, several directions are recommended for future research. First, the IGA-based study indicates that coarser spatial discretizations can achieve accuracy comparable to that of FEM. This observation suggests that adaptive mesh refinement within the IGA framework could be further exploited to enhance computational efficiency. Such an approach would facilitate the realistic heat transfer, including temperature-dependent thermal properties, heat conduction between the solid part and the metal powder, convection, and radiation.

As discussed above, the proposed semi-analytical framework may be further extended to the prediction of thermal stresses, strains, and distortions that arise during the LPBF process. Standard benchmark problems can be employed to validate these predictions, while systematic comparisons with experimental measurements and numerical simulation models incorporating temperature-dependent material properties are essential for assessing the accuracy and robustness of the proposed method. In addition, experimental investigations of phase distributions under various scanning strategies and process parameters would provide valuable data for validating and refining the thermal and metallurgical models developed in this work.

Furthermore, the increasing prevalence of Artificial Intelligence (AI) techniques in

additive manufacturing offers promising opportunities for future development. The complementary field in the semi-analytical method could potentially be approximated through AI-based surrogate models, inputting process parameters and part geometries. Such models may significantly reduce computational cost while maintaining satisfactory accuracy. Finally, AI-driven optimization of LPBF process parameters represents another promising avenue, enabling systematic exploration of the high-dimensional process space, including laser power, scan speed, hatch spacing, scan strategy, preheated temperature, powder characteristics, material properties, and so on, to improve part quality, minimize defects, and enhance overall manufacturing efficiency.

APPENDIX

APPENDIX A. DERIVATION OF TEMPERATURE FIELD DUE TO GAUSSIAN SOURCE

We introduce the time delay $r^2/8\alpha$ for a point source to represent a 3D Gaussian laser source. Mathematically, the temperature fields are the same due to the two kinds of sources. Firstly, consider a point source with the time delay, Eq. (2.7) is written as

$$\tilde{T}^{(I)}(x_i,t)=\frac{QA}{4\rho c_p(\pi\alpha(t-\tilde{t}^{(I)}+r^2/8\alpha))^{\frac{3}{2}}}\exp\left(\frac{-(R^{(I)})^2}{4\alpha(t-\tilde{t}^{(I)}+r^2/8\alpha)}\right). \tag{A.1}$$

Now, we consider a 3D Gaussian source activated at $t=\tilde{t}^{(I)}$ with energy distribution as

$$q(x_i)=\frac{2Q}{\sigma^3\pi\sqrt{\pi}}\exp\left(-\frac{(R^{(I)})^2}{\sigma^2}\right). \tag{A.2}$$

$x_i^{(I)}$ is the center of the Gaussian source. The distance between the point of interest and the Gaussian source center is $R^{(I)}$. $\sigma=r/\sqrt{S_f}$, and r is the laser spot radius. The Gaussian source's shape factor, determining the energy concentration, is denoted with S_f. The temperature distribution due to the Gaussian source is by integration of the temperature field of the distributed input energy

$$T(x_i,t)=\frac{2QA}{\sigma^3\pi\sqrt{\pi}}$$
$$\int_{-\infty}^{\infty}\int_{-\infty}^{\infty}\int_{-\infty}^{x_3^{(I)}}\exp\left(-\frac{(x_1'-x_1^{(I)})^2+(x_2'-x_2^{(I)})^2+(x_3'-x_3^{(I)})^2}{\sigma^2}\right)\frac{\exp(\frac{-(R')^2}{4\alpha(t-\tilde{t}^{(I)})})}{4\rho c_p(\pi\alpha(t-\tilde{t}^{(I)}))^{\frac{3}{2}}}\mathrm{d}x_1'\mathrm{d}x_2'\mathrm{d}x_3', \tag{A.3}$$

where

$$R'=\sqrt{(x_1-x_1')^2+(x_2-x_2')^2+(x_3-x_3')^2}. \tag{A.4}$$

The integration has the close-form

$$T(x_i,t)=\frac{2QA}{\rho c_p\pi\sqrt{\pi}}\frac{1}{(4\alpha(t-\tilde{t}^{(I)})+\sigma^2)^{(3/2)}}\exp\left(\frac{-(R^{(I)})^2}{4\alpha(t-\tilde{t}^{(I)})+\sigma^2}\right). \tag{A.5}$$

When $S_f=2$, Eq. (A.5) is the same as Eq. (A.1).

APPENDIX B. DERIVATION OF MODULATION FACTOR

A net zero heat loss through the arc segment of θ_0 near the regular source can be achieved. At the point on the arc boundary with θ_0, the temperature decreased to e^{-3} of the temperature at point p Fig. 2.5. This value is chosen to capture high-temperature zones and make subsequent derivation easy. Certainly, the ratio of the temperatures between the two points can be smaller with larger θ_0. The points on the boundary segment with $x_1=R_c\cos\theta$ and $x_2=R_c\sin\theta$, the heat loss rate across the boundary segment due

to the regular source I at time t is written as an integral

$$\tilde{g}^{(I)}(\theta_0,t)=\int_0^{\theta_0}\frac{\nu}{(t-\tilde{\tau}^{(I)})^{(3/2)}} \exp\left(\frac{-(R_c\cos\theta-\tilde{x}_1^{(I)})^2-(R_c\sin\theta-\tilde{x}_2^{(I)})^2}{4\alpha(t-\tilde{\tau}^{(I)})}\right)\left(\frac{-2\tilde{x}_1^{(I)}R_c\cos\theta-2\tilde{x}_2^{(I)}R_c\sin\theta+2R_c^2}{4\alpha(t-\tilde{\tau}^{(I)})R_c}\right)R_c\mathrm{d}\theta. \tag{B.1}$$

Since the regular source I is located at $(R_c-d,0,0)$. Then, Eq. (B.1) becomes

$$\tilde{g}^{(I)}(\theta_0,t)=\int_0^{\theta_0}\frac{\nu}{(t-\tilde{\tau}^{(I)})^{(3/2)}}\exp\left(\frac{-(R_c-d)^2-R_c^2+2R_c(R_c-d)\cos\theta}{4\alpha(t-\tilde{\tau}^{(I)})}\right)\left(\frac{-(R_c-d)R_c\cos\theta+R_c^2}{2\alpha(t-\tilde{\tau}^{(I)})}\right)\mathrm{d}\theta. \tag{B.2}$$

Integrating the heat loss rate of the line along the x_3 direction yields

$$\begin{aligned}\tilde{\phi}^{(I)}(\theta_0,t)&=\tilde{g}^{(I)}(\theta_0,t)\int_{-\infty}^{\tilde{x}_3^{(I)}}\exp\left(\frac{-(x_3-\tilde{x}_3^{(I)})^2}{4\alpha(t-\tilde{\tau}^{(I)})}\right)\mathrm{d}x_3\\&=\sqrt{\pi\alpha(t-\tilde{\tau}^{(I)})}\tilde{g}^{(I)}(\theta_0,t),\end{aligned} \tag{B.3}$$

where $-\infty$ and $\tilde{x}_3^{(I)}$ are the lower and upper limits of the integral. Similarly, for the image source J located at $(R_c+d,0,0)$, the heat loss rate across the boundary segment due to the image source J at time t is

$$\tilde{g}^{(J)}(\theta_0,t)=\int_0^{\theta_0}\frac{\epsilon^{(J)}\nu}{(t-\check{\tau}^{(J)})^{(3/2)}}\exp\left(\frac{-(R_c+d)^2-R_c^2+2R_c(R_c+d)\cos\theta}{4\alpha(t-\check{\tau}^{(J)})}\right)\left(\frac{-(R_c+d)R_c\cos\theta+R_c^2}{2\alpha(t-\check{\tau}^{(J)})}\right)\mathrm{d}\theta. \tag{B.4}$$

the integration of the heat loss rate through the same boundary area is written as

$$\begin{aligned}\check{\phi}^{(J)}(\theta_0,t)&=\check{g}^{(J)}(\theta_0,t)\int_{-\infty}^{\check{x}_3^{(J)}}\exp\left(\frac{-(x_3-\check{x}_3^{(J)})^2}{4\alpha(t-\check{\tau}^{(J)})}\right)\mathrm{d}x_3,\\&=\sqrt{\pi\alpha(t-\check{\tau}^{(J)})}\check{g}^{(J)}(\theta_0,t).\end{aligned} \tag{B.5}$$

The activation time of regular source I and image source J are identical, (i.e. $\check{\tau}^{(J)}=\tilde{\tau}^{(I)}$ in Eqs. (B.3) and (B.5)). For both regular and image sources, the heat loss rate proportionally changes in the x_3 direction. When $|\check{\phi}^{(J)}|=|\tilde{\phi}^{(I)}|$, the net heat loss rate over the boundary segment is zero, and the adiabatic boundary conditions are achieved on average. However, we need to integrate the heat loss rate in time to enforce a net zero heat loss over time. For the regular source I, integrate the heat loss rate of the lateral surface in Eq. (B.3) on a time duration

$$\tilde{\Phi}^{(I)}=\int_{t_s}^{t_e}\int_0^{\theta_0}\frac{\nu\sqrt{\pi\alpha}}{t-\tilde{\tau}^{(I)}}\exp\left(\frac{-(R_c-d)^2-R_c^2+2R_c(R_c-d)\cos\theta}{4\alpha(t-\tilde{\tau}^{(I)})}\right)\left(\frac{-(R_c-d)R_c\cos\theta+R_c^2}{2\alpha(t-\tilde{\tau}^{(I)})}\right)\mathrm{d}\theta\mathrm{d}t, \tag{B.6}$$

where t_s is the starting time for heat loss calculation, and t_e is the end time. t_s and t_e should capture the period when steep temperature gradients happen on the part boundary due to the laser sources. We propose the integral bounds as $t_s=\tilde{\tau}^{(I)}+d^2/10\alpha$ and

$t_e = \tilde{\tau}^{(I)} + d^2/\alpha$. At $t = t_e$, the flux at $(R_c, 0)$ decreases to less than 5% of its peak value at $t = t_s$ from Eq. (2.18). After t_f, the temperature field due to the regular source is sufficiently smooth to be captured numerically. For the image source, the heat loss within a time duration is written as

$$\breve{\Phi}^{(J)} = \int_{t_s}^{t_e}\int_0^{\theta_0} \frac{\epsilon^{(J)} \nu\sqrt{\pi\alpha}}{t-\breve{\tau}^{(J)}} \exp\left(\frac{-(R_c+d)^2 - R_c^2 + 2R_c(R_c+d)\cos\theta}{4\alpha(t-\breve{\tau}^{(J)})}\right)\left(\frac{-(R_c+d)R_c\cos\theta + R_c^2}{2\alpha(t-\breve{\tau}^{(J)})}\right) \mathrm{d}\theta\mathrm{d}t. \tag{B.7}$$

To enforce $|\tilde{\Phi}^{(I)}| = |\breve{\Phi}^{(J)}|$ for the approximate adiabatic boundary conditions, $\epsilon^{(J)}$ is given as

$$\epsilon^{(J)} = \left| \frac{\displaystyle\int_{t_s}^{t_e}\int_0^{\theta_0} \frac{\nu\sqrt{\pi\alpha}}{t-\tilde{\tau}^{(I)}} \exp\left(\frac{-(R_c-d)^2 - R_c^2 + 2R_c(R_c-d)\cos\theta}{4\alpha(t-\tilde{\tau}^{(I)})}\right)\left(\frac{-(R_c-d)R_c\cos\theta + R_c^2}{2\alpha(t-\tilde{\tau}^{(I)})}\right) \mathrm{d}\theta\mathrm{d}t}{\displaystyle\int_{t_s}^{t_e}\int_0^{\theta_0} \frac{\nu\sqrt{\pi\alpha}}{t-\breve{\tau}^{(J)}} \exp\left(\frac{-(R_c+d)^2 - R_c^2 + 2R_c(R_c+d)\cos\theta}{4\alpha(t-\breve{\tau}^{(J)})}\right)\left(\frac{-(R_c+d)R_c\cos\theta + R_c^2}{2\alpha(t-\breve{\tau}^{(J)})}\right) \mathrm{d}\theta\mathrm{d}t} \right|. \tag{B.8}$$

The $\epsilon^{(J)}$ in Eq. (B.8) is simplified as:

$$\epsilon^{(J)} = \left| \frac{\displaystyle\int_{t_s}^{t_e}\int_0^{\theta_0} \frac{1}{t-\tilde{\tau}^{(I)}} \exp\left(\frac{-(R_c-d)^2 - R_c^2 + 2R_c(R_c-d)\cos\theta}{4\alpha(t-\tilde{\tau}^{(I)})}\right)\left(\frac{-(R_c-d)R_c\cos\theta + R_c^2}{2\alpha(t-\tilde{\tau}^{(I)})}\right) \mathrm{d}\theta\mathrm{d}t}{\displaystyle\int_{t_s}^{t_e}\int_0^{\theta_0} \frac{1}{t-\breve{\tau}^{(J)}} \exp\left(\frac{-(R_c+d)^2 - R_c^2 + 2R_c(R_c+d)\cos\theta}{4\alpha(t-\breve{\tau}^{(J)})}\right)\left(\frac{-(R_c+d)R_c\cos\theta + R_c^2}{2\alpha(t-\breve{\tau}^{(J)})}\right) \mathrm{d}\theta\mathrm{d}t} \right|. \tag{B.9}$$

Assuming $t_0 = \tilde{\tau}^{(I)} = \breve{\tau}^{(J)}$. Then, $t_s - t_0 = \frac{d^2}{10\alpha}$, $t_e - t_0 = \frac{d^2}{\alpha}$.

$$\epsilon^{(J)} = \left| \frac{\displaystyle\int_{t_s}^{t_e}\int_0^{\theta_0} \frac{1}{t-t_0} \exp\left(\frac{-d^2}{4\alpha(t-t_0)}\right)\exp\left(\frac{R_c(R_c-d)(\cos\theta-1)}{2\alpha(t-t_0)}\right)\left(\frac{-(R_c-d)R_c\cos\theta + R_c^2}{2\alpha(t-t_0)}\right) \mathrm{d}\theta\mathrm{d}t}{\displaystyle\int_{t_s}^{t_e}\int_0^{\theta_0} \frac{1}{t-t_0} \exp\left(\frac{-d^2}{4\alpha(t-t_0)}\right)\exp\left(\frac{R_c(R_c+d)(\cos\theta-1)}{2\alpha(t-t_0)}\right)\left(\frac{-(R_c+d)R_c\cos\theta + R_c^2}{2\alpha(t-t_0)}\right) \mathrm{d}\theta\mathrm{d}t} \right|. \tag{B.10}$$

The ratio of integrated heat flux due to a regular source and an image source $\epsilon^{(J)}(t)$ at time t is written as

$$\epsilon^{(J)}(t) = \left| \frac{\displaystyle\int_0^{\theta_0} \frac{1}{t-t_0} \exp\left(\frac{R_c(R_c-d)(\cos\theta-1)}{2\alpha(t-t_0)}\right)\left(\frac{-(R_c-d)R_c\cos\theta + R_c^2}{2\alpha(t-t_0)}\right) \mathrm{d}\theta}{\displaystyle\int_0^{\theta_0} \frac{1}{t-t_0} \exp\left(\frac{R_c(R_c+d)(\cos\theta-1)}{2\alpha(t-t_0)}\right)\left(\frac{-(R_c+d)R_c\cos\theta + R_c^2}{2\alpha(t-t_0)}\right) \mathrm{d}\theta} \right|, \tag{B.11}$$

and defining the term $\tilde{L}^{(I)}(t,\theta_0)$ and $\breve{L}^{(J)}(t,\theta_0)$ as

$$\tilde{L}^{(I)}(t,\theta_0) = \int_0^{\theta_0} \exp\left(\frac{R_c(R_c-d)(\cos\theta-1)}{2\alpha(t-t_0)}\right)\left(\frac{-(R_c-d)R_c\cos\theta + R_c^2}{2\alpha(t-t_0)}\right) \mathrm{d}\theta, \tag{B.12}$$

$$\breve{L}^{(J)}(t,\theta_0) = \int_0^{\theta_0} \exp\left(\frac{R_c(R_c+d)(\cos\theta-1)}{2\alpha(t-t_0)}\right)\left(\frac{-(R_c+d)R_c\cos\theta + R_c^2}{2\alpha(t-t_0)}\right) \mathrm{d}\theta. \tag{B.13}$$

Eq. (B.12) is rewritten as

$$\tilde{L}^{(I)}(\mu,\theta_0) = \int_0^{\theta_0} \exp\big(\mu(\cos\theta-1)\big)\left(-\mu\cos\theta + \frac{R_c^2}{2\alpha(t-t_0)}\right) \mathrm{d}\theta, \tag{B.14}$$

where $\mu = \frac{R_c(R_c-d)}{2\alpha(t-t_0)}$. To determine the upper bound of the integration, define

$$\tilde{M}^{(I)}(\theta) = \exp\left(\frac{R_c(R_c-d)(\cos\theta-1)}{2\alpha(t-t_0)}\right), \tag{B.15}$$

θ_0 satisfy the criteria

$$\frac{\tilde{M}^{(I)}(\theta_0)}{\tilde{M}^{(I)}(0)} = \exp\left(\frac{R_c(R_c-d)(\cos\theta_0-1)}{2\alpha(t-t_0)}\right) = e^{-3}. \tag{B.16}$$

Then,

$$\frac{R_c(R_c-d)(\cos\theta_0-1)}{2\alpha(t-t_0)} = -3, \tag{B.17}$$

which is

$$\mu(\cos\theta_0-1) = -3. \tag{B.18}$$

Let $p = \mu(-\cos\theta+1)$, then Eq. (B.14) is rewritten as

$$\tilde{L}^{(I)} = \int_0^{\mu(-\cos\theta_0+1)} e^{-p}\left(p + \frac{R_c d}{2\alpha(t-t_0)}\right)\frac{\mathrm{d}p}{\mu\sin\theta}, \tag{B.19}$$

where $\cos\theta = 1-\frac{p}{\mu}$ and $\sin\theta = \frac{\sqrt{2p\mu-p^2}}{\mu}$, and $\tilde{L}^{(I)}$ is rewritten as

$$\tilde{L}^{(I)} = \int_0^{\mu(-\cos\theta_0+1)} e^{-p}\left(p + \frac{R_c d}{2\alpha(t-t_0)}\right)\frac{\mathrm{d}p}{\sqrt{2p\mu-p^2}}. \tag{B.20}$$

Since $p \ll \mu$,

$$\tilde{L}^{(I)} = -\frac{1}{\sqrt{\mu}}\int_0^{\mu(-\cos\theta_0+1)} e^{-p}\left(p + \frac{R_c d}{2\alpha(t-t_0)}\right)\frac{1}{\sqrt{2p}}\mathrm{d}p, \tag{B.21}$$

$$\tilde{L}^{(I)} = -\frac{1}{\sqrt{2\mu}}\int_0^{3}(e^{-p})\sqrt{p} + \frac{R_c d}{2\alpha(t-t_0)}\frac{e^{-p}}{\sqrt{p}}\mathrm{d}p. \tag{B.22}$$

Similarly for the image source, Eq. (B.13) is written as

$$\check{L}^{(J)} = -\frac{1}{\sqrt{2\lambda}}\int_0^{3\frac{R_c+d}{R_c-d}}(e^{-p})\sqrt{q} - \frac{R_c d}{2\alpha(t-t_0)}\frac{e^{-q}}{\sqrt{q}}\mathrm{d}q, \tag{B.23}$$

where $\lambda = \frac{R_c(R_c+d)}{2\alpha(t-t_0)}$ and $q = \lambda(-\cos\theta+1)$. Then, we have

$$\frac{\tilde{L}^{(I)}}{\check{L}^{(J)}} = \frac{\frac{1}{\sqrt{2\mu}}\int_0^{3}(e^{-p})\sqrt{p} + \frac{R_c d}{2\alpha(t-t_0)}\frac{e^{-p}}{\sqrt{p}}\mathrm{d}p}{\frac{1}{\sqrt{2\lambda}}\int_0^{3\frac{R_c+d}{R_c-d}}(e^{-q})\sqrt{q} - \frac{R_c d}{2\alpha(t-t_0)}\frac{e^{-q}}{\sqrt{p}}\mathrm{d}q}. \tag{B.24}$$

Since $R_c \gg d$, $\frac{R_c+d}{R_c-d} \approx 1$, integration of Eq. (B.24) leads to

$$\frac{\tilde{L}^{(I)}}{\tilde{L}^{(J)}} = \frac{\frac{1}{\sqrt{2\mu}}\left(k_1 + 2k_1\frac{R_c d}{2\alpha(t-t_0)}\right)}{\frac{1}{\sqrt{2\lambda}}\left(k_1 - 2k_1\frac{R_c d}{2\alpha(t-t_0)}\right)}. \tag{B.25}$$

Substitute Eq. (B.25) into Eq. (B.10), and the simplification of Eq. (B.10) leads to

$$\epsilon^{(J)} = \sqrt{\frac{R_c+d}{R_c-d}}\left|\frac{\int_{t_s}^{t_e}\exp\left(\frac{-d^2}{4\alpha(t-t_0)}\right)\left(\frac{1}{t-t_0}+2\frac{R_c d}{2\alpha(t-t_0)^2}\right)dt}{\int_{t_s}^{t_e}\exp\left(\frac{-d^2}{4\alpha(t-t_0)}\right)\left(\frac{1}{t-t_0}-2\frac{R_c d}{2\alpha(t-t_0)^2}\right)dt}\right|, \tag{B.26}$$

$$\epsilon^{(J)} \approx \frac{4R_c+d}{4R_c-d}\sqrt{\frac{R_c+d}{R_c-d}}. \tag{B.27}$$

APPENDIX C. FORMULATION OF ARC-LENGTH REPARAMETRIZATION

For a curve degree higher than one, an exact representation of arc-length parameterization is generally unattainable and must be approximated [1]. This part is dedicated to the transformation of the input B-spline curve $\mathscr{C}(\xi)$ into its approximate arc-length parameterized form. Such parameterization ensures that any variation within the curve parameter ξ, ranging from 0 to 1 in its parameter space, corresponds to a uniform progression from $\mathscr{C}(0)$ to $\mathscr{C}(1)$ along the curve path. In other words, incremental advancements in the parameter $\Delta\xi$ yield a sequence of points evenly spaced along the trajectory of the curve.

The "speed" of the parameter, commonly referred to as the Jacobian or the parametric speed of a curve $\mathscr{C}$, indicates the rate at which the arc length changes with respect to the curve parameter, denoted $ds/d\xi$. It is mathematically defined as

$$\mathscr{J} = \left\|\frac{d\boldsymbol{x}}{d\xi}\right\|_2 = \sqrt{\left(\frac{dx_1}{d\xi}\right)^2 + \left(\frac{dx_2}{d\xi}\right)^2 + \left(\frac{dx_3}{d\xi}\right)^2}. \tag{C.1}$$

A constant Jacobian, or uniform parametric speed along the curve, implies that the curve is parameterized linearly with respect to its arc length. Such a parameterization is particularly desirable as it reflects the consistent traversal speed of the laser source. The total arc length L can be evaluated as follows

$$L = \int_0^1 ds = \int_0^1 \left|\boldsymbol{x}'(\xi)\right| d\xi, \tag{C.2}$$

where $\left|\boldsymbol{x}'(\xi)\right| = \sqrt{\left(\frac{dx_1}{d\xi}\right)^2 + \left(\frac{dx_2}{d\xi}\right)^2 + \left(\frac{dx_3}{d\xi}\right)^2}$ represents the rate of change in arc length, capturing the geometric rate of traversal along the curve.

In the context of an arc-length parameterized curve, the relationship is articulated as

$$\left\| \boldsymbol{x}'(\xi) \right\| = L, \tag{C.3}$$

consistent across all values of the parameter ξ, where

$$L = \int_0^1 \left\| \boldsymbol{x}'(\xi) \right\| \mathrm{d}\xi \tag{C.4}$$

defines the total length of the input curve. The ideal extension ratio corresponds to L, given that our parametric domain $\hat{\Omega}$ spans $[0,1]$. For a parametric domain of length L_{param}, this ratio would be appropriately scaled to L/L_{param}.

By integrating the square of the difference between the derivative of the curve, $\left\| \boldsymbol{x}'(\xi) \right\|$, and the total curve length L over its parametric domain and substituting from Eq. (C.4), we obtain

$$\begin{aligned} \int_0^1 \left(\left| x'(\xi) \right| - L \right)^2 d\xi &= \int_0^1 \left| x'(\xi) \right|^2 d\xi - 2L \int_0^1 \left| x'(\xi) \right| d\xi + L^2 \int_0^1 1 d\xi \\ &= \int_0^1 \left| x'(\xi) \right|^2 d\xi - L^2. \end{aligned}$$

We define the energy function as follows

$$\mathscr{E}_{\text{ArcLength}} = \frac{1}{L^2} \int_0^1 \left| x'(\xi) \right|^2 d\xi. \tag{C.5}$$

The inclusion of the scaling factor $1/L^2$ in Eq. (C.5) normalizes the convergence criterion across curves with different arc lengths L.

The reparameterization process, illustrated in Fig. 1, establishes a relationship between the original curve parameter ξ and a reparameterized parameter $\hat{\xi}$ via a parameter transfer function

$$\xi = \xi(\hat{\xi}) = \sum_{i=0}^{m} \beta_i N_{i,\hat{p}}(\hat{\xi}), \quad \hat{\xi} \in \hat{\Omega} = [0,1], \tag{C.6}$$

where β_i are control coefficients, and $N_{i,\hat{p}}(\hat{\xi})$ are degree $\hat{p}$ B-spline basis functions.

Consider a parametric curve $\mathscr{C}(\xi) = [x_1(\xi), x_2(\xi), x_3(\xi)]^{\mathrm{T}}$, defined over the interval $\xi \in [0,1]$. This curve can be reparameterized by a parameter transfer function $\xi(\hat{\xi})$, ensuring that $\xi(0) = 0$ and $\xi(1) = 1$. The reparameterized curve is expressed as

$$\mathscr{C}(\xi) = \mathscr{C}\left(\xi(\hat{\xi})\right) = \left[x_1\left(\xi(\hat{\xi})\right), x_2\left(\xi(\hat{\xi})\right), x_3\left(\xi(\hat{\xi})\right) \right]^{\mathrm{T}}, \tag{C.7}$$

is referred to as the reparameterization of $\mathscr{C}(\xi)$.

Consider the Jacobian matrix of the curve $\mathscr{C}$, denoted by $\mathscr{J}_\xi = [x_{1,\xi}, x_{2,\xi}, x_{3,\xi}]^{\mathrm{T}}$. Assuming $\mathscr{J}_\xi^{\mathrm{T}} \mathscr{J}_\xi = x_{1,\xi}^2 + x_{2,\xi}^2 + x_{3,\xi}^2 > 0$, we obtain $\mathscr{J}_{\hat{\xi}}^{\mathrm{T}} \mathscr{J}_{\hat{\xi}} = (\xi_{\hat{\xi}})^2 * \mathscr{J}_{\boldsymbol{\xi}}^{\mathrm{T}} \mathscr{J}_{\boldsymbol{\xi}}$ by applying the chain rule, given that $\mathscr{J}_{\hat{\xi}} = \xi_{\hat{\xi}} \mathscr{J}_\xi$. Therefore, $\xi_{\hat{\xi}}$ must be non-zero for all $\hat{\xi} \in \hat{\Omega}$ to ensure a valid transformation of the Jacobian.

To ensure the curve reparameterization preserves bijectivity, $\xi(\hat{\xi})$ must be a non-decreasing monotonic function. This condition guarantees that $\xi(\hat{\xi})$ remains constant

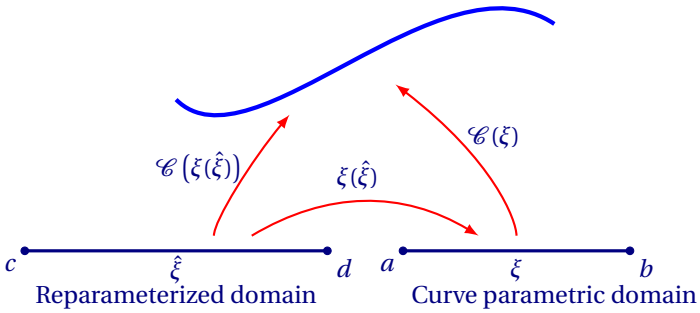

Figure 1: Schematic illustration of curve reparameterization

or increases across any interval within its domain. This monotonicity can be verified by examining the first derivative of $\xi(\hat{\xi})$

$$\frac{d\xi}{d\hat{\xi}} = \hat{p} \sum_{i=0}^{m-1} \frac{\beta_i - \beta_{i-1}}{\hat{\xi}_i - \hat{\xi}_{i-1}} N_{i,\hat{p}-1}(\hat{\xi}), \tag{C.8}$$

where $\hat{p}$ is the degree, and $N_{i,\hat{p}-1}(\hat{\xi})$ are the B-spline basis functions of degree $\hat{p}-1$.

Here, we derive the sufficient conditions to ensure the monotonicity of $\xi(\hat{\xi})$. Specifically, the weights associated with successive positions, denoted by β_i, must satisfy the following relationship

$$\beta_i \geq \beta_{i-1}, \ i = 1, 2, \ldots, m. \tag{C.9}$$

In other words, the weights in successive positions, β_i, should satisfy $\beta_i \geq \beta_{i-1}$. This constraint ensures that the slope of $\xi(\hat{\xi})$ (i.e., its first derivative) remains non-negative, thereby preserving the monotonicity of $\xi(\hat{\xi})$.

While it would be straightforward to directly incorporate the inequality conditions from Eq. (C.9) into a complex constrained optimization problem, this approach could significantly complicate the solution process. To avoid this complexity, we propose transforming the problem into an equivalent but simpler one with simple bound constraints, where the monotonicity constraints are naturally satisfied.

This simplification is achieved by reformulating the optimization problem in increments θ_i applied to the control coefficients β_i, rather than manipulating the coefficients directly. Consequently, the control points, now expressed through these increments, naturally fulfill the inequality constraints specified in Eq. (C.9). This leads to a streamlined optimization problem with simple bound constraints

$$\begin{cases} \beta_0 = \theta_0 = 0, \\ \beta_i = \beta_{i-1} + \theta_i, \quad \text{for } i = 1, 2, \ldots, m \end{cases} \tag{C.10}$$

where each $\theta_i \geq 0$. This approach ensures that each β_i automatically satisfies the required monotonicity without explicit constraint enforcement in the optimization process.

Finally, we solve the following simple bounded constrained optimization problem

$$\begin{aligned} &\underset{\theta_i}{\arg\min}\ \mathscr{E}\left(\theta_i;\ \mathscr{C}(\xi(\hat{\xi}))\right)_{\text{ArcLength}} = \frac{1}{L^2}\int_0^1 \left|x'(\xi)\right|^2 d\xi, \\ &\text{s.t.} \quad \theta_i \geq 0. \end{aligned} \tag{C.11}$$

ACKNOWLEDGEMENTS

Now, it is time to say goodbye to my PhD journey at TU Delft. Overall, I would say that my time in the Netherlands has been an amazing journey. It has not only provided me with top-tier academic training and valuable research experience, but also offered invaluable international life experiences and opportunities to exchange ideas with people from diverse backgrounds.

First and foremost, I would like to express my deepest and most heartfelt gratitude to my promotors, **Fred** and **Can**, for their continuous support, guidance, and encouragement throughout my PhD journey. Without their trust and support, I would not have had the opportunity to begin this tremendous journey. Their insightful advice, patience, and trust have been invaluable to the completion of this work. **Fred**, thank you for your creative ideas and critical suggestions whenever I faced challenges during my PhD. They always provided me with additional perspectives and solutions to the problems I encountered. **Can**, thanks for your patience and efforts spent on supervising me. Your rigorous academic attitude and dedication to research have greatly inspired me, and I will strive to carry these admirable qualities forward in my future life and career.

Besides, I would also like to thank the people in our CDM group. **Jun**, thanks for your trust and for introducing me to Fred and Can, which made this journey possible. **Alejandro**, thank you for your constructive suggestions during Charles meeting, which made the discussion more engaging. **Hans**, you look like a character straight out of The Lord of the Rings—and that's pretty awesome. I'm really impressed by your understanding of education and learning—it has helped me grow and improve during my PhD. **Matthijs**, your rigorous attitude toward teaching and research has deeply impressed me and inspired me to set higher standards for myself. **Haluk**, thank you for the discussions across our meetings. I wish you great success with your machine learning research in our group. **Omid**, I remember when we scheduled that topology optimization test—you did such a good job making sure everything was super organized. Wishing you all the best of luck with your future research. **Lise**, thanks so much for your support and great suggestions during the Charles meeting! Hope everything is going smoothly with the level set method and multimaterial optimization.

Apart from the professors in the CDM group, I would also like to thank my colleagues. **Kai**, thank you for giving me help and suggestions during my PhD in the last five years. I still remember that when I first arrived in Delft, you gave me your bikes for temporary use. I wish you all the best in your further academic journey. **Joran**, the most straightforward guy in the office! Your bravery and honesty have taught me so much. I really appreciate it! **Niles**, your politeness, courtesy, and gentlemanly nature have really impressed me. I hope everything's going great with you. **Maarten**, I've really enjoyed our conversations, even when we started with different opinions. It's been great how they've helped me see things from new perspectives! Hope everything's going well with you

and your girlfriend. **Breno**, thanks for your funny jokes that made our gathering even more enjoyable. I hope everything is going well in your life in the Netherlands. **Aditya**, **Yuheng**, **Rajit**, **Arnoud**, **Stijn**, **Casper**, **Ludovica**, **Sabiju**, **Vibhas**, **Marek**, **Manabendra**, **Yoo-Seong**, **Kawen**, and **Felix**, I would like to express my sincere thanks to all of you for the wonderful time we spent together, and I wish you every success in your research.

Moreover, I would like to express my heartfelt thanks to the Chinese community in PME, **Lidan**, **Yong**, **Hanqing**, **Zhichao**, aka big chao brother, **Zichao**, aka middle chao brother, **Mingkai**, **Minxing**, aka dalao, **Xinxin**, **Xiliang**, **Binbin**, **Xueying**, **Zhilin**, **Yuchen**, **Peiyu**, **Rui**, **Yujiang**, **Ze**, **Ruibo**, **Zhiwei**, **Yuxuan**, **Yueyue**. Thank you for the wonderful trips and the great time we shared together. Wish you all the best in your future research. A special thanks to **Sifeng**, the most friendly Chinese guy, thank you for organizing trips during holidays and inviting us to home for gatherings and parties.

In addition, to colleagues from my previous office, I'm really glad I met you all at the start of my PhD, and I had such a great time with you. **Ruben**, the most popular guy in PME! I still remember all those fun Dutch activities we did together, and they really helped me understand Dutch history and traditions better. Wish you great success in your research. **Ahmed**, I like your jokes about Egyptian history and the pyramids, and the burgers you recommended were great too. I wish you great happiness in life and every success in the future. **Serena**, your horse is super cute. I hope you both have lots of happy adventures together in the Netherlands. **Hava**, thanks for organizing cake's day and office outings. Your happiness and positive spirit have touched us all. To **Martin**, **George**, **Giulio**, **Stavros**, **Daria**, **Shirin**, and **Santiago**, the time we spent together in the old office was truly joyful and full of wonderful memories. I sincerely hope that your research continues to go smoothly and that your life ahead is filled with happiness, success, and everything you wish for.

To colleagues in PME. **Pierre**, the charming Frenchman! I always enjoy your jokes about French traditions and histories. I truly cherish the moments and trips we've shared together. They've been unforgettable. Wishing you all the best, and hope everything is going wonderfully for you! **Fredy**, your smile always brings so much joy to PME Square! I hope everything's going great with your research, and happiness stays with everything you do. **Ata**, you are so specialized in Asian culture and really good at making people laugh. Wishing you all the best in your research and a bright future ahead. **Hande**, you always appear at the same time as Hava and bring so much joy to our conversations. Wishing you all the best in completing your PhD research. To **Vincent**, the piano player, **Francesco**, the celebrity on the Kinder chocolate, **Nick**, **Filippo**, **Tufan**, **Mukund**, **Pieter**, **Ebrahim**, **Paulina**, **Seyed**, **Giorgos**, **Aditya** (in the other office), **Lucas**, **Qais**, **Lara**, **Yu-gyeong**, **Endre**, **Sahar**, **Dave**, **Domas**, **Chris**, **Malte**, **Anna**, **Nastaran**, and many others. It has been truly a pleasure to have you all with me throughout my PhD, and I wish you great success and all the best as you move forward in your careers.

Additionally, I am deeply grateful to the secretaries for their support throughout my PhD journey. **Marianne**, **Lisette**, **Marli**, **Sylviane**, **Natalija**, and **Eveline**, thanks for your patient administrative assistance, which has greatly helped me relocate from China, study and research in the Netherlands. Your help is invaluable to my research, providing essential backing throughout this journey.

To my friends at Delft, **Xue**, **Yaqi**, **Mengjie**, **Hang**, **Li**, **Yun**, **Yixuan**, **Junjie**, **Ye**, **Jinbao**,

Jiaxiang (aka Xiangzi), **Zhaorui**, **Shengren**, and others, thank you all for the wonderful time we shared together. I am truly grateful for the countless hours of badminton we played, the exciting football matches, and all the memorable outings. These moments have made my time in Delft incredibly special and unforgettable. May you all enjoy a smooth life and make progress in your research.

In the end, I would like to express my thanks to **my parents**:
感谢父母无私付出与一路支持鼓励，谨以此文感谢父母多年来的支持与陪伴。

Yang YANG
March 2026

CURRICULUM VITÆ

Yang YANG

05-08-1995 Born in Shashi, Hubei, China.

EDUCATION

2014–2018 Undergraduate in Civil Engineering
South China University of Technology, Guangzhou, China

2018–2021 Master in Structural Engineering
South China University of Technology, Guangzhou, China
Thesis: Study on basis functions in parameterized level set method and its application in solid-shell topology optimization

2021–2025 PhD in Precision and Microsystems Engineering
Delft University of Technology, Delft, The Netherlands
Thesis: Development and application of semi-analytical method for thermal simulation of laser powder bed fusion process
Promotor: Prof. dr. ir. A. (Fred) van Keulen
Supervisor: Dr. Can Ayas

List of Publications

4. **Yang Yang**, F. van Keulen, and C. Ayas, *Simulation of volumetric energy density effects on phase distribution in Ti–6Al–4V laser powder bed fusion process*, To be submitted.

3. T.P.A. Koenis, **Y. Yang**, M. L. Montero-Sistiaga, M.J. de Smit, and C. Ayas, *Efficient thermal modeling towards prevention of local overheating in laser powder bed fusion of magnesium*, To be submitted.

2. **Y. Yang**, Y. Ji, M. Möller, and C. Ayas, *Efficient thermal simulation in metal additive manufacturing via semi-analytical isogeometric analysis*, accepted on: Computer Methods in Applied Mechanics and Engineering.

1. **Y. Yang**, Y. Ji, M. Möller, and C. Ayas, *Computational efficient process simulation of geometrically complex parts in metal additive manufacturing*, published on: International Journal of Heat and Mass Transfer, 248, 127059 (2025).

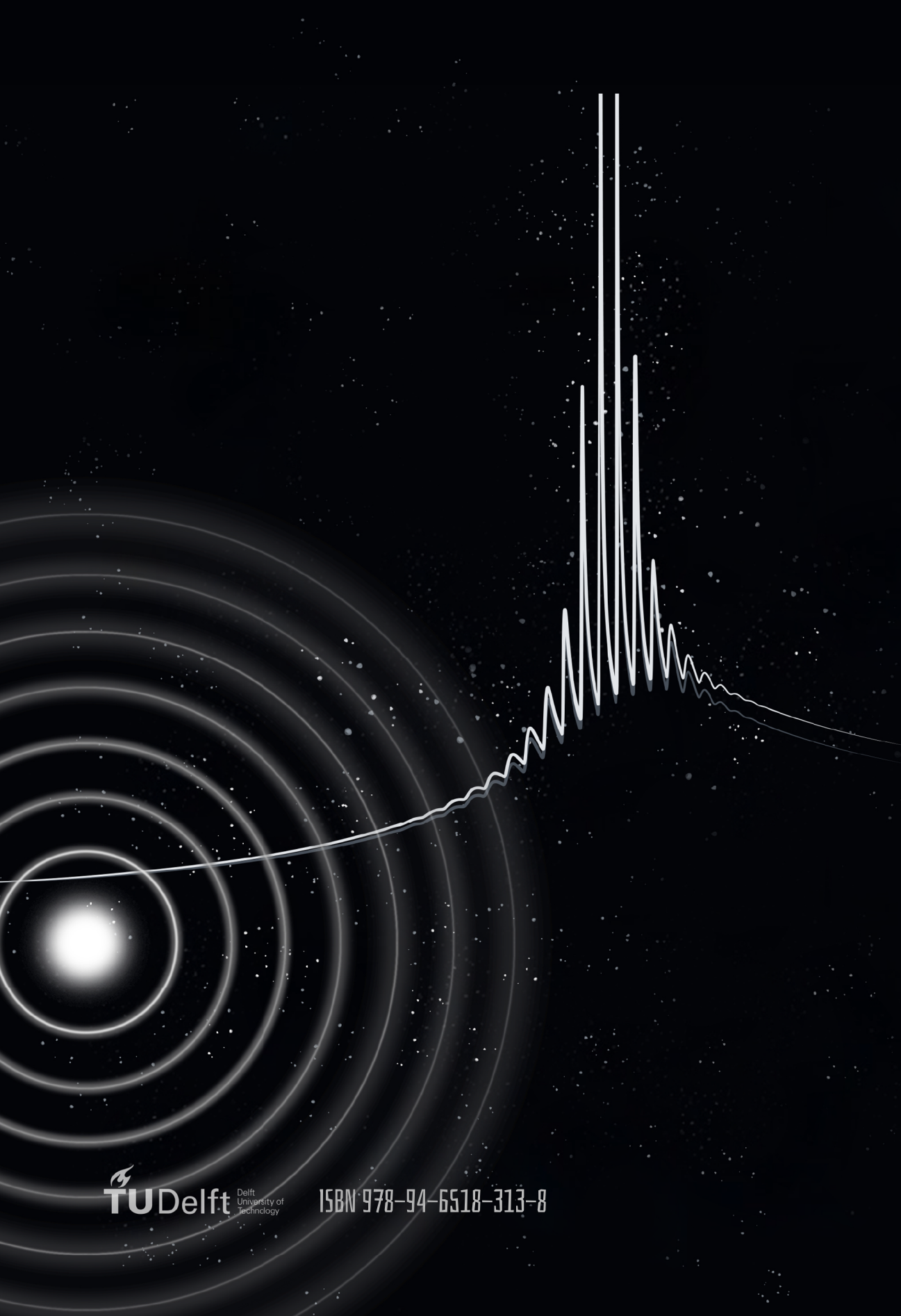

TU Delft Delft University of Technology

ISBN 978-94-6518-313-8